

Politecnico di Torino



PhD in Material Science and Technology

Cycle XXIV

*Hybrid organic/inorganic nanotubes
of imogolite type*

Candidate: Dr. Cristina Zanzottera

Supervisors: Prof. Barbara Bonelli, Prof. Edoardo Garrone

Prof. Christian Fernandez

*“Over a threshold of complexity,
significance and precision become
mutually exclusive”*

(L. Zadeh)

Table of Contents

Introduction.....	1
Chapter 1 – Imogolite, a unique inorganic nanotubular material	
1.1. Inorganic nanotubes.....	9
1.2. Natural hydroxyaluminosilicates (HAS)	9
1.2.1. Structure of natural imogolite.....	10
1.2.2. Structure of natural protoimogolite allophane.....	14
1.2.3. Structure of natural halloysite.....	15
1.2.4. Conclusions.....	17
1.3. Synthetic imogolite nanotubes.....	18
1.3.1. Hydrolysis of TEOS and $\text{AlCl}_3 \cdot 6\text{H}_2\text{O}$	20
1.3.2. Hydrolysis of TEOS and $\text{Al}(\text{NO}_3)_3 \cdot 9\text{H}_2\text{O}$	20
1.3.3. Hydrolysis of TEOS and Aluminum s-Butoxide (ASB)	22
1.3.4. Synthesis procedures suggested for industrial application.....	32
1.4. Properties and applications of imogolite.....	33
1.4.1. Chemical surface properties and adsorption applications.....	33
1.4.2. Electronic properties and relative applications.....	35
1.4.3. Mechanical properties and applications in composites technology.....	36
1.4.4. Biomedical applications.....	37
1.4.5. Antibacterial properties of clays.....	39
1.5. References.....	43

Chapter 2 – Modified imogolite nanotubes: state of the art

2.1. Chemical functionalization of imogolite nanotubes.....	51
2.2. Direct chemical modifications.....	53
2.2.1. Aluminogermanate imogolite nanotubes, Ge-Imo.....	53
2.2.2. Iron-containing imogolite nanotubes, Fe-Si-Imo and Fe-Ge-Imo.....	54
2.3. Post-synthesis chemical modifications.....	56
2.3.1. Hydrophobization of imogolite inner surface.....	56
2.3.2. Phosphorilation of imogolite outer surface.....	57
2.4. References.....	59

Chapter 3 – Methyl-imogolite

3.1. Synthesis.....	63
3.2. FESEM and HR-TEM characterizations.....	63
3.3. XRD and FT-IR characterizations.....	65
3.4. MAS NMR characterization.....	69
3.5. Porosity characterization by N ₂ adsorption/desorption isotherms....	71
3.6. CH ₄ adsorption.....	74
3.7. Conclusions.....	76
3.8. References.....	77

Chapter 4 – Aminated methyl-imogolite

4.1. Introduction.....	81
4.2. Synthesis.....	82
4.3. FESEM and XRD characterizations.....	82
4.4. FT-IR and MAS NMR characterizations.....	84
4.5. Porosity characterization by N ₂ adsorption/desorption isotherms.....	92
4.6. XPS and TGA-Mass characterizations.....	95
4.7. Conclusions.....	97
4.8. CO ₂ adsorption.....	97
4.8.1. FT-IR measurements.....	97
4.8.2. Volumetric measurements.....	100
4.8.3. Conclusions.....	102
4.9. References.....	103

Chapter 5 – Stability of imogolite-type materials

5.1. Introduction.....	107
5.2. MAS NMR measurements.....	108
5.2.1. Cross polarization (CP) study of Me-Imo outgassed at 500 °C.....	114
5.2.2. ²⁷ Al MQMAS study of Me-Imo-NH ₃ ⁺ -30 outgassed at 500 °C.....	118
5.3. TGA-Mass measurements.....	120

5.4. XRD patterns.....	121
5.5. Conclusions.....	122
5.6. References.....	123

Chapter 6 – Acidity and basicity of imogolite-type materials: a FT-IR study

6.1. Introduction.....	127
6.2. Surface sites of imogolite-type materials.....	128
6.3. FT-IR spectra of imogolite-type materials outgassed at high temperatures.....	132
6.4. NH ₃ adsorption.....	134
6.5. CO adsorption.....	140
6.6. Conclusions.....	145
6.7. References.....	146

Appendix I – Characterization techniques.....147

Appendix II - MAS-NMR sequences

A.II.1. Introduction.....	153
A.II.2. Magic Angle Spinning (MAS)	155
A.II.3. Cross Polarization (CP) technique.....	157
A.II.4. Multiple-Quantum MAS (MQMAS) technique.....	160
A.II.5. Simulated ¹ H and ¹³ C NMR spectra of 3-APS.....	162
A.II.6. References.....	166

**Appendix III – Imogolite as a possible negative control for
HARNs, High-Aspect Ratio Nanomaterials**

A.III.1. Introduction.....	169
A.III.1.1. Materials and methods.....	170
A.III.1.2. Results and discussion.....	173
A.III.1.3. Conclusions.....	180
A.III.2. Toxicology of synthetic halloysite.....	180
A.III.3. Toxicology of asbestos.....	182
A.III.4. Toxicology of carbon nanotubes.....	182
A.III.5. References.....	184
Conclusions.....	187
Acknowledgments.....	195
Publications, congress and school partecipations.....	199

Introduction

Inorganic nanotubes like MoS₂ and WS₂, first reported in 1992 [1] and 1993 [2] by Tenne's group, were the first nanotubular materials that succeeded the discovery of the most famous carbon nanotubes in 1991 by Iijima [3], promoting an intense experimental interest in the field. Besides other metal oxide/hydroxide nanotubular structures [4-11], a unique inorganic single-walled aluminosilicate material called *imogolite*, discovered in 1962 by Yoshinaga and Aomine in Japanese soils of volcanic origin [12], has attracted many researchers' interest due to its potential applications as anions/cations retention from water [13-17], catalysis [18,19], gas adsorption, separation and storage [13-15], scaffold for biomedical applications [20] and inorganic nanofiller for polymer matrixes [21-23]. Being an analogue material to carbon nanotubes, it can represent an intriguing different source for new technological applications.

The aim of the present PhD project is to describe the developments obtained in imogolite research field, concerning the synthesis and characterization of two new modified imogolite nanotubes, either by direct or post-synthesis reactions, as compared to unmodified synthetic imogolite.

Synthetic imogolite was obtained for the first time in 1972 by Crawdick *et al.* [24] and patented in 1984 [25], by a sol-gel synthesis in acid environment. In a way similar to the formation of carbon nanotubes, a single sheet of flat gibbsite, Al(OH)₃, in presence of silicates with Al:Si ratio of 2:1, eventually curls up, by the joining of the silicate and gibbsite layers (as Si-O bonds are shorter than Al-O bonds), leading to the replacement of one side of the gibbsite octahedral sheet by a silica tetrahedra. The silanols groups formed, face towards the inside of the tube. Chemical composition of imogolite is given by $(OH)_3Al_2O_3SiOH$, describing the layers of atoms from the exterior to interior of the tube: both inner and outer surface are hydrophilic. Similarly, carbon nanotubes form in order to minimize the energy of the dangling bonds at the edges of graphite sheets. However, they possess a wide range of diameters and numbers of sheets in the walls compared with the relatively well defined diameter and single sheet nature of imogolite tubes.

The main purpose of chemically modifying synthetic materials is the expected increased range of technological applications that can be achieved. Moreover, variables such as purity, composition, reproducibility, and specifically designed features can be often better controlled in synthetic procedures rather than using natural clay specimens, which typically contain impurities and are often not easily available.

Particularly, for nanotubular structures it is critical to develop methods suitable to control the functionality of their internal and external surfaces.

The first new hybrid material of imogolite type was obtained by direct synthesis. The complete hydrophobization of the internal surface was achieved and a new material, methyl-imogolite, labeled as Me-Imo, with stoichiometric formula, $(OH)_3Al_2O_3SiCH_3$, was collected [26,27]. The presence of a hydrophobic inner surface along with an outer hydrophilic one could be in principle exploited in adsorption processes aimed at gas separation (*e.g.* hydrocarbon recovery from wet gaseous streams) or storage: for this reason, volumetric adsorption of methane was tested and compared to imogolite.

Methyl-imogolite represented the starting material for the subsequent post-synthesis silylation reaction with 3-aminopropyltriethoxysilane (3-APS) in anhydrous conditions. MAS NMR (Magic Angle Spinning Nuclear Magnetic Resonance) technique was a crucial tool to demonstrate the successful synthesis, which eventually led to the collection of a new aminated hydrophobic material, labeled as Me-Imo-NH₂.

Structure and textural features of Me-Imo and Me-Imo-NH₂ were studied by combining different techniques, such as XRD (X-ray Diffraction), FE-SEM (Field Emission Scanning Electron Microscopy), HR-TEM (High Resolution Transmission Electron Microscopy), Porosimetry, XPS (X-Ray Photoelectron Spectroscopy), TGA-MS (Thermal Gravimetric Analysis Mass Spectrometry), MAS NMR and FT-IR (Fourier Transform Infrared), and compared to unmodified imogolite. Moreover, stability of each type of nanotubes was estimated as well as the acidity/basicity properties of their surfaces, by recording FT-IR spectra after dosing increasing pressure of gaseous probe molecules, such as NH₃ and CO, at different pre-treatment outgassing temperatures.

Finally, imogolite was tested in a preliminary study as possible negative control for HARNs, High Aspect Ratio Nanomaterials.

References

- [1] R. Tenne, L. Margulis, M. Genut, G. Hodes, *Nature* 360 (1992) 444.
- [2] L. Margulis, G. Salitra, R. Tenne, M. Talianker, *Nature* 365 (1993) 113.
- [3] S. Iijima, *Nature* 354(6348) (1991) 56.
- [4] S. Hu, X. Ling, T. Lan, X. Wang, *Chem. Eur. J.* 16 (2010) 1889.
- [5] L. Pu, X.M. Bao, J.P. Zou, D. Feng, *Angew. Chem. Int. Ed.* 40 (2001) 1490.
- [6] J. Sha, J.J. Niu, X.Y. Ma, J. Xu, X.B. Zhang, Q. Yang, D. Yang, *Adv. Mater.* 14 (2002) 1219.
- [7] A. Albu-Yaron, T. Arad, R. Popovitz-Biro, M. Bar-Sadan, Y. Prior, M. Jansen, R. Tenne, *Angew. Chem. Int. Ed.* 44 (2005) 4169.
- [8] S.J. Son, X. Bai, S.B. Lee, *Drug Discovery Today* 12 (2007) 650.
- [9] M. Bar-Sadan, I. Kaplan-Ashiri, R. Tenne, *Eur. Phys. J. Spec. Top.* 149 (2007) 71.
- [10] R. Tenne, G. Seifert, *Annu. Rev. Mater. Res.* 39 (2009) 387.
- [11] C.N.R. Rao, A. Govindaraj, *Adv. Mater.* 21 (2009) 4208.
- [12] N. Yoshinaga, A. Aomine, *Soil Sci. Plant Nutr.* 8(3) (1962) 22.
- [13] P.I.Pohl, J.L.Faulon, D.M.Smith, *Langmuir* 12 (1996) 4463.
- [14] W.C.Ackerman, D.M.Smith, J.C.Huling, Y. Kim, J.K.Bailey, C.J. Brinker, *Langmuir* 9 (1993) 1051.
- [15] M.A.Wilson, G.S.H.Lee, R.C.Taylor, *Clays Clay Miner.* 50(3) (2002) 348.
- [16] B. Bonelli, I. Bottero, N. Ballarini, S. Passeri, F. Cavani, E. Garrone, *J. Cat.* 264 (2009) 15.
- [17] K.J. MacKenzie, M.E. Bowden, J.W.M. Brown, R.H. Meinhold, *Clays Clay Miner.* 37(4) (1989) 317 and references therein.
- [18] S.Imamura, Y.Hayashi, K.Kajiwara, H.Hoshino, C.Kaito, *Ind. Eng. Chem. Res.* 32 (1993) 600.
- [19] S. Imamura, T. Kokubu, T. Yamashita, Y. Okamoto, K. Kajiwara, H. Kanai, *J.Catal.* 160 (1996) 137.
- [20] K. Ishikawa, T. Akasaka, S. Abe, Y. Yawaka, M. Suzuki, F. Watari, *Bioceramics Develop. App.* 1 (2011) 1.
- [21] P. Calvert, *Nature* 357 (1992) 365.
- [22] K. Shikinakaa, Y. Koizumia, Y. Osadab, K. Shigehara, *Polym. Adv. Technol.* 22 (2011) 1212.
- [23] K. Yamamoto, H. Otsuka, S.I. Wada, D. Sohnd, A. Takahara, *Soft Matter* 1 (2005) 372.
- [24] C.P.G. Cradwick, V.C. Farmer, J.D. Russell, C.R. Masson, K. Wada, N. Yoshinaga, *Nat. Phy. Sc.* 240 (1972) 187.
- [25] V.C. Farmer, US Patent 4,252,779.
- [26] I. Bottero, B. Bonelli, S. Ashbrook, P. Wright, W. Zhou, M. Tagliabue, M. Armandi, E. Garrone, *Phys. Chem. Chem. Phys.*, 13 (2011) 744 -750.
- [27] B. Bonelli, I. Bottero and E. Garrone, Italian patent 0001380065.

Chapter 1

*Imogolite,
a unique inorganic
nanotubular material*

1.1. Inorganic nanotubes

The discovery of carbon nanotubes in 1991 by Iijima [1] has significantly attracted researchers' attention as potential model systems for nanotechnology due to their unexpected properties and applications in electronics, composite materials and electrochemistry [1-8]. Iijima realized that graphite could be bent to form multi walled tubes with different chiralities, term which refers to the way hexagonal carbon rings are arranged with respect to the tube axis. However, several problems in carbon nanotube technology remain to be overcome as the development of a low-temperature synthetic process with high yield as well as precise control over nanotube dimensions, are of crucial importance.

On the other hand, inorganic nanotubes like MoS₂ and WS₂, first reported in 1992 [9] and 1993 [10] by Tenne's group, were the first inorganic nanotubes that succeeded the discovery of carbon nanotubes, promoting an intense experimental interest in the field. Besides other metal oxide/hydroxide nanotubular structures [11-18], single-walled aluminosilicates, like natural [19] and synthetic [20] imogolite, halloysite nanotubes [21], the specular imogolite tube, and single and double-walled aluminogermanate nanostructures [22], have been rediscovered in the past decades as potential materials for several technological applications, which will be presented in detail in the following paragraphs. Besides nanotubular structures, inorganic fullerene-like nanoparticles, including BN [23-27], BC₂N [25], GaS [28], TiO_x [29,30], have also been showing to have interesting perspectives.

1.2. Natural hydroxyaluminosilicates (HAS)

Natural hydroxyaluminosilicates (HAS) are secondary mineral phases of critical importance to the biogeochemical cycle of aluminum [31]. Two discrete forms of HAS have been distinguished by both their stoichiometries and coordination of aluminum and silicon [32]: HAS_A, also called *protoimogolite*, which is formed under conditions where $[Al] > [Si(OH)_4]$, with Si:Al ratio of 0.5 and all aluminum atoms being present in octahedral coordination; HAS_B, *protoimogolite allophane*, is instead formed under conditions where $[Al] < [Si(OH)_4]$ and has a Si:Al ratio of 1.0 with half aluminum atoms in tetrahedral coordination.

Among HAS_A and HAS_B, *halloysite* [21,33,34] and *imogolite*, have also been identified on the basis of dispersion characteristics in aqueous media, XRD, DTA (Differential Thermal Analysis) [35] and IR [36,37] measurements, although SEM [34,35,38], TEM [37,39] and early MAS NMR measurements in 1982 [40] resulted to be crucial tools to clearly discriminate *ITMs*, *Imogolite-Type Materials*, as they are overall defined. Three hypotheses are generally accepted on how *ITMs* are formed

1. Aluminum and silicon are released by weathering in the Eluvial (E) horizon and migrate downwards until inorganic aluminum and H₄SiO₄ form proto-imogolite sols once the soil pH is sufficiently high [41]. These sols may be precipitated as *ITMs*.
2. The upper part of the podzolic profile (O, E and B horizons) is dominated by metallorganic complexes, which are responsible for the formation of the Bhs horizon. Here the aluminum and silicon activities would be governed by the simultaneous equilibrium with imogolite and interlayered hydroxy-Al in 2:1 layer silicates.
3. Iron and aluminum released by weathering complexes with organic matter precipitate in the B horizon according to classical podzolisation theory, or adsorb onto already formed secondary Fe-oxide and Al-oxide minerals [42]. Microbes subsequently degrade some of the organic matter and the released aluminum combines with soil solution of H₄SiO₄ to form imogolite, while Fe forms ferrihydrite [43].

1.2.1. Structure of natural imogolite

Imogolite is a short-range nanotubular ordered aluminosilicate with an Al:Si ratio of 2:1. Its occurrence was first demonstrated in 1962 by Yoshinaga and Aomine in clay fractions of soil (*Imogo*) derived from glassy volcanic sources [19]. After the initial discovery, it has also been detected in Spodosols in Scotland, Canada and in northwestern United States [44-47, Figure 1].

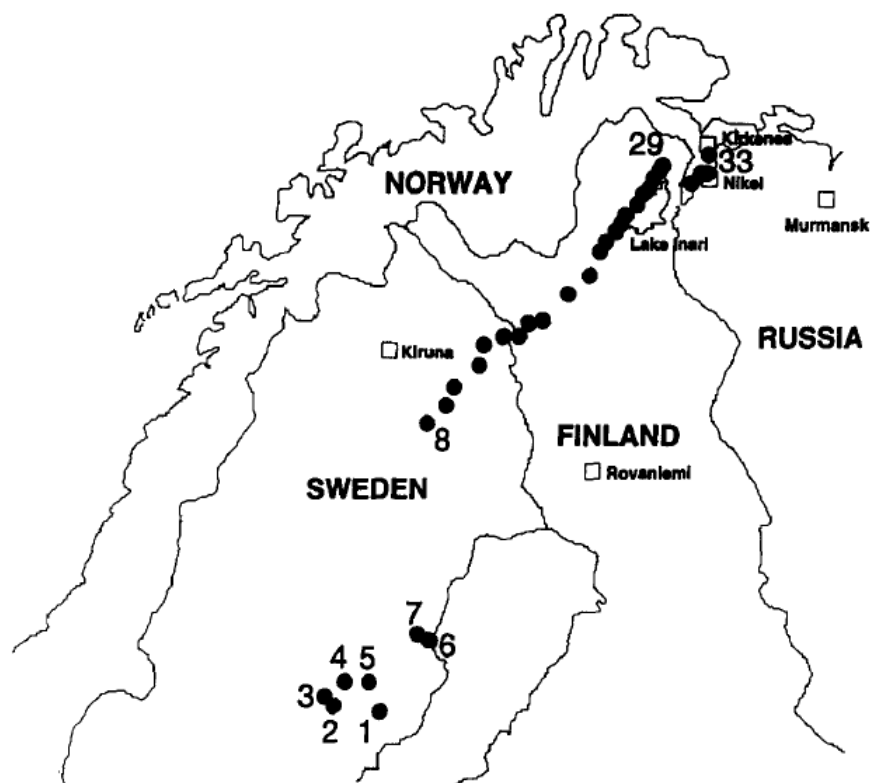


Figure 1: Geographical location of natural imogolite sites [47].

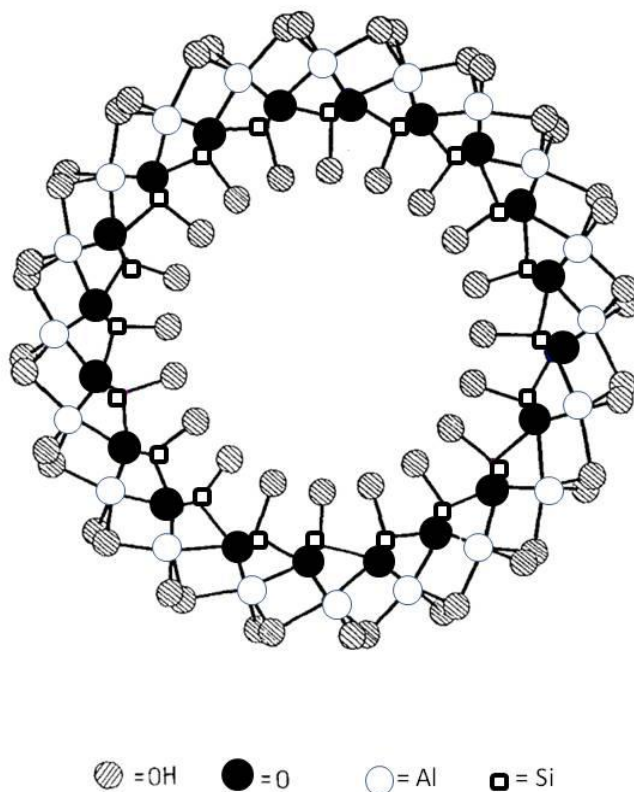


Figure 2: Structure of imogolite nanotube.

In a way similar to the formation of carbon nanotubes, a single sheet of flat gibbsite, $\text{Al}(\text{OH})_3$, in presence of silicates with Al:Si ratio of 2:1, eventually curls up, by the joining of the silicate and gibbsite layers (as the Si–O bonds are shorter than Al–O bonds), leading to the replacement of one side of the gibbsite octahedral sheet by a silica tetrahedra. The silanols groups formed, face towards the inside of the tube.

Chemical composition of imogolite mineral is given by $(\text{OH})_3\text{Al}_2\text{O}_3\text{SiOH}$, describing the layers of atoms from the exterior to interior of the tube (Figure 2): both inner and outer surface are hydrophilic. Similarly, carbon nanotubes form in order to minimize the energy of the dangling bonds at the edges of graphite sheets. However, they possess a wide range of diameters and numbers of sheets in the walls compared with the relatively well defined diameter and single sheet nature of imogolite tubes. Electron micrographs have shown that imogolite tubes are formed rarely isolated while tend to aggregate in spider web networks with different degrees of order [47-52]. Moreover, the number and dispersion of bundles appears to be pH dependent [39,40]. The consequence of this packing reflects the peculiar porosity of imogolite nanotubes (Figure 3).

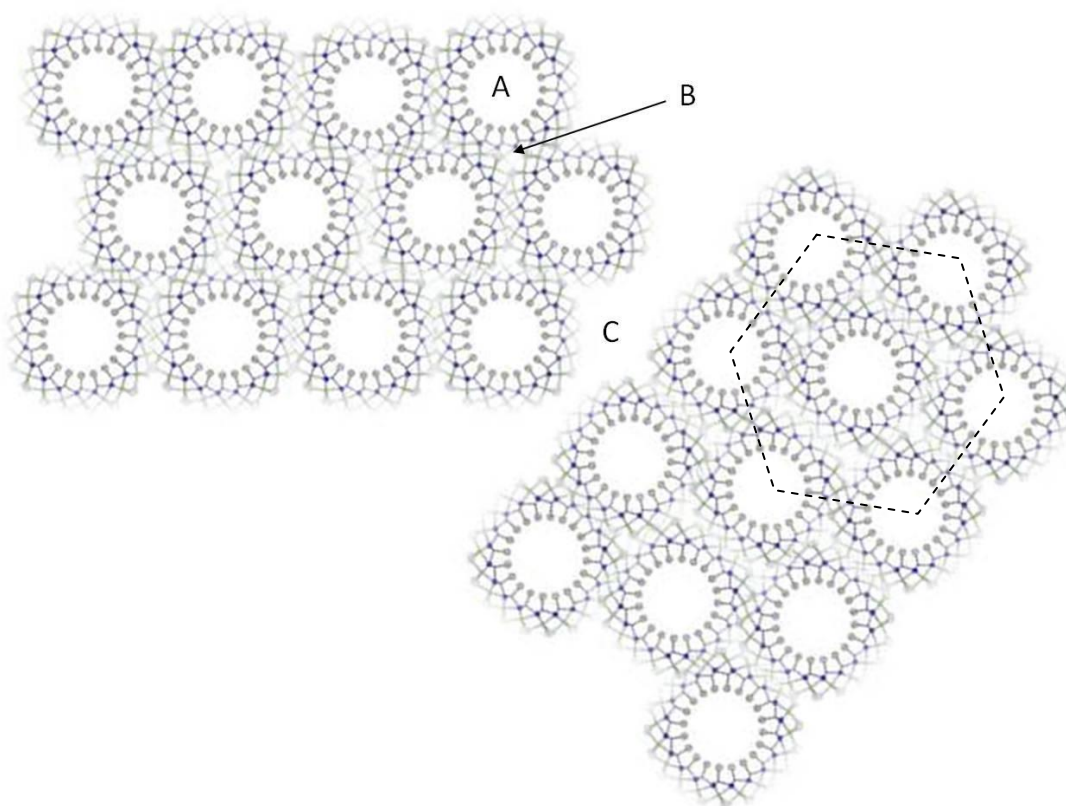


Figure 3: Type of pores found in imogolite. Hexagonal packing of nanotubes is considered.

Three main types of pores can be distinguished

- i. Intra-tube pores (type A).
- ii. Inter-tube spaces, which are the spaces between three aligned tubes in a regular packing (type B). These holes are so small (0.3–0.4 nm) that they can be ignored, according to literature, in any discussion of adsorption [49,53].
- iii. Mesopores, which are the empty spaces between bundles of tubes (type C).

The resulting pore size relationship is: $C > A > B$. A TEM image of bundles of natural imogolite is shown in Figure 4 [39].

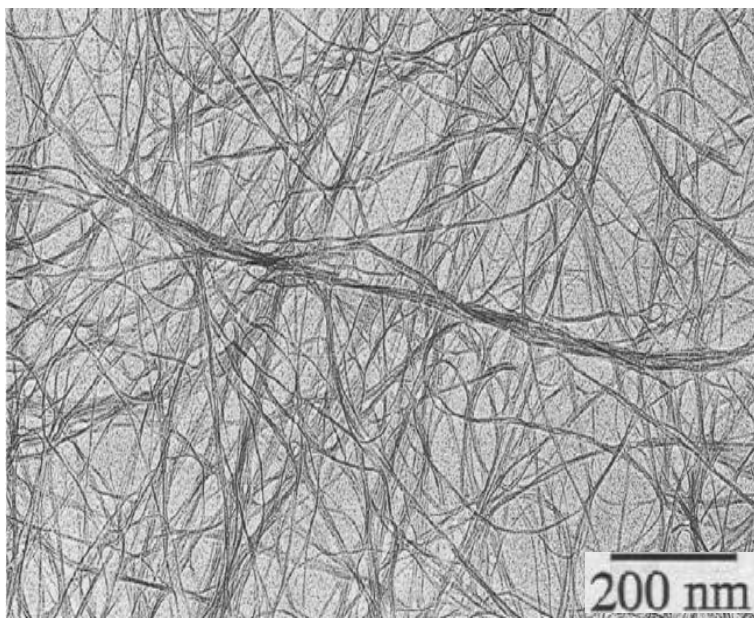


Figure 4: TEM image of natural imogolite [39].

Recently, electrophoresis analyses and acid–base potentiometric titrations on natural imogolite [54], confirmed the geometrical distribution of surface charge groups, i.e. negative SiO^- inner groups and positive AlOH_2^+ groups located outside, respectively, according to the following reactions



However, only the positive counter ions seem to have a significant effect on the electrokinetic properties of this clay mineral. Since 1969 [35], because of its unique chemical structure with high surface area [55] and surface reactivity [56], Wada proposed imogolite as a possible gas and ion adsorbent. Therefore, once synthetic imogolite was successfully obtained for the first time in 1971 [20], its physical, chemical and electronic properties have been widely studied in the following years. They will be reported and discuss thereafter, along with those of protoimogolite and halloysite.

1.2.2. Structure of natural protoimogolite allophane

Protoimogolite allophane is an amorphous aluminosilicate mineral composed of hollow spherical and not tubular nanostructures (Figure 5), despite the similar composition of its walls with imogolite, consisting of inner silica and outer alumina layers [57-61]. Wada in 1977 [59] and Parfitt in 1980 [62] were able to explain the different morphology by the presence of some defects and pores occurring during the geological formation of allophane.

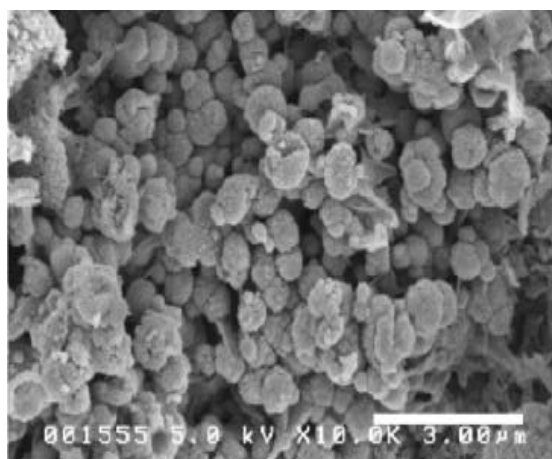


Figure 5: Scanning Electron Microscopy (SEM) image of protoimogolite allophane [64].

The first synthesis of allophane ever reported was in 1988 by Wada and co-workers [63]. Thermal analyses, XRD patterns, FTIR and MAS NMR measurements performed were helpful to highlight also the differences between natural and synthetic allophanes.

Further studies suggested that their peculiar surface properties [56] and high surface area [57,60] make allophanes, besides imogolite, suitable candidates for ionic and gas adsorption due to their amphoteric ion exchange activity [65-73]. A very recent and outstanding application wants the use of allophane for inject technology process [74].

1.2.3. Structure of natural halloysite

Imogolite and halloysite are naturally occurring aluminosilicate minerals with different Al:Si ratio, 2:1 and 1:1, respectively (Figure 6). Despite this, their morphology can be described as specular. In fact, halloysite nanotubes consist of a gibbsite octahedral sheet, $\text{Al}(\text{OH})_3$, which is modified by siloxane groups not at the inner surface, as the case of imogolite, but at the outer surface. The resulting stoichiometry is: $\text{Al}_2\text{Si}_2\text{O}_5(\text{OH})_4 \cdot n\text{H}_2\text{O}$. It can grow into long multiwalled tubes, which are similar to some extent to multiwalled carbon nanotubes [75].

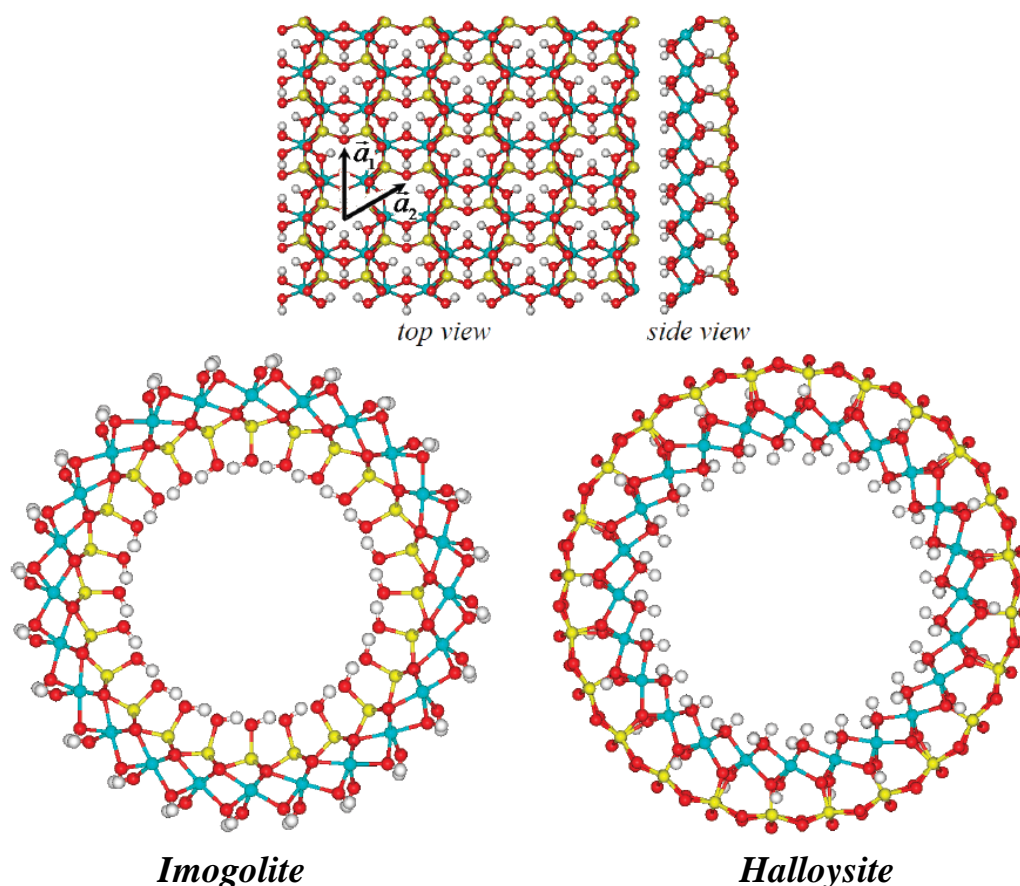


Figure 6: Structure of halloysite monolayer (upper image) and cross section views of imogolite and halloysite nanotube. White atoms are H, red O, gray Al, and yellow Si [76].

However, it is also possible to find layered halloysite structures, which occur mainly in two different polymorphs, the hydrated form, with formula $\text{Al}_2\text{Si}_2\text{O}_5(\text{OH})_4 \cdot 2\text{H}_2\text{O}$, and the anhydrous form having the same chemical composition as kaolinite, $\text{Al}_2\text{Si}_2\text{O}_5(\text{OH})_4$. The size of dehydrated halloysite particles varies from 0.5 to 1 μm in length and 15 to 100 nm in inner diameter, depending on the substrate [77,78]. The average Al-O, Si-O, and O-H bond lengths calculated for the anhydrous form of halloysite nanotube [76] are equal to 1.88, 1.68, and 0.96 Å, respectively. These values are in agreement with those reported for imogolite nanotubes (1.89 and 1.68 Å for Al-O and Si-O bond, respectively) [79]. Although kaolinite is a planar sheet, it is interesting to compare halloysite distances with kaolinite reported X-ray data (1.87 and 1.62 Å for Al-O and Si-O bonds, respectively) [80]. Figure 7 shows a TEM image of halloysite nanotubes.

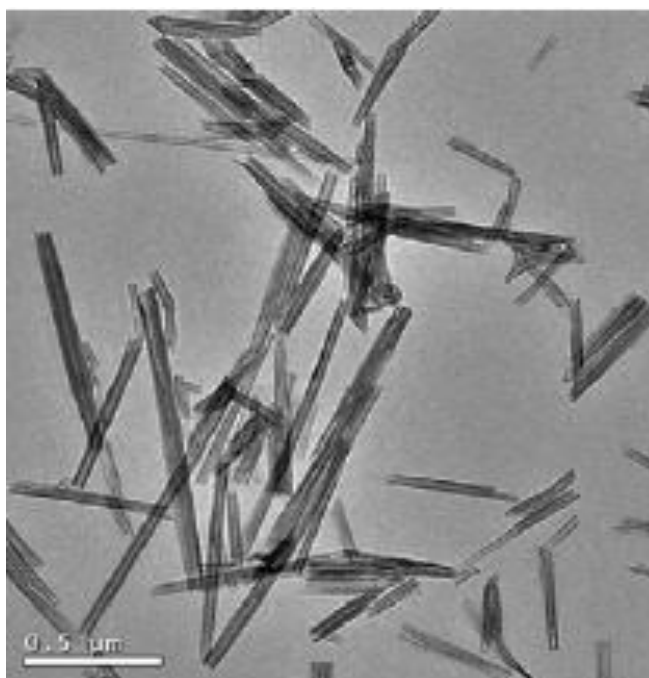


Figure 7: TEM image of halloysite nanotubes [81].

Even though much less studied than imogolite and carbon nanotubes, halloysite nanotubes have been rediscovered as attractive materials, as confirmed by the vast recent literature about their applications. Price *et al.* [78,82-84] and other authors [85,86] studied halloysite as potential material for drug delivery and biomedical applications [87]. Moreover, a supramolecular adduct of DNA-wrapped halloysite nanotubes has been also obtained for the first time. This result extends once more the analogy with multiwalled carbon nanotubes [88,89].

Halloysite has also been tested as a support for immobilization of catalyst molecules [90-93], as adsorbent for gas [94,95] and pollutants [96,97], nonetheless for the controlled release of anticorrosion agents, herbicides and fungicides [98-100]. As inorganic nanofillers, they demonstrated to improve mechanical performance of cements and polymers [101-107]. Particularly, the successful synthesis of capric [81] and stearic [108] acid/halloysite composites makes them potential candidates for thermal energy storage. Recently, they have also been used as additives for biomass technology [109].

1.2.4. Conclusions

Protoimogolite allophane, imogolite, and halloysite commonly coexist in volcanic ash soils. Their different properties are related to their structure and morphology.

Allophanes are composed of small hollow spherules with specific surface areas of approximately 800 m²/g [62]. Samples with Al/Si molar ratios close to 2.0 have a gibbsite Al(OH)Al outer surface, and their surface properties appear to be related to the presence of defects.

Imogolite has a tubular morphology and a reported specific surface area between 250 (or lower) and 1500 m²/g [62]. The spread of values reported may depend on several aspects, including the relative concentration of amorphous phase, which may affect the surface area value, but also the experimental technique used, *e.g.* Brunauer-Emmett-Teller (BET) method vs. Ethylene Glycol Monoethyl Ether measurement (EGME) [110]. Nevertheless, the larger surface area and the fewer defect sites on imogolite, as compared with allophane, may account for the different reactivity of these two mineral species.

Halloysites have surface properties which are related to its morphology and the number of edge sites. Tubes have a Si-O-Si outer surface [111,112] that resulted to be less reactive, *e.g.* towards phosphate, than the Al(OH)Al surface.

1.3. Synthetic imogolite nanotubes

Synthetic imogolite was obtained for the first time in 1972 by Crawdick *et al.* [20] and patented in 1984 [113]. Briefly, it is a sol-gel synthesis in acid environment in which a silicon precursor, generally TEOS (tetraethoxysilane) is let react with an aluminum precursor, $\text{AlCl}_3 \cdot 6\text{H}_2\text{O}$ [20,114], $\text{Al}(\text{NO}_3)_3 \cdot 9\text{H}_2\text{O}$ [115] or Aluminum sec-Butoxide (ASB) [116]. In order to take into account possible ways to scale up imogolite synthesis for industrial applications, other aspects should be considered beyond the reproducibility of the methods. For instance, reagents cost. Recently, interesting contributions to perform batch and flow systems reaction as well as high syntheses yield have been given by Abidin *et al.* [117] and Levard *et al.* [118]. The detailed synthesis procedures as well as improvements and modifications that were introduced in this PhD work will be discussed in the next paragraphs.

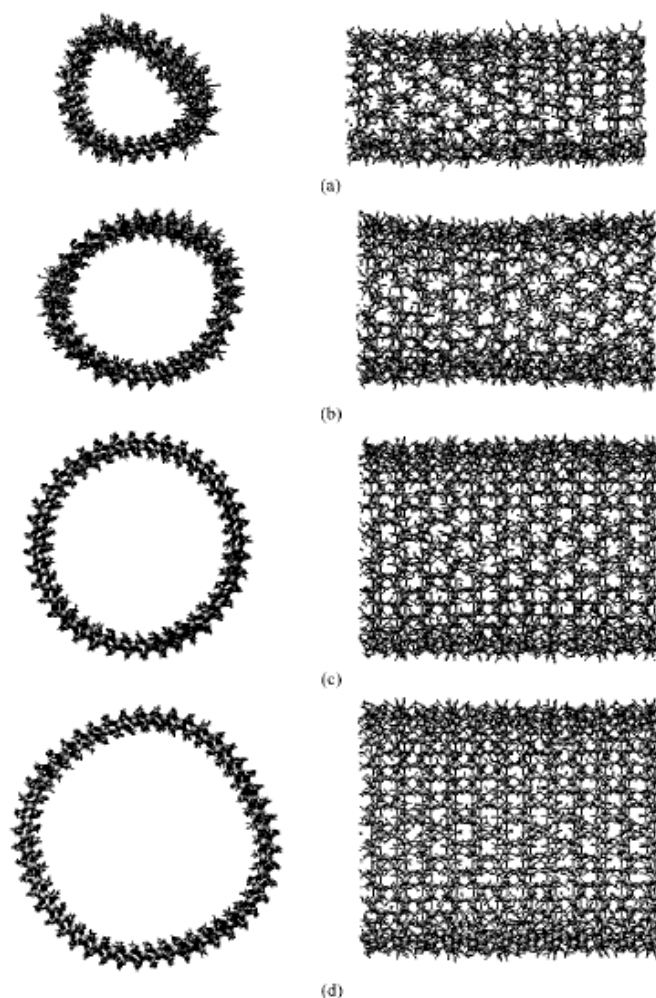


Figure 8: Molecular structures of tubular gibbsite after MD simulations with different number of gibbsite units (Nu): (a) 12; (b) 16; (c) 20; (d) 24 [119].

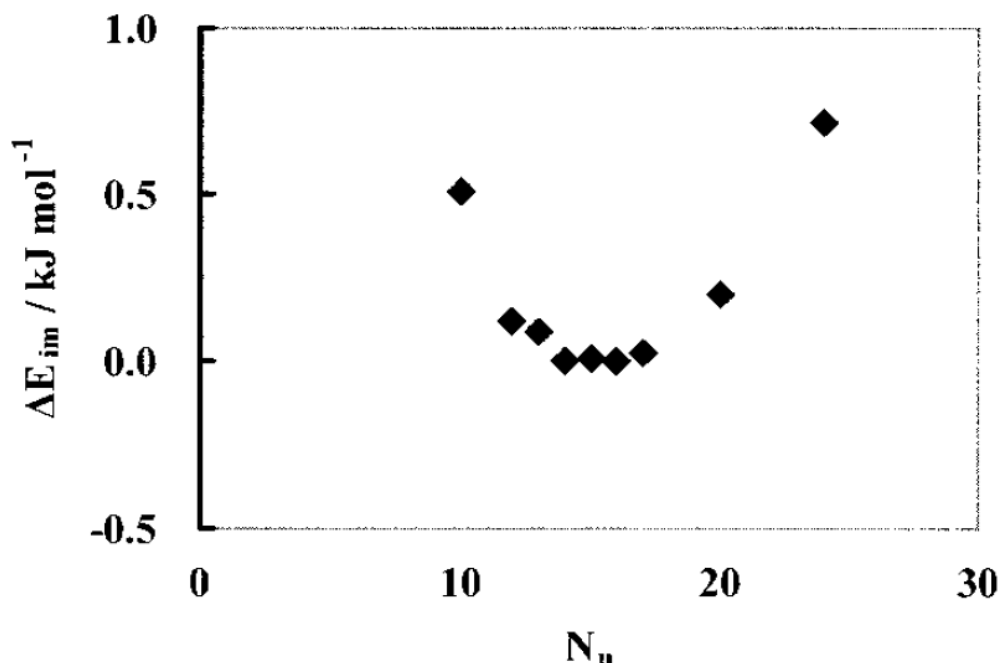


Figure 9: Total energy of imogolite, expressed as ΔE , for several numbers of gibbsite units, i.e. 10, 12, 13, 14, 15, 16, 17, 20, and 24, relative to the minimum energy corresponding to $N_u = 16$ [119].

General evidence obtained for synthetic imogolite nanotubes, if compared to natural samples, showed that their porosity is comparable. However, synthetic products are not identical to natural materials, mainly because their diameter resulted to be significantly larger than that of natural imogolite. Moreover, synthesis conditions may affect the structural composition, as theoretical calculations have demonstrated [51]. The natural form of imogolite is likely to have 10 units, as Crawdick *et al.* suggested [20]. However, the model with 12 gibbsite units around the perimeter is the most likely structure according to a lot of authors [79,119-126]. Only few authors proposed instead the presence of 14-16 units [119,125]. Figure 8 shows the molecular dynamics simulations results for 12 to 24 gibbsite units, Figure 9 the correspondent energies.

Despite some variances, which Dovesi *et al.* explained could be due to different geometries considered as well as different types of computational methods implemented [127], it is generally accepted that the reason for the expanded size should be attribute to the high temperature (100 °C) used in the synthesis, not achieved in natural occurring process, which serves to stretch over the Si-O bond.

1.3.1. Hydrolysis of TEOS and $\text{AlCl}_3 \cdot 6\text{H}_2\text{O}$

According to the early synthesis procedures proposed by Crawdick, Wada and co-workers [20,114], tetraethoxysilane [TEOS] was added dropwise to 2.4 mmol/L aluminum chloride ($\text{AlCl}_3 \cdot 6\text{H}_2\text{O}$) aqueous solution to achieve 1.8 Al:Si ratio. The pH of the solution was first increased to 5.0 by using 0.1 mol/L sodium hydroxide aqueous solution to allow the hydrolysis of the precursors. Afterwards, the solution was acidified by adding 1.0 mmol of hydrochloric acid and 2.0 mmol of acetic acid per liter of the solution. The acidified solution was then refluxed at 100 °C for 5 days. Recently, details about the growth mechanism of nanotubes according to this procedure were reported [128,129]. Particularly, Nair and co-workers introduced little modifications in order to better control the dimension and morphology of the resulting nanotubes [130]. Moreover, they suggested a scheme for nanotubes self-assembly rather different from that proposed for the first time by Bursill [131]. The originally kinetically driven mechanism suggested that the quantity of nanotubes formed grows substantially with the reaction time, with all the precursors being consumed by *ca* 120 h of synthesis time. Thus, the formation of “proto-imogolite” precursors took place early in the reaction, and these precursors provided nuclei to the growth and formation of nanotubes during the polymerization step.

In contrast to this approach, a thermodynamically driven self-assembly process seems possible to operate. In this case, nanotubes of specific dimensions are expected to self-assemble as dictated by precursor solution properties and temperature, which are the controlling parameters. Additionally, nanotubes are formed at an early stage in the reaction and their structure, both in terms of length and diameter, remains essentially identical throughout the synthesis, as DLS (Dynamic Light Scattering) measurements strongly indicates.

1.3.2. Hydrolysis of TEOS and $\text{Al}(\text{NO}_3)_3 \cdot 9\text{H}_2\text{O}$

In 2011 [132], TEM technique was used to follow imogolite synthesis steps comparing two methods: the first was the method described above (labeled as S-I), the second (S-II) was instead a modified method proposed for the first time by Farmer in 1983 [115], in which aluminum chloride precursor is replaced by $\text{Al}(\text{NO}_3)_3 \cdot 9\text{H}_2\text{O}$.

Particularly, a solution of TEOS was added to a 5 mM aqueous solution of $\text{Al}(\text{NO}_3)_3 \cdot 9\text{H}_2\text{O}$ to achieve an Al:Si ratio of 2:1. Then a 1×10^{-2} M NaOH solution was added at a rate of 0.5 mL/min until an Al:Si:OH ratio of 2:1:4 was obtained, reaching a pH value of 5.0. The mixture was then stirred vigorously for 60 min and heated to 95 °C for 10 days. Finally, a 0.1 M solution of NH_4OH was added until the pH got to 8.0, yielding a transparent gel which was separated and washed with deionized water by centrifuging. During both syntheses, samples were taken at 0, 24, 48, 72, 96, 120, 168, 192 and 240 h before the end of the hydrolysis process. The corresponding TEM images are reported in Figure 10. This study made it possible to establish that the formation of imogolite consists of two steps: the first one is the formation of nanometric precursors of imogolite, obtained by a self-assembly process achieved after aging times of 24 h for S-I and 48 h for S-II, while the second step is the formation and further increase of the concentration of imogolite nanotubes as a result of the aging process.

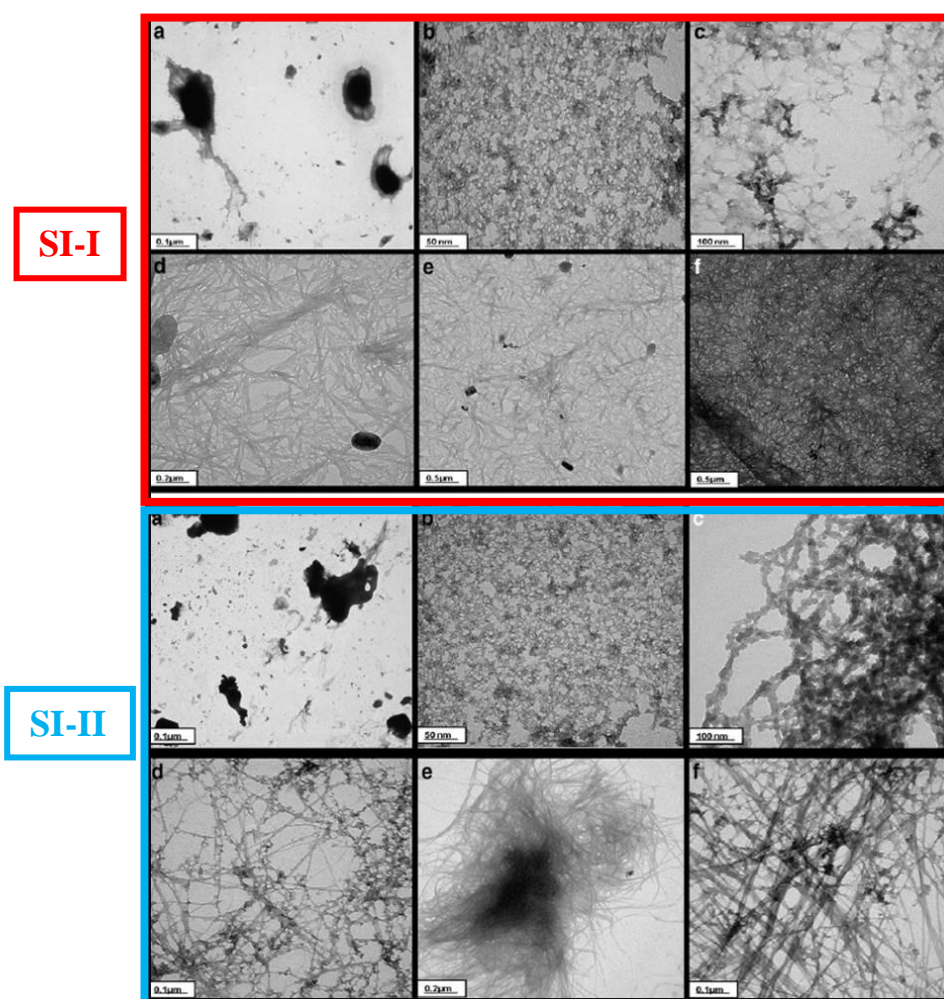


Figure 10: TEM images of imogolite samples obtained using the S-I and S-II method. (a) 0 h, (b) 24 h, (c) 72 h, (d) 120 h, (e) 168 h, and (f) 240 h [132].

As a whole, TEM analysis of S-I and S-II allowed establishing the structures of the intermediary products and their evolution during the aging process, identifying globular, necklace-type, and nanotube structures which condense at longer aging times. The formation of necklace-type structures, intermediate between the imogolite globular structures and nanotubes, coincides with a significant increase of the IEP (Isoelectric Point), of the order of two pH units.

1.3.3. Hydrolysis of TEOS and Aluminum s-Butoxide (ASB)

The guidelines proposed by Farmer *et al.* in 1978 [116] are quite similar: at 20 °C TEOS (Tetra-ethoxysilane) and Al(s-butoxide)₃ were added to a 75 mM aqueous solution of HClO₄ in the molar ratios Si:Al:HClO₄ = 1.x:2:1. A slight excess of TEOS was used in order to prevent the preferential formation of gibbsite during hydrolysis. The solution was stirred for 18 h, diluted to 20 mM, autoclaved at 100°C for 4 days, dialyzed for at least 4 days against deionized water and then dried at 50 °C. Reaction conditions resulted to be very strict, and unsuccessful syntheses lead to amorphous protoimogolite allophane, which can be clearly distinguished by XRD and FT-IR measurements [36,133-135]. A systematic study analogue to that reported in the last paragraph [136], on the mechanism of formation of single-walled aluminosilicate nanotubes obtained with ASB precursor, was performed via combined ESI-MS (Electron Spray Ionization Mass Spectrometry) and NMR characterization by Nair and co-workers [137]. They showed that nanotube assembly is preceded by the formation of precursors that already possess a similar chemical coordination environment of aluminum and silicon atoms, as well as an inherent tendency to form curved nanostructures. The condensation of these proto-nanotube precursors into larger nanoparticles upon heating (as observed by DLS measurements and by the disappearance of these species in ESI-MS spectra) provides a clear connection to the subsequent formation of ordered nanotubes. The rearrangement into nanotubes is accomplished by the conversion of tetra-coordinated groups of the precursor species to a fully octahedral configuration.

In this PhD work, was followed the latter procedure since it resulted to be the most reproducible on lab scale, introducing little modifications that will be explained below and taking always into account that attention must be paid when grinding the dried sample to collect fine grains.

In fact, it is known that mechanical treatment can affect imogolite morphology and structure [138]. In order to reduce synthesis time, dialysis method was replaced by a filtration step, using Whatman Anopore filters (0.02 μm), and so obtaining purified imogolite sol in few hours instead of few days. Moreover, a further final step was introduced to remove the highest amount of amorphous phase, which can be formed in variable amount during the reaction [114]. Therefore, the dried powder was then washed, collected after filtration against deionized water, for a night long. As can be seen from XRD (Figure 11) and FT-IR (figure 12) results, crystallinity and purity are improved.

XRD patterns of fresh and washed filtered imogolite present four main peaks at 3.77, 5.53 (shoulder), 9.89 and 13.3 2θ , respectively. The first peak at 3.77 2θ is the most intense and it is assigned to the reflection of (100) planes: the d_{100} , as calculated by the Bragg's Law, is 2.34 nm and it is directly correlated with the angle of package of nanotubes.

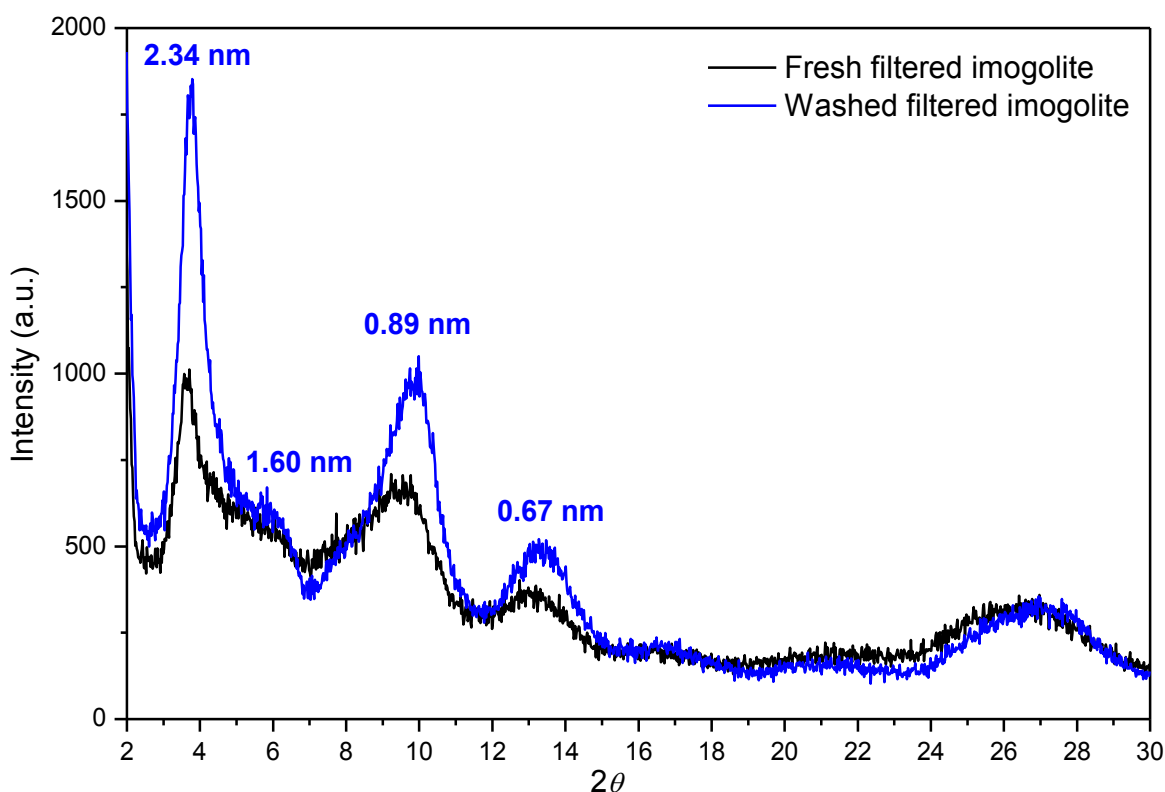


Figure 11: XRD patterns of fresh filtered imogolite (black line) and washed filtered imogolite (blue line).

As a consequence, the shape of the peaks can be expected to be not completely symmetric due to the presence of other coinciding bands. For example, little modifications in position of this main (011) peak should occur with the variation of the packaging angle.

This explains the shoulder at $5.53\ 2\theta$ (1.60 nm), assigned again to (110) planes, that does not always appear in imogolite XRD patterns. Interestingly, the washing treatment enhanced its intensity. The peak at $9.90\ 2\theta$ (0.89 nm) is instead assigned to a repetition of the structural unit along the tube, whereas that at $13.3\ 2\theta$ (0.67 nm) is caused by the reflection of (211) planes [20,130]. The broad band at $24\text{-}30\ 2\theta$ is proper imogolite reflections, as simulated diffraction patterns confirm [139]. No agreement is achieved about nanotubes arrangement. In fact, the majority of authors believe it is hexagonal [51,127,140]. Nevertheless, the monoclinic displacement has been also proposed [130,141].

FT-IR spectra of KBr supporting wafers of fresh filtered imogolite and residual water confirm that filtration method can be successfully used to obtain pure imogolite tubes, as residual water spectrum does not show the typical 990 and $944\ \text{cm}^{-1}$ bands, assigned to Si-O and Al-O stretching vibrations [142].

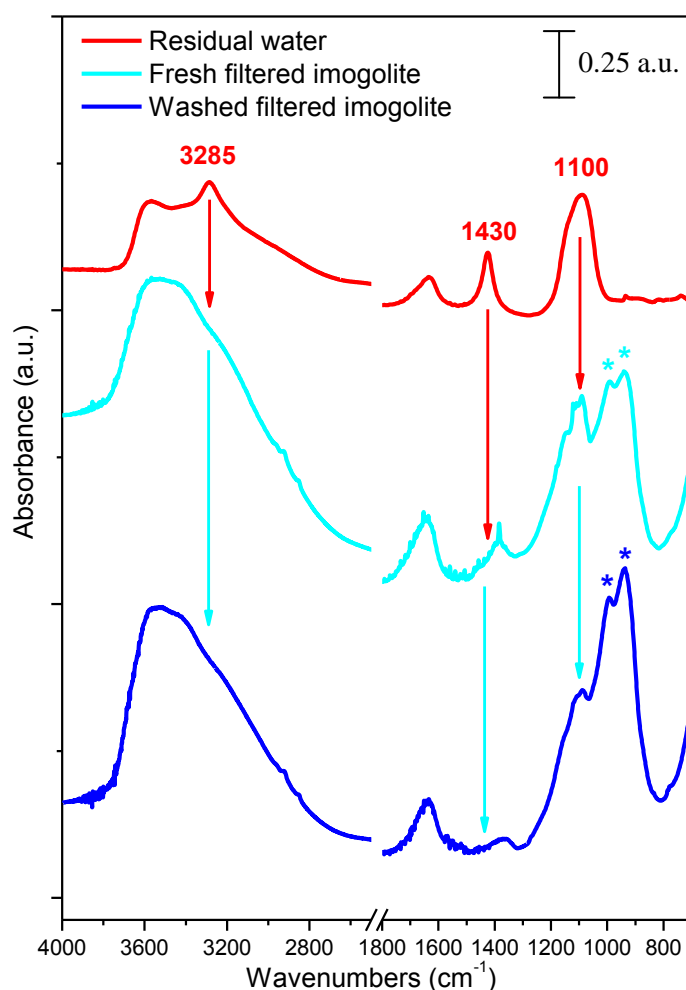


Figure 12: FT-IR spectra of KBr self supporting wafers of fresh filtered imogolite (light blue line), washed filtered imogolite (blue line) and residual water (red line).

Moreover, the broad absorption at high frequencies is due to the stretching vibration of the hydroxyl groups at the inner and outer surfaces, which are involved in hydrogen bonding with adsorbed water molecules, as detected by the band at 1640 cm^{-1} . Additionally, external hydroxyl groups may also interact with hydroxyl groups of neighboring nanotubes. The presence of amorphous alumino-silicate species, are identified by the peaks at 1100 , 1400 and 3285 cm^{-1} . Filtration was able to remove a large amount of amorphous phase, even if the final washing reduced almost totally also the stretching band at 1100 cm^{-1} , still present in the fresh filtered powder.

In conclusion, a purified imogolite sample can be obtained by combining simple filtration/washing methods. Similarly, Levard and co-workers were able to obtain purified germanium-containing imogolite tubes [143]. Particularly, they showed how dialysis method is effective for final purification of nanotubes by means of MAS NMR technique (Figure 13).

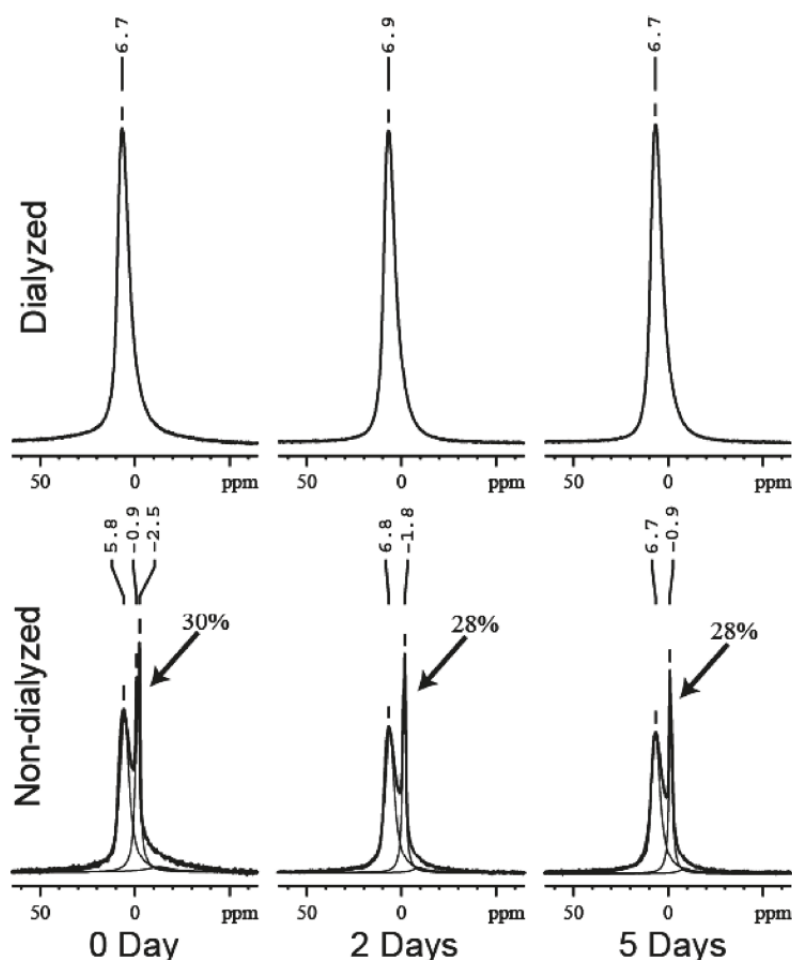


Figure 13: ^{27}Al MAS NMR spectra of (top) dialyzed samples and (bottom) no dialyzed samples. Proportion of monomeric Al is obtained by line-fitting after $t = 0, 2, \text{ and } 5$ days of aging [143].

As already discussed above, surface area values for imogolite are known to vary from 250 m²/g (or lower) up to thousands of square meters per gram [110]. An imogolite sample with total surface of 1378 m²/g has been obtained for the first time, due to particularly likely controlled operative conditions, confirming how the reproducibility of this synthesis is hard to achieve. On the contrary, statistically imogolite samples with surface of *ca* 300 m²/g are obtained.

The adsorption/desorption isotherms of N₂ on two selected imogolite samples outgassed at 300°C are shown in Figure 14a. Corresponding BET Specific Surface Area (SSA) in m²/g (total, internal and external) and porosity features are gathered in Table 1. It turned out that the outer gibbsite-like surface constitutes about 70% of the imogolite surface area, in agreement with the literature [55]. The choice of this particular outgassing temperature derives from a recent study of Bonelli *et al.* [135], in which dehydration effects on BET specific surface area of imogolite were elucidated. Since adsorbed water on imogolite nanotubes is completely removed only at 300 °C, thus the effective surface area should be estimated only on pretreated samples at least at this temperature. In fact, the presence of water at temperature below 300 °C has demonstrated to have a negative effect on the total surface area value. Each isotherms are of Type I typical of microporous materials, according to IUPAC (International Union of Pure and Applied Chemistry) classification [144].

Figure 14b reports the corresponding Pores Size Distribution (PSD). They were calculated by applying the Non Local-Density Functional Theory (NL-DFT) method to adsorption branches of isotherms.

Calculations show the presence of micropores with an inner diameter ranging from of 0.87 to 0.95 nm. This finding fits with the dimension of the nanotubes inner space. Pore dispersion from 1 to 1.5 nm is more evident in sample B, which has the highest surface area value. Geometrical considerations about the expected theoretical surface area of imogolite can be done, as proposed by Arai *et al.* [55]. They expected that the ratio of outer tube surface area to inner tube surface area should be equal to the ratio of the radii, *i.e.* the gibbsite area is *ca* 2.3 times greater than the silicate area. The average total number of hydroxyl surface sites can be estimated by tritium exchange. Normalizing to 1 g of imogolite and assuming that edge sites make a negligible contribution to the total sites,

$$X + Y = 0.013 \text{ mol/g} = 7.61 \cdot 10^{21} \text{ sites} \quad (\text{Eq. 3})$$

Table 1: Textural parameters of two samples of imogolite, as derived from combined XRD patterns and N₂ adsorption isotherms at 77 K.

Sample	BET SSA (m ² /g)	Internal SSA (m ² /g)	External SSA (m ² /g)	Total pore vol. (cm ³ /g)	Micropores vol. (cm ³ /g) ^a	Inner diameter (nm) ^b	Outer diameter (nm) ^c
Imogolite sample A	355	237	118	0.19	0.10	0.95	2.79
Imogolite sample B	1378	920	458	0.69	0.38	0.87	2.68

^a As evaluated by applying the α_s method.

^b As calculated by NL-DFT method to the adsorption branch of the isotherm.

^c As calculated by the $d_{(100)}$ reflection peak of XRD patterns according to an hexagonal packing.

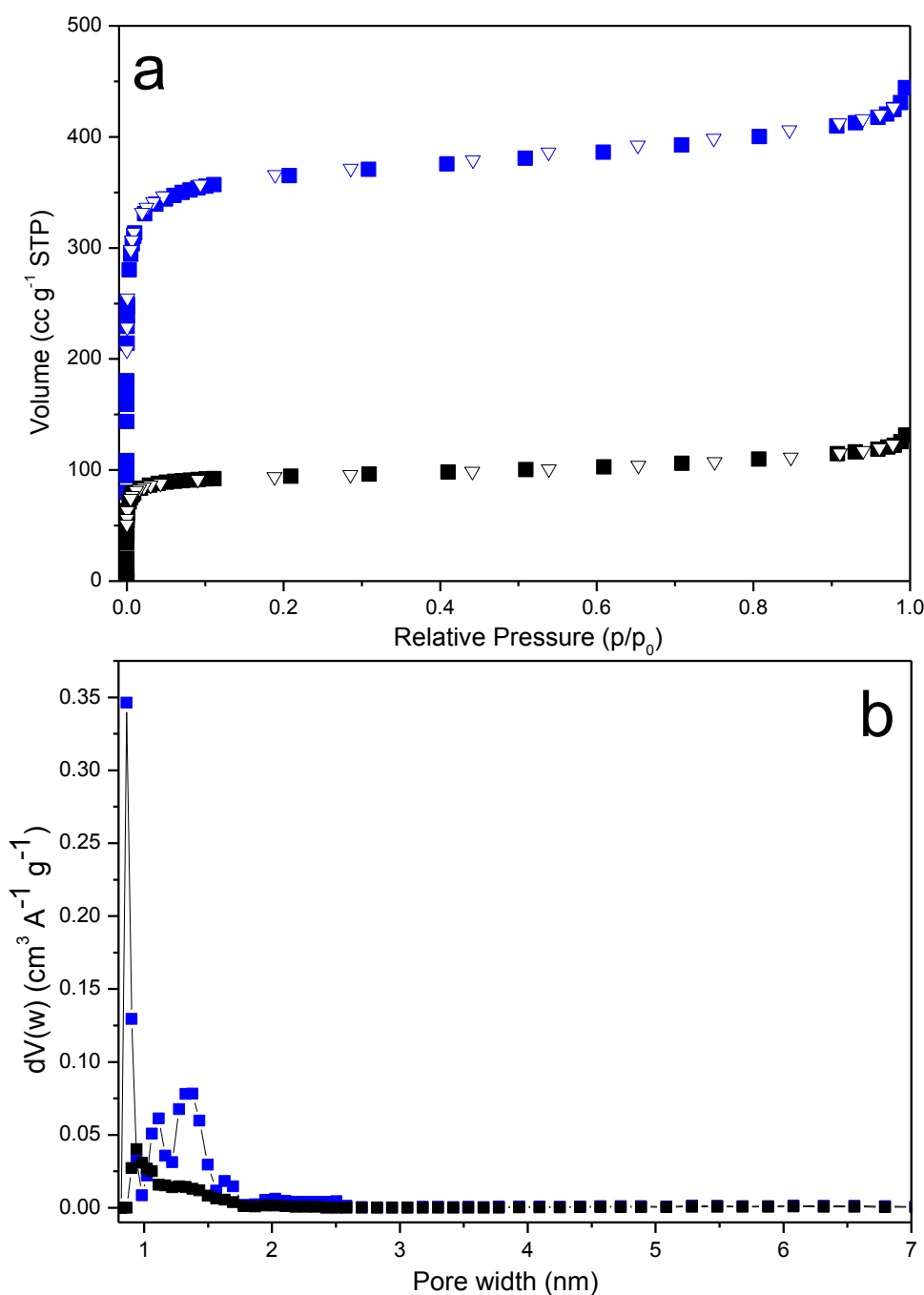


Figure 14: (a) N₂ adsorption (square) and desorption (triangle) of imogolite sample A (black) and sample B (blue); (b) Correspondent PSDs (NL-FDT method).

where,

$$X = \text{gibbsite sites/g} = X / 1.2 \cdot 10^9 \text{ sites} \quad (\text{Eq. 4})$$

$$Y = \text{silicate sites/g} = Y / 7.9 \cdot 10^{18} \text{ sites} \quad (\text{Eq. 5})$$

Since the gibbsite area is 2.3 times greater than the silicate area, then:

$$X(7.9 \cdot 10^{18} \text{ sites}) = 2.3Y(1.2 \cdot 10^9 \text{ sites}) \quad (\text{Eq. 6})$$

Combining equations (3) and (6) and solving,

$$X = 5.915 \cdot 10^{21} \text{ gibbsite (outer tube) sites/g of imogolite}$$

$$Y = 1.693 \cdot 10^{21} \text{ silicate (inner tube) sites/g of imogolite.}$$

This is equivalent to 493 m² of gibbsite surface area and 214 m² of silicate specific surface area, per gram of imogolite, and yields an estimated total surface area of 707 m²/g, in reasonable agreement with the high values estimated by the EGME method (1000 m²/g) [110].

Besides the standard synthetic procedures, in this work a systematic study to assess the influence of acidity, in terms of HClO₄ concentration, on the synthesis yield and morphology of the resulting nanotubes, was also performed. Particularly, 10 batch reactions were run simultaneously, in order to obtain comparable results, keeping constant the Al:Si ratio (2:1) while varying the H⁺ content, from 0.07 to 1.3. XRD patterns (figure 15) and selected FE-SEM images (figure 15), showed that imogolite nanotubes start forming at [H⁺] = 0.6 M, even if the main reflection peak, corresponding to the (100) planes, is well defined only from [H⁺] = 1 M.

Particularly, if the solution is further diluted before the polymerization steps, more disperse bundles of nanotubes may be obtained, as confirmed by electron microscopy. For the same purpose, other authors proposed different post synthesis manipulations, e.g. ultrasonication of dried powder [145], further acidification in HCl 0.1 M [146] or droplet evaporation [147]. Moreover, it resulted clear that imogolite synthesis is not successful in too poor acidic media, leading to the formation of amorphous aggregates.

As a whole, despite well known reproducibility problems that may occur mainly to variation of temperature and pressure during the polymerization step [130,148], the molar ratio used in standard procedures can be considered well defined. An analogue study was performed in 1994 [149], assessing in this case the influence of the [ASB]/[TEOS] molar ratio on the synthesis results, at constant acidity (1 M). Similarly to my results, it turns out that fairly small deviations from the stoichiometric value $[ASB]/[TES] = 2$ markedly change the particle morphology and composition.

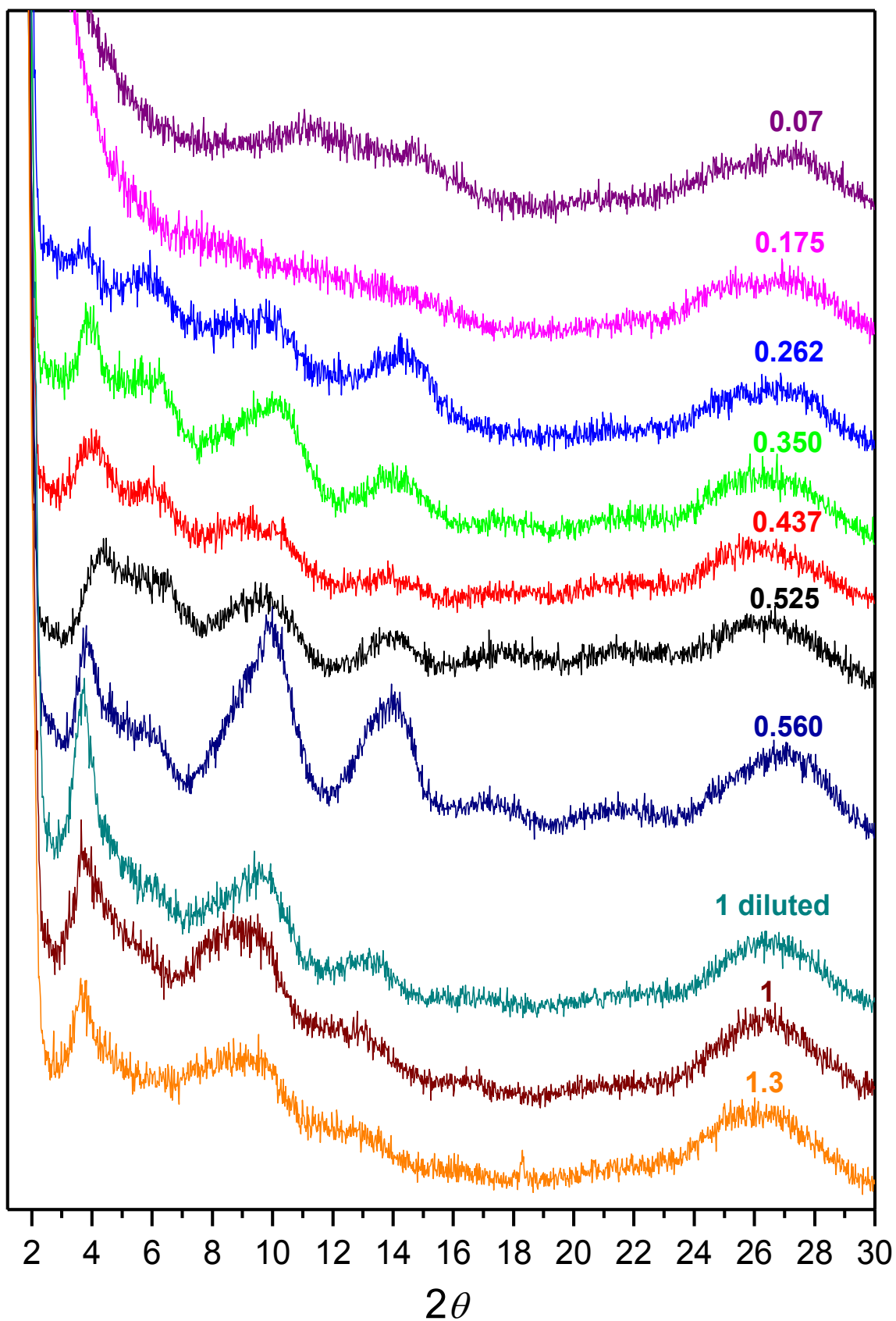


Figure 15: XRD patterns of batch reactions to obtain imogolite nanotubes at different acidity content, $\text{Al}:\text{Si}:\text{H}^+ = 2:1:x$. The value close to each pattern indicates the correspondent value of x used. Particularly, the effect of dilution at $[\text{H}^+] = 1 \text{ M}$ was also studied.

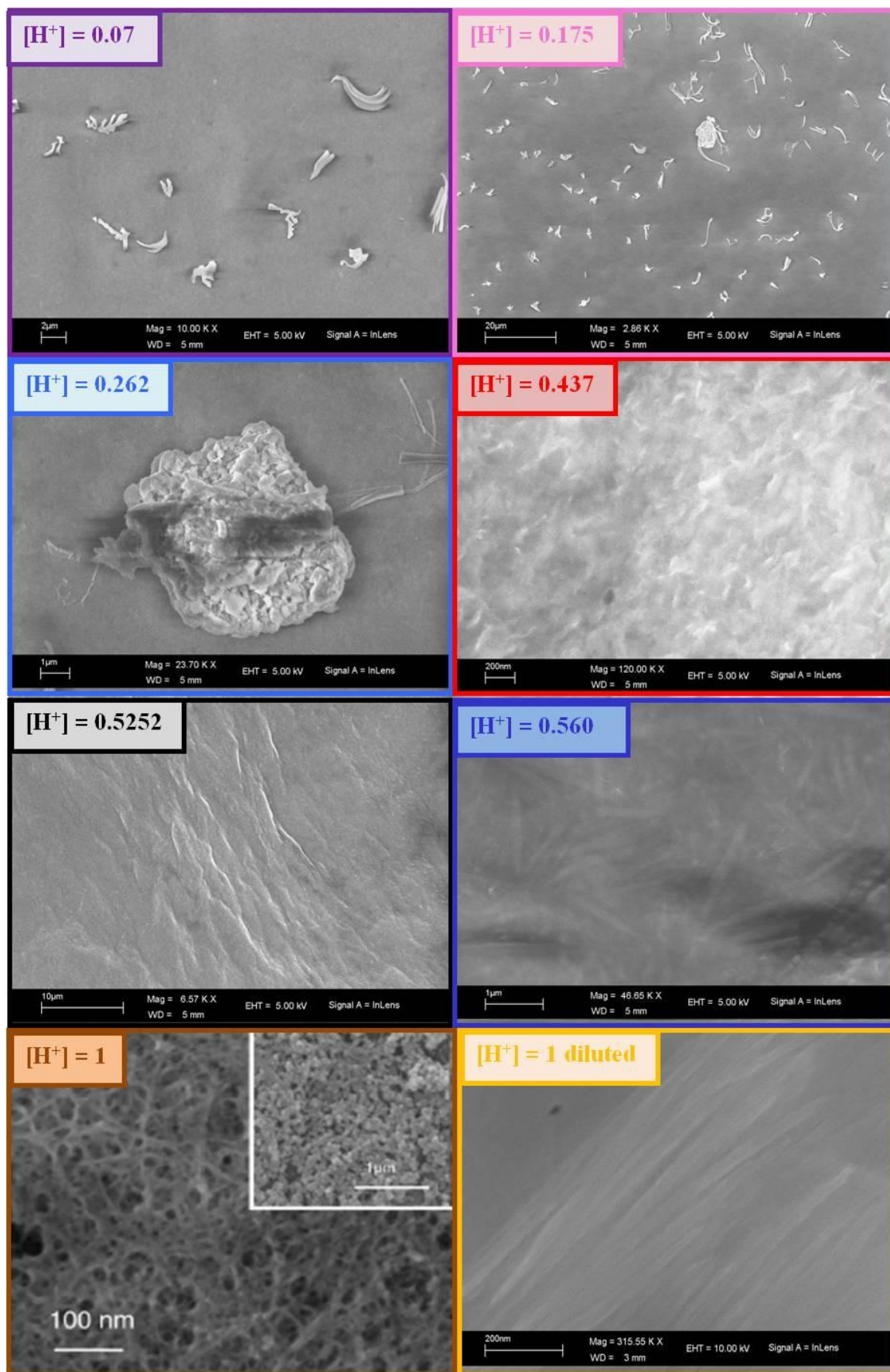


Figure 16: Selected FE-SEM pictures of imogolite nanotubes at different synthesis conditions $[Al:Si:H^+ = 2:1:x]$.

1.3.4. Synthesis procedures suggested for industrial application

Besides the synthetic routes described above, other possible ways to obtain imogolite nanotubes have been proposed, using different silicon precursors from TEOS. Abidin and co-workers [117] reviewed in detail these kind of methods, pointing out their pro and cons, eventually proposing a new synthesis procedure which seem to be promising for further development in industrial field by combination of batch and flow systems. Imogolite nanotubes can be prepared by three different methods:

- (a) TEOS hydrolysis using different aluminum precursors (described above).
- (b) Hydrolysis of commercial sodium silicate [150].
- (c) Hydrolysis of fused sodium silicate [151].

It is reasonable to expect that for industrial application:

- (a) TEOS reagent is relative expensive.
- (b) Desalination process has to be done to remove sodium excess by centrifugation during the preparation of imogolite precursor, therefore increasing the number of industrial units.
- (c) High temperature is needed during preparation of fused sodium silicate.

The new Abidin's method wants instead the use of polysilicic acid as orthosilicic source. It is generally accepted that colloidal polysilicic acid can be prepared easily and it is less expensive than TEOS and fused sodium silicate. Moreover, dissolution process of polysilicic acid seems applicable not only in batch apparatus, but also in flow systems.

In 2009, Levard and co-workers [118] proposed instead an alternative route to imogolite fibers starting from more concentrated (decimolar) solution in mild conditions (low temperature and ambient pressure) by simply allowing for slower growth kinetics. The first try to produce imogolite at 25 °C by Wada in 1987 [149] was not successful, besides it pointed out an important aspect, *i.e.* that too much concentrated solutions prevent the formation of nanotubes, thus suggesting dilution before the polymerization at around 100 °C.

Levard found that the initial concentration of reagents is not a limiting factor for imogolite synthesis under mild conditions: with decimolar solutions, the first tubular structures are formed at as little as 14 days of aging and evolve into long fibers, with a remarkable yield. This result may stimulate a renewed interest in these structures, despite the slow reaction kinetics, and open the road for large scale applications.

1.4. Properties and applications of imogolite

1.4.1. Chemical surface properties and adsorption applications

In 2001, Gustafsson [68] proposed the existence of a weak positive charge distributed on the outer surface of synthetic imogolite, whereas the inner silanols group may develop a negative charge, depending on pH, according to the same reactions proposed for natural imogolite surfaces [54],



Guimarães and co-workers [79] estimated a charge distribution in a line with that of Gustafsson. They also found that the SiOH bonds are more ionic than the Al(OH)Al ones and suggested that the former should be more acidic than the latter. The spectroscopic characterization of the acidity of synthetic imogolite, recently reported by Bonelli *et al.* [135], highlighted the surface properties of nanotubes by means of FT-IR spectroscopy, dosing NH₃ and CO as probe molecules. First of all, it resulted that below 300 °C, nanotubes are partially filled with water, and therefore, only few Al³⁺ Lewis sites at the outer surface may be accessed by probes. Particularly, this conclusion is in fair agreement with the molecular dynamic simulation results obtained by Creton *et al.* [152], who suggested that water density can be expected to be higher inside the tubes rather than outside. Additionally, the shape of nanotubes, which varies with the water density, influences the electrostatic potential and, thus, determines the places where the adsorption occurs. If the sample is outgassed at 300 °C, water is definitely removed, as FT-IR spectra confirm and the inner surface, covered by silanols, becomes actually accessible to probe molecules.

In fact, interaction with ammonia resulted to be strong, probably due to multiple interactions with more than one silanol group, while CO dosage showed the formation of the expected band at 2157 cm^{-1} , due to the interaction of the gas with the inner silanols [153], together with a minor band at *ca* 2190 cm^{-1} probably due to CO adsorbed on weak Al^{3+} Lewis sites at the outer surface. Further studies performed in this PhD work on the acidity of imogolite like materials will be reported in Chapter 6.

Apart from the charge distribution in the imogolite layer, it is interesting to analyze the electrostatic potential generated by the charge distribution inside and outside the nanotubes because this potential and its spatial variation will drive the adsorption and the dynamics of interaction of ions and molecules. Obviously, the potential depends on both charges and positions of atoms and therefore it is also influenced by the geometry of the tubes. Figure 17 shows the Electrostatic Potential (EP) map of the imogolite model evaluated by Creton and co-workers [152].

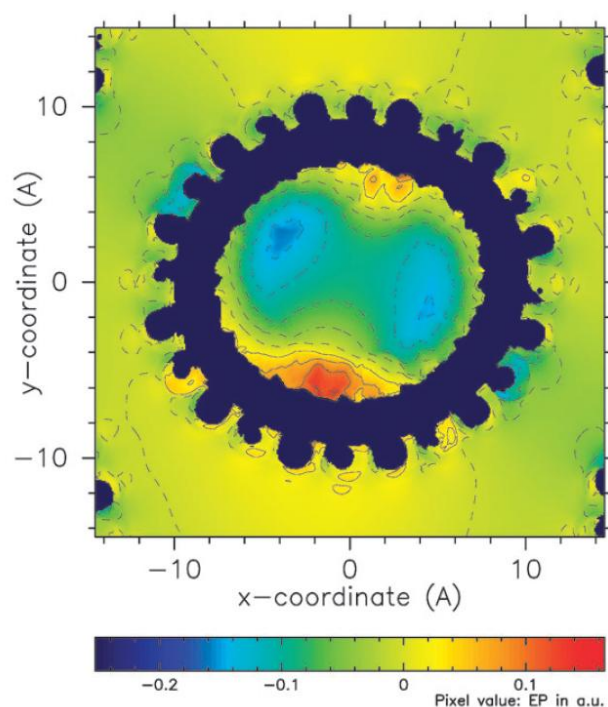


Figure 17: Electrostatic Potential (EP) map of imogolite model in 2D [152].

The figure reveals that, while the potential has mostly negative values both inside (blue color) and outside (blue/green color) the tube, localized regions of positive potential appear in those places where the surface becomes flatter (yellow to red color).

Accordingly, a more negative potential occurs in those places in the external void where the tube surface is more curved. The mean value of the electric field inside the tube was evaluated to be about $5.7 \cdot 10^{-9}$ V/m, which is of the order of magnitude of fields measured in the CaA and NaRbY zeolites [154,155]. For the properties described above, imogolite has been proposed as excellent candidate for water adsorbent and sensor [152,156-163], ion retention/catalysis [55,66,135,136,145,149,164-172] and gas adsorption (*e.g.* CO₂ and CH₄) [53,161,173].

1.4.2. Electronic properties and relative applications

The electronic properties of nanotubes material may depend essentially on their chirality and diameter. Bursill *et al.* [131] for the first time pointed out that a relatively wide band gap should be expected for imogolite, ranging from 3.7-4.7 eV (Figure 18a and 18b) [120,122,174] to 10 eV [79], therefore behaving as an insulator material. Electronic properties of imogolite are reasonably analogue to those of α -Al₂O₃ (8.75 eV, experimental; 7.77 eV [175]) and gibbsite structure (*ca* 10 eV [175,176]). However, if compared to other inorganic nanotubular structures, for instance, MoS₂ nanotubes [177], their band gap value belongs to the semiconducting range. Particularly, it is determined by tube geometry (armchair or zigzag), and tends to vanish for very small diameters.

Particularly, Guimarães *et al.* [79] showed that all imogolite nanotubes have a wide band gap of *ca.* 10 eV, independently on their chirality. This property makes imogolite nanotubes interesting examples of layered heterophase nanotubular systems. Further investigations of their stability could help in the fabrication of similar systems, for example composed of few monolayers of different III-V semiconductors.

Recently, a polypyrrole (ppy) coated imogolite was successfully obtained [178]. Comparing with both pure imogolite and ppy-imogolite, conductivity of ppy-imogolite were measured to be ten times that of pure imogolite in wide range of voltages, thus suggesting that further studies should be useful to engineer new imogolite-composite materials with different electronic properties.

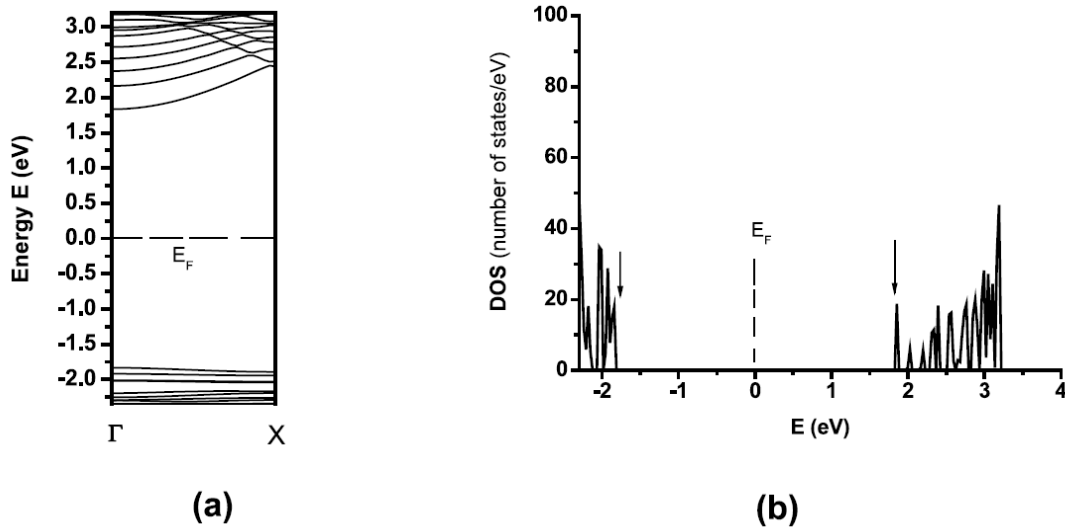


Figure 18: The energy bands of the single-walled imogolite nanotube and the electron density of states: (a) the energy bands near the Fermi level, showing the direct and wide energy gap, (b) the total electron density of states [120].

1.4.3. Mechanical properties and applications in composites technology

Mechanical properties of nanotubes can be obtained by computational methods [25,27,179,180] or experimentally by estimation of the Young’s modulus (Y). Particularly, the Y modulus of imogolite nanotubes has been calculated [25] by performing a series of relaxation calculations for different values of the cell length in the direction of the tube axis, and thus imposing either tensile or compressive strain on the nanotube. It is then possible to calculate the second derivative of the total energy with respect to the axial strain, which enables us to calculate the Young’s modulus, as defined by the following equation (Eq. 7):

$$Y = \frac{1}{V_0} \cdot \left(\frac{\partial^2 E}{\partial \epsilon^2} \right)_{\epsilon=0} \quad (\text{Eq. 7})$$

where V_0 is the equilibrium volume, ϵ the strain, and the E the total energy. The results obtained for zigzag and armchair configurations show that imogolite nanotubes have Young’s moduli which fall in the range 175–390 GPa. In comparison to C [27], BC_3 [27], BN [27] and BC_2N [25] nanotubes, imogolite results to be less stiff. Particularly, imogolite Young’s moduli is in the same order of magnitude as for MoS_2 (*ca* 230 GPa) [177] and GaS (*ca* 270 GPa) [28] nanotubes.

Polymers reinforced with imogolite as inorganic nanofiller form new composite/hybrid materials with increased mechanical [181-183] and also optical properties [183,184, Figure 19], which opens new perspectives for interesting technological applications.



Figure 19: Transparency of in situ hybrid (upper) and blend (lower) imogolite/PVA films. The thickness of films is ca 100 nm [183]. Imogolite shows to be optically transparent in the multilayer film [184].

1.4.4. Biomedical applications

Inorganic-enzyme hybrids have attracted increasing attention for the development of next generation biosensor and active biological coatings [185-196]. Immobilization of enzyme on a solid support should offer advantages for both industrial and analytical purposes, for instance, eliminating the risk of sample contamination, simplifying sample handling, as well as better separation of enzyme from solution that contains substrate and product [189]. As a nanoscale support, nanotubes of unique physicochemical properties, like imogolite, represent interesting candidates for stable immobilization of enzymes.

Carbon nanotubes have been already used to this purpose by testing the covalent and non-covalent interactions on their surfaces [190-192]. However, some drawbacks emerged. The main expected problem was the water insolubility of carbon nanotube that severely limited their biotechnological applications, since almost all enzymatic reactions in animal cells occur in bodily fluid containing mostly water [193,194]. As a consequence, imogolite should be recommended as support for enzyme immobilization. Moreover, the 3-dimensional network of imogolite hydrogel formed in aqueous solution [195] can significantly increase the loading for enzyme immobilization and provide a scaffold for a much controlled enzymatic activities. By the interaction of pepsin *via* phosphoric acid groups interacting with imogolite surface, a nanofiber/pepsin hybrid hydrogel was obtained by Inoue and co-workers in 2006 [196]. Figure 20 shows a schematic representation and photograph of imogolite/pepsin hybrid hydrogel [197].

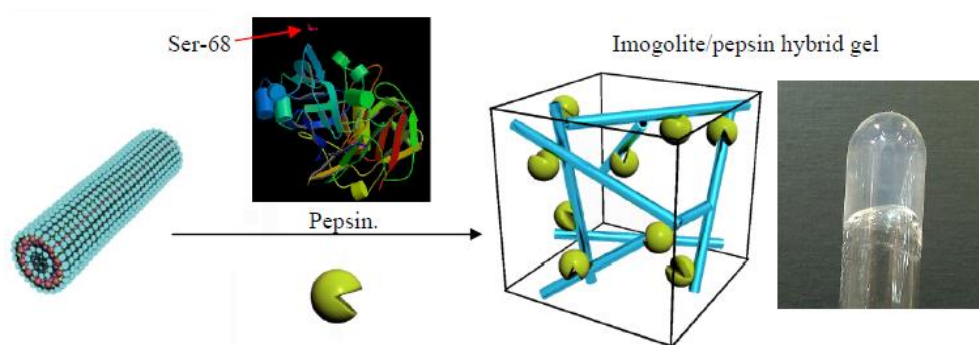


Figure 20: Schematic representation and photograph of imogolite/pepsin hybrid hydrogel [197].

Particularly, immobilization of enzyme is achieved by forming a strong electrostatic interaction between positively charged imogolite and negatively charged pepsin. According to this method, a high loading of enzyme immobilization was achieved. Similar behavior has been observed for enzymes immobilized at the inner surface of halloysite [119]. A Complex gel of type I collagen and imogolite nanofibers was also successfully prepared by addition of a fine dispersion of nanotubes to the collagen solution at pH 4 [197]. In 2011, a comparative study between carbon and imogolite nanotubes [198] revealed that imogolite material has better and suitable topography, roughness, wettability as well as high protein adsorption capacity, as compared to carbon nanotubes, *i.e.* properties that make imogolite an excellent candidate to be used as scaffold for the mineralization of osteoblasts (Figure 21).

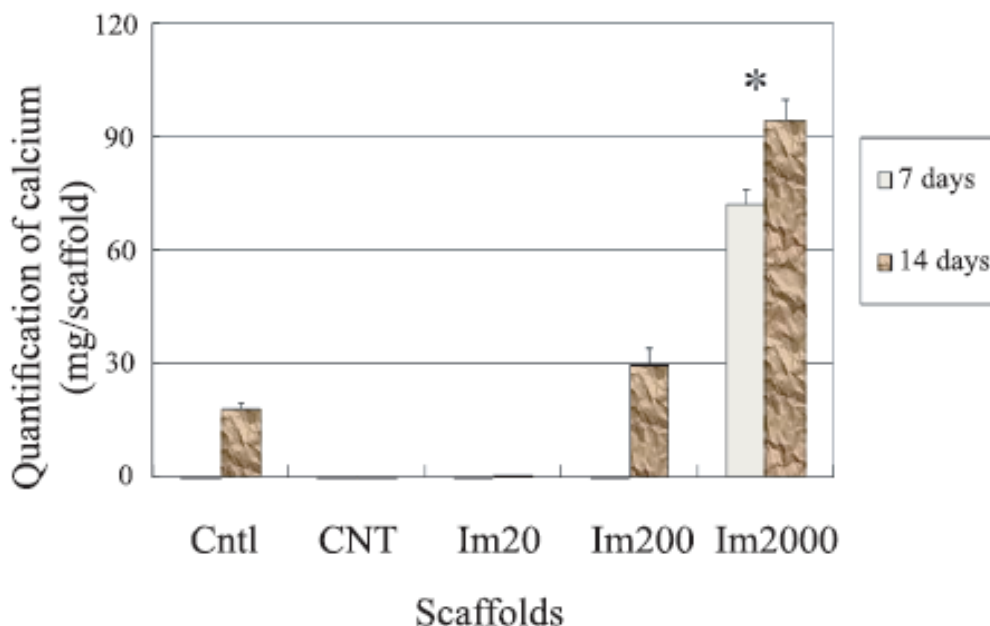


Figure 21: Quantification of mineralization by evaluation of calcium deposition in the human osteoblast cells type seeded onto different scaffolds. Particularly, imogolite slurry was diluted by deionized water to concentrations of 0.01 mg/mL and 0.1 mg/mL. Then, imogolite slurry was poured into a cell culture dish of 60mm diameter and let drying for seven and fourteen days at room temperature. To prepare carbon nanotubes scaffolds, a dilute solution of tubes in 99.5 % ethanol (5 µg/mL) was dispersed by ultrasonication and then spotted onto a cell culture dish. A cell culture dish without additives was used as a control (Cntl). The scaffolds with imogolite at 20, 200, and 2000 µg/dish are labeled Im20, Im200, Im2000, respectively [199].

1.4.5. Antibacterial properties of clays

The development of materials with the ability to inhibit bacterial growth have been of great interest in recent years due to their potential use in everyday products like paints, coatings, hospital utensils etc. [200]. Natural clays are known for their antibacterial properties, despite the mechanism by which they operate has not clearly been identified in each situation. The key advantages of inorganic antimicrobial agents are improved chemical stability, high ion exchange capacity, high surface area, thermal resistance, safety to the user and long lasting action period, which are lacking in organic antimicrobial agents [201,202]. A variety of physical and/or chemical processes can make clays antibacterial. Physical bactericide effect can occur by surface attraction between clay minerals and bacteria [203].

Among these, basic oxides, like MgO, CaO and ZnO, showed to own these properties [202]. However, other type of clays, such as montmorillonite, allophane, imogolite and halloysite, need to be make antibacterial by changing their structure with thermal treatment or mechanical grinding [5], or by chemisorption of known bactericidal elements like Ag [205,206], Cu [66,170,207], Co [208,209].

Montmorillonite is a layered clay of the smectite family [210,211]. Smectites, classified as 2:1 phyllosilicate clays, have a unit crystal lattice formed by one alumina octahedral sheet intercalated between two silica tetrahedral sheets. As layered clays, the introduction of structural alterations, for example by the mechanical and thermal collapsing of the interlayers, showed a decreasing swelling capacity of the raw clay as well as different distribution of the surface charges, thus improving their antibacterial properties [204,212]. The same positive effect was shown by metallic silver-exchanged montmorillonite dispersed in water, able to positively attract and adsorb negatively charged bacteria [213]. Modified montmorillonites are also good adsorbent for charged or non-charged organic molecules like aflatoxins, salicylic acid, herbicides and fungicides [212,214-217], confirming that the antibacterial performance is affected by the availability of the ionic silver to be in contact with the bacteria.

Due to its morphology and high surface area, *allophanes* [218] are expected to play a disinfectant role for specific bactericidal activities rather different from other inorganic carriers [208]. Bactericidal activities against *E. Coli* and *S. Aureus* in water of two kinds of natural allophonic specimens, silver-loaded and phosphorous-silver loaded, respectively, have been recently examined in comparison to those of silver-loaded zeolite [209]. The allophonic samples showed a remarkably high contribution towards sterilization and greater effectiveness in comparison to zeolite materials. This evidence was explained by the presence of many impurities in natural allophane, like ferrhydrite (Fe_2O_3), α -quartz, imogolite, halloysite and similar aluminosilicates. Particularly, ferrhydrites have large specific surface area similar to allophane, so they can cooperate to adsorb and fix various anions of phosphate. Hence, for sterilization purpose, such low-crystalline iron compounds conceivably play an important role. Moreover, in the case of aluminosilicate impurities, other studies demonstrated that the presence of Al-humus complexes is related to the amount of toxic aluminum in Andosols horizons [46,219,220].

However, in contrast to non-allophanic Andosols, allophanic Andosols (*i.e.* where allophane, imogolite and allophane-like materials are present) seldom show Al toxicity, even when they contain large amounts of Al-humus complexes [221,222]. Because most allophanic Andosols are formed at a soil pH greater than 5, aluminum is relatively insoluble and it is not released into the soil solution. This indicates that the presence of allophanic materials reduces aluminum toxicity, especially to plants.

So far, *imogolite* Cu(II) adsorption capacity has been estimated in few studies [66,170,207]. It resulted that quantitatively adsorption of Cu(II) by imogolite was less than that achieved by allophanes, presumably because fewer sites are available for chemisorption on imogolite nanotubes. Moreover, Electron Spin Resonance (ESR) measurements showed that Cu²⁺ ions adsorbed as a monomer on two types of surface sites: the preferred ones were likely adjacent Al-OH groups binding with copper by a binuclear mechanism, while the weaker ones occurred at isolated Al-OH or Si-OH groups [66]. The adsorption of three copper species, the hydrated cupric ion, bisglycine Cu(II) and a Cu(II)-humic acid complex, was also investigated by Electron Paramagnetic Resonance (EPR) [207]. The EPR spectra of copper complexes adsorbed on natural montmorillonite (reference material) and imogolite showed that the amount and type of adsorption depends on the size and chemical nature of the ligands. Particularly, evidence from the copper-glycine system indicate that probably at least two types of complex are formed. Additionally, for montmorillonite it is suggested that they correspond to the adsorption onto interlayers. Finally, EXAFS (Extended X-Ray Absorption Fine Structure) studies were also performed on natural Cu(II)-imogolite sample and its catalytic activity has been tested towards the decomposition of *tert*-butyl hydroperoxide and 1,1-bis(*tert*-butyldioxy)cyclododecane, respectively [170].

As compared to natural unloaded imogolite and Cu-SiO₂ catalyst, in case of *tert*-butyl hydroperoxide cracking (Figure 22a), Cu-imogolite showed a higher activity with respect to reference materials, while the unexpected rather high activity of the unloaded imogolite was explained by the presence of iron impurities. However, in case of the decomposition of 1,1-bis(*tert*butyldioxy) cyclododecane (Figure 22b), activities of unloaded imogolite and Cu-imogolite were comparable. Stable hydrosols of Ag⁺ and bimetallic nanoparticles (Au/Ag, Au/Pt, and Ag/Pt) immobilized on imogolite fibers were obtained for the first time in 1995 [205]. It turned out that colloidal stability is achieved by adsorption of particles on nanotubes and no stabilizing polymers are required.

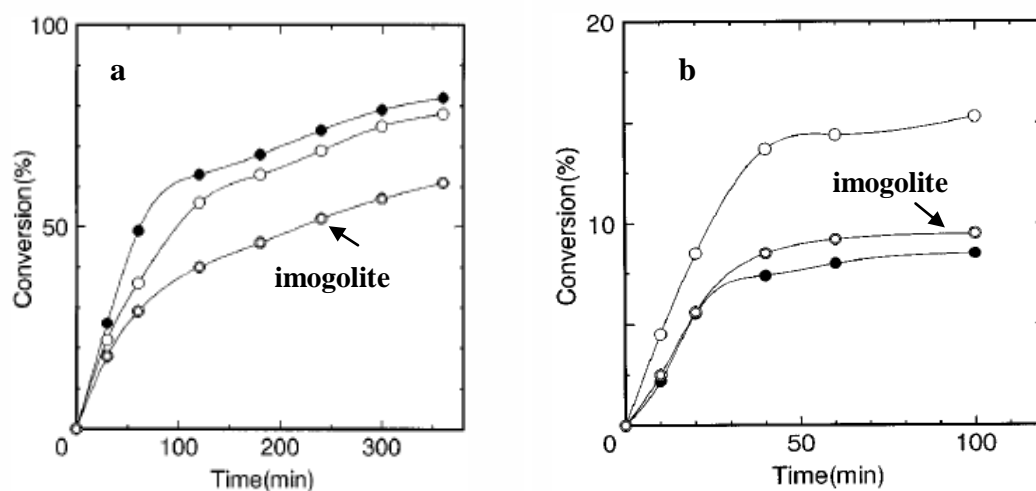


Figure 22: (a) Decomposition of tert-butyl hydroperoxide at 90 °C.

[tert-butyl hydroperoxide] = 0.1M, catalyst: 0.1 g, solvent: chlorobenzene (50 ml). The amount of Cu loaded is 2.59 wt. %;

(b) Decomposition of 1,1-bis(tert-butylidioxy)cyclododecane at 70 °C.

[1,1-bis(tert-butylidioxy)cyclododecane] = 0.05 M, catalyst: 0.1 g, solvent: chlorobenzene (50 ml).

Symbols: (●) Cu-imogolite, (written) imogolite and (○) Cu-SiO₂ [170].

Particularly, bimetallic particles consist of layers of metals, rather than a mixture at the atomic level, except in the case of Au/Ag. Moreover, imogolite fibers do not absorb or scatter light, thus their optical property makes them convenient for the estimation of optical properties of adsorbed metallic particles.

As far as the applications of Cu-loaded and Ag-loaded imogolite are concerned, no studies were further performed, except for colloids of Ag⁺-imogolite for which optical properties were identified [205]. However, no antibacterial tests with modified imogolite have been ever reported as well as the effective toxicology of imogolite nanotubes themselves.

1.5. References

- [1] S. Iijima, *Nature* 354(6348) (1991) 56.
- [2] A.F. Ismail, P.S. Goh, S.M. Sanip, M. Aziz, *Sep. Purif. Technol.* 70 (2009) 12.
- [3] J. Wang, Y. Chen, W.J.J. Blau, *Mater. Chem.* 19 (2009) 7425.
- [4] V.N. Popov, *Mater. Sci. Eng. R-Rep.* 43 (2004) 61.
- [5] B.L. Allen, P.D. Kichambare, A. Star, *Adv. Mater.* 19 (2007) 1439.
- [6] H. Zhang; G.P. Cao, Y.S. Yang, *Energy Environ. Sci.* 2 (2009) 932.
- [7] H.J. Dai, A. Javey, E. Pop, D. Mann, W. Kim, Y.R. Lu, *NanoToday* 1 (2006) 1.
- [8] H.J. Dai, *Acc. Chem. Res.* 35 (2002) 1035.
- [9] R. Tenne, L. Margulis, M. Genut, G. Hodes, *Nature* 360 (1992) 444.
- [10] L. Margulis, G. Salitra, R. Tenne, M. Talianker, *Nature* 365 (1993) 113.
- [11] S. Hu, X. Ling, T. Lan, X. Wang, *Chem. Eur. J.* 16 (2010) 1889.
- [12] L. Pu, X.M. Bao, J.P. Zou, D. Feng, *Angew. Chem. Int. Ed.* 40 (2001) 1490.
- [13] J. Sha, J.J. Niu, X.Y. Ma, J. Xu, X.B. Zhang, Q. Yang, D. Yang, *Adv. Mater.* 14 (2002) 1219.
- [14] A. Albu-Yaron, T. Arad, R. Popovitz-Biro, M. Bar-Sadan, Y. Prior, M. Jansen, R. Tenne, *Angew. Chem. Int. Ed.* 44 (2005) 4169.
- [15] S.J. Son, X. Bai, S.B. Lee, *Drug Discovery Today* 12 (2007) 650.
- [16] M. Bar-Sadan, I. Kaplan-Ashiri, R. Tenne, *Eur. Phys. J. Spec. Top.* 149 (2007) 71.
- [17] R. Tenne, G. Seifert, *Annu. Rev. Mater. Res.* 39 (2009) 387.
- [18] C.N.R. Rao, A. Govindaraj, *Adv. Mater.* 21 (2009) 4208.
- [19] N. Yoshinaga, A. Aomine, *Soil Sci. Plant Nutr.* 8(3) (1962) 22.
- [20] C.P.G. Cradwick, V.C. Farmer, J.D. Russell, C.R. Masson, K. Wada, N. Yoshinaga, *Nat. Phy. Sc.* 240 (1972) 187.
- [21] T.F. Bates, F.A. Hildebrand, A. Swineford, *Am. Mineral.* 35 (1950) 463.
- [22] S.I. Wada, K. Wada, *Clays and Clay Min.*, 30(2) (1982) 123.
- [23] F. Jensen, H. Toftlund, *Chem. Phys. Lett.* 201 (1993) 95.
- [24] N.G. Chopra, R.J. Luyken, K. Cherrey, V.H. Crespi, M.L. Cohen, S.G. Louie, A. Zettl, *Science* 269 (1995) 966.
- [25] E. Hernandez, C. Goze, P. Bernier, A. Rubio, *Phys. Rev. Lett.* 80 (1998) 4502.
- [26] O. Stéphan, Y. Bando, A. Loiseau, F. Willaime, N. Shramchenko, T. Tamiya, T. Sato, *Appl. Phys. A* 67 (1998) 107.
- [27] E. Hernandez, C. Goze, P. Bernier, A. Rubio, *Appl. Phys. A* 68 (1999) 287.
- [28] T. Köhler, T. Frauenheim, Z. Hajnal, G. Seifert, *Phys. Rev. B* 69 (2004) 193403.
- [29] A.N. Enyashin, G. Seifert, *Phys. Status Solidi B* 242 (2005) 1361.
- [30] C. Ducati, E. Barborini, S. Vinati, P. Milani, P.A. Midgley, *Appl. Phys. Lett.* 87 (2005) 201906.
- [31] C. Exley, *J. Inorg. Biochem.* 97 (2003) 1.
- [32] F.J. Doucet, C. Schneider, S.J. Bones, A. Kretchmer, I. Moss, P. Tekely, C. Exley, *Geochim. Cosmochim. Acta* 65 (2001) 2461.
- [33] G.J. Churchman, R.M. Carr, *Clays and Clay Miner.* 23 (1975) 382.
- [34] H. Eswaran, *Clay Minerals* 9 (1972) 281.
- [35] K. Wada, N. Yoshinaga, *Am. Mineral.* 54 (1969) 50.
- [36] Farmer V.C., A.R. Fraser, J.D. Russell, N. Yoshinaga, *Clay Min.* 12 (1977) 55.
- [37] S.I. Wada, Y. Kakuto, *Soil Sci. Plant Nutr.* 45(4) (1999) 947.
- [38] S.J. Van der Gaast, K. Wada, S.I. Wada, Y. Kakuto, *Clays and Clay Min.* 33(3) (1985) 237.
- [39] J. Karube, *Clays and Clay Minerals*, 46(5) (1998) 583.
- [40] P.F. Barron, M.A. Wilson, A.S. Campbell, R.L. Frost, *Nature* 299 (1982) 616.
- [41] V.C. Farmer, The role of inorganic species in the transport of aluminium in podzols. In: D. Righi and A. Chauvel, *Podzols and Podzolization. Assoc. Franc. Etude Sol, Plaisir*, (1987) 187.
- [42] W.H. McDowell, T. Wood, *J. Soil Sci.* 137 (1984) 23.
- [43] P. Buurman, L.P. Van Reeuwijk, *J. Soil Sci.* 35 (1984) 447.
- [44] J.M. Tait, N. Yoshinaga, B.D. Mitchell, *Soil Sci. Plant Nutr.* 24 (1978) 145.
- [45] C. Wang, J.A. McKeague, H. Kodama, *Soil Sci. Soc. Am. J.* 50 (1986) 711.
- [46] R.A. Dahlgren, F.C. Ugolini, *Geochim. Cosmochim. Acta*, 53 (1989) 1897.
- [47] J.P. Gustafsson, P. Bhattacharya, D.C. Bain, A.R. Fraser, W.J. McHardy, *Geoderma* 66 (1995) 167.
- [48] A.G. Jongmans, P. Verburg, A. Nieuwenhuys, F. van Oort, *Geoderma* 64 (1995) 327.

- [49] M.A. Wilson, N.H. Tran, A.S. Milev, G.S. Kamali Kannangara, H. Volk, G.Q.M. Lu, *Geoderma* 146 (2008) 291.
- [50] H. Hoshino, H. Urakawa, N. Donkai, K. Kajiwara, *Polym. Bull.* 36 (1996) 257.
- [51] P.I. Pohl, J. Faulon, D.M. Smith, *Langmuir* 12 (1996) 4463.
- [52] J.A. Davis, Surface complexation modeling of uranium(VI) adsorption on natural mineral assemblages. U.S. Nuclear Regulatory Commission. NUREG/CR-6708 (2001).
- [53] M.A. Wilson, G.S.H. Lee, R.C. Taylor, *Clays and Clay Min.* 50(3) (2002) 348.
- [54] H. Tsuchida, S. Ooib, K. Nakaishi, Y. Adachi, *Coll. Surf. A: Physicochem. Eng. Aspects* 265 (2005) 131.
- [55] Y. Arai, M. McBeath, J.R. Bargar, J. Joye, J.A. Davis, *Geochim. Cosmochim. Acta* 70 (2006) 2492.
- [56] B.K.G. Theng, M. Russel, G.J. Churchman, R.L. Parfitt, *Clays and Clay Min.* 30(2) (1982) 143.
- [57] Y. Kitagawa, *Am. Mineral.* 56 (1971) 465.
- [58] T. Henmi, K. Wada, *Am. Mineral.* 61 (1976) 379.
- [59] S. Wada, K. Wada, *Clay Miner.* 12 (1977) 289.
- [60] P.L. Hall, G.J. Churkman, B.K.G. Theng, *Clays and Clay Miner.* 33 (1985) 345.
- [61] S.J. van der Gaast, K. Wada, S.I. Wada, Y. Kakuto, *Clays and Clay Miner* 33 (1985) 237.
- [62] R.L. Parfitt, T. Henmi, *Clays and Clay Miner.* 28 (1980) 285.
- [63] K. Wada, M. Wilson, Y. Kakuto, S.I. Wada, *Clays and Clay Minerals* 36(1) (1988) 11.
- [64] H. Maeda, Y. Hashimoto, E. Hideki Ishida, *App. Clay Sc.* 44 (2009) 71.
- [65] B.K.G. Theng, *Nature* 238 (1972) 150.
- [66] C.J. Clark, M.B. McBride, *Clays and Clay Miner.* 32 (1984) 291.
- [67] E. Hanudin, N. Matsue, T. Henmi, *Clay Sci.* 11 (1999) 57.
- [68] J.P. Gustafsson, *Eur. J. Soil Sci.* 52 (2001) 639.
- [69] H. Hashizume, B.K.G. Theng, A. Yamagishi, *Clay Miner.* 37 (2002) 551.
- [70] A.A. Jara, A. Violante, M. Pigna, M. de la luz Mora, *Soil Sci. Soc. Am. J.* 70 (2006) 337.
- [71] E. Montarges-Pelletiera, S. Bogenezza, M. Pelletiera, A. Razafitianamaharavao, J. Ghanbajab, B. Lartigesa, L. Michota, *Colloids and Surfaces A: Physicochem. Eng. Aspects* 255 (2005) 1.
- [72] H. Nishikiori, K. Kobayashi, S. Kubota, N. Tanaka, T. Fujii, *App. Clay Sc.* 47 (2010) 25.
- [73] Y. Arai, D.L. Sparks, J.A. Davis, *Environ. Sci. Technol.* 39 (2005) 2537.
- [74] S.V. Desrousseaux, O.J.C. Poncet, European Patent 1694510 (2006).
- [75] E. Joussein, S. Petit, J. Churchman, B. Theng, D. Righi, B. Delvaux, *Clay Miner.* 40 (2005) 383.
- [76] L. Guimarães, A.N. Enyashin, G. Seifert, H.A. Duarte, *J. Phys. Chem. C*, 114(26) (2010) 11358.
- [77] Y.M. Lvov, D.G. Shchukin, H. Mohwald, R.R. Price, *ACS Nano* 2 (2008) 814.
- [78] N.G. Veerabadran, R.R. Price, Y.M. Lvov, *ACS Nano* 2 (2007) 115.
- [79] L. Guimarães, A.N. Enyashin, J. Frenzel, T. Heine, H.A. Duarte, G. Seifert, *ACS Nano* 1 (2007) 362.
- [80] R.B. Neder, M. Burghammer, T. Grasl, H. Schulz, A. Bram, S. Felder, *Clays and Clay Min.* 47 (1999) 487.
- [81] D. Mei, B. Zhang, R. Liu, Y. Zhang, J. Liu, *Solar Energy Mat. Solar Cells* 95 (2011) 2772.
- [82] R.R. Price, B.P. Gaber, Y. Lvov, *J. Microencapsul.* 18 (2001) 713.
- [83] Y.M. Lvov, D.G. Shchukin, H. Mohwald, R.R. Price, *ACS Nano* 2 (2008) 814.
- [84] N.G. Veerabadran, D. Mongayt, V. Torchilin, R.R. Price, Y.M. Lvov, *Macromol. Rapid Commun.* 24 (2009) 99.
- [85] S.R. Levis, P.B. Deasy, *Int. J. Pharm.* 253 (2003) 145.
- [86] H.M. Kelly, P.B. Deasy, E. Ziaka, N. Claffey, *Int. J. Pharm.* 274 (2004) 167.
- [87] E. Horváth, J. Kristóf, R. Kurdi, É. Makó, V. Khunová, *J. Therm. Anal. Calorim.* 105 (2011) 53.
- [88] M.H. Shamsi, K.E. Geckeler, *Nanotechnology* 19 (2008) 075604.
- [89] G. Zijian, J.S. Peter, S. Chi, *T. Adv. Mater.* 10 (1998) 701.
- [90] G.S. Machado, K.A.D. de Freitas Castro, F. Wypych, S. Nakagaki, *J. Mol. Catal. A: Chem.* 283 (2008), 99.
- [91] S. Nakagaki, K. Castro, G.S. Machado, M. Halma, S.M. Drechsel, F. Wypych, *J. Braz. Chem. Soc.* 17 (2006) 1672.
- [92] S. Nakagaki, F. Wypych, *J. Colloid Interface Sci.* 315 (2007) 142.
- [93] L. Wang, J. Chen, L. Ge, Z. Zhu, V. Rudolph, *Energy Fuels* 25 (2011) 3408.
- [94] Y. Lin, K. Mo Ng, C.M. Chan, G. Sun, J. Wu, *J. Coll. Interf. Sci.* 358 (2011) 423.
- [95] S.A. Hashemifard, A.F. Ismail, T. Matsuura, *J. Coll. Interf. Sci.* 359 (2011) 359.
- [96] Y. Xie, D. Qian, D. Wu, X. Ma, *Chem. Eng. J.* 168 (2011) 959.

- [97] P. Luo, J.S. Zhang, B. Zhang, J.H. Wang, Y.F. Zhao, J.D. Liu, *Ind. Eng. Chem. Res.* 50 (2011) 10246.
- [98] R.R. Price, B.P. Gaber, U.S. Patent 5,651,976.
- [99] D.G. Shchukin, M. Zheludkevich, K. Yasakau, S. Lamaka, M.G.S. Ferreira, H. Mohwald, *Adv. Mater.* 18 (2006) 1672.
- [100] D.G. Shchukin, H. Mohwald, *Adv. Funct. Mater.* 17 (2007) 1451.
- [101] K. Hedicke-Höchstötter, G.T. Lim, V. Altstädt, *Compos. Sci. Technol.* 69 (2009) 330.
- [102] C. Liu, Y.F. Luo, Z.X. Jia, B.C. Zhong, S.Q. Li, B.C. Guo, D.M. Ji, *eXPRESS Poly. Lett.* 5(7) (2011) 591.
- [103] Y. Lin, K. Mo Ng, C.M. Chan, G. Sun, J. Wud, *J. Coll. Interf. Sci.* 358 (2011) 423.
- [104] K. Prashantha, M.F. Lacrampe, P. Krawczak, *eXPRESS Poly. Lett.* 5(4) (2011) 295.
- [105] Y. Tang, S. Deng, L. Ye, C. Yang, Q. Yuan, J. Zhang, C. Zhao, *Composites: Part A* 42 (2011) 345.
- [106] Y. Wang, I. Deen, I. Zhitomirsky, *J. Coll. Interf. Sci.* 362 (2011) 367.
- [107] A. Javadi, Y. Srithep, S. Pilla, C.C. Clemons, S. Gong, L.S. Turng, *Poly. Eng. Sc.* 51(9) (2011) 1815
- [108] D. Mei, B. Zhang, R. Liu, H. Zhang, J. Liu, *Int. J. Energy Res.* 35 (2011) 828.
- [109] M. Mondragón, M.A. Cortes, E. Arias, C. Falcony, O. Zelaya-Angel, *Poly. Eng. Sc.* 51(9) 2011 1808.
- [110] J. Harsh, J. Chorover, E. Nizeyimana, Allophane and imogolite. In: J.B. Dixon, D.G. Schulze (Eds.), *Soil Mineralogy with Environmental Applications*, vol. SSSA book series. Soil Science Society of America, (2002) 291.
- [111] T.F. Bates, *Amer. Mineral.* 44 (1959) 78.
- [112] E.W. Radoslovich, *Amer. Mineral.* 48 (1963) 368.
- [113] V.C. Farmer, US Patent 4,252,779.
- [114] S.I. Wada, A. Eto, K. Wada, *J. Soil Sc.* 30 (1979) 347.
- [115] V.C. Farmer, M.J. Adams, A.R. Fraser, F. Palmieri, *Clay Miner.* 18 (1983) 459.
- [116] V.C. Farmer, A.R. Fraser in M. M. Mortland and V.C. Farmer (Eds.), *Proc. Int. Clay Conf.*, Oxford, (1978), Elsevier, Amsterdam, 547.
- [117] Z. Abidin, N. Matsue, T. Henmi, *Jap. J. App. Phys.* 47(6) (2008) 5079.
- [118] C. Levard, A. Masion, J. Rose, E. Doelsch, D. Borschneck, C. Dominici, F. Ziarelli, J.Y. Bottero, *J. Am. Chem. Soc.* 131 (2009) 17080.
- [119] K. Tamura, K. Kawamura, *J. Phys. Chem. B* 106 (2002) 271.
- [120] L. Li, Y. Xia, M. Zhao, C. Song, J. Li, X. Liu, *Nanotechnology* 19 (2008) 175702.
- [121] S. Konduri, S. Mukherjee, S. Nair, *Phys. Rev. B* 74 (2006) 033401.
- [122] F. Alvarez- Ramirez, *Phys. Rev. B* 76 (2007) 125421.
- [123] L. Guimarães, A.N. Enyashin, J. Frenzel, T. Heine, H.A. Duarte, G. Seifert, *ACS Nano* 1 (2008) 362.
- [124] S. Konduri, S. Mukherjee, S. Nair, *ACS Nano*, 1(2007) 393.
- [125] J.P. Gustafsson, *Clays and Clay Miner.* 49 (2001) 73.
- [126] M. Zhao, Y. Xia, L. Mei, *J. Phys. Chem. C*, 113 (2009) 14834.
- [127] R. Demichelis, Y. Noël, P. D'Arco, L. Maschio, R. Orlando, R. Dovesi, *J. Mat. Chem.* 20 (2010) 10417.
- [128] M.A. Wilson, G.S.H. Lee, R.C. Taylor, *J. Non-Cry. Solids* 296 (2011) 172.
- [129] H. Yang, C. Wang, Z. Su, *Chem. Mater.* 20 (2008) 4484.
- [130] S. Mukherjee, V.M. Bartlow, S. Nair, *Chem. Mater.* 17 (2005) 4900.
- [131] L.A. Bursill, J.L. Peng, L.N. Bourgeois, *Ph. Magazine*, 80(1) (2000) 105.
- [132] N. Arancibia-Miranda, M. Escudey, M. Molina, M.T. García-González, *J. Non-Cry. Solids* 357 (2011) 1750.
- [133] U.S. Lundström, N. van Breemen, D. Bain, *Geoderma* 94 (2000) 91.
- [134] G.H. Koenderink, S.G. J.M. Kluijtmans, A.P. Philipse, *J. Coll. Interf. Sci.* 216 (1999) 429.
- [135] B. Bonelli, I. Bottero, N. Ballarini, S. Passeri, F. Cavani, E. Garrone, *J. Cat.* 264 (2009) 15.
- [136] S. Imamura, Y. Hayashi, K. Kajiwara, H. Hoshino, C. Kaito, *Ind. Eng. Chem. Res.* 32 (1993) 600.
- [137] G. Ipek Yucelen, R. Prosad Choudhury, A. Vyalikh, U. Scheler, H.W. Beckham, S. Nair, *J. Am. Chem. Soc.* 133 (2011) 5397.
- [138] T. Henmi, N. Yoshinaga, *Clay Min.* 16 (1981) 139.
- [139] B.K. Vainshtein, *Diffraction of X-Ray by Chain Molecules*, Elsevier, Amsterdam, 1966, 328.
- [140] J. Zang, S. Nair, D.S. Sholla, *J. of Chem. Phys.* 134 (2011) 184103.
- [141] W. On Yah, K. Yamamoto, N. Jiravanichanun, H. Otsuka, A. Takahara, *Materials* 3(3) (2010) 1709.
- [142] J.J. Fitzgerald, C. Murali, C.O. Nebo, M.C. Fuerstenau, *J. Coll. Interf. Sci.* 151 (1992) 299.
- [143] C. Levard, J. Rose, A. Thill, A. Masion, E. Doelsch, P. Maillet, O. Spalla, L. Olivi, A. Cognigni, F. Ziarelli, J.Y. Bottero, *Chem. Mater.* 22 (2010) 2466.

- [144] S.J. Gregg, K.S.W. Sing, Adsorption, Surface Area and Porosity, 2nd ed; Academic Press: (1982) London
- [145] M. Tani, C. Liu, P.M. Huang, Geoderma 118 (2004) 209.
- [146] Y. Kuroda, M. Tamakoshi, J. Murakami, K. Kuroda, J. Ceramic Soc. Jap. 115(3) (2007) 233.
- [147] H.X. Yang, Z.H. Su, Chinese Science Bulletin 52(16) (2007) 2301.
- [148] S.I. Wada, Clays and Clay Min. 35(5) (1987) 379.
- [149] L. Liz Marzan, A.P. Philipse, Coll. Surf. A: Phys. Eng. Asp. 90 (1994) 95.
- [150] S.I. Wada, C. Sakimura, Clay Sci. 11 (2000) 115.
- [151] J. Hu, G.S. Kamali Kannangara, M.A. Wilson, N. Reddy, J. Non-Crys. Solids 347 (2004) 224.
- [152] B. Creton, D. Bougeard, K.S. Smirnov, J. Guilment, O. Poncelet, Phys. Chem. Chem. Phys. 10 (2008) 4879.
- [153] G. Ghiotti, E. Garrone, C. Morterra, F. Boccuzzi, J. Phys. Chem. 83 (1979) 2863.
- [154] F. Jousse, E. Cohen de Lara, J. Phys. Chem. 100 (1996) 233.
- [155] G.L. Marra, A.N. Fitch, A. Zecchina, G. Ricchiardi, M. Salvalaggio, S. Bordiga and C. Lamberti, J. Phys. Chem. B, 101 (1997) 10653.
- [156] J. Zang, S. Chempath, S. Konduri, S. Nair, David S. Sholl, J. Phys. Chem. Lett. 1 (2010) 1235.
- [157] K.S. Smirnov, D. Bougeard, J. Phys. Condens. Matter 22 (2010) 284115.
- [158] S. Konduri, H.M. Tong, S. Chempath, S. Nair, J. Phys. Chem. C 112 (2008) 15367.
- [159] J. Zang, S. Konduri, S. Nair, D.S. Sholl, ACSNano 3(6) (2009) 1548.
- [160] D.Y. Kang, J. Zang, E.R. Wright, A.L. McCanna, C.W. Jones, S. Nair, ACSNano 4(8) (2010) 4897.
- [161] M. Tani, C. Liu, P.M. Huang, 17th symposium WCSS, 14-21 August 2002, Thailand.
- [162] F. Ohashi, S. Tomura, K. Akaku, S. Hayashi, S.I. Wada, J. Mat. Science 39 (2004) 1799.
- [163] J. Oh, S. Chang, J. Jang, S. Roh, J. Park, J. Lee, D. Sohn, W. Yi, Y. Jung, S.J. Kim, J Mater Sci: Mater Electron 18 (2007) 893.
- [164] J.P. Gustafsson, Clays and Clay Min. 49(1) (2001) 73.
- [165] C. Su, J.B. Harsh, Clays and Clay Min. 41(4) (1993) 461.
- [166] C. Su, J.B. Harsh, P.M. Bertsch, Clays and Clay Min. 40(3) (1992) 280.
- [167] R.L. Parfitt, A.D. Thomas, R.J. Atkinson, R.S.C. Smart, Clays and Clay Min. 22 (1974) 455.
- [168] H. Yamada, J. Michalik, J. Sadlo, J. Perlinska, S. Takenouchi, S. Shimomura, Y. Uchida, App. Clay Sc. 19 (2001) 173.
- [169] L.M. Liz-Marzan, A.P. Philipse, J. Phys. Chem. 99 (1995) 15120.
- [170] S. Imamura, T. Kokubu, T. Yamashita, Y. Okamoto, K. Kajiwara, H. Kanai, J. Cat. 160 (1996) 137.
- [171] L. Denaix, I. Lamy, J.Y. Bottero, Coll. Surf. A 158 (1999) 315.
- [172] J.B. Harsh, S.J. Traina, J. Boyle, Y. Tang, Clays and Clay Miner. 40(6) (1992) 700.
- [173] W.C. Ackerman, D.M. Smith, J.C. Huling, Y.W. ah Kim, J.K. Bailey, C.J. Brinkertps, Langmuir 9 (1993) 1051.
- [174] M. Zhao, Y. Xia, L. Mei, J. Phys. Chem. C 113 (2009) 14834.
- [175] Z. Lodziana, J.K. Norskov, J. Chem. Phys. 115 (2001) 11261.
- [176] J. Frenzel, A.F. Oliveira, H.A. Duarte, T. Heine, G. Seifert, Anorg. Allg. Chem. 631 (2005) 1276.
- [177] G. Seifert, H. Terrones, M. Terrones, G. Jungnickel, T. Frauenheim, Phys. Rev. Lett. 85 (2000) 146.
- [178] Y. Lee, B. Kim, W. Yi, A. Takahara, D. Sohn, Bull. Korean Chem. Soc. 27(11) (2006) 1815.
- [179] I. Kaplan-Ashiri, S.R. Cohen, K. Gartsman, V. Ivanovskaya, T. Heine, G. Seifert, I. Wiesel, H.D. Wagner, R. Tenne, Proc. Natl. Acad. Sci. U.S.A. 103 (2006) 523.
- [180] I. Kaplan-Ashiri, S.R. Cohen, K. Gartsman, R. Rosentsveig, G. Seifert, R. Tenne, J. Mater. Res. 19 (2004) 454.
- [181] P. Calvert, Nature 357 (1992) 365.
- [182] K. Shikinakaa, Y. Koizumia, Y. Osadab, K. Shigehara, Polym. Adv. Technol. 22 (2011) 1212.
- [183] K. Yamamoto, H. Otsuka, S.I. Wada, D. Sohnd, A. Takahara, Soft Matter 1 (2005) 372.
- [184] N. Jiravanichanuna, K. Yamamotoa, A. Irie, H. Otsukaa, A. Takaharaa, Synthetic Metals 159 (2009) 885.
- [185] S.D. Putney, P.A. Burke, Nat. Biotechnol. 16 (1998) 153.
- [186] A. Jungbauer, R. Hahn, Curr. Opin. Drug Disc. Dev. 7 (2004) 248.
- [187] S.A. Maskarinec, D.A. Tirrell, Curr. Opin. Biotechnol. 16 (2005) 422.
- [188] M. Staiano, P. Bazzicalupo, M. Rossi, S. D'Auria, Mol. Biosys. 1 (2005) 354.
- [189] E.C.A. Stigter, G.J. de Jong, W.P. van Bennekom, Anal. Chim. Acta 619 (2008) 231.
- [190] J.J. Gooding, R. Wibowo, J.Q. Liu, W.R. Yang, D. Losic, S. Orbons, F.J. Mearns, J.G. Shapter, D.B. Hibbert, J. Am. Chem. Soc. 125 (2003) 9006.

- [191] X.Yu, D. Chattopadhyay, I. Galeska, F. Papadimitrakopoulos, J.F. Rusling, *Electrochem. Commun.* 5 (2003) 408.
- [192] S.S. Karajanagi, A.A. Vertegel, R.S. Kane, J.S. Dordick, *Langmuir* 20 (2004) 11594.
- [193] F. Pompeo, D.E. Resasco, *Nano Lett.* 2 (2002) 369.
- [194] A. Star, D.W. Steurman, J.R. Heath, J.F. Stoddart, *Angew. Chem. Int. Ed.* 41 (2002) 2508.
- [195] A.P. Philipse, A.M. Wierenga, *Langmuir* 14 (1998) 49.
- [196] N. Inoue, H. Otsuka, S.I. Wada, A. Takahara, *Chem. Lett.* 35 (2006) 194.
- [197] W. On Yah, K. Yamamoto, N. Jiravanichanun, H. Otsuka, A. Takahara, *Materials* 3 (2010) 1709.
- [198] A. Nakano, N. Teramoto, G. Chen, Y. Miura, M. Shibata, *J. App. Poly. Sc.* 118 (2010) 2284.
- [199] K. Ishikawa, T. Akasaka, S. Abe, Y. Yawaka, M. Suzuki, F. Watari, *Bioceramics Develop. App.* 1 (2011) 1.
- [200] L.B. Williams, D.W. Metge, D.D. Eberl, R.W. Harvey, A.G. Turner, P. Prapaipong, A.T. Poret-Peterson, *Environ. Sci. Technol.* 45 (2011) 3768.
- [201] B. Li, S. Yu, J.Y. Hwang, S. Shi, *J. Miner. Mater. Charact. Eng.* 1 (2002) 61.
- [202] J. Sawai, T. Yoshikawa, *J. App. Microbiology* 96 (2004) 803.
- [203] F.G. Ferris, W.S. Fyfe, T.J. Beveridge, *Chem. Geol.* 63 (1987) 225.
- [204] R.M. Torres Sánchez, *Colloid Surf. A* 127 (1997) 135.
- [205] L.M. Liz-Marzan, A.P. Philipse, *J. Phys. Chem.* 99 (1995) 15120.
- [206] S.M. Magaña, P. Quintana, D.H. Aguilar, J.A. Toledo, C. Ángeles-Chávez, M.A. Cortés, L. León, Y. Freile-Peigrín, T. López, R.M. Torres Sánchez, *J. Molecular Cat. A: Chemical* 281 (2008) 192.
- [207] B.A. Goodman, H.L. Green, D.B. McPhail, *Geoch. and Cosmochim.* 48 (1984) 2143.
- [208] Y. Onodera, T. Iwasaki, A. Chatterjee, T. Ebina, T. Satoh, T. Suzuki, H. Mimura, *App. Clay Sc.* 18 (2001) 123.
- [209] Y. Onodera, T. Iwasaki, A. Chatterjee, T. Ebina, T. Satoh, T. Suzuki, H. Mimura, *App. Clay Sc.* 18 (2001) 135.
- [210] D.M. Moore, R.C. Reynolds, *X-ray Diffraction and the Identification and Analysis of Clay Minerals*, second ed., Oxford University Press, (1997) NewYork.
- [211] C. Viseras, C. Aguzzi, P. Cerezo, A. Lopez-Galindo, *Appl. Clay Sci.* 36 (2007) 37.
- [212] E. Bojemueller, A. Nennemann, G. Lagaly, *Appl. Clay Sci.* 18 (2001) 277.
- [213] C.H. Hu, M.S. Xia, *Appl. Clay Sci.* 31 (2006) 180.
- [214] B. Lombardi, M. Baschini, R.M. Torres Sánchez, *Appl. Clay Sci.* 24 (2003) 43.
- [215] M. Damonte, R.M. Torres Sánchez, M. dos Santos Afonso, *Appl. Clay Sci.* 36 (2007) 86.
- [216] J.W. Jaynes, R. Zartman, W. Hudnall, *Appl. Clay Sci.* 36 (2007) 197.
- [217] F. Bonina, M. Giannossi, L. Medici, C. Puglia, V. Summa, F. Tateo, *Appl. Clay Sci.* 36 (2007) 77.
- [218] S. Wada, K. Wada, *Clay Miner.* 12 (1977) 289.
- [219] T. Takahashi, T. Fukuoka, R.A. Dahlgren, *Soil Sci. Plant Nutr.* 41 (1995) 119.
- [220] Y. Yagasaki, J. Mulder, M. Okazaki, *Geoderma* 137 (2006) 40.
- [221] R.A. Dahlgren, M. Saigusa, F.C. Ugolini, *Adv. Agron.* 82 (2004) 113.
- [222] M. Nanzyo, R.A. Dahlgren, S. Shoji in: *Volcanic Ash Soils – Genesis, Properties and Utilization*, S. Shoji, R.A. Dahlgren, M. Nanzyo, Elsevier, Amsterdam (1993) 145.

Chapter 2

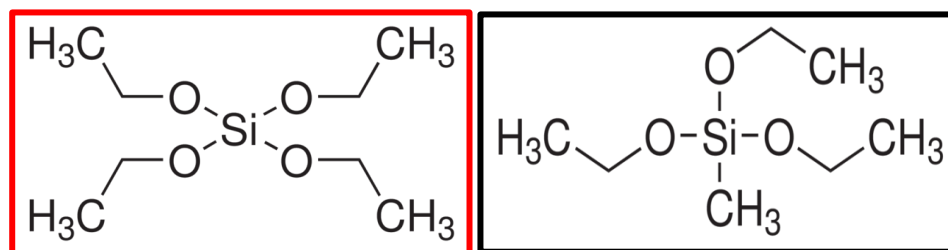
*Modified imogolite nanotubes:
state of the art*

2.1. Chemical functionalization of imogolite nanotubes

The main purpose of chemically modifying synthetic materials is the expected increased range of technological applications that can be achieved. Moreover, variables such as purity, composition, reproducibility, and specifically designed features can be often better controlled in synthetic procedures rather than using natural clay specimens, which typically contain impurities and are often not easily available. Particularly, for nanotubular structures it is critical to develop methods suitable to control the functionality of their internal and external surfaces.

Direct chemical modifications of imogolite have been obtained so far by three main routes:

1. In 2009, a new imogolite structure was patented [1,2], according to an analogue procedure described in Chapter 1, replacing TEOS precursor with TEMS, triethoxymethylsilane (Scheme 1).



Scheme 1: TEOS (red) and TEMS (black) structures.

Such imogolite-type nanotubes present inner hydrophobic surface and outer (still) hydrophilic surface. TEMS molecule has one of the valences occupied by a non-hydrolyzable Si-C bond, where a functional group, i.e. methyl group, CH₃, is attached to the silicon atom.

The resulting new stoichiometric formula, describing the chemical composition of the tubes from the outer to the inner surface, is the following



2. Wada *et al.* for the first time in 1982 [3], and recently Nair *et al.* [4-6], Levard *et al.* [7-12] and Ramirez co-workers [13,14], reported detailed studies on the formation of single and double walled aluminogermanate imogolite-type nanotubes, labeled as Ge-Imo, replacing TEOS precursor with GeCl_4 or TEOG (tetraethyl orthogermanate).
3. Ookawa *et al.* in 2006 successfully collected ironsilicate imogolite-type nanotubes, by replacing Al^{3+} atoms with Fe^{3+} [15]. Afterwards, Alvarez-Ramirez [14] performed interesting theoretical studies, which were useful to better understand Fe-Imo structure. Electronic effects due to the inclusion of ferric ions were also estimated.

Post-synthesis chemical modifications of imogolite have been instead obtained according to the following routes:

1. Nair and co-workers in 2011 [16] were able to modify the inner surface of imogolite by replacing Si-OH groups with acetyl and chloride groups, using acetyl chloride, methyltrimethoxysilane and trichlorosilane.
2. Imo-ODPA (octadecyl phosphonic acid) was synthesized by Park *et al.* in 2008 [17]. More disperse and aligned nanotubes were collected with improved affinity for polymer matrixes. Actually, phosphate groups are expected to react with the outer gibbsite-like surface of imogolite, as another recent work confirmed [18]. Aluminogermanate nanotubes were also modified by the same procedure [19].
3. Amination of the internal surface [20] and both internal/external surface [21] of imogolite (Imo-NH₂) was successfully obtained by Johnson *et al.* in 1990 by using 3-APS (3-aminopropyltriethoxysilane) in aqueous solutions.

2.2. Direct chemical modifications

2.2.1. Aluminogermanate imogolite nanotubes, Ge-Imo

Nair and co-workers successfully synthesized Ge-Imo nanotubes with AlCl_3 precursor according to an analogue procedure described in Chapter 1, except that silicon source, TEOS, was substituted by GeCl_4 [4] or TEOG [6]. As the case of silicon-containing imogolite, the synthesis procedure for Ge-imogolite consists of three main steps: base hydrolysis of a solution of aluminum and germanium monomers, stabilization of the suspension and heating at 95 °C.

The main differences of the resulting Ge-tubes from imogolite nanotubes, which appeared from both synthesis procedures, are the considerably shorter length of Ge-Imo tubes (*ca* 15 nm vs. *ca* 100 nm of imogolite) and their wider diameters (*ca* 3.3 nm vs. *ca* 2.2 nm). According to the authors, the XRD peak positions are in agreement with a monoclinic and not hexagonal arrangement, both for Imo and Ge-Imo. As discussed in Chapter 1, this is still a debating topic. Additionally, nitrogen adsorption measurements at 77 K showed that the pore size distribution of Ge-Imo is narrow. Computational studies confirmed their results [5].

Levard and co-workers were able to obtain analogue aluminogermanate tubes following a quite similar synthetic route [10]. Moreover in 2011 [11], they performed a systematic study to sort out if the initial hydrolysis of aluminum and germanium precursors in NaOH solution can affect the nanotubes formation. They found that a successful synthesis was sensitive to the hydrolysis ratio used ($R = n_{\text{OH}}/n_{\text{Al}}$, corresponding to the total n_{OH} added and not corrected for residual acidity). Particularly, they concluded that a ratio of at least 1.5 is necessary to form tubular structures. Additionally, nanotubes formed at $R = 2$ have a significant proportion of defects in the external gibbsite layer, while well crystallized Ge-imogolite is obtained at $R = 2$ and $R = 2.5$. On the contrary, less ordered phases are formed if R is increased beyond 2.5. Interestingly, they were also able to obtain, as the case of imogolite nanotubes [22], large quantities (*ca* 60 mg) of single-walled Ge-Imo nanotubes [8], optimizing synthesis conditions from initial decimolar (and not millimolar) concentration of reagents. Moreover, for the first time they evidenced the formation of double walled aluminogermanate nanotubes ([9], Figure 1), and proposed a kinetic growth model [12].

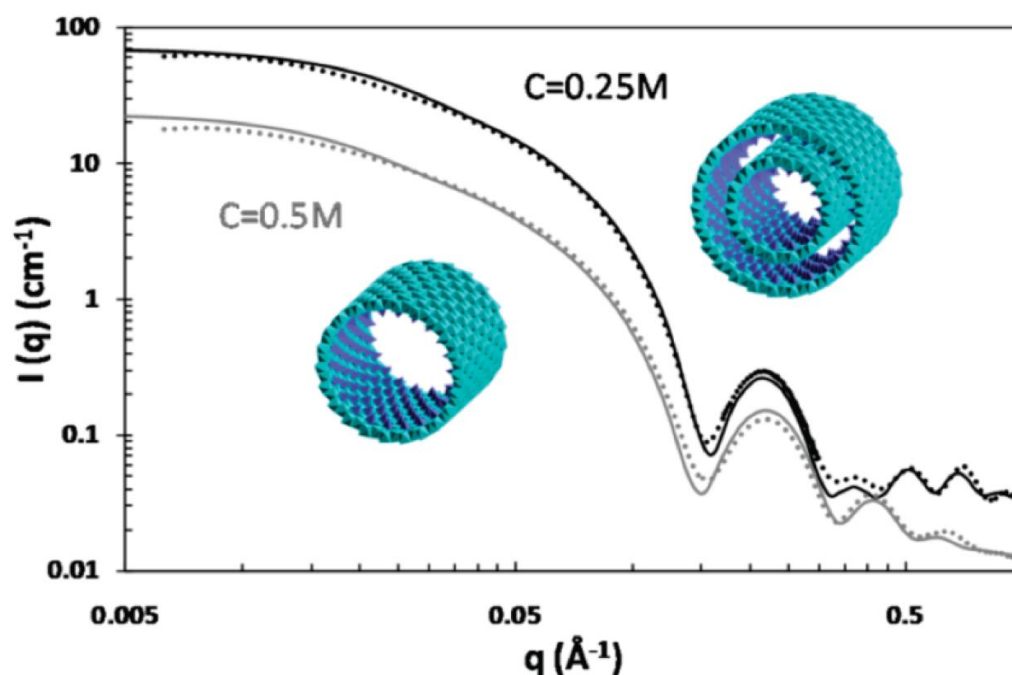


Figure 1: SAXS (Small Angle X-Ray Scattering) curves of $[\text{Al}^{3+}]$ equal to 0.5 and 0.25 molar of Ge-Imo tubes. Experimental data (dots) and theoretical results (full line) of the represented structure are plotted [9].

Alvarez-Ramirez [13] performed ab initio simulation on imogolite and Ge-imogolite, estimating a band gap range for Ge-Imo of 4.3-4.8 eV. Overall, both silicon and germanium imogolite-type nanotubes, can be considered insulators.

2.2.2. Iron-containing imogolite nanotubes, Fe-Si-Imo and Fe-Ge-Imo

The original work of Ookawa and co-workers in 2006 [15] showed for the first time the attempt to synthesize Fe-containing imogolite material using NaSiO_4 , FeCl_3 and AlCl_3 with atomic ratio, $\text{Fe}/(\text{Fe}+\text{Al})$, between 0.05 and 0.1. Ferric cations are incorporated directly to an aqueous solutions of Na_4SiO_4 and $\text{AlCl}_3 \cdot 6\text{H}_2\text{O}$. UV-vis and XANES (X-Ray Absorption Near-Edge Structure) spectra showed that the preferred coordination of ferric ions is octahedral. However, the electronic effect of the substitution of Al^{3+} by the Fe^{3+} is not totally understood. Interestingly, Fe-Imo resulted to be able to catalyze the oxidation of benzene to phenol. An analogue synthetic procedure was followed by post impregnation of iron ions.

Recently, Alvarez-Ramirez [14] carried out theoretical studies on Fe-Si-Imo and Fe-Ge-Imo nanotubes, showing new structural peculiarities as well as their electronic properties (Figure 2).

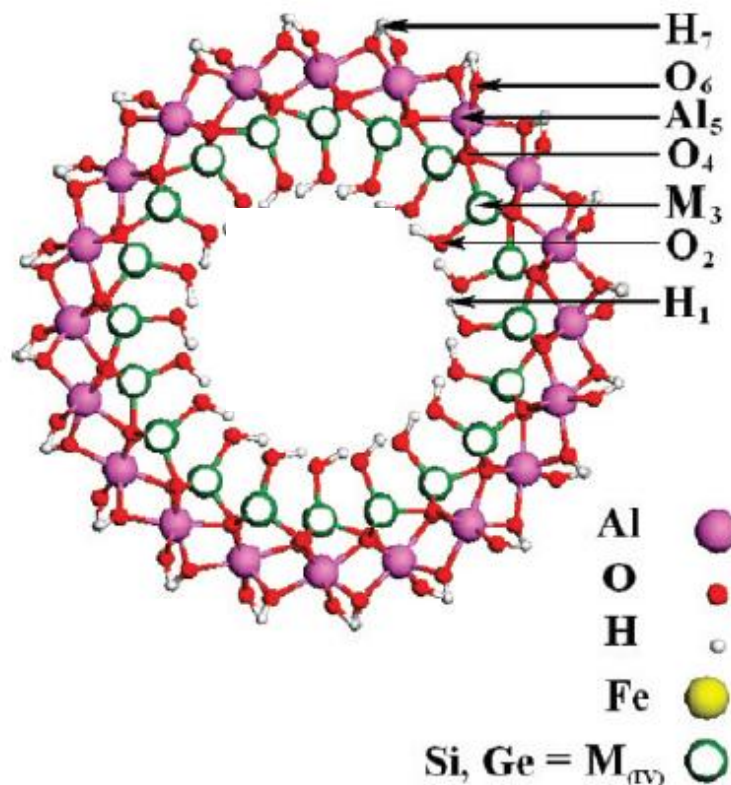


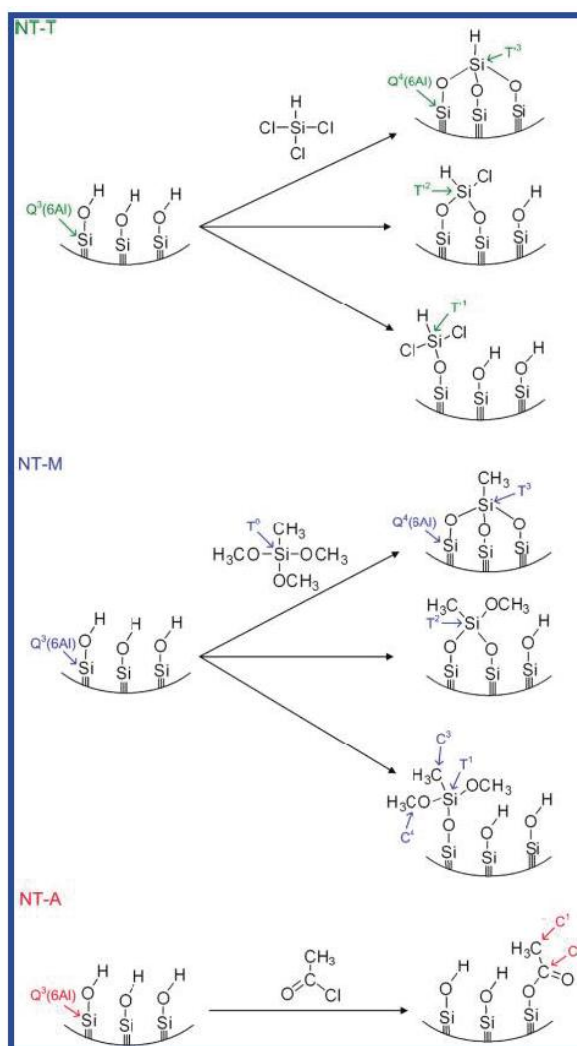
Figure 2: Section of imogolite nanotube, in which ferric ions can replace Al^{3+} sites [14].

As regards to iron ions localization, they can be identified in three different sites. The first iron position corresponds to the isomorphic substitution of aluminum ions by ferric ions, as already noticed by Ookawa *et al.* [15]. The two remaining iron configurations correspond instead to the case of iron adsorption on the inner or outer surface of imogolite, thus producing defect sites. As a consequence, electronic states are altered. The effects of the Fe concentration in the range 0.05-0.1 were analyzed. Particularly, in case of silicon containing imogolite, a small concentration of iron showed not to alter significantly the shape of the valence band outside the band gap region. However, the contribution of surface defects produces a shift of the Fermi level, generating a reduction of the band gap value from *ca* 4.7 to 2.0-1.4 eV, and from 4.2 to 2.6-1.0 eV for the Fe-silicon and Fe-germanium imogolite-like nanotubes, respectively.

2.3. Post-synthesis chemical modifications

2.3.1. Hydrophobization of imogolite inner surface

In 2011, Nair and co-workers [16] successfully synthesized hybrid imogolite nanotubes by covalently immobilization of organic functional groups inside the tubes. The functionalizing reagents were acetyl chloride, trimethylmethoxysilane and trichlorosilane (Scheme 2). Detailed physic-chemical characterization showed that chemical modification preserves nanotubes structure, and the variation in size and type of organic reagents allows the control of the tubes pore volume. As an example of the potential new applications, they showed how the hydrophobization can control surface hydrophilicity as well as water uptake.



Scheme 2: Reactions at the imogolite inner surface by acetyl chloride (NT-A), trichlorosilane (NT-T) and methyltrimethoxysilane (NT-M) [16].

Overall, they addressed once again the challenging problem of modifying inorganic nanotubular materials by introducing appropriate functional groups, so increasing the number of their technological applications, *e.g.* as more size- and shape-selective catalysts, sensors and composite membranes for gas separation.

2.3.2. Phosphorilation of imogolite outer surface

Adding pure imogolite sample to an aqueous solution of octadecyl phosphonic acid (ODPA) (1/3.5 weight ratio), Imo-ODPA nanotubes are obtained [17]. Tetradecyl phosphonic acid (TPDA) was also used, thus Imo-TPDA tubes were collected. The main evidence of the outer surface modification of imogolite, by reaction of Al–OH groups with phosphonic acid, was the improved dispersion of fibers, which prevents their aggregation. This can be explained by interconnections occurring between close side chains. Particularly, octadecyl hydrocarbons showed to be more strongly interconnected to each other rather than with tetradecyl chains. However, Imo-ODPA diameter, *ca* 5.1 nm, is similar to the diameter of the Imo-TDPA, *ca* 4.7 nm, even though octadecyl acid has longer alkyl chains (Figure 3).

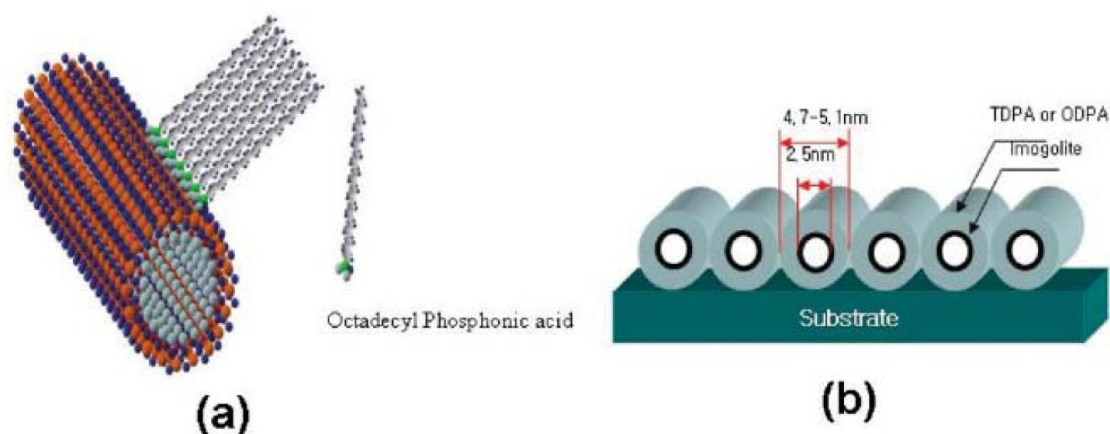
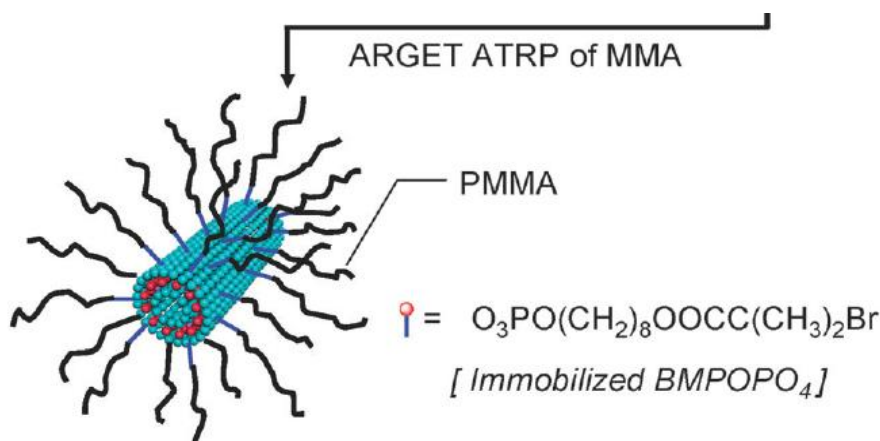


Figure 3: (a) *Chemical structure of octadecyl phosphonic acid modified imogolite, Imo-ODPA, and (b) dimension of Imo-ODPA and Imo-TDPA imogolite on the solid surface [17].*

These kinds of post functionalization are of paramount importance to build polymer/inorganic nanotubes composites.

As a recent study confirmed [18], hydrophobization of the external surface of imogolite can be achieved owing to its intrinsic reactivity towards phosphates. Particularly, a poly(methyl methacrylate), PMMA, grafted imogolite (PMMA/Imo) was obtained by ARGET ATRP (Activators Regenerated by Electron Transfer for Atom Transfer Radical Polymerization) technique. The designed ATRP initiator was the ammonium salt of 8-(2-bromo-2-methylpropanoyloxy) octyl phosphate [BMPOPO₄(NH₄)₂], which has both a 2-bromoisobutyrate group, necessary for ATRP initiator moiety, and a phosphate group, which can interact with imogolite surface. After some manipulations, MMA polymer was added and the final composite (Scheme 3) was isolated by precipitation from methanol. The concrete applications of this polymer-grafted are still under investigation. Dispersion state of PMMA/Imo and Imo in water/chloroform phase is shown in Figure 4.



Scheme 3: Schematic representation for the preparation of PMMA/Imo [18].

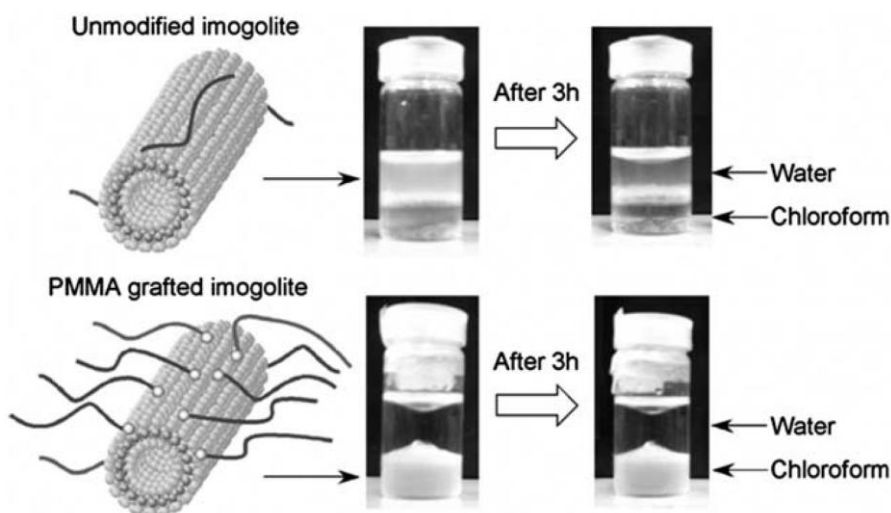


Figure 4: Dispersion state of PMMA/Imo and unmodified Imo in H₂O/CCl₄ phase [23].

2.4. References

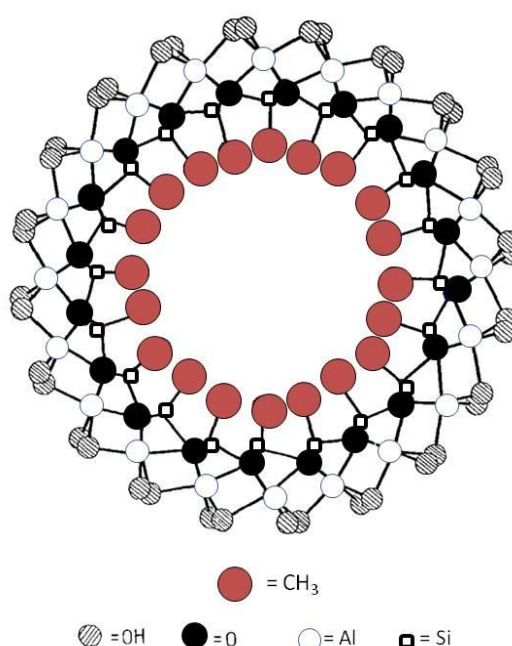
- [1] I. Bottero, B. Bonelli, S. Ashbrook, P. Wright, W. Zhou, M. Tagliabue, M. Armandi, E. Garrone, *Phys. Chem. Chem. Phys.* 13 (2011) 744.
- [2] B. Bonelli, I. Bottero and E. Garrone, Italian patent 0001380065.
- [3] S.I. Wada, K. Wada, *Clays and clay Min.* 30(2) (1982) 123.
- [4] S. Mukherjee, V.M. Bartlow, S. Nair, *Chem. Mater.* 17 (2005) 4900.
- [5] S. Konduri, S. Mukherjee, S. Nair, *ACSNano* 1(5) (2007) 393.
- [6] S. Mukherjee, K. Kim, S. Nair, *J. Am. Chem. Soc.* 129 (2007) 6820.
- [7] B. Hoang Bac, Y. Song, M. Hun Kim, Y.B. Lee, M. Kang, *Chem. Commun.* 38 (2009) 5740.
- [8] C. Levard, J. Rose, A. Masion, E. Doelsch, D. Borschneck, L. Olivi, C. Dominici, O. Grauby, J.C. Woicik, J.Y. Bottero, *J. Am. Chem. Soc.* 130 (2008) 5862.
- [9] P. Maillet, C. Levard, E. Larquet, C. Mariet, O. Spalla, N. Menguy, A. Masion, E. Doelsch, J. Rose, A. Thill, *J. Am. Chem. Soc.* 132 (2010) 1208.
- [10] C. Levard, J. Rose, A. Thill, A. Masion, E. Doelsch, P. Maillet, O. Spalla, L. Olivi, A. Cognigni, F. Ziarelli, J.Y. Bottero, *Chem. Mater.* 22 (2010) 2466.
- [11] C. Levard, A. Masion, J. Rose, E. Doelsch, D. Borschneck, L. Olivi, P. Chaurand, C. Dominici, F. Ziarelli, A. Thill, P. Maillet and J. Y. Bottero, *Phys. Chem. Chem. Phys.* 13 (2011) 14516.
- [12] P. Maillet, C. Levard, O. Spalla, A. Masion, J. Rose, A. Thill, *Phys. Chem. Chem. Phys.* 13 (2011) 2682.
- [13] F. Alvarez-Ramírez, *Phy. Rev. B* 76 (2007) 125421.
- [14] F. Alvarez-Ramírez, *J. Chem. Theory Comput.* 5 (2009) 3224.
- [15] M. Ookawa, Y. Inoue, M. Watanabe, M. Suzuki, T. Yamaguchi, *Clay Sci.* 12 (2006) 280.
- [16] D.Y. Kang, J. Zang, C.W. Jones, S. Nair, *J. Phys. Chem. C* 115 (2011) 7676.
- [17] S. Park, Y. Lee, B. Kim, J. Lee, Y. Jeong, J. Noh, A. Takahara, D. Sohn, *Chem. Commun.* 28 (2007) 2917.
- [18] W. Ma, H. Otsuka, A. Takahara, *Chem. Commun.* 47 (2011) 5813.
- [19] B. Hoang Bac, Y. Song, M. Hun Kim, Y.B. Lee, M. Kang, *In. Chem. Comm.* 12 (2009) 1045.
- [20] L.M. Johnson, T.J. Pinnavaia, *Langmuir* 6 (1990) 307.
- [21] L.M. Johnson, T.J. Pinnavaia, *Langmuir* 7 (1991) 2636.
- [22] C. Levard, A. Masion, J. Rose, E. Doelsch, D. Borschneck, C. Dominici, F. Ziarelli, J.Y. Bottero, *J. Am. Chem. Soc.* 131 (2009) 17080.
- [23] K. Yamamoto, H. Otsuka, S.I. Wada, D. Sohn, A. Takahara, *Polymer* 46 (2005) 12386.

Chapter 3

Methyl-imogolite

3.1. Synthesis

At room temperature, TEMS (triethoxymethylsilane) and $\text{Al}(\text{s-butoxide})_3$ are added to a 75 mM aqueous solution of HClO_4 in the molar ratios $\text{Si}:\text{Al}:\text{HClO}_4 = 1.x:2:1$. A slight excess of TEMS is used in order to prevent the preferential formation of gibbsite during hydrolysis. The solution is stirred for 18 h, diluted to 20 mM, autoclaved at 100 °C for 4 days, dialyzed for at least 4 days against deionized water and then, after drying at 50 °C, Me-Imo powder is collected (Scheme 1).



*Scheme 1: Schematic representation of Me-Imo nanotubes structure.
Stoichiometric formula: $(\text{OH})_3\text{Al}_2\text{O}_3\text{SiCH}_3$.*

3.2. FE-SEM and HR-TEM characterizations

FE-SEM and HR-TEM images are shown in Figure 1 and Figure 2, respectively. Electron microscopy images show a material composed of interwoven bundles of nanotubes, similar to those of Imo. However, Me-Imo fibers have larger diameter (*ca* 15-20 nm) and longer length (*ca* 200 nm) as compared to Imo nanotubes. Fibers are therefore more loosely bound and more free to assume a close packed configuration.

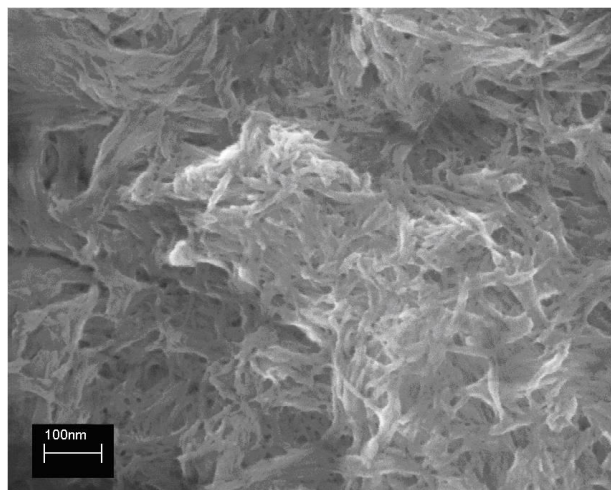


Figure 1: FE-SEM image of Me-Imo bundles of nanotubes.

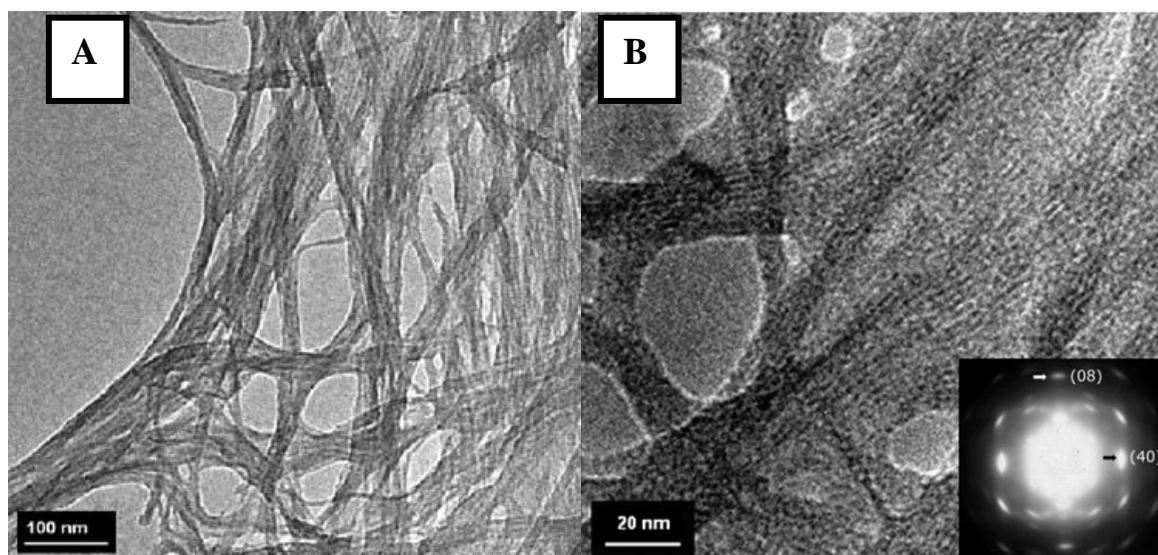


Figure 2: HR-TEM micrographs of Me-Imo taken at two different magnifications degrees. Inset of panel 2B: SAED taken from a bundle of few nanotubes.

These features are comparable to Ge-Imo nanotubes, which have wider diameter but shorter length in contrast with Imo [1]. The dimension of tubes estimated by HR-TEM corresponds with the value obtained by FE-SEM measurements. However, the observed fibers appear to be rather longer (*ca* 500 nm vs. 200 nm) than those visible by SEM microscopy. SAED (Selected Area Electron Diffraction) pattern is indexed according to repeat units within the nanotubes (viewed perpendicular to the nanotubes axis, taken as their *c*-axis), with $c = 8.0 \text{ \AA}$ and $a = b = 5.6 \text{ \AA}$, in compliance with the nomenclature of Bursill *et al.* [2]. The *c* repeat unit corresponds to three AlO_6 octahedra along the tube axis, whereas *a* and *b* refer to an Al–Al distance within the curved wall, perpendicular to the tube axis.

3.3. XRD and FT-IR characterizations

XRD patterns of Me-Imo nanotubes (Figure 3a) show a higher degree of long-range order as compared to Imo (Figure 4). All peaks are more intense because of the more ordered packing of nanotubes. Particularly, the peak due to the (100) reflection is at $3.62\ 2\theta$: the cell parameter a , corresponding to a centre-to-centre distance between two aligned nanotubes is calculated to be 2.4 nm, assuming a hexagonal packing; with Imo, the cell parameter is 2.3 nm, *i.e.* slightly smaller.

As can be seen from several XRD patterns of Me-Imo tubes obtained in different batch syntheses (dash blue lines), the position of this main peak can slightly vary due to temperature and pressure variations during the polymerization step. Actually, if it is run at too high temperature ($T \geq 105^\circ\text{C}$), impurities can be formed, as detected by the peak centered at *ca* $18.5\ 2\theta$. According to literature [3,4], this can disclose the presence of an aluminum oxide polymorph called nordstrandite, which shows a typical reflection at $18\text{--}19\ 2\theta$. Morphology of synthetic nordstrandite is known to vary according to synthesis conditions [5], from roughly rectangular to either ovoidal single particles or clusters of acicular crystals. Figure 3b shows the star-like morphology of nordstrandite phase obtained in this study.

The peak at $8.83\ 2\theta$ (0.99 nm) is assigned to the repetition of the structural c unit along the tube (001), whereas the signal at $12.31\ 2\theta$ is caused by the reflection of (211) planes (0.72 nm) [1,6]. Interestingly, all peaks of Me-Imo diffraction pattern are slightly shifted to lower angles, as compared to those of imogolite. The same slight variation has been observed by Konduri *et al.* [7] in mixed oxide nanotubes, where silicate groups are partially substituted by germanate groups. In case of Ge-imogolite [8], the longer distance between nanotubes was ascribed to their lower curvature, due to the greater length of the Ge–O bond with respect to the Si–O bond [8]. For Me-Imo, two orders of factors are thought to be involved. Firstly, a larger curvature could be caused by the presence of methyl groups, for either steric (*i.e.* the methyl group is larger than the hydroxyl group) or electronic effects.

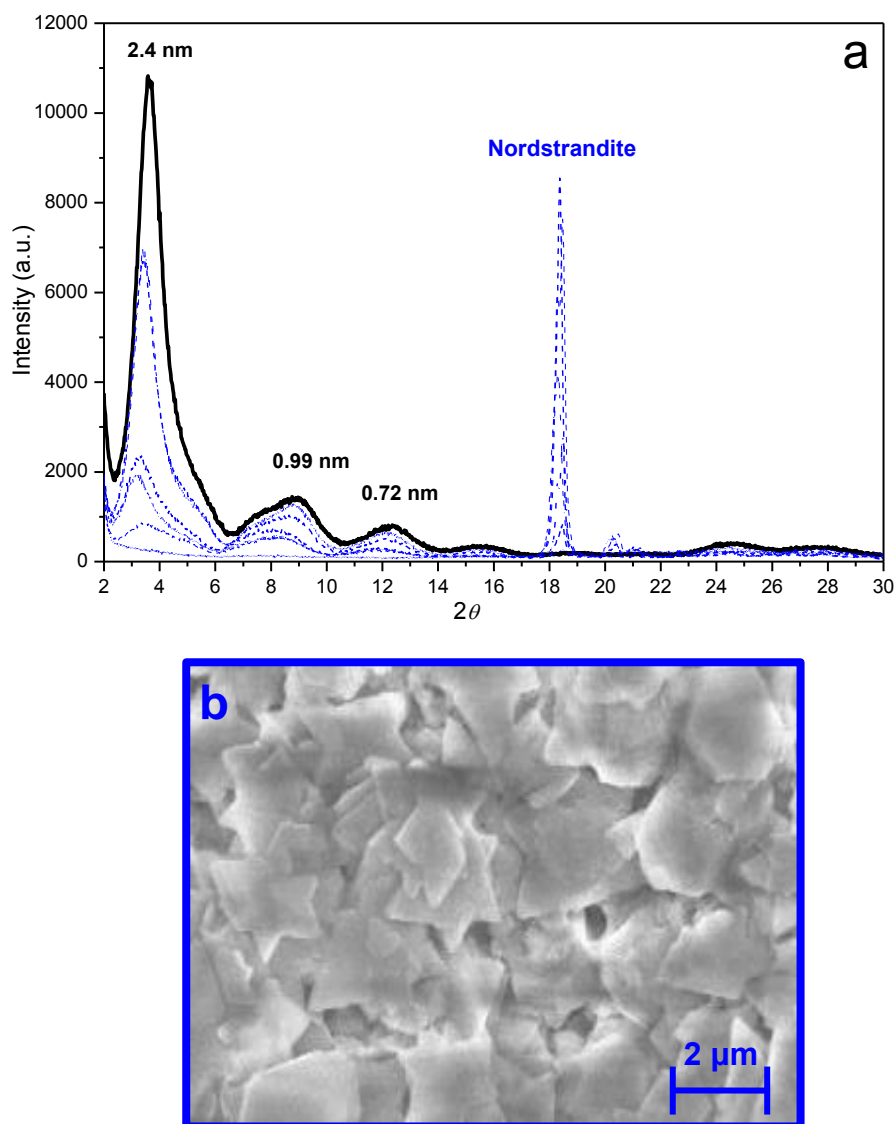


Figure 3: (a) XRD patterns of pure Me-Imo (black) and Me-Imo with nordstrandite impurity (blue), which can be formed during batch syntheses if temperature and pressure of the polymerization temperature is not completely controlled; (b) FE-SEM image of nordstrandite phase.

Indeed, Sidorkin *et al.* [9] reported that the calculated Si–O bond length in the series of $(\text{HO})_3\text{Si-X}$ and $(\text{CH}_3\text{O})_3\text{Si-X}$ compounds is affected by the electronegativity of the X substituent: the presence of methyl groups in place of hydroxyl ones could have the same effect, inducing a relaxation of the structure and a shift of the energy minimum towards nanotubes with a higher number of units in the circumference [10]. Alternatively, the larger cell parameter could be explained by the increased distance between nanotubes, caused by the absence of external charges, as discussed above.

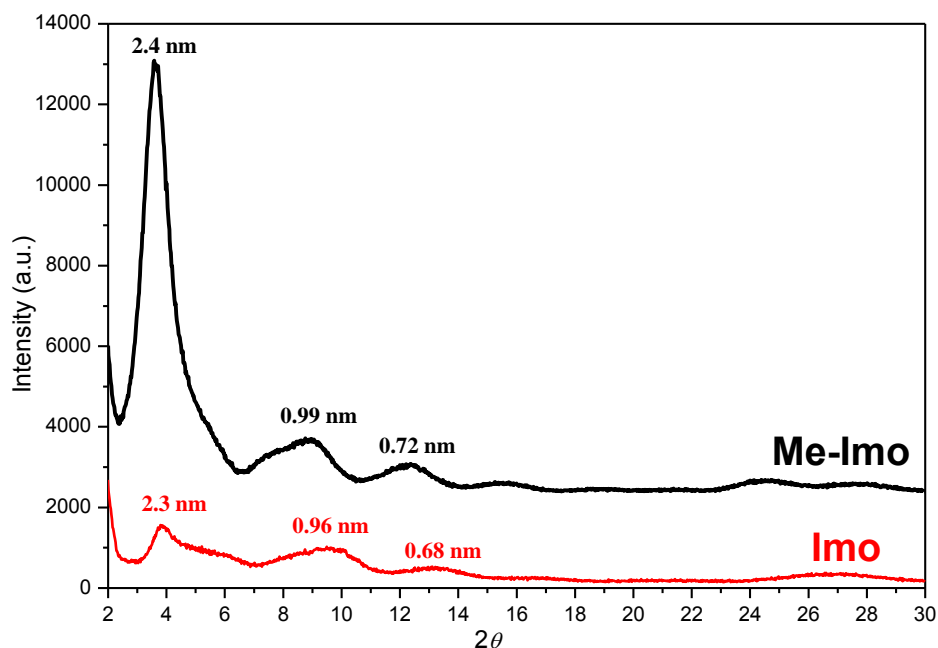


Figure 4: XRD patterns of pure Me-Imo (black) and Imo (red).

Figure 5 reports the FT-IR spectra of a self-supporting KBr wafer of Me-Imo in the 4000-1200 cm^{-1} range. Imogolite spectrum is also shown for comparison. Both samples present a prominent band at 1644 cm^{-1} , due to the bending mode of adsorbed water on nanotubes surfaces, and a broad and intense absorption in the OH stretch region (3800–3000 cm^{-1}), assigned to the presence of outer Al(OH)Al groups. Particularly, water in Imo is expected to be more concentrated inside the tubes [11], while for Me-Imo is adsorbed on the outer surface, due to the complete hydrophobization of the inner surface. In fact, only Me-Imo sample presents the following peculiar signals

1. **1275 cm^{-1} band**, due to the bending mode of Si-CH₃ groups.
2. **2973 and 2919 cm^{-1} bands**, assigned to the asymmetric and symmetric stretching modes of Si-CH₃ groups, respectively.
3. A sharp **band at 777 cm^{-1}** due to the Si-C stretching vibration [12-14].

In the 900-1000 cm^{-1} range, all bands characteristic for the imogolite structure [2,15] are present. The 910 cm^{-1} band can be assigned to Al-O stretching vibrations, whereas the band at 954 cm^{-1} is assigned to Si-O stretching vibrations.

The modification of the structure, by introducing methyl groups at the inner surface, affects the Si-O and O-Al bonds, leading to a shift of their vibrational frequencies. In fact, if compared to Imo, these two bands are found at slightly lower wavenumbers. The same result was obtained by Konduri *et al.* [7] on Ge-Imo: the band at 930 cm^{-1} shifts to 910 cm^{-1} for wider diameter nanotubes. Coherently, it is also obvious that the 995 cm^{-1} band, typical of Si-OH bending vibration [16], is not present in Me-Imo spectrum.

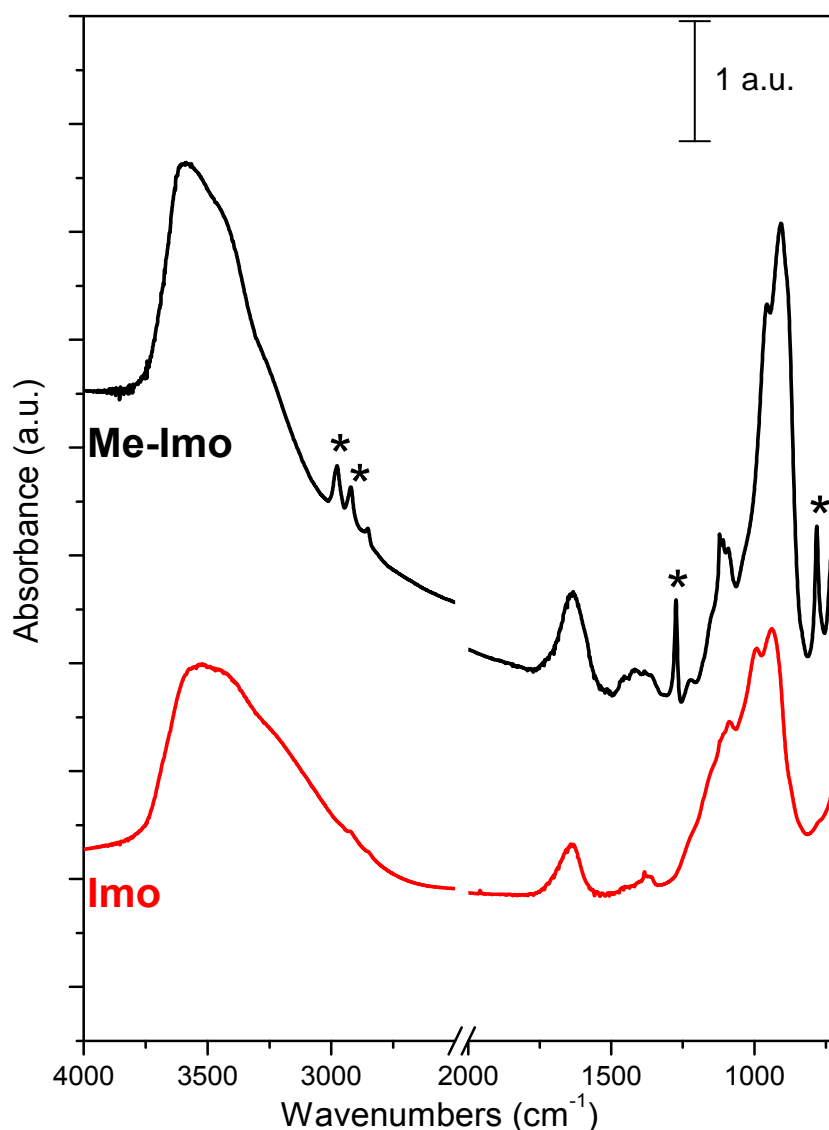


Figure 5: FT-IR spectra of KBr self-supporting wafer of Me-Imo (black) and Imo (red) tubes. Peculiar bands of Me-Imo (asterisks) are found at: $2973/2919\text{ cm}^{-1}$, assigned to the asy/sym $\nu(\text{CH}_3)$ of Si- CH_3 inner group, 1275 cm^{-1} , due to the correspondent $\delta(\text{CH}_3)$ and $\nu(\text{Si-C})$ modes, identified by the 777 cm^{-1} band. Coherently, the typical Si-OH bending vibration mode at 995 cm^{-1} , is not seen in Me-Imo spectrum.

3.4. MAS NMR characterization

MAS NMR measurements were collected at ENSICAEN, Ecole Nationale Supérieure d'Ingénieurs of Caen (France), during my PhD foreign period in collaboration with Prof. Fernandez's research group. Experimental evidence found are in agreement with the results already discussed.

Quantitative ^{27}Al MAS NMR signal (Figure 6) show that aluminum is in octahedral arrangement, as confirmed by the presence of a single peak for both samples at *ca* 4.9 ppm. In fact, according to literature [17], Al^{VI} atoms show an intense peak at 5 ppm. Moreover, this value is reasonably close to that of aluminum atom in gibbsite (*ca* 8.9 ppm, [18]).

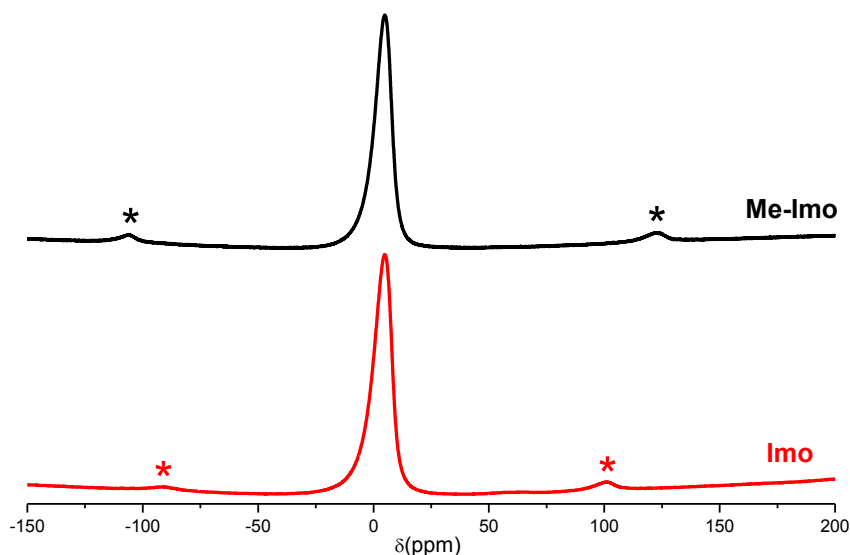


Figure 6: ^{27}Al MAS NMR spectra of fresh Me-Imo (black) and Imo (red). Spinning side bands are labeled with asterisks.

However, ^{29}Si MAS NMR spectrum presents two different sharp peaks at -43 and -79 ppm for fresh Me-Imo and Imo, respectively (Figure 7). A chemical shift value of $\delta(-43)$ is typical for tetrahedral silicon atoms bonded to one carbon and three aluminum atoms through oxygen bridges [10,19], while the sharp signal at -79 ppm corresponds to isolated silicon tetrahedral sites sharing three oxygen atoms with octahedral aluminum atoms [20-22]. No components at -79 ppm are present for Me-Imo nanotubes, confirming the total absence of silanols group as well as un-reacted silicon precursor.

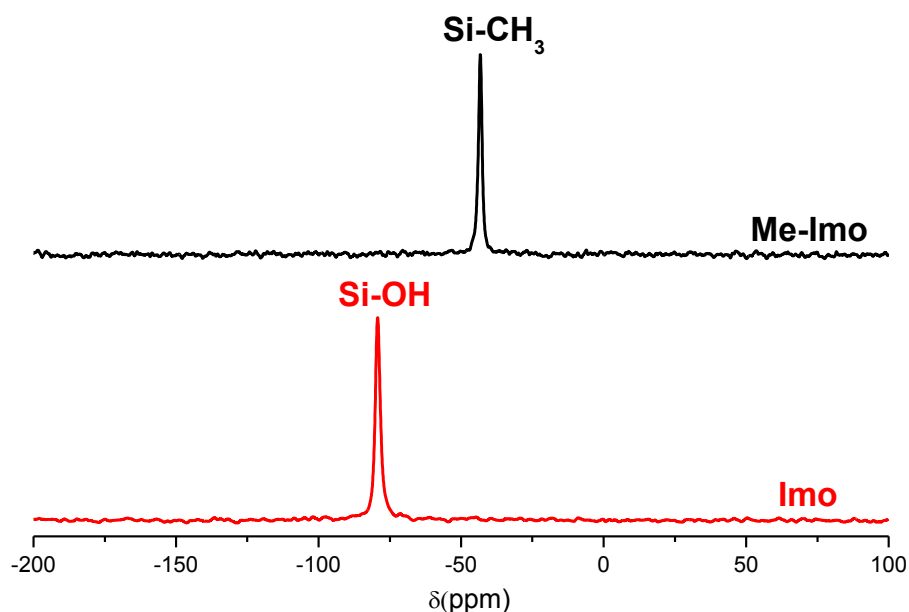


Figure 7: ^{29}Si MAS NMR spectra of fresh Me-Imo (black) and Imo (red) nanotubes.

An analogue result was obtained by CP $\{^1\text{H}\}$ - ^{29}Si measurements (Figure 8). Additionally, CP $\{^1\text{H}\}$ - ^{13}C spectrum (Figure 9), proper only of Me-Imo, presents a ^{13}C peak at *ca* -1.6 ppm, a chemical shift value reasonably close to that of ^{13}C of the reference compound, TMS (tetramethylsilane), which is at 0 ppm.

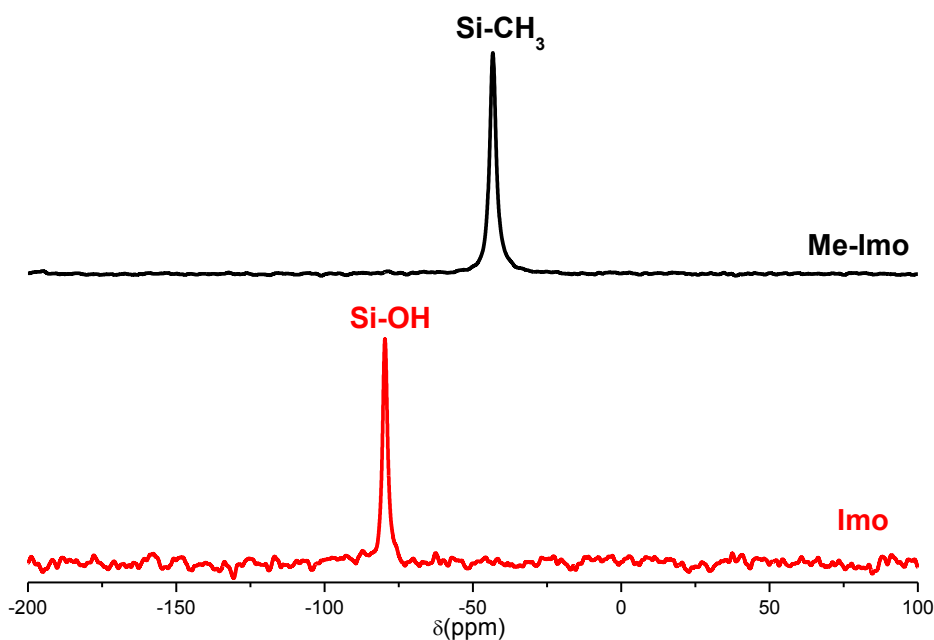


Figure 8: CP $\{^1\text{H}\}$ - ^{29}Si MAS NMR spectra of fresh Me-Imo (black) and Imo (red).

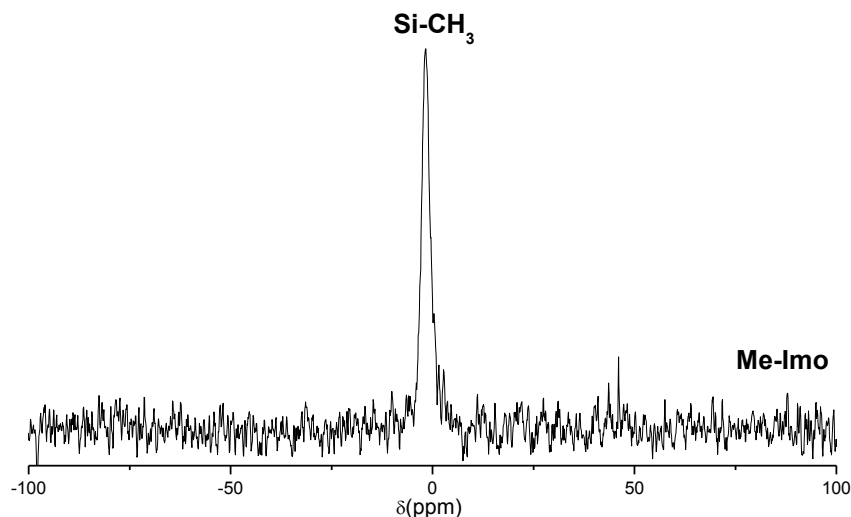


Figure 9: CP $\{^1\text{H}\}$ - ^{13}C MAS NMR spectra of fresh Me-Imo nanotubes.

3.5. Porosity characterization by N_2 adsorption/desorption isotherms

The adsorption/desorption isotherms of N_2 at nominal 77 K for several methyl imogolite samples outgassed at 300 °C and obtained from different successful batch syntheses are reported in Figure 10a, while the relative Pore Size Distributions (PSDs), calculated applying the Non Local-Density Functional Theory (NL-DFT) method to adsorption branches of isotherms, are shown in Figure 10b. Correspondent XRD patterns are reported in Figure 10c. Table 1 gathered the correspondent textural parameter, as derived from combined XRD patterns (Figure 10c) and N_2 adsorption isotherms.

Table 1: Textural parameters of five Me-Imo samples outgassed at 300 °C and obtained from several successful batch syntheses, as derived from combined XRD patterns and N_2 adsorption isotherms at 77 K.

Sample	BET SSA (m^2/g)	Internal SSA (m^2/g)	External SSA (m^2/g)	Total pore vol. (cm^3/g)	Micropores vol. (cm^3/g) ^a	Inner diameter (nm) ^b	Outer diameter (nm) ^c
#1 Me-Imo	1145	366	779	0.68	0.24	1.63	2.76
#2 Me-Imo	819	281	538	0.53	0.12	1.63	3.01
#3 Me-Imo	671	250	421	0.43	0.10	1.64	2.99
#4 Me-Imo	665	265	400	0.39	0.09	1.64	2.98
#5 Me-Imo	530	218	312	0.30	0.09	1.59	3.11

^a As evaluated by applying the α_s method.

^b As calculated by NL-DFT method to the adsorption branch of the isotherm.

^c As calculated by the $d_{(100)}$ reflection peak of XRD patterns according to an hexagonal packing.

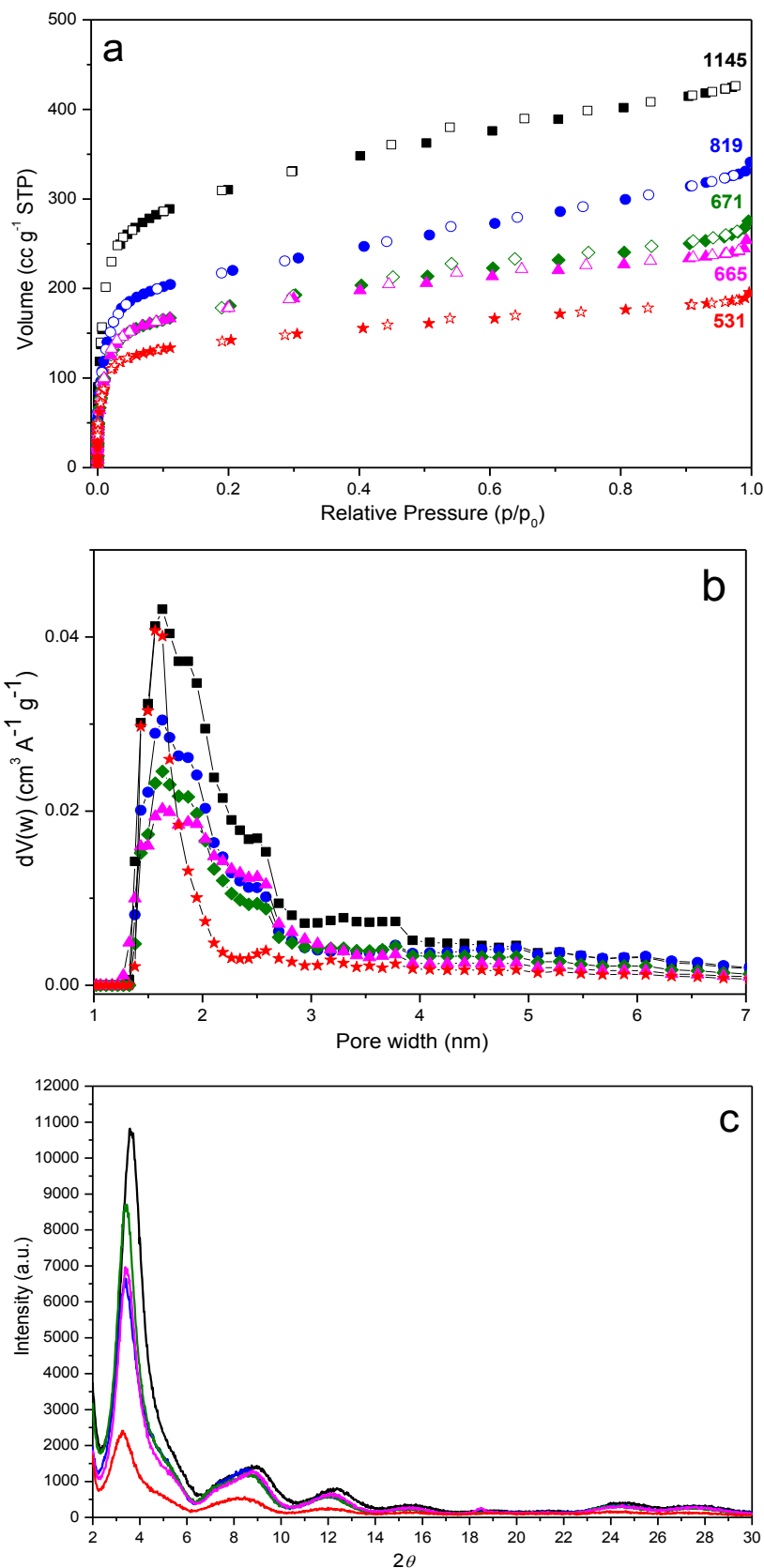


Figure 10: (a) N_2 adsorption and desorption isotherms of several Me-Imo samples. Numbers close to each curve indicate the corresponding BET SSA value. Relative (b) PSDs (NL-FDT method) and (c) XRD patterns.

Besides imogolite, BET SSA value of Me-Imo is negatively affected by the presence of adsorbed water molecules or other impurities, which limit N₂ accessibility [23]. As a consequence, a suitable pretreatment in vacuum is necessary to estimate the real surface area. Porosimetry analyses showed that methyl-imogolite nanotubes with quite different textural parameters can be statistically obtained. All samples show type I shape isotherms typical of microporous materials. The very limited hysteresis loop can be due to limited external mesopores, most probably derived from slit mesopores among bundles. Moreover, they have a comparable inner diameter, while total and micropores volumes decrease as the BET SSA values decrease, till a minimum value of 0.30 and 0.09 cm³/g, respectively. This general trend could be evident also from the decreasing intensity of the main XRD peak, even if cannot be considered a reliable feature in each case. In fact, the main reflection of Me-Imo #3 (green) with surface area of 671 m²/g has a higher intensity as compared to Me-Imo #2 (blue) and Me-Imo #4 (fuchsia), characterized by surface areas of 819 and 665 m²/g, respectively.

As a whole, Me-Imo #1 (black) is the sample with the highest surface area (1145 m²/g). Textural parameters are compared to those of the best common imogolite sample obtained in Table 2. Figure 11a and 11b present the corresponding adsorption/desorption isotherms and pore size distributions, respectively. Surface area of Me-Imo resulted to be roughly more than twice as that of imogolite. Inner diameter length is also increased from 0.95 nm to 1.63 nm, thus confirming the increased SSA value recorded. In fact, larger pores may form as cavities in the fibrous network of heterogeneous imogolite bundles.

Actually, it is necessary to highlight that small deviations can occur between porosimetry and FE-SEM/HR-TEM results, probably due to the applied method for the calculation of the PSD (zeolites kernel), which is not able to accurately describe the structure of imogolite nanotubes.

Table 2: Textural parameters of Imo and Me-Imo, outgassed at 300 °C, as derived from combined XRD patterns and N₂ adsorption isotherms at 77 K.

Sample	BET SSA (m ² /g)	Internal SSA (m ² /g)	External SSA (m ² /g)	Total pore vol. (cm ³ /g)	Micropores vol. (cm ³ /g) ^a	Inner diameter (nm) ^b	Outer diameter (nm) ^c
Me-Imo	1165	423	742	0.68	0.24	1.63	2.76
Imo	355	237	118	0.19	0.10	0.95	2.79

^a As evaluated by applying the α_s method.

^b As calculated by NL-DFT method to the adsorption branch of the isotherm.

^c As calculated by the $d_{(100)}$ reflection peak of XRD patterns according to an hexagonal packing.

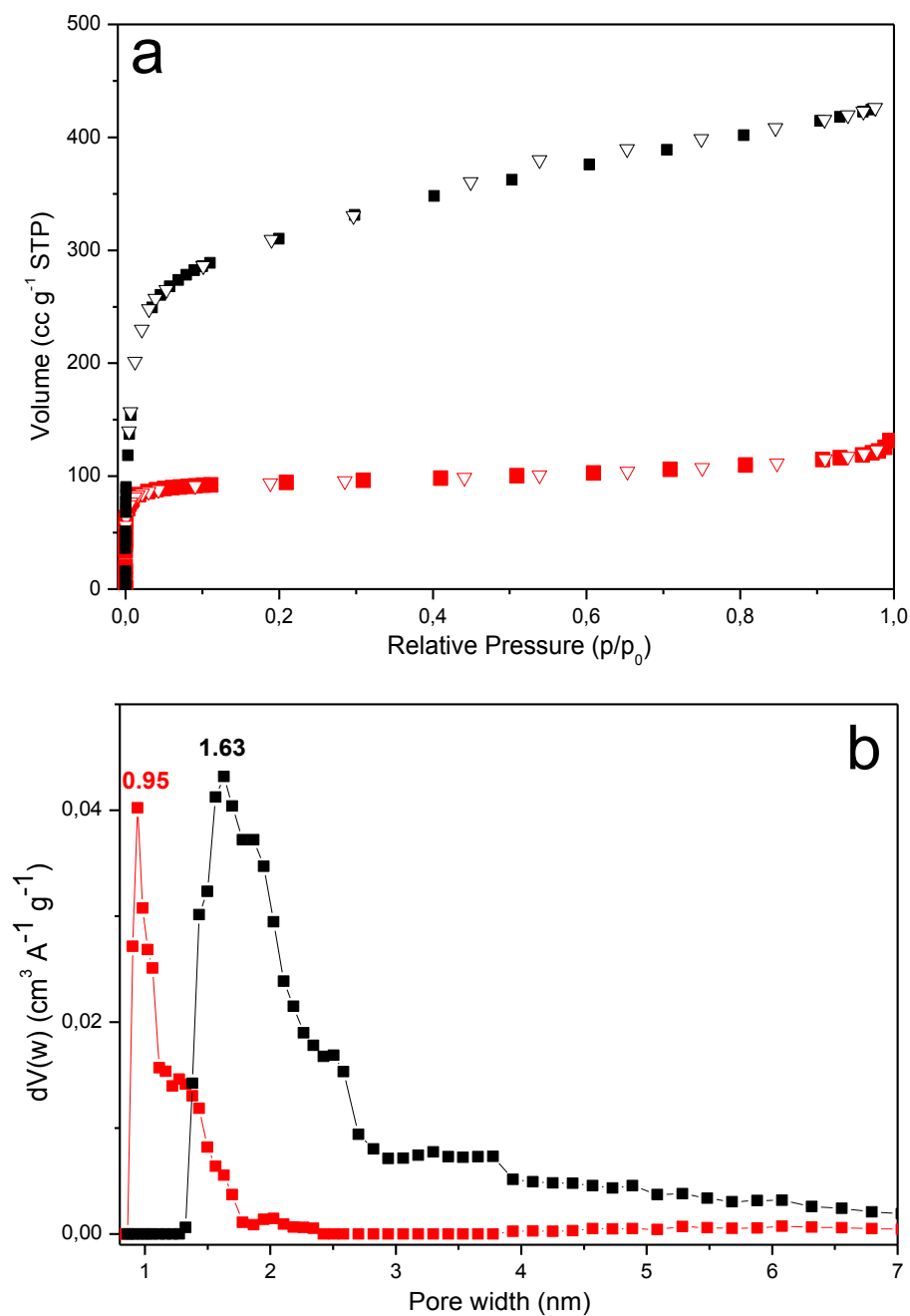


Figure 11: (a) N_2 adsorption (square) and desorption (triangle) of Me-Imo (black) and Imo (red); (b) Correspondent PSDs (NL-FDT method).

3.6. CH_4 adsorption

The presence of a hydrophobic inner surface along with an outer hydrophilic one could be in principle exploited in adsorption processes aimed at gas separation (*e.g.* hydrocarbon recovery from wet gaseous streams) or storage: for this reason, adsorption of methane was tested at 30 °C on Imo and Me-Imo, previously outgassed at 300 °C.

For each sample, the first adsorption run was followed by a desorption step and a second adsorption run was carried out after re-outgassing the samples at 300 °C, to check process reversibility and materials stability. As shown by Figure 12, both type of nanotubes can reversibly adsorb methane in the explored pressure range; furthermore, second adsorption run values are not affected by the additional outgassing treatment, confirming thermal stability of the adsorbent. Curve-fits obtained by assuming a Langmuir model of adsorption, show good agreement with experimental points: both the maximum adsorbed volumes (76.81 and 29.65 cm³/g for Me-Imo and Imo, respectively) and equilibrium constants (0.03 and 0.06 bar⁻¹ for Me-Imo and Imo, respectively), were calculated.

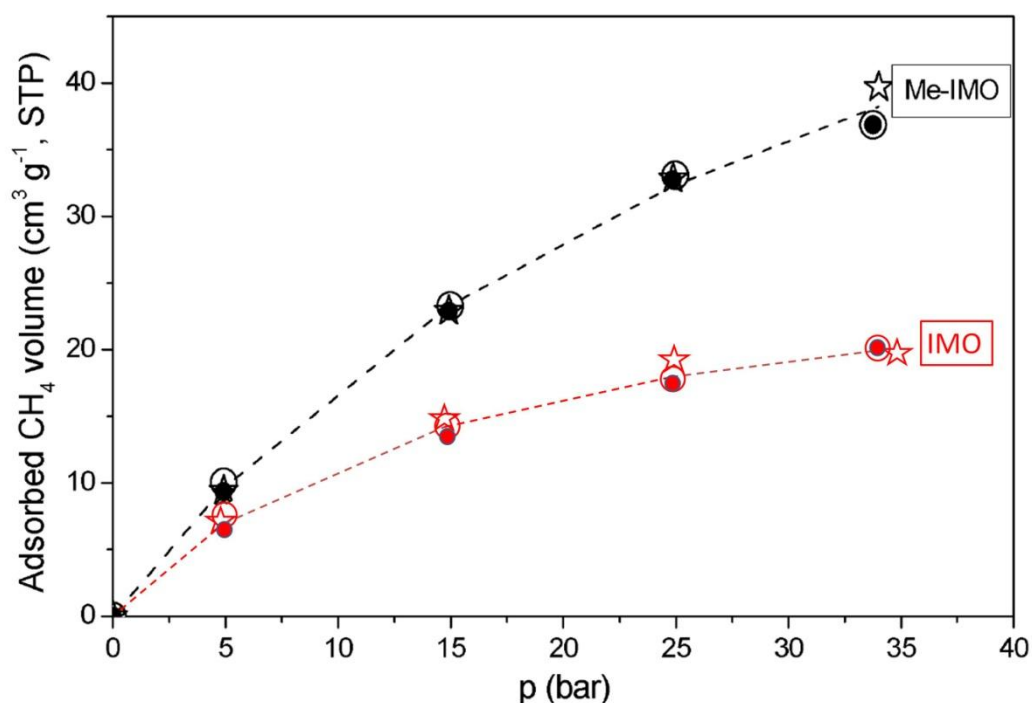


Figure 12: *CH₄ adsorption isotherms at 30 °C in the 5–35 bar pressure range measured on Me-Imo and Imo previously outgassed at 300 °C. Full circles: 1^o adsorption run; empty circles: desorption run; stars: 2^o adsorption run performed after re-outgassing at 300 °C. Dotted lines: curve-fits obtained by assuming a Langmuirian adsorption model [23].*

Although the obtained average specific capacities are not still comparable to those reported by other materials generally proposed as efficient methane adsorbents [24-26], it results that Me-Imo adsorption capacity at 35 bar is 2.7% w/w, *i.e.* about 2.5 times larger than that of Imo (1.4% w/w), in agreement with both its larger pore volume and the presence of a methylated surface.

3.7. Conclusions

Overall, in this chapter a brief review about chemical modifications of imogolite nanotubes, either by direct or post synthesis routes, was presented. Particularly, synthesis procedure and bare characterizations of the original hydrophobic imogolite structure, Me-Imo, were described in detail as well as its potential application as methane adsorbent. Methyl-imogolite represents the starting material in this PhD work for the subsequent post-synthesis amination, which will be present in the next chapter.

3.8. References

- [1] S. Mukherjee, V.M. Bartlow, S. Nair, *Chem. Mater.* 17 (2005) 4900.
- [2] L.A. Bursill, J.L. Peng, L.N. Bourgeois, *Ph. Mag.* 80(1) (2000) 105.
- [3] A. Violante, P.M. Huang, *Clays and clay Min.* 41(5) (1993) 590.
- [4] P. Violante, A. Violante, J.M. Tait, *Clays and Clay Min.* 30(6) (1982) 431.
- [5] A. Violante, P. Violante, *Clays and Clay Min.* 28 (1980) 425.
- [6] P.D.G. Cradwick, V.C. Farmer, J.D. Russell, K. Wada, N. Yoshinaga, *Nature Phys. Sci.* 240 (1972) 187.
- [7] S. Konduri, S. Mukherjee, S. Nair, *ACSNano* 1(5) (2007) 393.
- [8] S. Mukherjee, K. Kim, S. Nair, *J. Am. Chem. Soc.* 129 (2007) 6820.
- [9] V.F. Sidorkin, V.A. Shagun, V.A. Pestunovich, *Russ. Chem. Bull.* 48 (1999) 1049.
- [10] B.L. Su, M. Roussel, K. Vause, X.Y. Yang, F. Gilles, L. Shi, E. Leonova, M. Edèn, X. Zou, *Micr. Mes. Mater.* 105 (2007) 49.
- [11] B. Creton, D. Bougeard, K.S. Smirnov, J. Guilment, O. Poncelet, *Phys. Chem. Chem. Phys.* 10 (2008) 4879.
- [12] R.A.C.M.M. van Swaaij, A.J.M. Berntsen, W.G.J.H.M. van Sark, H. Herremans, J. Bezemer, W.F. van der Weg, *J. Appl. Phys.* 76 (1994) 251.
- [13] H. Wieder, M. Cardona, C.R. Guarnieri, *Phys. Stat. Sol. B* 92 (1979) 99.
- [14] G. Ambrosone, U. Coscia, S. Lettieri, P. Maddalena, C. Privato, S. Ferrero, *Thin Solid Films*, 403 (2002) 349.
- [15] V.C. Farmer, A.R. Fraser, J.D. Russell, N. Yoshinaga, *Clay Min.* 12 (1977) 55.
- [16] G.H. Koenderink, S.G.J.M. Kluijtmans, A.P. Philipse, *J. Colloid Inter. Sci.* 216(1999) 429.
- [17] J.J. Fitzgerald, C. Murali, C.O. Nebo, M.C. Fuerstenau, *J. Colloid Inter. Sci.* 151 (1991) 299.
- [18] P. Straka, *Acta Geodyn. Geomater.* 7(4)(160) (2010) 461.
- [19] K. Yamamoto, T. Tatsumi, *Chem. Mater.* 20 (2008) 972.
- [20] B. Bonelli, I. Bottero, N. Ballarini, S. Passeri, F. Cavani, E. Garrone, *J. Catal.* 264 (2009) 15.
- [21] K.J. MacKenzie, M.E. Bowden, J.W.M. Brown, R.H. Meinhold, *Clays and Clay Min.* 37(4) (1989) 317.
- [22] B.A. Goodman, J.D. Russell, B. Montez, E. Olfield, R.J. Kirkpatrick, *Phys. Chem. Miner.* 12 (1985) 342.
- [23] I. Bottero, B. Bonelli, S. Ashbrook, P. Wright, W. Zhou, M. Tagliabue, M. Armandi, E. Garrone, *Phys. Chem. Chem. Phys.* 13 (2011) 744.
- [24] V.C. Menon, S. Komarneni, *J. Porous Mater.* 5 (1998) 43.
- [25] M. Eddaoudi, J. Kim, N. Rosi, D. Vodak, J. Watcher, M. O'Keeffe, O.M. Yaghi, *Science* 295 (2002) 469.
- [26] I. Senskova, S. Kaskel, *Micr. Mes. Mater.* 112 (2008) 108.

Chapter 4

Aminated methyl-imogolite

4.1. Introduction

Functionalization of an inorganic material surface by means of alkoxy derivatives could be a complicated process [1-5], especially when the amount of grafting substance is large. The first attempt to carry out silylation reactions with hydrolyzed 3-aminopropyltriethoxysilane (3-APS) in aqueous media on Imo was reported by Johnson and Pinnavia in 1990 [6,7]. A selective modification of the external surface was achieved if a little amount of 3-APS is used [6], while both surfaces are silylated if the amine precursor is present in excess [7].

In this study for the first time the selective functionalization of the external surface of Me-Imo is proposed, thus obtaining a new material, labeled Me-Imo-NH₂. Amino-ligands are known to offer reactive sites for reversible adsorption of CO₂ [8], which will be indeed studied by means of IR spectroscopy and volumetric measurements. Me-Imo, contrary to nearly all cases in surface chemistry, can be considered an all-surface system, of which the gross formula is simply (OH)₃Al₂O₃Si-CH₃. The full functionalization with 3-APS of the external surface of Me-Imo should lead in principle to a substance with a defined gross formula, **NH₂-(CH₂)₃-Si(O)₃Al₂O₃SiCH₃**.

This helps in choosing the amount of 3-APS to be used. The most evident choice is a molar ratio 1:1 between (OH)₃Al₂O₃SiCH₃ and 3-APS. Besides this composition, a sample with a loading only *ca* one third of APS amount was considered and preferentially used, for the following reasons:

- Due to the rigid structure of methyl-imogolite, not all external Al(OH) groups can possibly react.
- The bulky aminopropyl groups are likely to cover the surface even at loadings lower than the theoretical one.
- A “diluted” grafted phase is preferable when carrying out structural and spectroscopic studies, being better defined.

4.2. Synthesis

Me-Imo was obtained as described in Chapter 3. Few milligrams of the sample were then dried at 150 °C in vacuum for 4 hours to remove moisture before the treatment with 3-APS. To a stirred suspension of Me-Imo in anhydrous toluene (*ca* 60 ml), 3-APS was added in the molar ratios Me-Imo:3-APS = 1:0.3 or 1:1. The resulting mixture was then re-fluxed at 100 °C for 12 h under a nitrogen atmosphere. The slurry was cooled to room temperature and washed with toluene, the product then filtered and dried at room temperature. Powder collected by introducing a 1:1 molar ratio will be labeled as Me-Imo-NH₂-100, while for the 1:0.3 ratio, Me-Imo-NH₂-30. Finally, in order to remove adsorbed water without altering the nature of the surface, samples have been pretreated usually at 150 °C in vacuum.

4.3. FE-SEM and XRD characterizations

FE-SEM micrograph of Me-Imo-NH₂-30 is shown in Figure 1a. Morphology seems to be unaltered after the grafting procedure. Analogously to Imo [9] and Me-Imo [10], Me-Imo-NH₂-30 results to be formed of interwoven fibers.

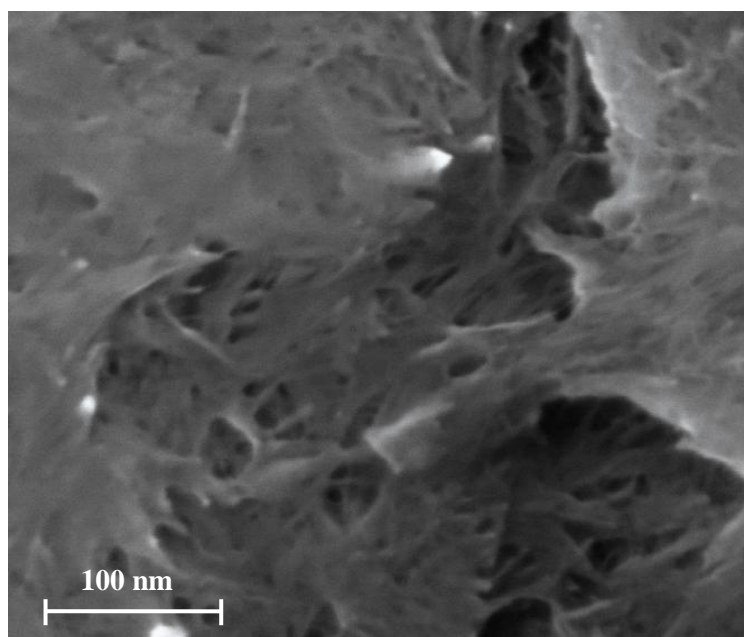


Figure 1: FE-SEM image of Me-Imo-NH₂-30.

Figure 2 compares the XRD patterns of Me-Imo (curve *a*), Me-Imo-NH₂-30 (curve *b*) and Me-Imo-NH₂-100 (curve *c*). It is noteworthy that all diffraction patterns show basically the same reflections, although at different intensities, so ruling out the possibility that functionalization only introduce some disordering in the nanotube array, making the distance between nanotubes to vary from point to point of the nanotube itself. The packing array is probably either hexagonal or tetragonal. Configuration could indeed depend on the water content, because nanotubes cross section may change from elliptic to circular, on varying the amount of water [11].

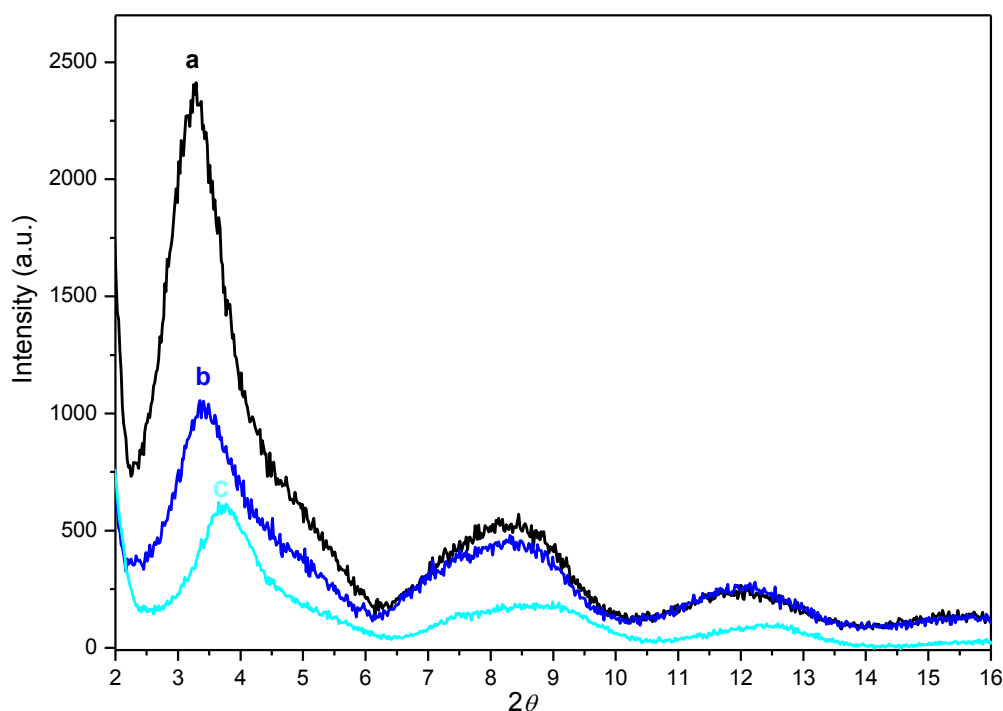


Figure 2: XRD patterns of Me-Imo (black, curve *a*), Me-Imo-NH₂-30 (blue, curve *b*) and Me-Imo-NH₂-100 (light blue, curve *c*).

For a moderate loading, reflections at relatively high angles are nearly untouched by the presence of the grafted phase. Moreover, the reflection at *ca* $2\theta = 3.40^\circ$, typical of the ordering of nanotubes, is almost at the same 2θ value. However, its intensity has severely decreased by the presence of moderate amounts of grafted 3-APS.

These evidence can be explained considering that the amination process does not alter in a systematic way the distance between nanotubes, contrary to what expected from a naïve point of view, but it just introduces disorder among the tubes. Actually, only larger amounts of grafted material perturb both peaks position and intensity.

In fact, the reflection of the main peak in curve *c* occurs at a slightly higher value, so suggesting that the presence of aminopropyl chains can make the nanotubes come closer.

According to the literature, the loss of order because of functionalization with 3-APS has been already noted for mesoporous materials [1,12-14].

4.4. FT-IR and MAS NMR characterizations

Figure 3 reports the FT-IR spectra of Me-Imo and Me-Imo-NH₂-30 self-supporting wafers outgassed at 150 °C. No molecular water is present, as shown by the absence of the scissors mode band at 1630 cm⁻¹ (downward arrow).

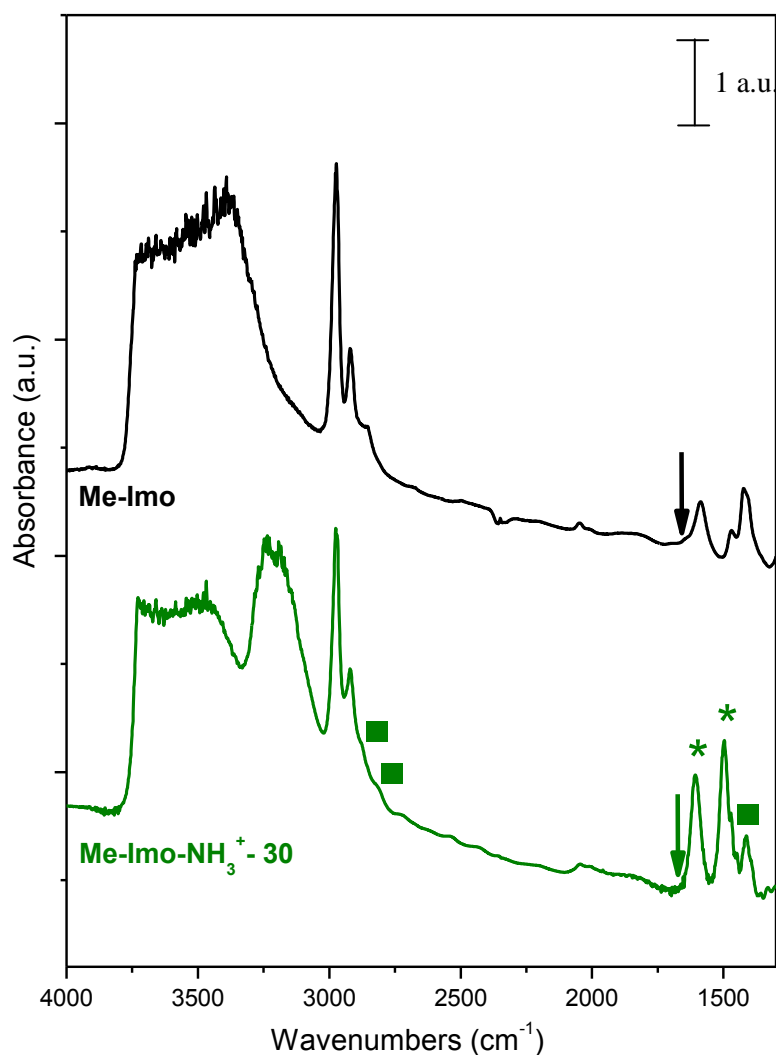
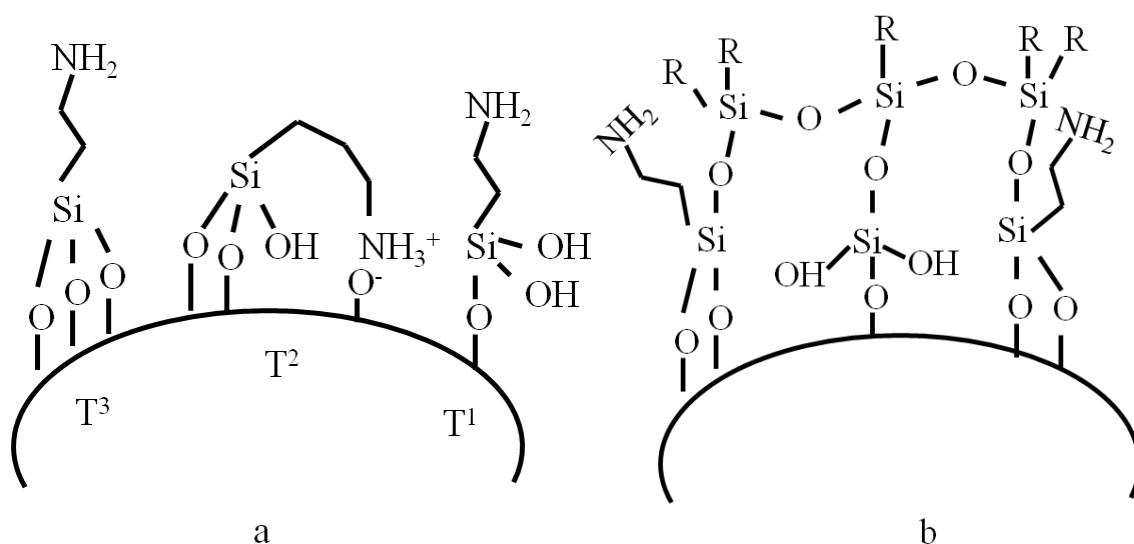


Figure 3: FT-IR spectra of Me-Imo (black) and Me-Imo-NH₃⁺-30 (green) outgassed at 150 °C.

The 2970, 2920 and 1273 cm^{-1} bands of Me-Imo- NH_2 -30 are the stretching and bending modes of methyl groups, respectively; bands at 2878 and 2823 cm^{-1} are instead due to the stretching modes of CH_2 groups (squares). In the C-H and N-H bending region, the 1414 cm^{-1} band is related to CH_2 groups (square). Interestingly, the bands at 1608 and 1497 cm^{-1} (asterisks) are not due to the primary amine functionality, but to deformation modes of primary ammonium groups R-NH_3^+ , as observed on aminated aluminosilicates [2,15].

The fact that protonated grafted species are formed, despite the synthesis is run in anhydrous condition, could be explain considering the variety of mechanisms by which 3-APS is known to graft silica [16] and alumina [17] surfaces, respectively. Scheme 1a and 1b present the most probable arrangements that can be expected to be evidenced on methyl-imogolite surface [6,7].



Scheme 1: Possible (a) T^x species on alumina external surface; (b) oligomerization of 3-APS precursor.

The assignment of protonated species is confirmed by the spectra in Figure 4, which compares the N-H bending IR region of the sample as prepared, and the same after a mild treatment with a 0.001 M NaOH solution, able to convert ammonium ions into substituted amine species.

The absorption envelope in the upper curve is due to aluminol species only, while the corresponding envelope in the lower spectrum of Me-Imo- NH_3^+ -30 (from now on) is broader and more complex. An Evans window (Fermi resonance effect) is probably present at *ca* 3200 cm^{-1} [18], a frequency close to overtones and combination modes of low-lying absorptions.

The more marked broadness of the O-H stretching absorption can be explained by H-bonding interaction between un-exchanged aluminol species, still present on the outer surface, and grafted 3-APS.

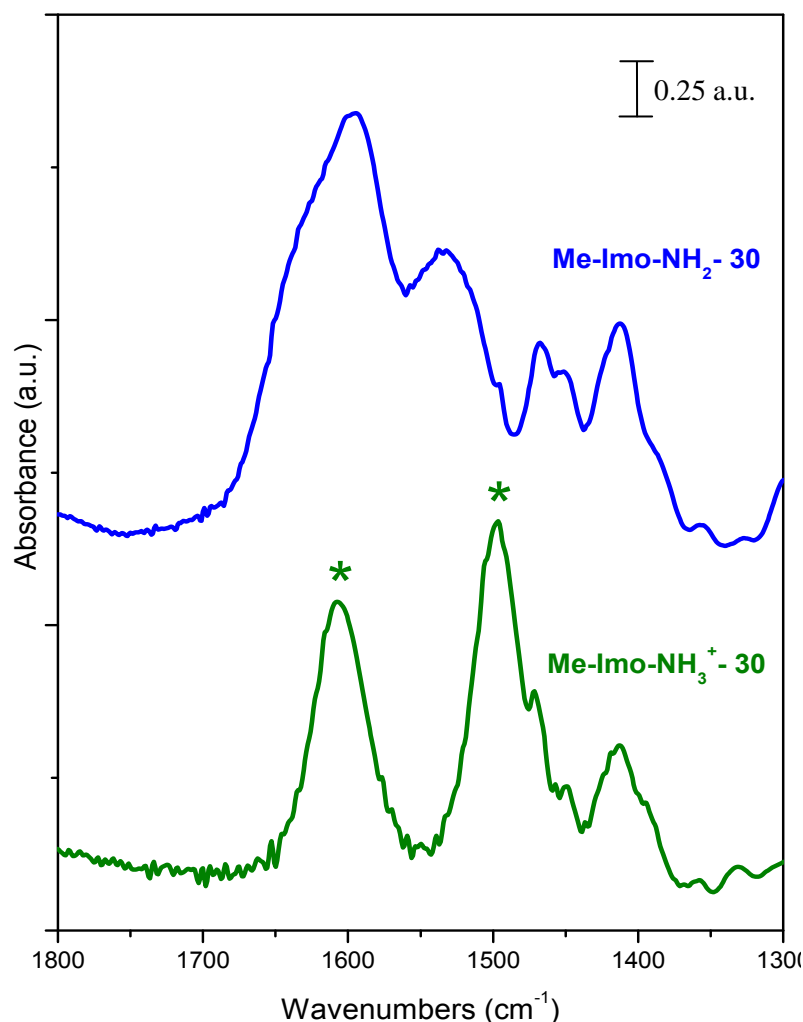


Figure 4: FT-IR spectra of Me-Imo-NH₂-30 (blue) and Me-Imo-NH₃⁺-30 (green).

MAS NMR investigations are in agreement with FT-IR results and confirm the expected grafting mechanism proposed in Scheme 1a and 1b. The aminated sample analyzed is protonated Me-Imo-NH₃⁺-30. Despite it is generally assumed to be difficult to discriminate between protonated and unprotonated terminal amino groups [16], more specific interpretations can be given if experimental and simulated NMR patterns are compared. Particularly, ¹H and ¹³C NMR simulated spectra of fresh 3-APS and 3-APS protonated are gathered in Appendix II.

Figure 5a compares the ^{29}Si MAS NMR spectra of Me-Imo and Me-Imo-NH $_3^+$ -30 outgassed at room temperature. The former has a resonance at *ca* -43 ppm corresponding to Si-CH $_3$ species on the inner surface [10]. The same peak is also present in Me-Imo-NH $_3^+$ -30 with similar intensity, showing, as expected, that the inner surface remains unaffected because the 3-APS grafting is likely taking place on the outer surface of the Me-Imo nanotubes (on the aluminum side).

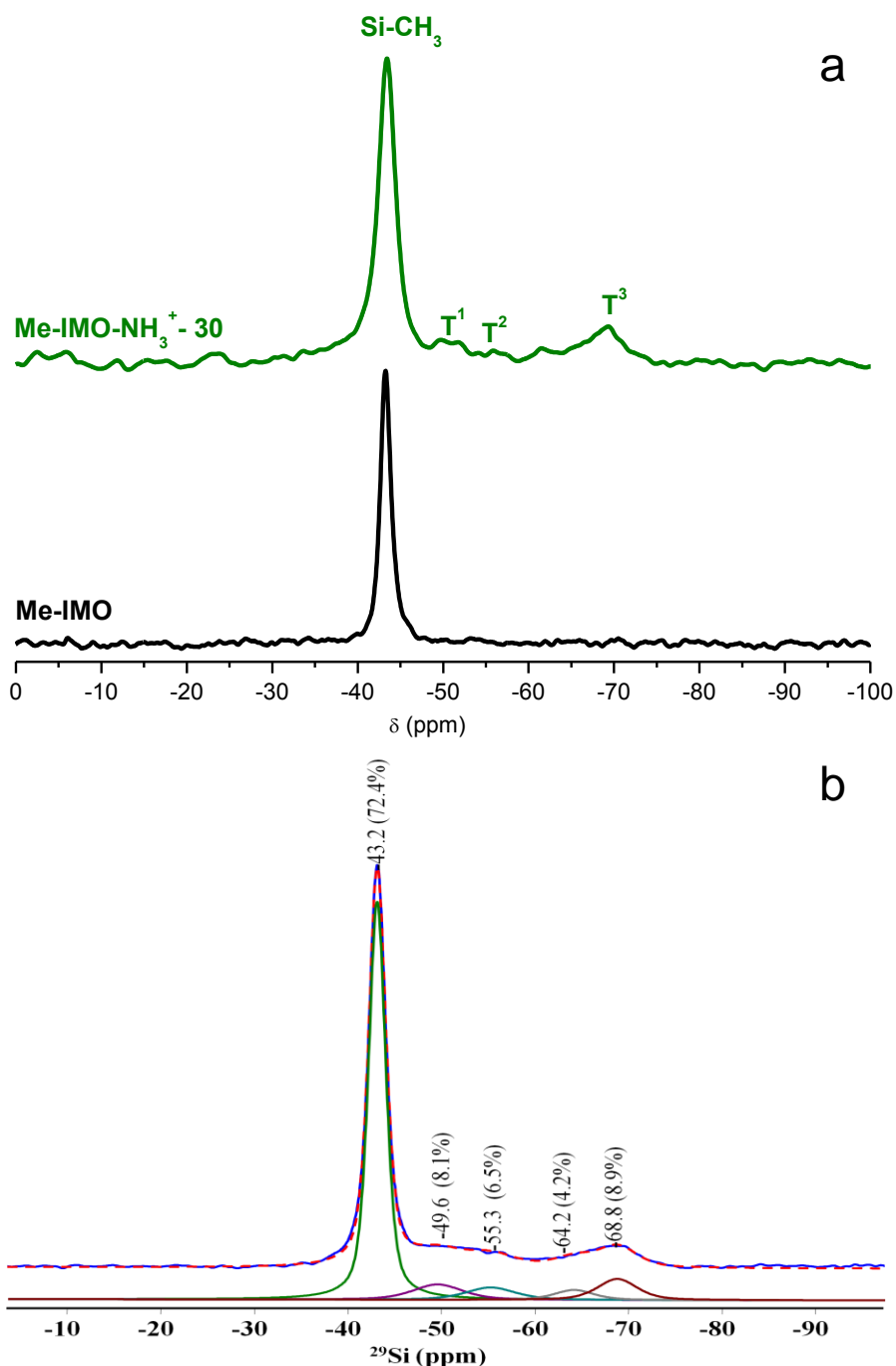


Figure 5: (a) ^{29}Si MAS NMR spectra of Me-Imo-NH $_3^+$ -30 (green) and Me-Imo (black) outgassed at room temperature; (b) deconvolution of ^{29}Si MAS NMR spectrum of Me-Imo-NH $_3^+$ -30.

Strong evidence for the 3-APS grafting is given on the spectrum of Me-Imo-NH₃⁺-30 by both the absence of a resonance at -45 ppm where ungrafted APS should appear [19], and the presence of a broad resonance in the -(50-69) ppm range, which can be assigned to one (*ca* -50 ppm), two (*ca* -54/-60 ppm) and three-legged (-69 ppm) grafted species (Scheme 1a, Figure 5b) [6,7,16,17,20-25]. The new peak at *ca* -64 ppm may indicate silicon atoms being in different environment, *i.e.* involved in the polymerization of 3-APS (Scheme 1b). The ratio of the integrated areas of the broad peak (3-APS) and -43 ppm peak (inner Si-CH₃) is approximately equal to 0.30, a value coinciding with the synthesis molar ratio, Me-Imo:3-APS = 1:0.3. This result is the first evidence that the aminated precursor reacted quantitatively.

Figure 6 shows the CP {¹H}-¹³C MAS NMR spectrum of Me-Imo-NH₃⁺-30 outgassed at room temperature and 150 °C. Traces of toluene are expectedly found in fresh Me-Imo-NH₃⁺-30 sample, as detected by the presence of two peaks at 128 and 124 ppm, respectively.

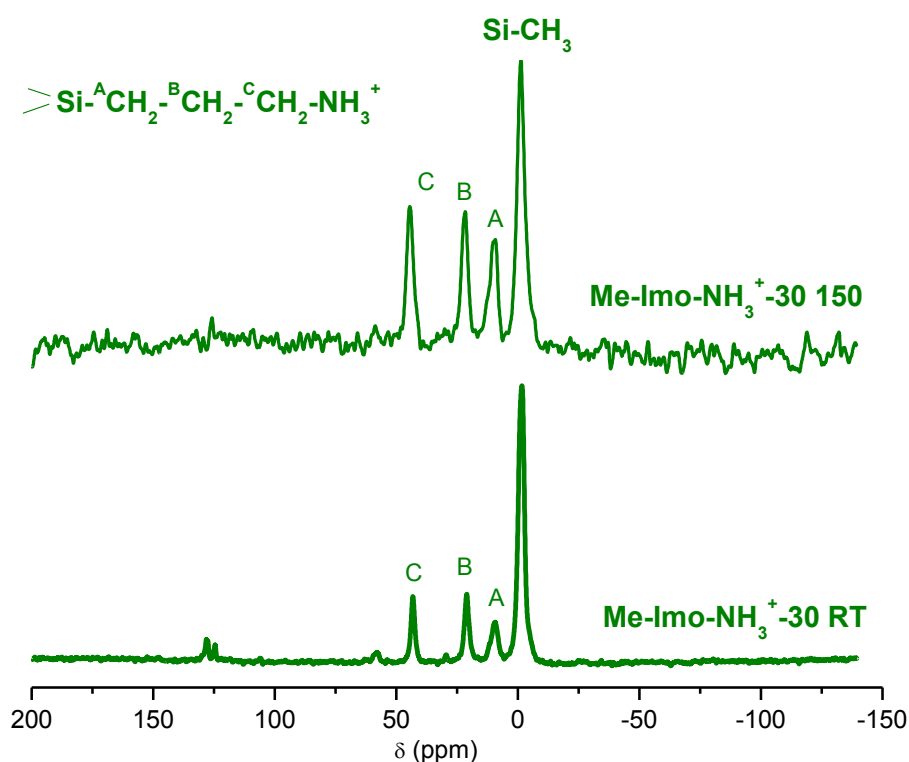


Figure 6: CP {¹H}-¹³C MAS NMR spectrum of Me-Imo-NH₃⁺-30 outgassed at room temperature and 150 °C.

Nevertheless, thermal treatment at 150°C is enough to completely removed the solvent impurity. Moreover, the three characteristic resonances at 9.8, 21.7 and 44.4 ppm, corresponding to the three carbon atoms in the hydrocarbon chain of the aminopropyl group [16,20,26], are proper only of the aminated sample, while the -1.0 ppm peak is assigned to the carbon atom of the Si-CH₃ species, common to both samples. No other resonance can be observed in the ¹³C spectrum, confirming that the ethoxy groups are fully eliminated during the grafting process. In fact, simulated ¹³C NMR pattern of pure 3-APS (Appendix II) shows two peaks at 18 and 59 ppm, respectively.

Figure 7 presents the comparison between CP {¹H}-¹³C MAS NMR of Me-Imo-NH₃⁺-30 and Me-Imo outgassed at 150 °C.

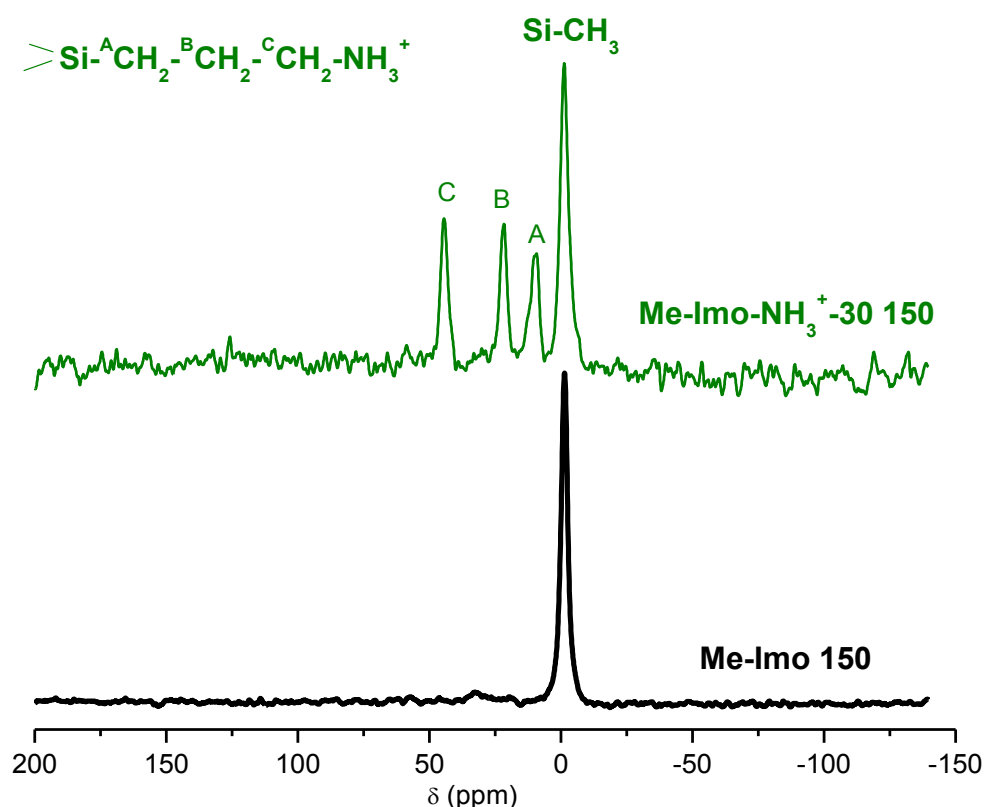


Figure 7: CP {¹H}-¹³C MAS NMR spectrum of Me-Imo-NH₃⁺-30 and Me-Imo outgassed at 150°C.

¹H-Echo spectrum of Me-Imo-NH₃⁺-30 outgassed at 150 °C is shown in Figure 8. Well resolved peaks are present, corresponding to hydrogen atoms of inner methyl groups bonded to silicon as well as those of the aminopropyl chain, which thus appears to be non-degraded during the reaction.

Particularly, the more shifted methylene group (C) of the chain is that which is directly bonded to the amino group (D). Evidence of the protonation of terminal NH₂ groups are the presence of resonances at *ca* 7 ppm, which may indicate their particular orientations on the surface. In fact, as compared to simulated patterns, ¹H-Echo NMR spectrum of unprotonated 3-APS does not show peaks at higher chemical shift than 4 ppm.

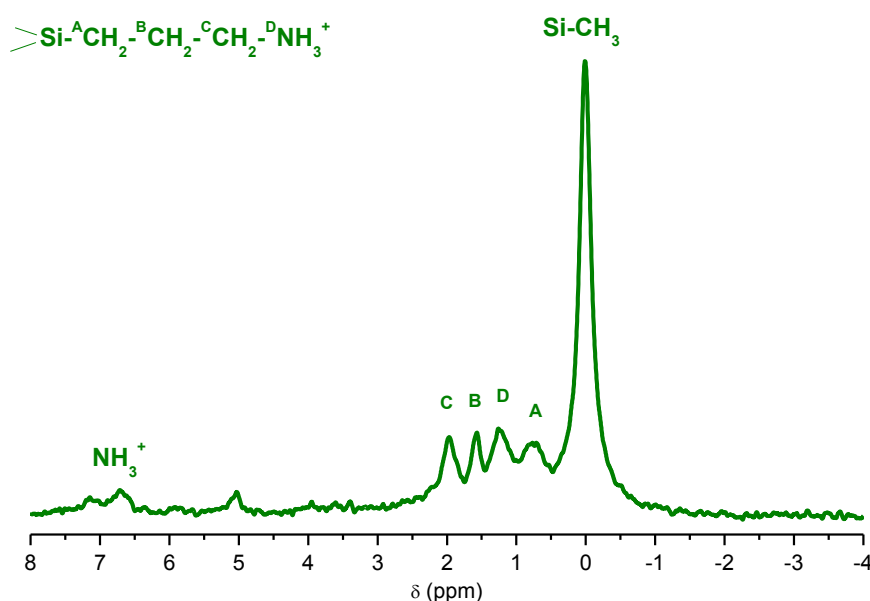


Figure 8: ¹H- Echo MAS NMR spectra of Me-Imo-NH₃⁺-30 outgassed at 150 °C.

Furthermore, 2D HETCOR (Heteronuclear Correlation) ¹H-¹³C experiment of Me-Imo-NH₃⁺-30 outgassed at 150 °C (Figure 9) confirms that no correlation between outer chains and inner methyl groups is present, thus it can be concluded that they belong to different domains.

Finally, on ²⁷Al MAS NMR spectra of Me-Imo-NH₃⁺-30 and Me-Imo outgassed at room temperature (Figure 10), a similar resonance is observed at *ca* 5 ppm in both cases, showing that the coordination of the aluminum atoms is not affected by the functionalization process.

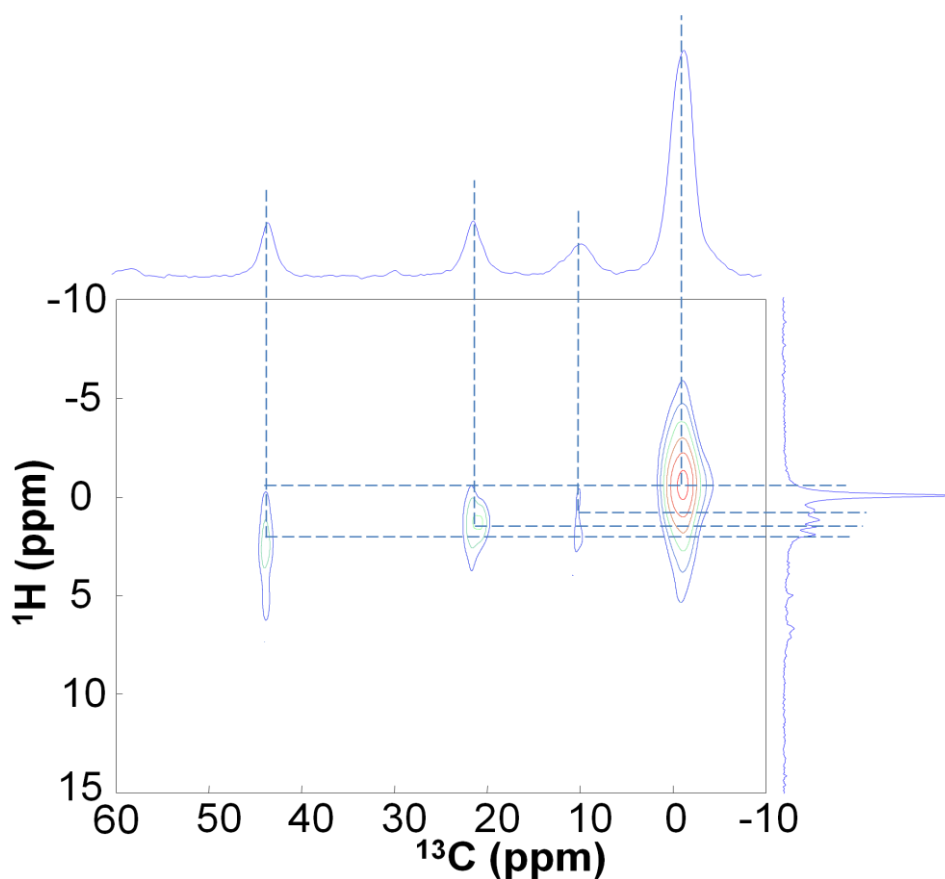


Figure 9: 2D HETCOR ^1H - ^{13}C experiment of Me-Imo-NH_3^+-30 outgassed at $150\text{ }^\circ\text{C}$.

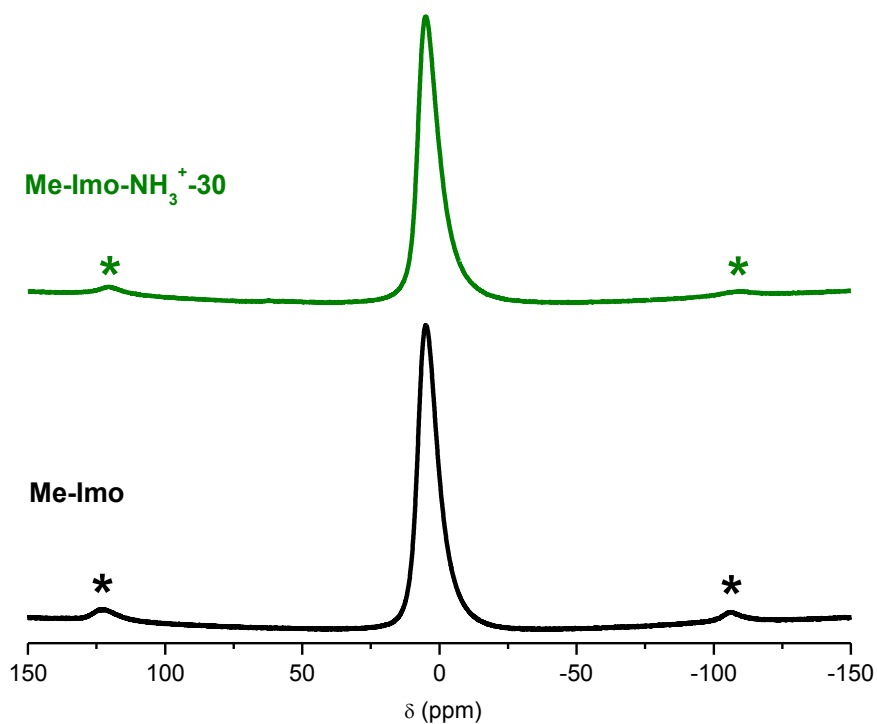


Figure 10: ^{27}Al MAS NMR spectra of Me-Imo-NH_3^+-30 (green) and Me-Imo (black) outgassed at room temperature.

Hence, from NMR and FT-IR spectra it can be confirmed that 3-APS was selectively grafted on the external surface and aminopropyl chains remained intact. These observations lead to the proposition that external silicon atoms are present in different environments, *i.e.* involved in T^x protonated species ($x=1,2,3$) and partially also in the oligomerization of 3-APS.

4.5. Porosity characterization by N_2 adsorption/desorption isotherms

Figure 11a reports N_2 isotherms at 77 K of Me-Imo outgassed at 300°C and Me-Imo-NH₃⁺-30 outgassed at 150°C and 300°C, respectively. Relative Pore Size Distributions (PSDs) and XRD patterns are shown in Figure 11b and 11c. Both Me-Imo and Me-Imo-NH₃⁺-30 show a Type IV isotherm, with limited hysteresis loops. BET SSA is 665 m²/g for Me-Imo, while that of Me-Imo-NH₃⁺-30 outgassed at 150 °C is slightly smaller (518 m²/g). Correspondingly, a limited loss of total pores volume occurred, basically due to a decrease in microporosity (Table 1). However, if the aminated sample is outgassed at 300 °C, total and external surface are drastically decreased, from 518 to 303 m²/g and from 499 to 189 m²/g, respectively. In this case, Type II isotherm seems to be obtained.

Table 1: Textural parameters of Me-Imo-NH₃⁺ and the corresponding Me-Imo source outgassed at 150 °C and 300 °C, respectively, as derived from combined XRD patterns and N_2 adsorption isotherms at 77 K.

Sample	BET SSA (m ² /g)	Internal SSA (m ² /g)	External SSA (m ² /g)	Total pore vol. (cm ³ /g)	Micropores vol. (cm ³ /g) ^a	Inner diameter (nm) ^b	Outer diameter (nm) ^c
Me-Imo-300	665	265	400	0.39	0.09	1.64	2.98
Me-Imo-NH ₃ ⁺ -30 outgassed at 150 °C	518	19	499	0.35	0.004	1.57	2.99
Me-Imo-NH ₃ ⁺ -30 outgassed at 300 °C	303	114	189	0.32	0.004	1.65	3.05

^a As evaluated by applying the α_s method.

^b As calculated by NL-DFT method to the adsorption branch of the isotherm.

^c As calculated by the $d_{(100)}$ reflection peak of XRD patterns according to an hexagonal packing.

As it will be explained in Chapter 5, when the stability of Imo, Me-Imo and Me-Imo-NH₂ samples will be discussed in detail, 150 °C seems to be the limiting pretreatment temperature that can guarantee the structural integrity of the aminated sample. In fact, beyond this temperature, the aminated external group is completely lost, as MAS NMR spectra at higher outgassing temperature in ultra high vacuum will confirm. PSDs of Me-Imo and Me-Imo-NH₃⁺-30 show indeed a decrease of the pores population at *ca* 2 nm, along with some formation of mesopores. A possible mechanism for the decrease in microporosity is the blockage of pores mouth by grafted 3-APS, while a grafting at the inner wall seeming unlikely.

Finally, it can be interestingly noticed that the intensity of the XRD (100) reflection for Me-Imo-NH₃⁺-30 outgassed at 300 °C, grows upon thermal treatment. This behavior can be explained by a more ordered packaging of nanotubes due to water removal [11], in contrast with what usually observed with both Imo [9] and Me-Imo [10]. Moreover, even if the external aminopropyl group is not present, nanotubes integrity is preserved.

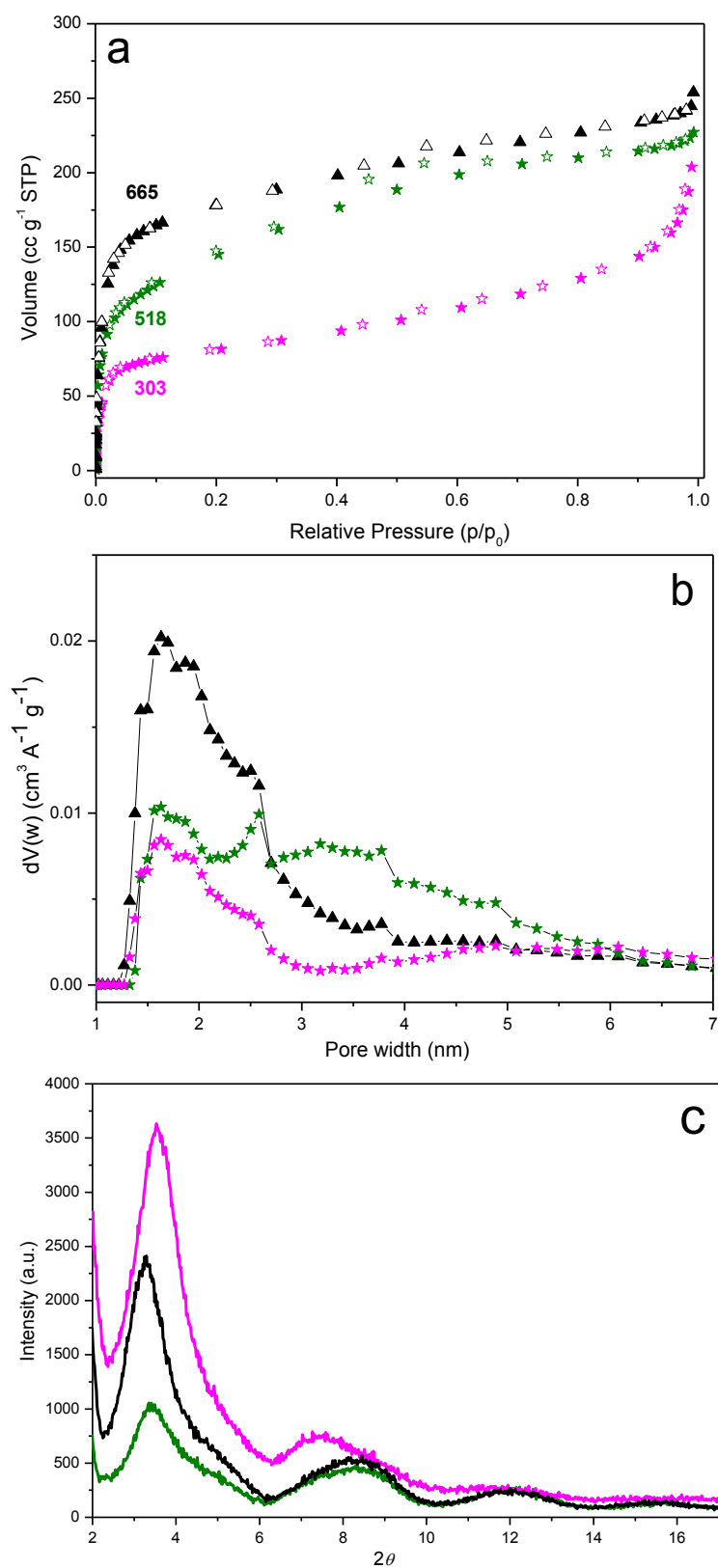


Figure 11: (a) N_2 adsorption and desorption isotherms of Me-Imo-300 (black), Me-Imo-NH₃⁺-30 outgassed at 150 °C (green) and Me-Imo-NH₃⁺-30 outgassed at 300 °C (pink). Numbers close to each curve indicate the corresponding BET SSA value; (b) PSDs (NL-FDT method) and (c) XRD patterns.

4.6. XPS and TGA-Mass characterizations

XPS spectra of Me-Imo-NH₃⁺-30 and Me-Imo are shown in Figure 12. As expected, N_{1s} line at 399.4 eV is present only in the aminated sample. O_{1s} line at 531.8 eV is specifically assigned to atoms connected to silicon atom (Si_{2p} at 101.8 eV) [27]. As a surface characterization technique, XPS results proof that amino-silanes are present at the outer surface, as reported in the literature for similar systems [28,29]. Chlorine contamination from perchloric acid, used in the hydrolysis step of the synthesis, is evidenced by the peak at *ca* 200 eV.

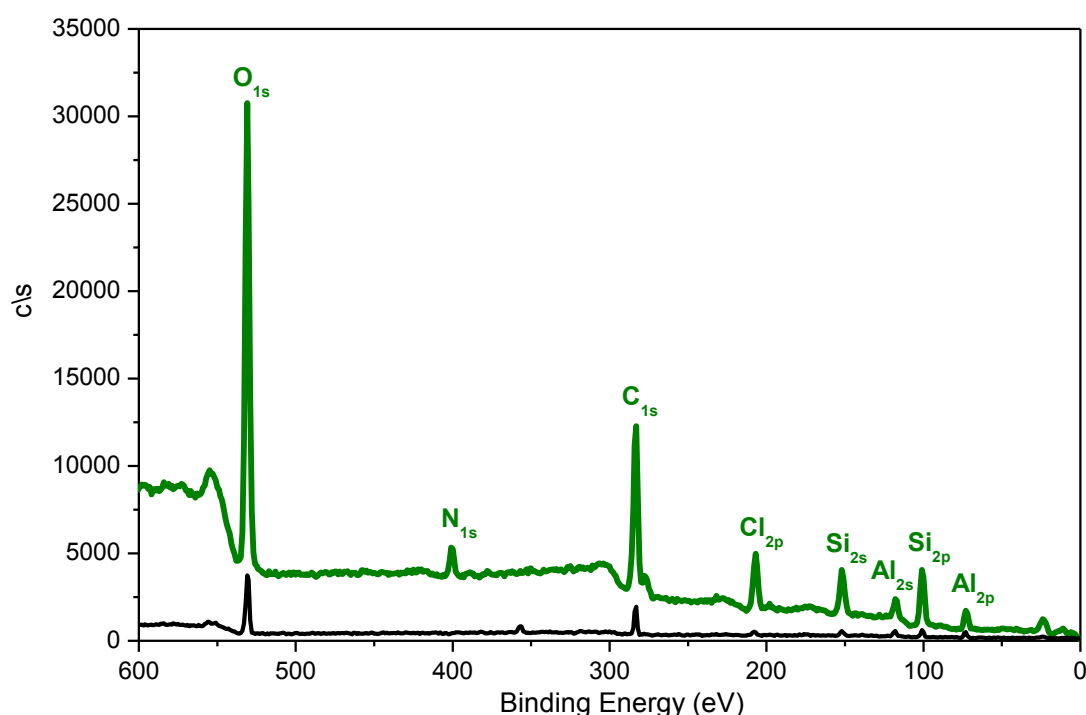


Figure 12: XPS spectra of Me-Imo-NH₃⁺-30 (green) and Me-Imo (black). As expected, N_{1s} line is present only in the aminated sample.

Figure 13a reports both integral and differential thermo-gravimetric curves for Me-Imo and Me-Imo-NH₃⁺-30. Whereas with Imo, a prominent weight loss related to the release of molecular water occurs below 250 °C, with both Me-Imo and Me-Imo-NH₃⁺-30, the loss of molecular water is much more limited and occurs at lower temperatures, due to their higher hydrophobicity. The mass loss at about 325 °C with Me-Imo is related to the dehydroxylation of the outer surface [10], *i.e.* the removal of Al-OH groups: such process takes place at about the same temperatures with Imo [9].

With Me-Imo-NH₃⁺-30, the mass loss at higher temperatures is due to the decomposition of the organic moiety, because fragments like H₂O⁺, CH₃⁺, NH⁺, CH₄⁺, NH₂⁺, NH₃⁺, C₂H₄⁺ are released (Figure 13b). Little variations from MAS NMR results concerning Me-Imo-NH₃⁺ stability could be due to the different operating conditions, *i.e.* level of vacuum achieved.

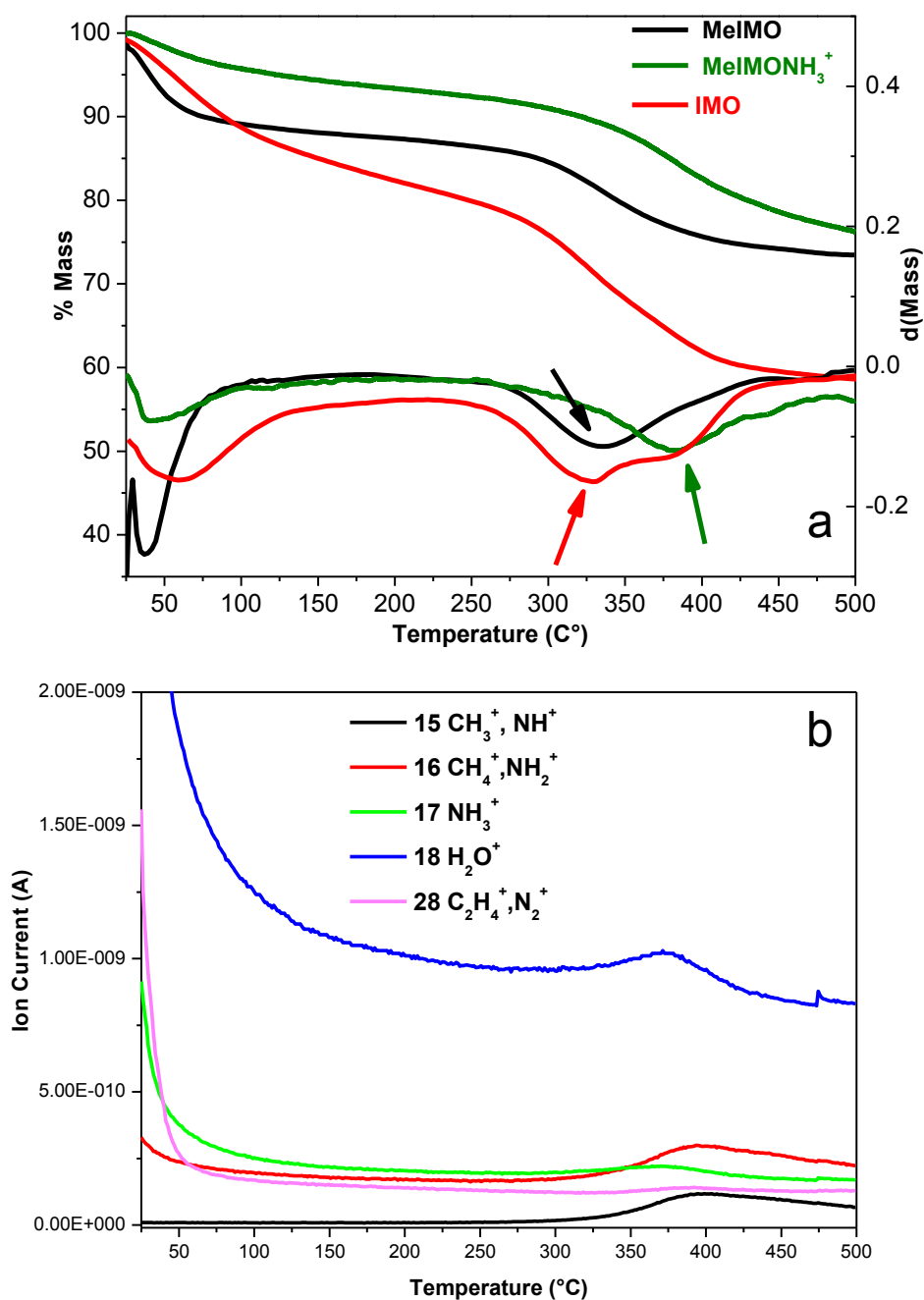


Figure 13: a) TGA analysis in flowing N₂ of Imo (red), Me-Imo (black) and Me-Imo-NH₃⁺-30 (green); b) Mass data for Me-Imo-NH₃⁺-30.

4.7. Conclusions

Synthesis procedure, structure and chemical properties of a new aminated nanotube material of the methyl-imogolite type by a post synthesis reaction have been described. Techniques employed confirmed the selective functionalization of the external surface. Reaction with 3-APS does not concern only the external portion of the nanotube bundles: it also brings about a limited loss in microporosity, probably because of grafting at the mouth of nanotubes, and an increased disorder in the alignment of nanotubes, without a big loss of specific surface area and without a sizable change in the distance between nanotubes. FT-IR spectroscopy shows that terminal NH₂ groups are protonated, and that a mild treatment with a dilute NaOH solution can bring back the expected amine functionality.

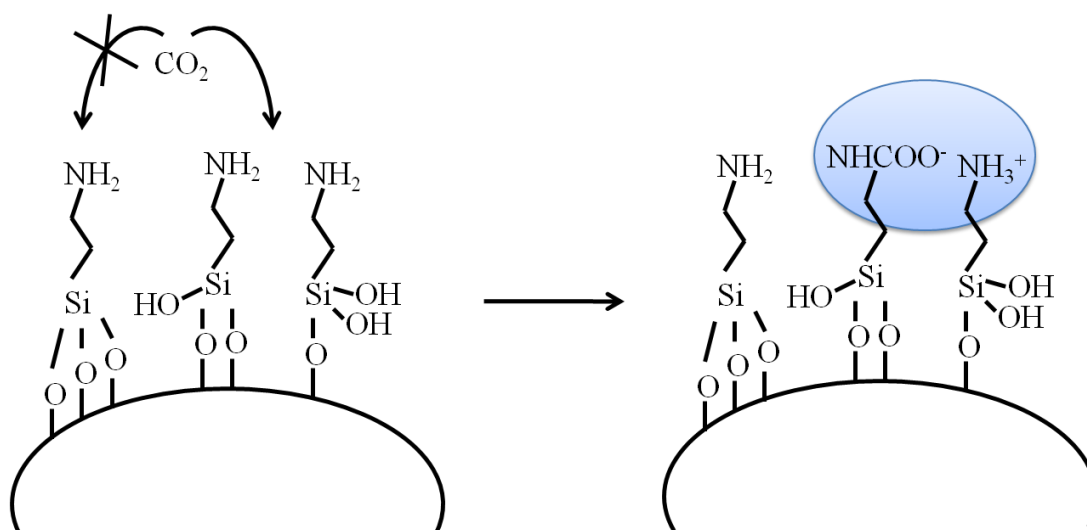
As a general conclusion, it is worth of note that, in contrast with the more famous carbon nanotubes, Imo-derived nanotubes may be functionalized under mild conditions by means of direct or post-synthesis procedure. In particular, properties of both the inner and the outer surface may be properly changed, and the hydrophilicity of the material may be modulated as well as porosity and thermal stability. This may open the way to new and promising applications.

4.8. CO₂ adsorption

4.8.1. FT-IR measurements

Figure 14a shows the FT-IR spectra in the 2400-2000 cm⁻¹ region of Me-Imo-NH₂-30 sample unprotonated in weak basic solution, as commonly suggested in literature [30,31] and outgassed at room temperature in interaction with CO₂ (pressure range 0-60 mbar). In order to obtain reversible adsorption of carbon dioxide on the surface of aminated adsorbents, at least two unprotonated amino-ligands should be available. In fact, interaction between CO₂ and primary amines (Scheme 2) in the gas phase, leads to the formation of alkylammonium carbamate species, according to the following reaction





Scheme 2: Schematic representation of alkylammonium carbamate species on the outer surface of Me-Imo-NH₂-30.

The presence of relative carbamic species is assigned to the coexistence of 1554, 1441 and 1330 cm⁻¹ bands [29]. With respect to literature, which refers mainly to mesoporous grafted adsorbents like SBA-15, the former band in case of imogolite-like materials is shifted from 1595 to 1554 cm⁻¹. Physisorbed gas (2339 cm⁻¹) and carbonate-like species [32,33] are also formed on Me-Imo-NH₂-30 surface, by the interaction of the gas with free aluminols on the surface, as the raising band at 1670 cm⁻¹ band present in both Me-Imo-NH₂-30 and Me-Imo samples (Figure 14b), confirms. Particularly, the position of this band at the surface of metal oxides refers to bidentate carbonates [33]. The result achieved is in agreement with the previous MAS NMR and FT-IR results on the fresh sample. In fact, the entire aminated precursor reacted with the surface, leading to the formation of different amino species (Scheme 1), leaving some free aluminol groups thus being able to react with carbon dioxide. For comparison, reactivity of imogolite towards CO₂ is shown in Figure 14c. It is evident that the gas may interact with nanotubes in different ways, *i.e.*

- 1) Me-Imo-NH₂-30, by forming quite reversible carbamic species (1554, 1441, 1330 cm⁻¹), physisorbed CO₂ (2339 cm⁻¹) and bicarbonate species (1670 cm⁻¹).
- 2) Me-Imo, by reversible physisorption as shown by the characteristic CO₂ peak at 2341 cm⁻¹. Carbonate-like species are also formed, as the presence of the 1670, 1451 and 1325 cm⁻¹ bands confirm. Accordingly, the 1554 cm⁻¹ band, typical of carbamic species, is not present, as highlighted by the downward arrow in Figure 14b.

- 3) Imo, by reversible H-bonding interaction with inner silanols group (2342 cm^{-1} band) and by the formation of carbonate-like species at the outer surface, which is known to be weakly basic [9] (1652 and 1410 cm^{-1} bands).

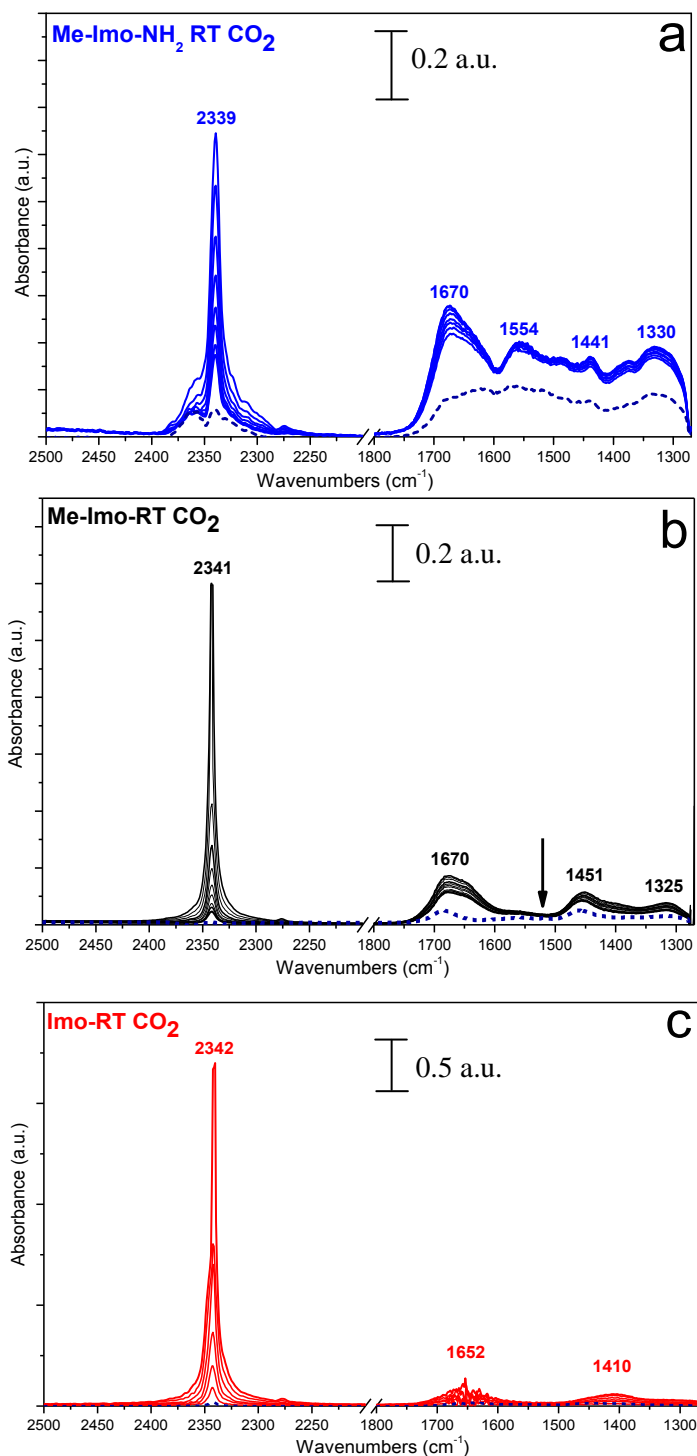


Figure 14: CO_2 dosage in the 0-60 mbar pressure range on (a) Me-Imo-NH₂-30, (b) Me-Imo and (c) Imo. All samples have been previously outgassed at room temperature.

4.8.2. Volumetric measurements

Figure 15 reports the CO₂ adsorption isotherms at 0 °C of unprotonated Me-Imo-NH₂-30 outgassed at 150 °C, as well as Imo and Me-Imo pretreated at 300 °C, up to 0.03 atm. Despite comparable volumetric CO₂ uptakes (cm³/g) are found (Table 2), Me-Imo-NH₂-30 resulted to adsorb a higher amount with respect to Imo as well as a slightly lower amount as compared to Me-Imo. This result is reasonable since not all the outer surface has been functionalized, as FT-IR evidence showed. Interestingly, the only Langmuir model interpolation of data revealed to be not satisfactory. On the contrary, combining Langmuir and Henry models (Table 2), curve fittings resulted to be acceptable. Comparable values of the thermodynamic constant of interaction (K_L) are found for Imo and Me-Imo, while a greater value is obtained in case of Me-Imo-NH₂-30 (Figure 16). These results are consistent with the presence of two adsorption sites at the inner and at the outer surface of the tubes, respectively.

Table 2: Textural parameters of Imo, Me-Imo and Me-Imo-NH₂-30, as derived from CO₂ adsorption isotherms at 0 °C. Parameters estimated by combining Langmuir (L) and Henry (H) models are also reported.

Sample	CO ₂ uptake (cm ³ /g)	V _L	K _L	K _H	Adj. R-square
Me-Imo-NH ₂ -30	36.5	16	345	345	0.99932
Me-Imo	41.6	17	281	280	0.99950
Imo	32.7	21	282	282	0.99502

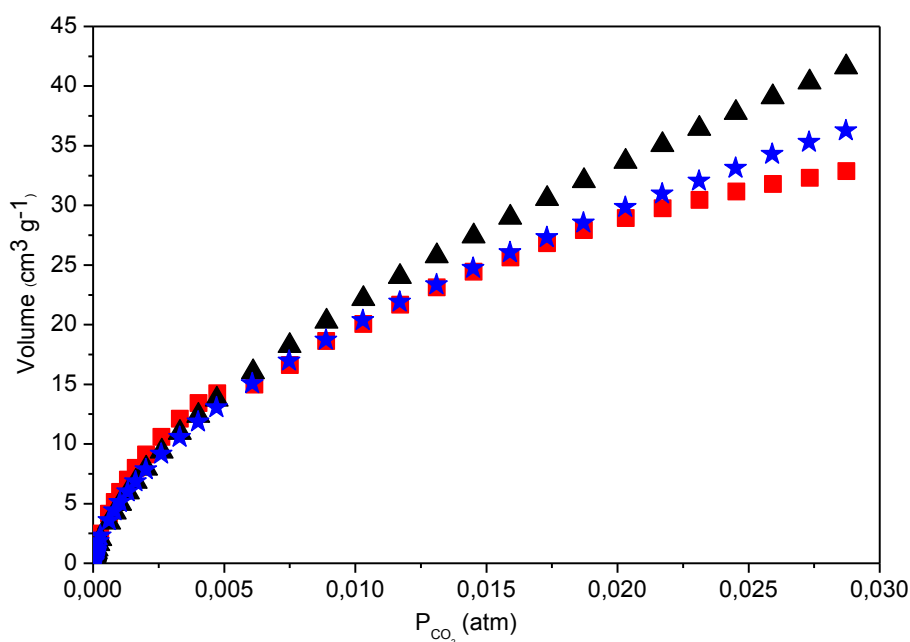


Figure 15: Volumetric CO₂ adsorption isotherms at 0°C on Me-Imo-NH₂-30 (stars), Me-Imo (triangles) and Imo (squares).

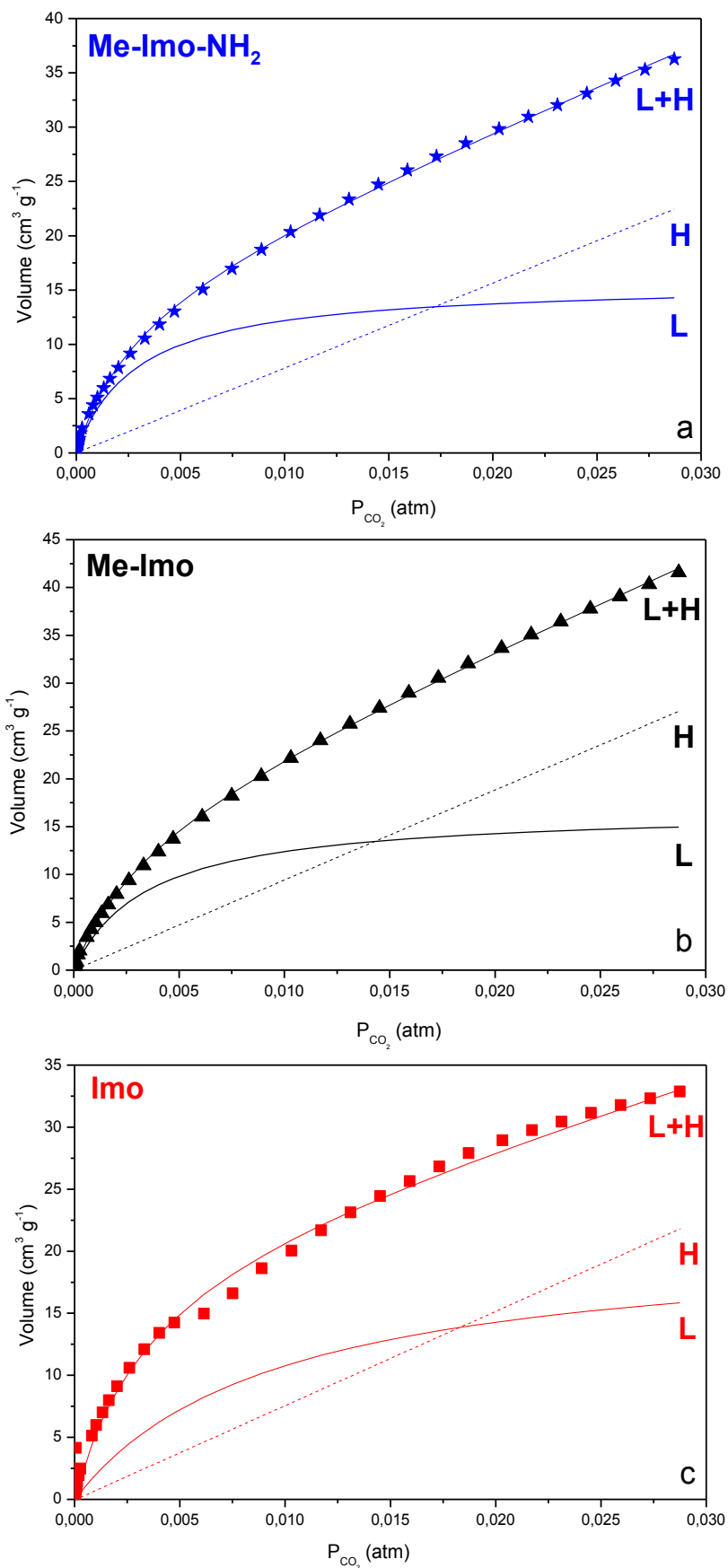


Figure 16: Curve-fits of volumetric CO_2 adsorption isotherms with Langmuir, Henry and combined Langmuir/Henry models for (a) Me-Imo-NH₂-30, (b) Me-Imo and (c) Imo.

Finally, Table 3 gathers volumetric CO₂ uptakes that have been estimated by other authors for common solid adsorbents, in the same operative conditions.

Table 3: Recent review of CO₂ uptake in the operative conditions of this study of common solid adsorbents.

Adsorbent	Amine precursor	BET SSA (m²/g)	CO₂ uptake (cc/g_{adsorbent} STP) at 0.03 atm and 0 °C	Reference
Me-Imo-NH ₂ -30	3-APS	518	36.5	This study
Me-Imo	---	665	41.6	This study
Imo	---	355	32.7	This study
Zeolite 13X	---	482	125	34
YO-MOF	---	---	20	35
MOF-5	---	811	17	36
Microporous Zn-MOF	---	41	4	37
Zn-Adeniate MOF	---	---	20	38
MOF SNU-77	DMA	3670	Comparable with Me-Imo-NH ₂	39
Aminated Silica gel	3-APS	---	9	40

4.8.3. Conclusions

Interaction of imogolite-like materials with carbon dioxide showed the presence of two adsorption sites at the inner and at the outer surface of the nanotubes, respectively. Besides the physisorbed gas, which is present in each sample, in case of Me-Imo and Imo, only reversible carbonate-like species are formed, while for Me-Imo-NH₂ quite reversible carbamic species are also present, confirming the successful functionalization. Moreover, comparable volumetric adsorption measurements of CO₂ are found, according to the following sequence

$$\text{Me-Imo} > \text{Me-Imo-NH}_2\text{-30} > \text{Imo}$$

This result is reasonable, since not all the outer surface of Me-Imo has been functionalized. As a whole, with the exception of Zeolite 13X [34], which is a well known good adsorbent, imogolite-like materials evidence comparable uptake capacity with common fresh and aminated MOF (Metal Organic Frameworks) materials.

4.9. References

- [1] V. Zelenak, D. Halamova, L. Gaberova, E. Bloch, P. Lewellyn, 116(1) (2008) 358.
- [2] N. Hiyoshi, K. Yogo, T. Yashima, *Micr. Mes. Mat.* 84 (2005) 357.
- [3] H. Zhao, J. Hu, J. Wang, L. Zhou, H. Liu, *Acta Phys. Chim. Sin.* 23(6) (2007) 801.
- [4] P.J.E. Harlick, A. Sayari, *Ind. Eng. Chem. Res.* 46 (2007) 446.
- [5] J.C. Hicks, C.W. Jones, *Langmuir* 22 (2006) 2676.
- [6] L.M. Johnson, T.J. Pinnavia, *Langmuir* 6 (1990) 307.
- [7] L.M. Johnson, T.J. Pinnavia, *Langmuir* 7 (1991) 2636.
- [8] E.M. Hampe, D.M. Rudkevich, *Tetrahedron* 59 (2003) 9619.
- [9] B. Bonelli, I. Bottero, N. Ballarini, S. Passeri, F. Cavani, E. Garrone, *J. Cat.* 264 (2009) 15.
- [10] I. Bottero, B. Bonelli, S. Ashbrook, P. Wright, W. Zhou, M. Tagliabue, M. Armandi, E. Garrone, *Phys. Chem. Chem. Phys.* 13 (2011) 744.
- [11] D.Y. Kang, J. Zang, E.R. Wright, A.L. McCanna, C.W. Jones, S. Nair, *ACS Nano* 4 (2010) 4897.
- [12] L. Wang, L. Ma, A. Wang, Q. Liu, T. Zhang, *Chinese J. Catal.* 28 (2007) 805.
- [13] G.P. Knowles, J.V. Graham, S.W. Delaney, A.L. Chaffee, *Fuel Process. Technol.* 86 (2005) 1435.
- [14] X. Xu, C. Song, J. Andresen, B. Miller and A. Scaroni, *Micr. Mes. Mat.* 62 (2003) 29.
- [15] F. Zengh, D.N. Tran, B.J. Busche, G.E. Fryxell, R. Shane Addleman, T.S. Zemanian, C.L. Aardahl, *Ind. Eng. Chem. Res.* 44(9) (2005) 3099.
- [16] G.S. Caravajal, D.E. Leyden, G.R. Quinting, G.E. Maciel, *Anal. Chem.* 60 (1988) 1776.
- [17] P. Yuan, P.D. Southon, Z. Liu, M.E.R. Green, J.M. Hook, S.J. Antill, C.J. Kepert, *J. Phys. Chem. C* 112 (2008) 15742.
- [18] G.D. Tewari, D.P. Khandelwal, H. D. Bist, V.P. Taya, *Can. J. Chemistry*, 61 (1983) 2745.
- [19] H. Ni, D.J. Aaserud, W.J. Simonsick Jr., M.D. Soucek, *Polymer* 41 (2000) 57.
- [20] D.L. Guerra, A.C. Batista, R.R. Viana, C. Airoidi, *Desalination* 275 (2011) 107.
- [21] Z. L. Da, Q. Q. Zhang, D. M. Wu, D. Y. Yang, F. X. Qiu, *eXPRESS Poly. Lett.* 1(10) (2007) 698.
- [22] R. Joseph, Z. Zhang, W.T. Ford, *Macromolecules*, 29 (1996) 1305.
- [23] K.W. Park, O.Y. Kwon, *Bull. Korean Chem. Soc.* 25(7) (2004) 965.
- [24] K. C. Vrancken, L. D. Coster, P. V. D. Voort, P. J. Grobet, E. F. Vansant, *J. Colloid Interf. Sci.* 170 (1995) 71.
- [25] H. Wang, J. Huang, S. Wu, C. Xu, L. Xing, L. Xu, Q. Kan, *Mat. Lett.* 60 (2006) 2662.
- [26] B. Wang, W. Liu, Y. Zhu, J. Yu; Z. Guo, *J. Wuhan University of Technology-Materials Sci. Ed.* 22 (2007) 453.
- [27] S Mukherjee, V.M. Bartlow, S. Nair, *Chem. Mater.* 17 (2005) 4900.
- [28] Z. Xu, Q. Liu, J.A. Finch, *Appl. Surf. Sci.* 120 (1997) 269.
- [29] A.C.C. Chang, S.S.C. Chuang, McM. Gray, Y. Soong, *Energy Fuels* 17 (2003) 468.
- [30] D.H. Huchital, E. Debesis, *Inorg. Chim. Acta* 98(2) (1985) 79.
- [31] J.K. Walker, R. Nakon, *J. Am. Chem. Soc.* 99 (25) (1977) 8359.
- [32] C. Morterra, G. Magnacca, *Cat. Today* 27 (1996) 497.
- [33] C. Morterra, L. Orto, *Mater. Chem. Phys.* 24 (1990) 247.
- [34] Z. Zhao, X. Cui, J. Ma, R. Li, *Int. J. Greenhouse Gas Control* 1 (2007) 355.
- [35] K.L. Mulfort, O.K. Farha, C.D. Malliakas, M.G. Kanatzidis, J.T. Hupp, *Chem. Eur. J.* 16 (2010) 276.
- [36] C.M. Lu, J. Liu, K. Xiao, A.T. Harris, *Chem. Eng. J.* 156 (2010) 465.
- [37] M. Xue, Z. Zhang, S. Xiang, Z. Jin, C. Liang, G.S. Zhu, S.L. Qiu, B. Chen, *J. Mater. Chem.* 20 (2010) 3984.
- [38] J. An, R.P. Fiorella, S.J. Geib, N.L. Rosi, *J. Am. Chem. Soc.* 131 (2009) 8401.
- [39] H.J. Park, D.W. Lim, W.S. Yang, T.R. Oh, M.P. Suh, *Chem. Eur. J.* 17 (2011) 7251.
- [40] O. Leal, C. Bolivar, C. Ovalles, J.J. Garcia, Y. Espidel, *Inorg. Chim. Acta* 240 (1995) 183.

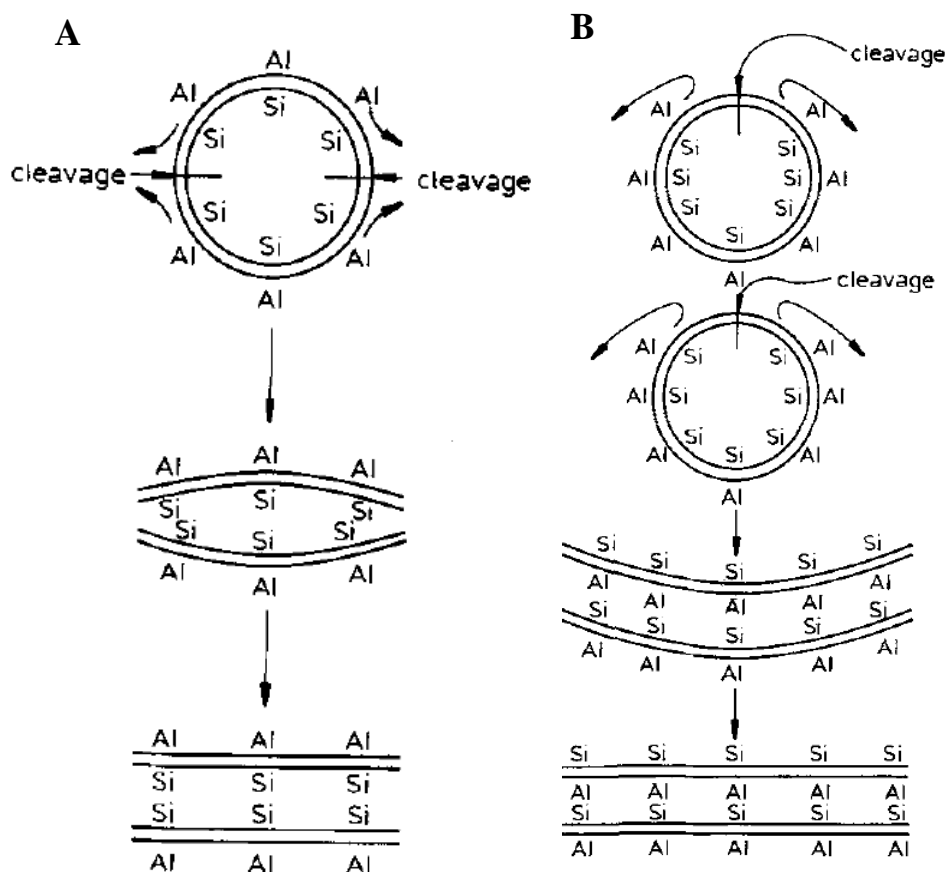
Chapter 5

Stability of imogolite-type material

5.1. Introduction

Besides physical-chemical properties, it is of paramount importance to study the thermal stability of solid materials, in terms of structural modifications and related features, due to thermal treatments up to high temperatures.

The collapsing mechanism of natural occurring imogolite and synthetic imogolite has been proposed for the first time by MacKenzie *et al.* in 1989 [1]. MAS NMR observations suggested that at least two fracture schemes may be encountered, leading to different lamellar structures (Scheme 1A and 1B).



Scheme 1: Collapsing mechanisms (A or B) proposed for Imo sample by MacKenzie et al. [1]

In general, elimination of the Si-OH groups is expected to proceed by cleavage of the nanotubes, which can have been started by dehydroxylation of some external Al-OH groups [2].

Firstly, the loss of structure integrity may happen across nanotubes diameter, causing the tubes to flatten with the formation of the following repeating sequence: Al-O-Si-O-Si-O-Al (Scheme 1A). A second mechanism proposed, wants instead the vertical cleavage of two adjacent nanotubes to happen. As a consequence, they eventually condensate in a different lamellar structure. In fact, in this second case hydroxyl elimination would occur between silanols groups of one tube and aluminol groups of a second tube, resulting in the following repeating units: Al-O-Si-O-Al-O-Si (Scheme 1B). Despite this, the latter mechanism was considered less likely, both on the basis of theoretical calculations and structural considerations, *i.e.* the presence of low concentration of Al-OH groups in close proximity, thus not allowing the condensation between close tubes [1].

Recently, new details about dehydration, dehydroxylation and partial rehydroxylation of imogolite up to 400 °C have been proposed by Nair and co-workers [3]. They agree with the first collapsing mechanism occurring for Imo and mentioned by MacKenzie. Moreover, they proposed in detail the structural changes referring to the dehydroxylation of the external nanotubular gibbsite layer, on the basis of ^{27}Al MAS-NMR measurements. Particularly, three different layer structure were identified in which Al(VI), Al(IV) and also Al(V) atoms are present, the latter being NMR-invisible for old instruments.

Nevertheless, no information is available for the irreversible collapsing mechanism of Imo and those of the new successfully synthesized hybrid imogolite-like materials, Me-Imo and Me-Imo-NH $_3^+$ -30.

5.2. MAS NMR measurements

Figure 1A and 1B show the ^{29}Si MAS NMR and ^{27}Al MAS NMR spectra of Imo outgassed at (a) 150 °C, (b) 300 °C and (c) 500 °C, respectively. A recent paper has demonstrated a quite reversible formation of silanols upon rehydration at 400 °C [3]. The quantitative ^{29}Si experiments reported here show instead that the irreversible collapsing of nanotubular imogolite into an allophane-like lamellar structure via silanol condensation, $\text{Q}^3(6\text{Al}) \rightarrow \text{Q}^4(6\text{Al})$, occurs at 500 °C, as clearly seen by the presence of a single broad peak centered at -93 ppm [1]. Moreover, this is also confirmed by the total disappearance of the -80 ppm peak, which is commonly assigned to the presence of $\text{Q}^3(6\text{Al})$ species in the imogolite nanotube structure, up to 400 °C [1,3].

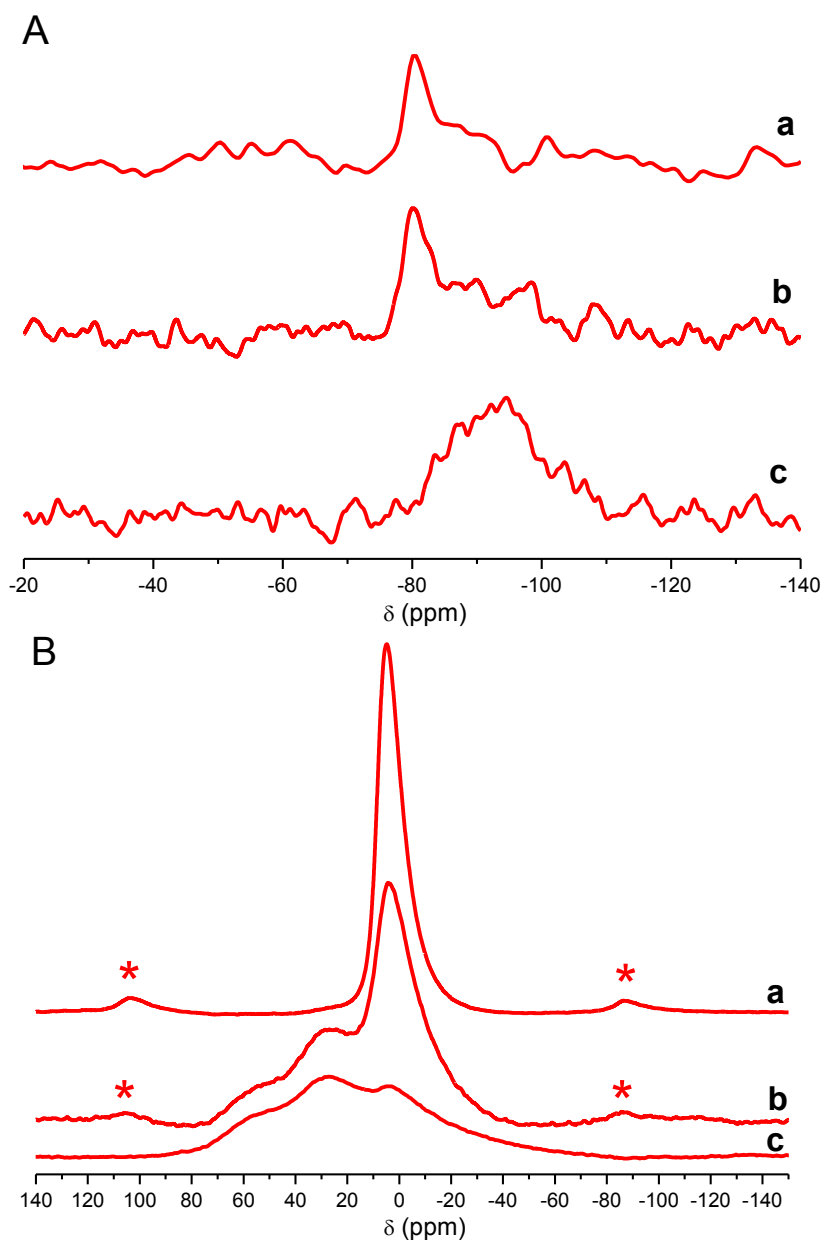


Figure 1: (A) ^{29}Si MAS NMR and (B) ^{27}Al MAS NMR spectra of Imo outgassed at (a) 150 °C, (b) 300 °C and (c) 500 °C. Stars denote spinning sidebands.

Irreversible morphological changes are expected also in ^{27}Al MAS NMR spectra. In fact, up to 150 °C, aluminum atoms are only VI coordinated, as shown by the presence of the single peak 4.5 ppm; at 300 °C, a partial contribution of Al(V) at *ca* 30 ppm [3] and Al(IV) at *ca* 60 ppm [3] appears, while at 500 °C the octahedral Al sites are only a minor part of a broad band in the 80 to -80 ppm range, in which the three different aluminum environments can be still distinguished. XRD patterns and N_2 physisorption isotherms reported in our recent paper have already foreseen these results [4]. Overall, for Imo the unique and most probable collapsing mechanism proposed by MacKenzie, which corresponds to the cleavage across the tubes, can be confirmed.

Interesting and quite different results with respect to Imo, were obtained for the two hydrophobic imogolite samples. Both samples turned out to be stable, as well as Imo, up to 150 °C. However, at 300 °C a small modification of the structure is evidenced, till the irreversible collapsing into a non-tubular structure at 500 °C.

Firstly, the effect of thermal treatment on the different samples was studied by ^{13}C NMR. CP $\{^1\text{H}\}$ - ^{13}C MAS-NMR of Me-Imo (Figure 2A) and Me-Imo-NH $_3^+$ -30 (Figure 2B) outgassed at (a) 150 °C, (b) 300 °C and (c) 500 °C, respectively, as well as ^{13}C MAS-NMR of the samples outgassed at 500 °C (d), confirmed that below 150 °C the grafted species stay nearly unaffected.

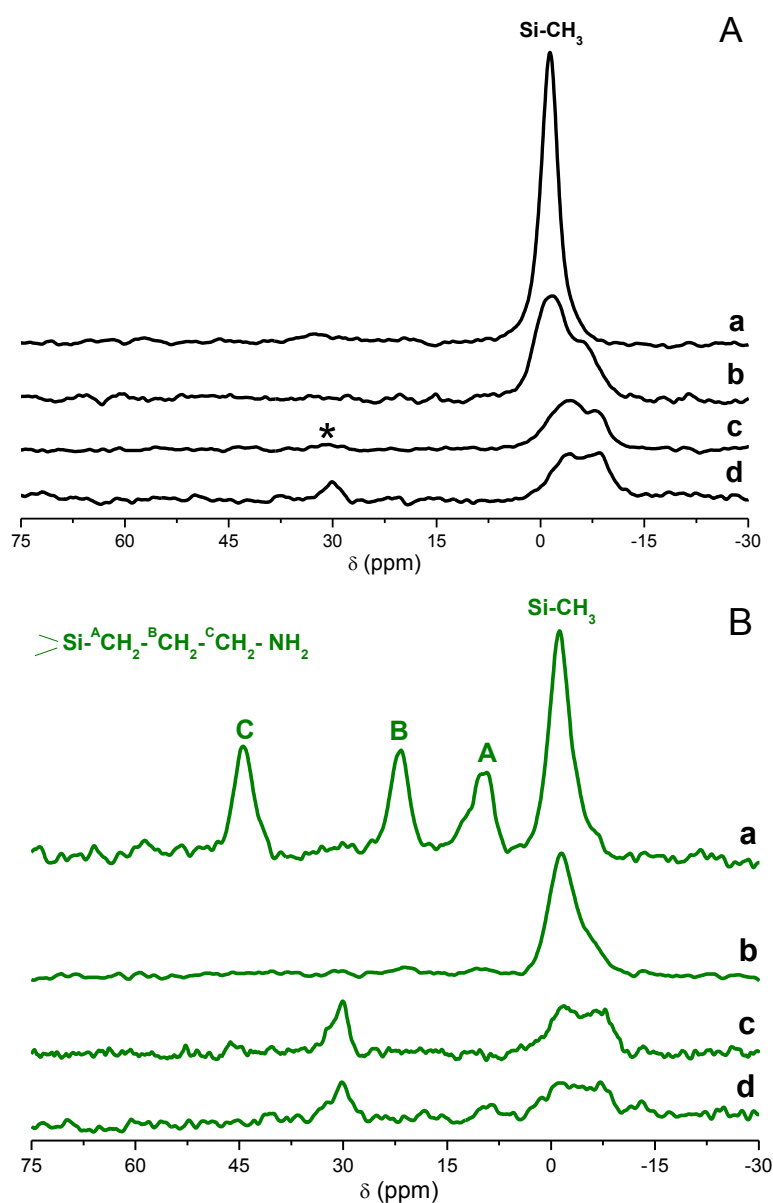


Figure 2: CP $\{^1\text{H}\}$ - ^{13}C MAS-NMR (A) Me-Imo and (B) Me-Imo-NH $_3^+$ -30 outgassed at (a) 150 °C, (b) 300 °C and (c) 500 °C. Relative ^{13}C MAS-NMR spectra are reported in curves d.

With Me-Imo-150, a single peak due to inner Si-CH₃ group, at -1.2 ppm is observed. It is indeed a reasonable chemical shift value for such species, since this type of bond is the same present in TMS (tetramethylsilane), *i.e.* the NMR reference used for silicon atom. However, at 300 °C the silicon environment of Me-Imo changes, as can be seen from the contribution of a second peak rising at *ca* -6 ppm. Carbon negative chemical shift in MAS NMR spectra are not so commonly found, as the lacking of literature reveals. However, they can be assigned to the presence of similar dendritic carbosilanes structures [5]. At 500 °C, nanotubes completely collapsed. The methyl species resonance shifts to the -4.3 to -8.6 ppm range and the decreased overall intensity shows a significant loss of the total amount of carbon atoms. A possible explanation could be that part of methyl groups leave the structure at 500°C, and part remains but with a different environment, as confirmed by the chemical shift change. Finally, a new peak at 30 ppm reveals the possibility that some of the methyl groups react with OH species, which lead to the formation of Si-CH₂-O-Al groups.

An analogue result was obtained for aminated Me-Imo-NH₃⁺-30. In fact, only up to 150°C the nanotube structure as well as the outer aminated surface is preserved. In fact, inner Si-CH₃ and methylene signals are present, at -1.2, 9.5, 21.8 and 44.5 ppm, respectively. At higher temperatures, starting from 300 °C, the grafted chain on the outer surface is almost lost, as the disappearance of the propyl carbon chain peaks revealed. Despite this, Si-CH₃ inner groups are still present. At 500 °C, both the CP {¹H}-¹³C MAS-NMR (c) and direct ¹³C (d) spectra show instead the formation of the new peaks at 30 ppm and negative chemical resonances in the 0 to -10 ppm range, respectively, at the same positions of those evidenced for Me-Imo-500. It is important to note that after 300 °C both side of the nanotubes present Si-CH₃ groups.

Overall, it is thus difficult to conclude on the actual mechanism of the collapsing process, as the above results seem to be in contradiction with previous theory.

Figure 3 and Figure 4 present the ²⁹Si MAS NMR spectra of Me-Imo and Me-Imo-NH₃⁺-30 outgassed at (a) 150 °C, (b) 300 °C and (c) 500 °C, respectively. Coherently with the previous results, silicon environment of the Si-CH₃ group starts changing at 300 °C, when a new peak arise at *ca* -90 ppm. T^x species of Me-Imo-NH₃⁺-30 are almost lost at 300 °C, even if tubes structure is maintained, while at 500 °C the same non-tubular phase as Me-Imo-500 is obtained.

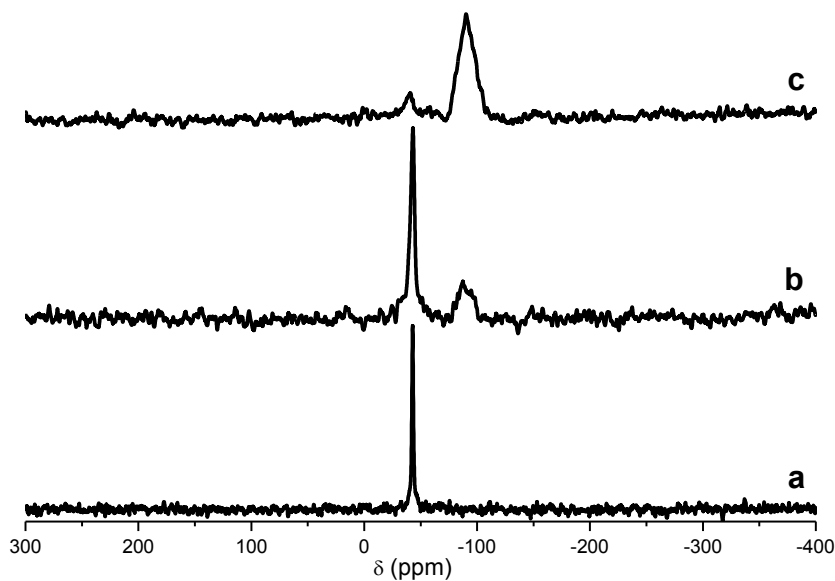


Figure 3: ^{29}Si MAS-NMR of Me-Imo outgassed at (a) 150 °C, (b) 300 °C and (c) 500 °C.

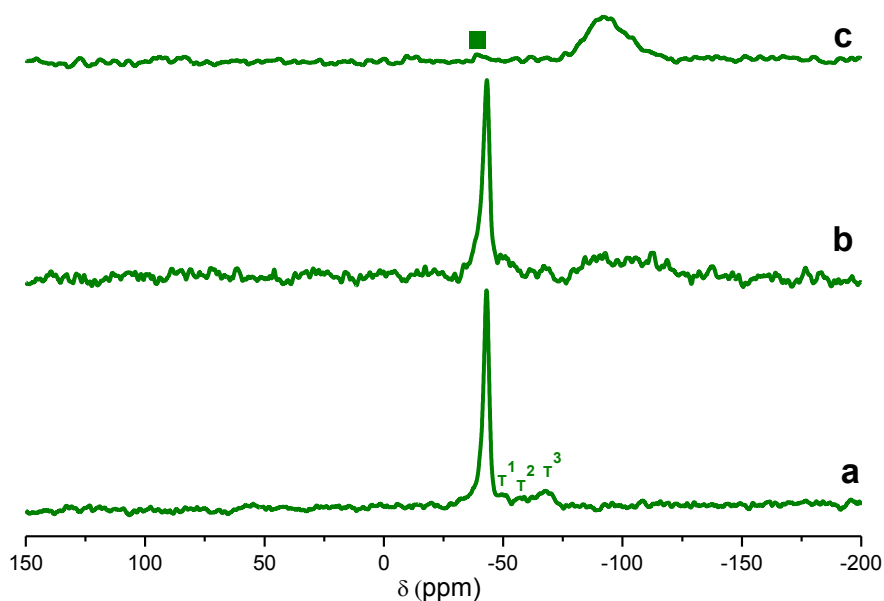


Figure 4: ^{29}Si MAS-NMR of Me-Imo- NH_3^+ -30 outgassed at (a) 150 °C, (b) 300 °C and (c) 500 °C.

The presence of a peak at -40 ppm and the peak centered at -90 ppm can be explained if it is assumed that some Si- CH_x species are actually included in the final structure, as well as the formation of Si-O-Si linked. The first resonance is consistent with the fact one part of the Si- CH_3 is present at the external surface of the laminar form, then following the second mechanism proposed by MacKenzie. The second peak is instead only possible if the CH_3 are removed, and if new bounds between silicon are created (Si-O-Si).

Moreover, the two hybrid imogolite samples seem to react in the same way, even if some modification on the surface decrease the accessibility to Al-OH groups and the possibility to form Si-CH₂-O-Al. Nevertheless, it is important to note that for Me-Imo-NH₃⁺-30 the total amount of carbon is much lower than on Me-Imo and the species Si-CH₃ and Si-CH₂-O-Al can be present in minority.

As a general comment, it is probable that with these two sample both collapsing mechanisms take place: the first one, when methyl groups are removed at high temperature (higher than 300 °C); the second one, if methyl groups of two closed nanotubes are able to create Si-CH₂-O-Al links. The latter mechanism seems to be less probable. However, it can explain why species at -40 ppm on ²⁹Si MAS NMR are present with very low intensity.

Finally, the ²⁷Al MAS NMR spectra of Me-Imo (figure 5) and Me-Imo-NH₃⁺-30 (figure 6) outgassed at (a) 150 °C, (b) 300 °C and (c) 500 °C are reported. Similar results to Imo are obtained (Figure 1B). In fact, at 300 °C, aluminum environment starts changing, accordingly to ²⁹Si and ¹³C MAS NMR evidence. However, it is remarkable that ²⁷Al MAS NMR spectra of Me-Imo and Me-Imo-NH₃⁺-30 at 300°C present less modification than at 150°C, as compared to same experiment on Imo. This is a strong evidence that the functionalized structure is less sensitive to the temperature. Moreover, both structures eventually show the same aluminum environment, which is in agreement with the fact that both samples collapsed in the same way.

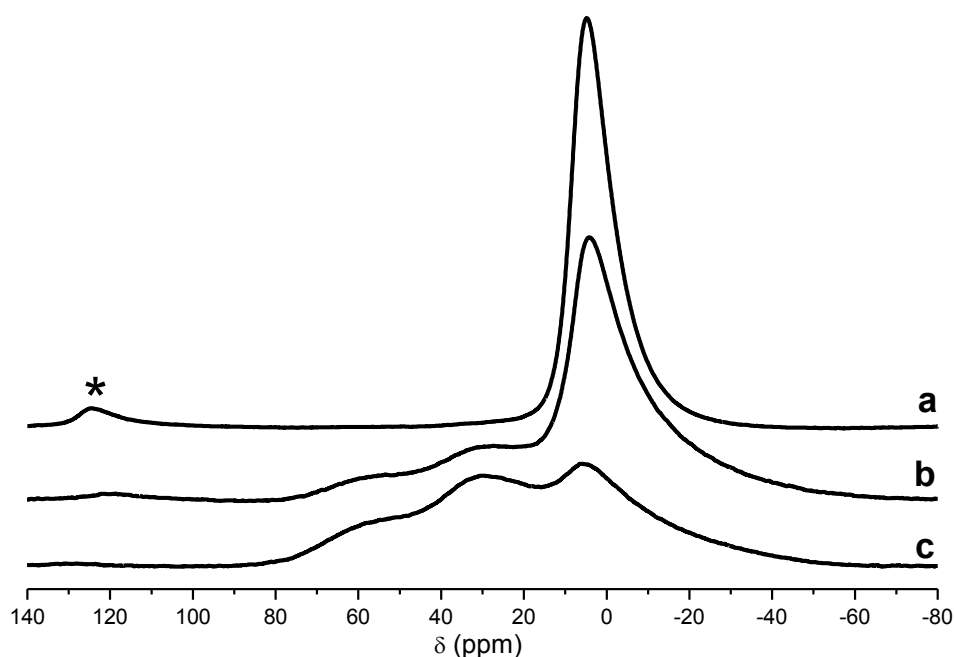


Figure 5: ²⁷Al MAS-NMR of Me-Imo outgassed at (a) 150 °C, (b) 300 °C and (c) 500 °C.

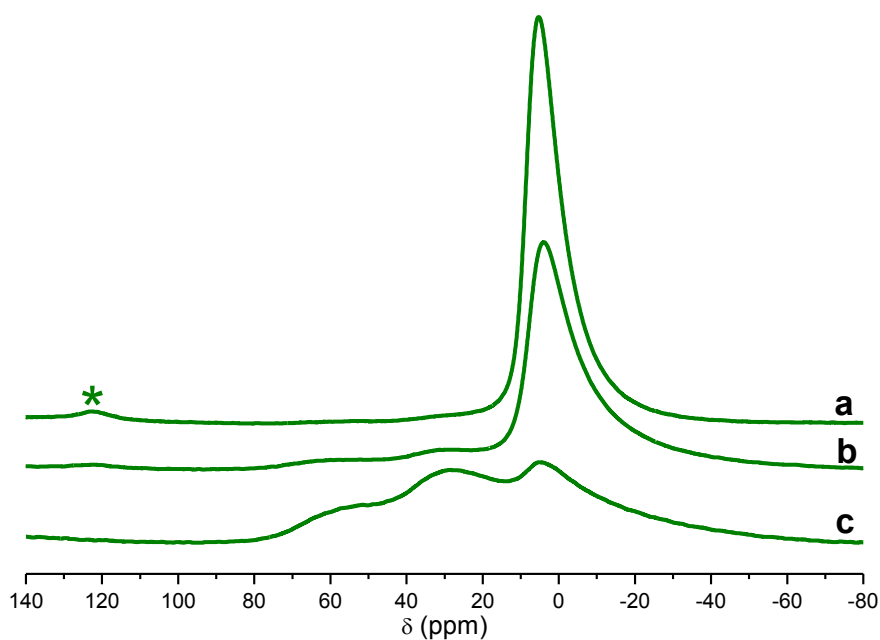


Figure 6: ^{27}Al MAS-NMR of Me-Imo- NH_3^+ -30 outgassed at (a) 150 °C, (b) 300 °C and (c) 500 °C.

5.2.1. Cross polarization (CP) study on Me-Imo outgassed at 500 °C

Basics of CP technique are discussed in Appendix II. In this section, cross polarization study on Me-Imo outgassed at 500 °C is presented. Particularly, CP dynamics of ^{29}Si nucleus provides information on the effective magnitude of the ^{29}Si - ^1H dipolar interaction experienced by the silicon nucleus. The gain in signal sensitivity is caused by the transfer of magnetization from ^1H to ^{29}Si during the τ_{CP} contact time (Figure 7), which ideally gives an enhancement in intensity by a factor of 5 ($= \gamma_{\text{H}}/\gamma_{\text{Si}}$) [6]. Moreover, this kind of sequence acts like a Si-H filter, since only silicon species that are dipolar couples to ^1H are detected by this rf pulse scheme [7].

For this dynamic study, the τ_{CP} range considered is 0.5-80 ms. Figure 8 shows the CP ^{29}Si - ^1H MAS spectra collected: two main peaks seem to be affected by the polarization, at -42 ppm and -90 ppm, respectively. In order to estimate the ^{29}Si magnetization, $M_{\text{Si}}(\tau_{\text{CP}})$, an analytical expression must be derived. Eq. 1a and 1b shows a simplified theoretical equation

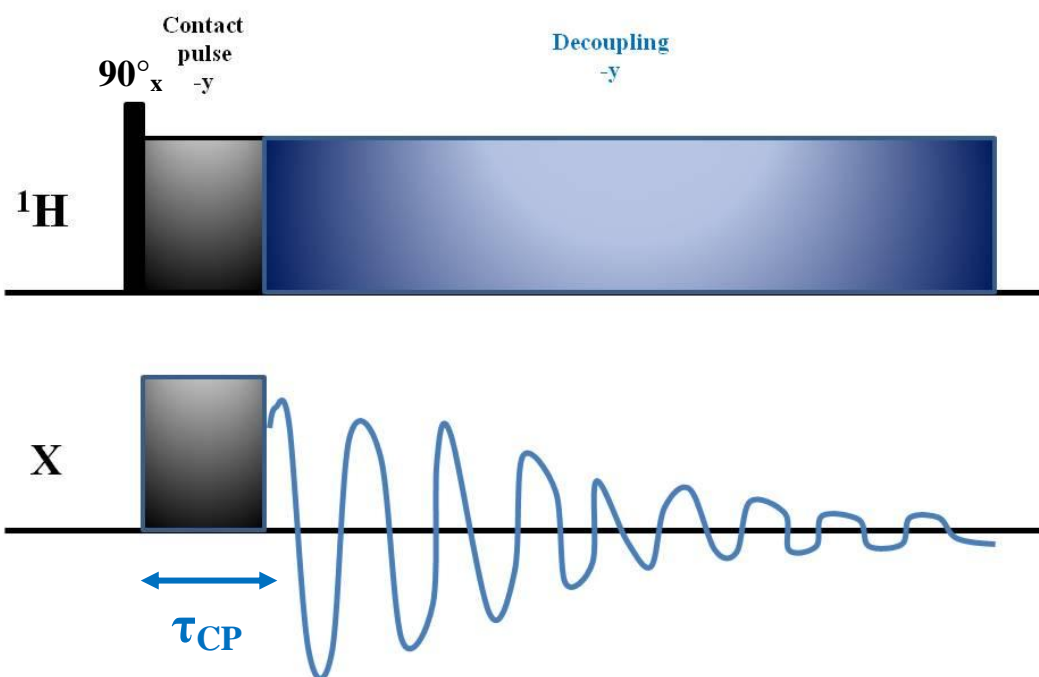


Figure 7: The CP (Cross Polarization) pulse sequence. The effect of the sequence is to transfer magnetization from the abundant ^1H spins to the X ($=^{29}\text{Si}$) spin via the agency of the dipolar coupling between ^1H and ^{29}Si spins.

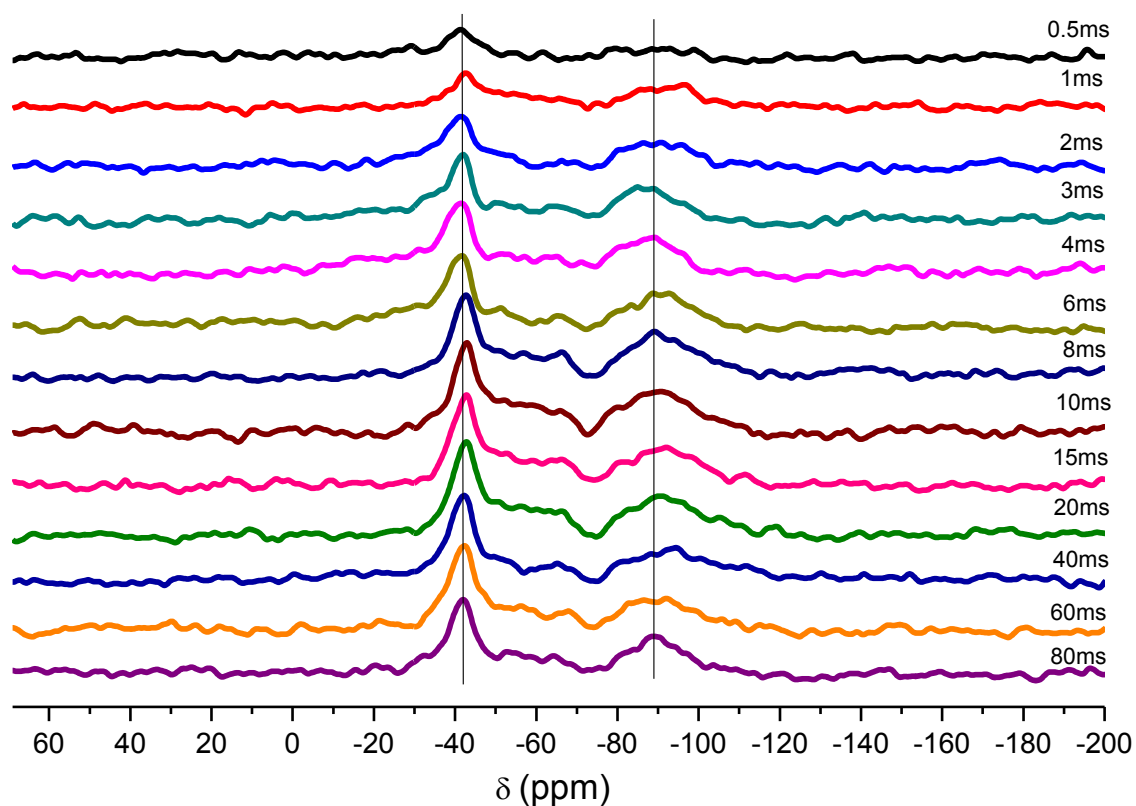


Figure 8: CP $\{^1\text{H}\}$ - ^{29}Si MAS dynamic study on Me-Imo outgassed at 500°C . τ_{CP} contact time was varied from 0.5 ms to 80 ms.

$$M_{Si}(t_{CP}) = \frac{M^H(0)}{1-\lambda} \cdot e^{-\frac{t_{CP}}{T_{1\rho}^H}} \cdot \left[1 - e^{\left(\frac{1}{T_{1\rho}^H} - \frac{1}{T_{SiH}}\right) \cdot t_{CP}} \right] \quad (\text{Eq. 1a})$$

$$\lambda = \frac{T_{SiH}}{T_{1\rho}^H} \quad (\text{Eq. 1b})$$

where $M^H(0)$, is the ^1H magnetization after the 90°_x ^1H pulse, $T_{1\rho}^H$ is the ^1H rotating-frame relaxation time, $T_{1\rho}^{Si}$ the ^{29}Si rotating-frame relaxation time and T_{SiH} is the ^1H - ^{29}Si CP time. Accordingly to literature concerning inorganic materials [7], we assume that $T_{1\rho}^{Si} \gg T_{1\rho}^H$. The time constants, T_{SiH} and $T_{1\rho}^H$, as well as $M^H(0)$, can be determined from a three-parameter least-squares fit of Eq. 1 to the signal intensities observed in the dynamic CP study. Figure 9 and 10 present the experimental data fitting for peak (-42 ppm) and peak (-90 ppm), respectively. Low and high τ_{CP} interpolation equations are also indicated. Table 1 gathers the estimated parameters.

Table 1: T_{SiH} and $T_{1\rho}^H$, and $M^H(0)$ parameters estimated by three parameter least-squares fit of Eq. 1.

Parameter	Peak (-42 ppm)	Peak (-90 ppm)
T_{SiH}	4.4 ms	1.7 ms
$T_{1\rho}^H$	225 ms	233 ms
$M^H(0)$	18.8 a.u.	6.7 a.u.

The values reported in Table 1 for both resonance show that the polarization of the species at -42 ppm is much slower than that of the species at -90 ppm, in agreement with the fact that the resonance at -42 ppm is attributed to Si-CH₃ at the inner surface. The mobility of the protons of the CH₃ groups strongly reduces their ability to polarize the attached silicon.

In a previous study, McCucheon *et al.* [8] found values of $T_{SiH} = 1.53$ ms and $T_{1\rho}^H = 15.7$ ms. These values were obtained for an imogolite at room temperature, *i.e.* for silicon in the form Q³(6Al) with an OH groups corresponding to the peak at -80 ppm on ^{29}Si MAS NMR of Imo.

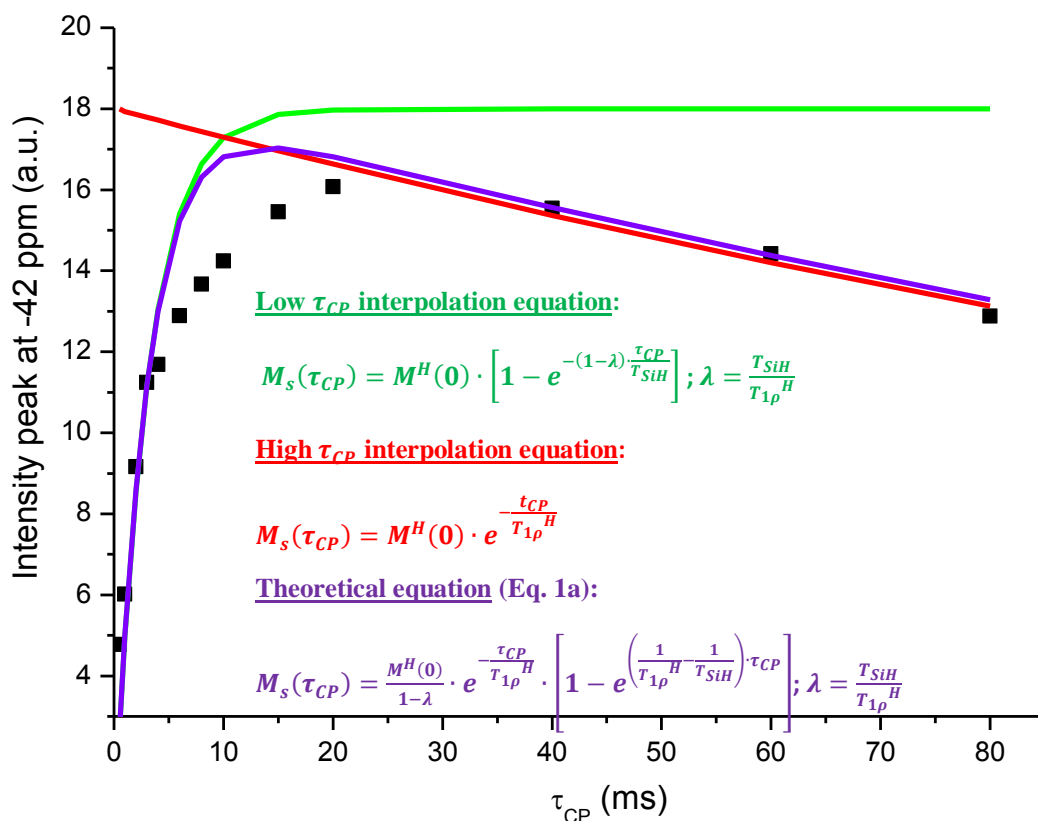


Figure 9: Experimental data fitting of the evolution of peak (-42 ppm) intensity at different τ_{CP} value. Low, high and theoretical equations of the ^{29}Si magnetization are displayed.

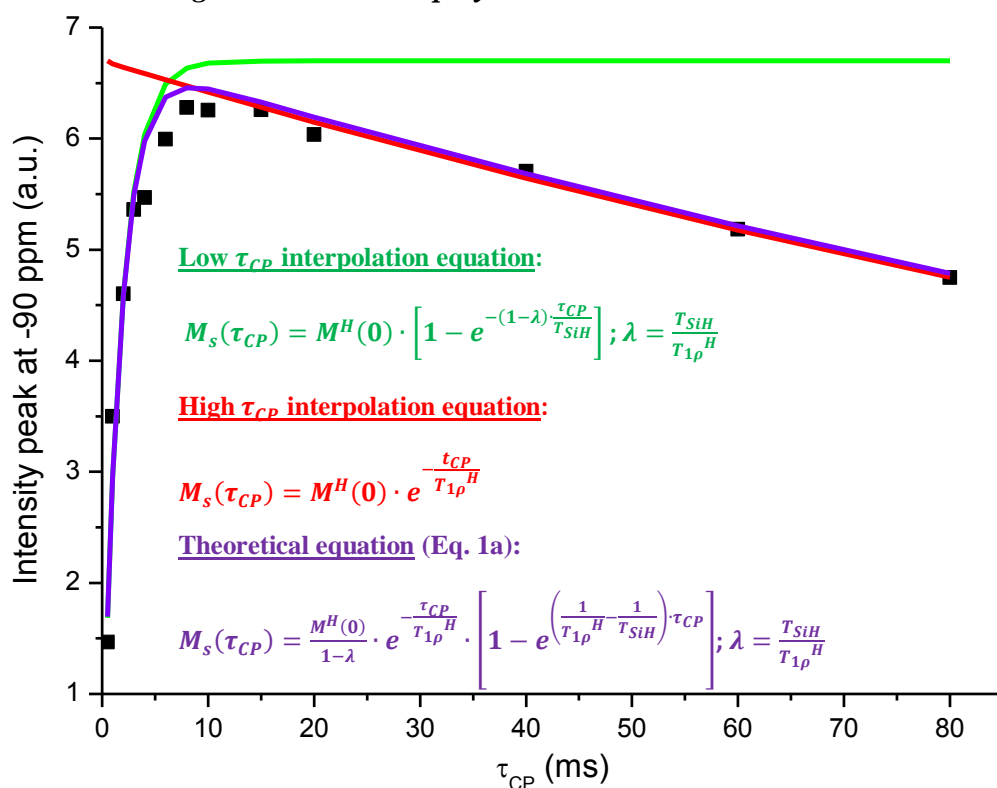


Figure 10: Experimental data fitting of the evolution of peak (-90 ppm) intensity at different τ_{CP} value. Low, high and theoretical equations of the ^{29}Si magnetization are displayed.

5.2.2. ^{27}Al MQMAS of Me-Imo- NH_3^+ -30 outgassed at 500 °C

Basics of bidimensional MQMAS technique are reported in Appendix II. In this section, quantitative and more practical analysis of the MQMAS spectrum of Me-Imo- NH_3^+ -30 outgassed at 500 °C, is discussed in detail.

Generally, an MQMAS spectrum of a solid sample can be schematically represented as shown in Figure 11 [9].

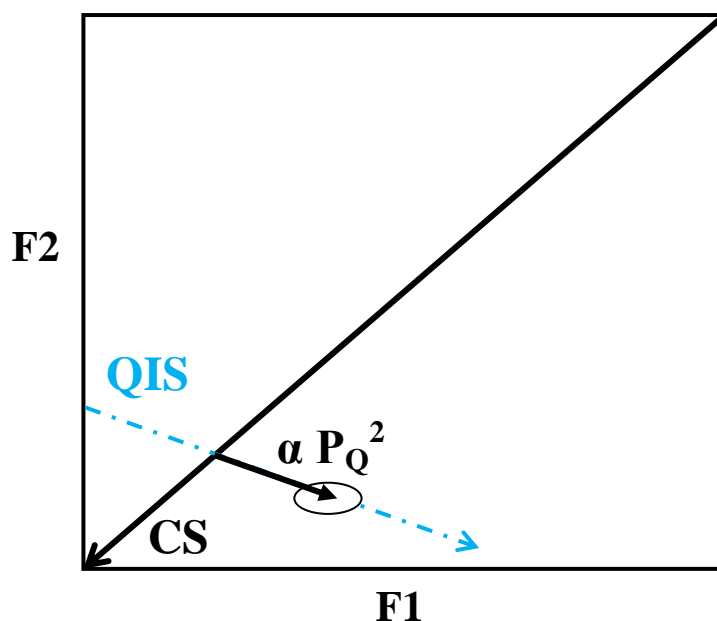


Figure 11: Representation of a general MQMAS spectrum with the relative main parameters. CS, chemical shift axis; QIS, quadrupolar axis (dot line); P_Q , second order quadrupolar effect (defined in the text).

It shows resonance bands aligned to an A-axis of slope R, function of the coherence p and parallel to F2-axis (ω_2), defined by the following equation (Eq. 2)

$$R(p) = p \cdot \frac{[36 \cdot I(I+1) - 17p^2 - 10]}{[36 \cdot I(I+1) - 27]} \quad (\text{Eq. 2})$$

The quadrupolar chemical shift, ω_{QIS} , is defined as follows (Eq. 3)

$$\omega_{QIS}(I, p) = \frac{\omega_Q^2}{\omega_0} \cdot K_0(p)C_0 = \frac{\omega_Q^2}{\omega_0} \cdot \frac{3p}{10} [4I(I+1) - 3p^2] = \xi(p)\omega_{QIS}(-1) \quad (\text{Eq. 3})$$

where I is the nucleus spin, ξ , defined as the slope of the quadrupolar axis, QIS-axis, ω_0 is the Larmor frequency, ω_Q is the quadrupolar splitting and $K_0(p)$ is the zero-rank coefficient of the central transition. Particularly, for ^{27}Al ($I = 3/2$), R and ξ values are $7/9$ and -3 , respectively. The chemical shift, δ_{CS} , and the second order quadrupolar effect parameter, P_Q (Eq. 4), are easily obtained by the projection of the gravity centers of resonance corresponding to the A-axis and QIS-axis. P_Q is a function of the quadrupolar coupling, C_Q , and of the tensor representing the electric field gradient, η_Q ,

$$P_Q = C_Q \cdot \sqrt{1 + \frac{\eta_Q^2}{3}} \quad (\text{Eq. 4})$$

If the quadrupolar interaction is negligible, the resonance would appear as a narrow peak of coordinates $(p\omega_0\delta_{\text{CS}}, -\omega_0\delta_{\text{CS}})$, on the multiple-quantum and mono-quantum direction, respectively. Thus, it is possible to define the chemical shift axis, CS-axis, passing from the origin (0,0) with slope of $-p$.

Figure 12 shows the MQMAS spectrum of Me-Imo-NH₃⁺-30 outgassed at 500 °C. As already discussed above, analogously to imogolite [1,3,10], thermal treatment on hydrophobic imogolite-like materials causes the collapsing of the nanotubular structure, so forming new Al(IV) and Al(V) sites, besides the original Al(VI). This spectra mainly shows that the three peak observed on the ^{27}Al MAS spectra (Figure 6) are distinct species and not the features of a single spectrum, as often happens with quadrupolar nuclei, such as Al.

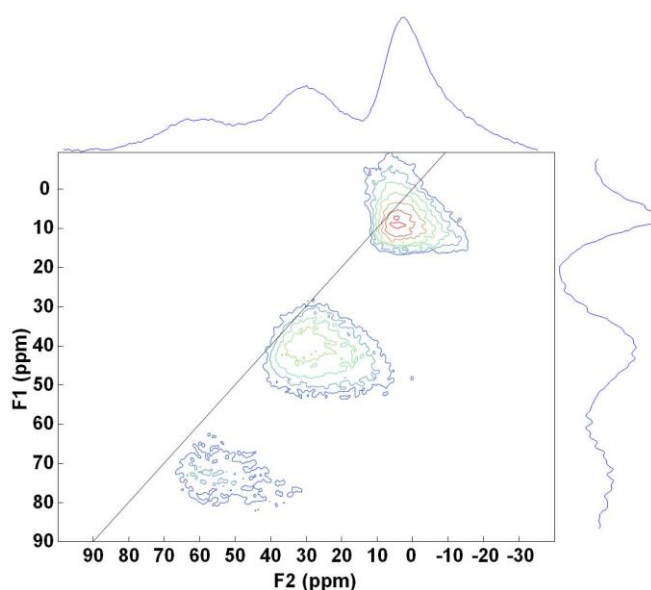


Figure 12: ^{27}Al MQMAS of Me-Imo-NH₃⁺-30 outgassed at 500 °C.

5.3. TGA-Mass measurements

Figure 13a and 13b show the mass fragments leaving the surface of Me-Imo-NH₃⁺-30 and Me-Imo, respectively.

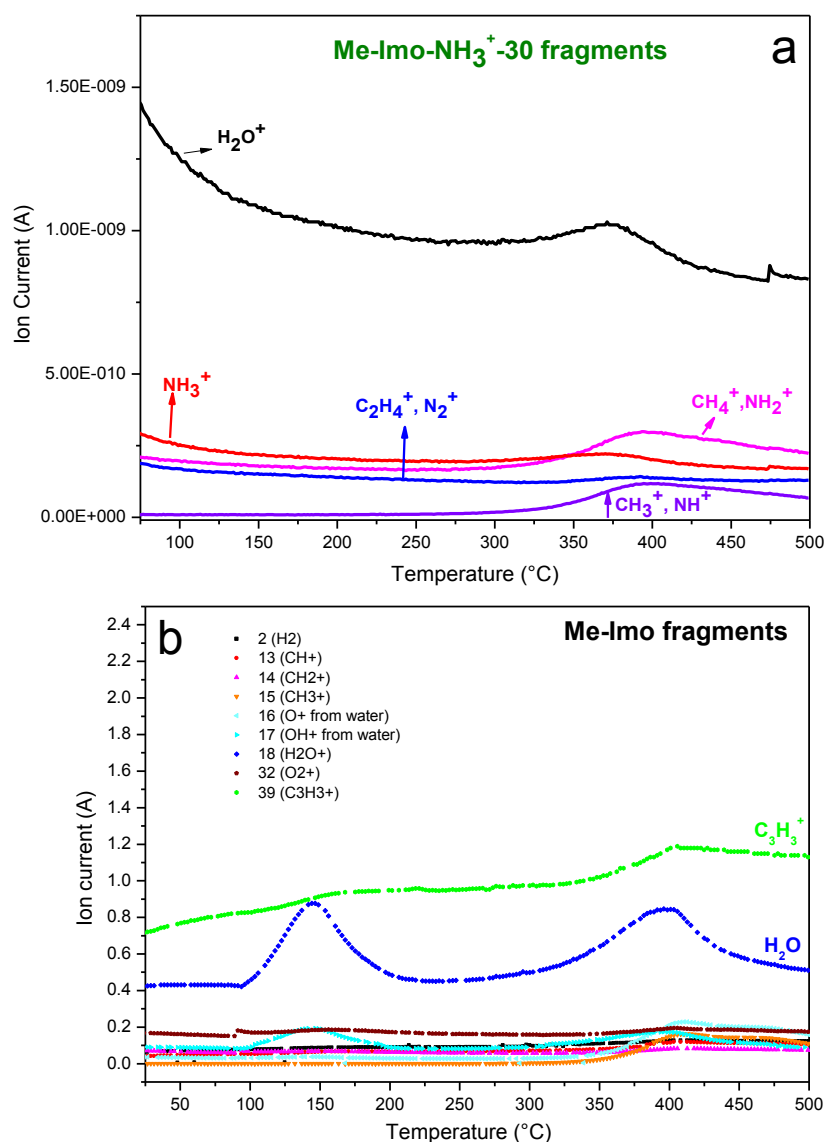


Figure 13: Mass fragments leaving the surface of (a) Me-Imo-NH₃⁺-30 and (b) Me-Imo.

As already discussed in Chapter 4, mass fragments released by aminated methyl-imogolite are H₂O⁺, CH₃⁺, NH⁺, CH₄⁺, NH₂⁺, NH₃⁺, C₂H₄⁺ confirming the decomposition of the outer organic layer and, consequently, the successful amination procedure of the material. Unexpectedly, the main fragment leaving Me-Imo surface, C₃H₃⁺, is not detected for Me-Imo-NH₃⁺-30.

Since MAS NMR results clearly evidenced that the two methylated imogolite materials collapse with the same mechanism, thus forming the same segregated phase, this result could be explained considering that the ethyl $C_2H_4^+$ fragment, which leaves Me-Imo- NH_3^+-30 surface, is not coming from the outer chain but from inner tubes.

5.4. XRD patterns

Figure 14 reports the comparison among the XRD patterns of fresh Imo, Me-Imo and Me-Imo- NH_3^+-30 , with the corresponding patterns of lamellar phases obtained by heating at 500 °C under Ar flux. The resulting single reflection at higher 2θ is coherent with lamellar phase patterns of aluminosilicates [11].

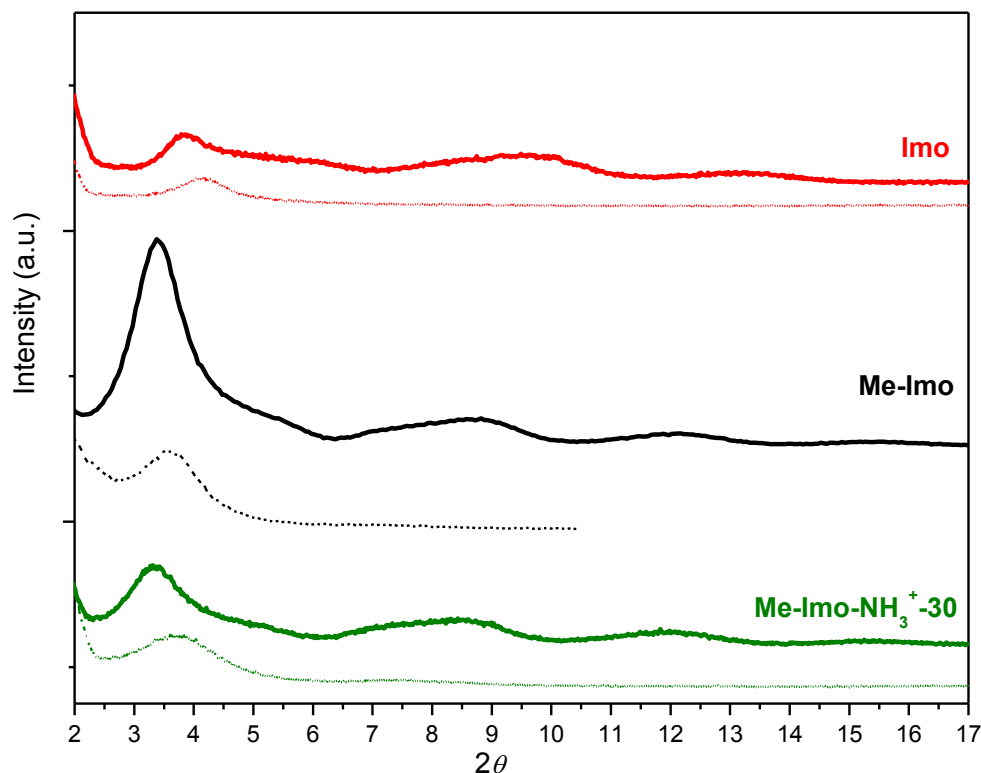


Figure 14: XRD patterns of fresh Imo (straight, red), Me-Imo (straight, black) and Me-Imo- NH_3^+-30 (straight, green) and the corresponding patterns (dot lines) of samples heated at 500 °C under Ar flux.

5.5. Conclusions

XRD diffraction showed that nanotubes integrity of Imo, Me-Imo and Me-Imo-NH₃⁺-30 is maintained up to 300 °C.

TGA-MS analysis revealed that grafted amino groups of Me-Imo-NH₃⁺-30 start to decompose above 150 °C. Mass fragments leaving the surface of aminated methyl-imogolite are H₂O⁺, CH₃⁺, NH⁺, CH₄⁺, NH₂⁺, NH₃⁺, C₂H₄⁺, confirming the decomposition of the outer organic layer and, consequently, the successful amination procedure of the material.

Collapsing of the structure is evidenced instead by the formation of a lamellar phase at 500 °C. With Imo, the mechanism proposed wants the cleavage of nanotubes to happen across their diameter, causing the formation of the following repeating sequence, Al-O-Si-O-Si-O-Al. With hybrid imogolite-like samples the mechanism is much more complex. Two processes seem to act subsequently: the first one, when methyl groups are removed at high temperature (higher than 300 °C); the second one, if methyl groups of two closed nanotubes are able to create Si-CH₂-O-Al links.

5.6. References

- [1] K.J.D. MacKenzie, M.E. Bowden, I.W.M. Brown, R.H. Meinhold, *Clays and Clay Min.* 37(4) (1989) 317.
- [2] M.A. Wilson, K. Wada, S.I. Wada, Y. Kakuto, *Clay Miner.* 23 (1988) 175.
- [3] D.Y. Kang, J. Zang, E.R. Wright, A.L. McCanna, C.W. Jones, S. Nair, *ACSNano* 4(8) (2010) 4897.
- [4] B. Bonelli, I. Bottero, N. Ballarini, S. Passeri, F. Cavani, E. Garrone, *J. Cat.* 264 (2009) 15.
- [5] C. Kim, S. Son, B. Kim, *J. Organomet. Chem.* 588 (1999) 1.
- [6] A. Pines, M.G. Gibby, J.S. Waugh. *J. Chem. Phys.* 56 (1972) 1776.
- [7] J. Skibsted, S. Rasmussen, D. Herfort, H.J. Jakobsen, *Cement & Concrete Comp.* 25 (2003) 823.
- [8] A. McCutcheon, J. Hu, G.S. Kamali Kannangara, M.A. Wilson, N. Reddy, *J. of Non-Crist. Sol.* 351 (2005) 1967.
- [9] "Caracterization et quantification de l'aluminium dans les zeolithes desaluminees par RMN haute-resolution a l'etat solide" PhD Thesis, Anne-Agathe Quoineaud, Universite de Caen, Laboratoire Catalyse et Spectrochimie, LCS, 2002.
- [10] M. Hatakeyama, T. Hara, N. Ichikuni, S. Shimazu, *Bull. Chem. Soc. Jpn.* 84(6) 656.
- [11] J.P. Gustafsson, *Clays Clay Miner.* 49 (1) (2001) 73.

Chapter 6

Acidity and basicity of imogolite-type materials: a FT-IR study

6.1. Introduction

Catalytic and adsorptive properties of solids depend on their surface chemistry. Particularly, FT-IR technique can provide direct information about the functional groups and adsorbed species present on the surface, as well as their coordination and strength of interaction [1,2]. As a consequence, information about the acidity/basicity of the material can be acquired. However, in order to discriminate between bulk and surface species, a study of the interaction between solid adsorbents and probe molecules must be performed [1-5]. The alteration of the spectral features as a result of the adsorption can provide information about the surface sites. An ideal FT-IR measurement should meet these main criteria [4,6]:

- The extinction coefficients of the informative bands must be as high as possible. Moreover, these bands should be in spectral regions in which the sample is transparent.
- Probe molecules should not cause any chemical modification of the surface and they need to be small enough to avoid steric hindrance of the adsorption. Additionally, they should have spectral parameters that are sensitive to the sites states on which they are adsorbed.

Probe molecules may be classified according to their abilities to test surface acidic sites, basic sites and oxygen vacancies.

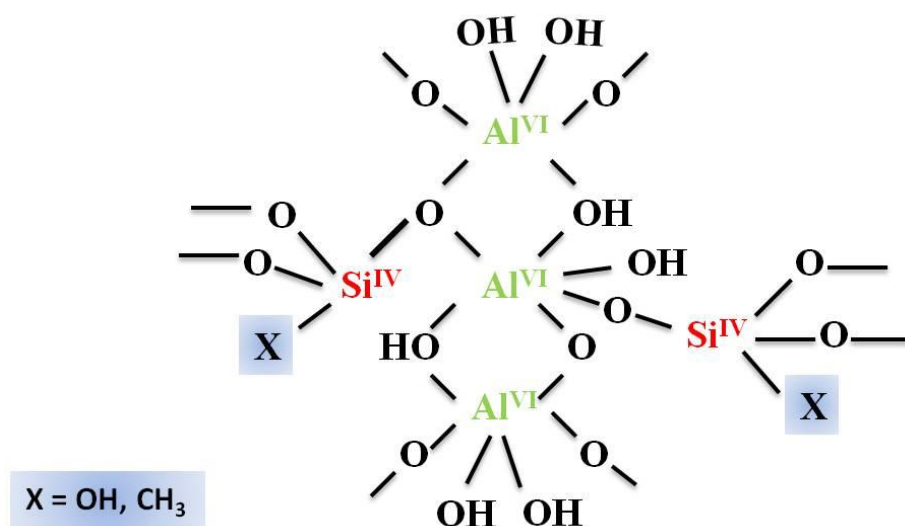
There are two kind of surface acidity, Lewis and Brønsted. Brønsted acid sites are surface hydroxyl groups that provide H^+ species for protonation of bases, whereas Lewis sites are cus cations. It follows that probe molecules for determination of surface acidity may be strong or weak bases [7,8]. The most frequently used strong base is *ammonia* [7,9-11]. NH_3 can interact with acidic Brønsted and Lewis sites through the lone pair of the nitrogen atom. Particularly, the interaction with acidic Brønsted sites can lead to the formation of ammonium ions. Monodentate, bidentate, tridentate species might be formed depending on the number of sites interacting with the protons of each ammonium ion [12,13]. Such structures have different vibrational activities due to their different local group symmetry.

At high dosing pressures, ammonia may interact also with silanols, forming very weak H-bonded species [12,14].

Surface basicity has instead to be estimated by dosing an appropriate probe molecule, which must have an acidic part. Out of the possible probes, *carbon monoxide* is widely used. It can give an interaction of the acid/base type, as a consequence of a polarization of the 5σ lone pair orbital, mainly localized on the carbon atom. As the 5σ lone pair orbital has a partial antibonding character, CO adsorption causes an increase of the $\nu(\text{CO})$ stretching frequency (free molecule $\nu(\text{CO})$ value is 2143 cm^{-1}), whose extent measures the strength of the acid-base interaction [15].

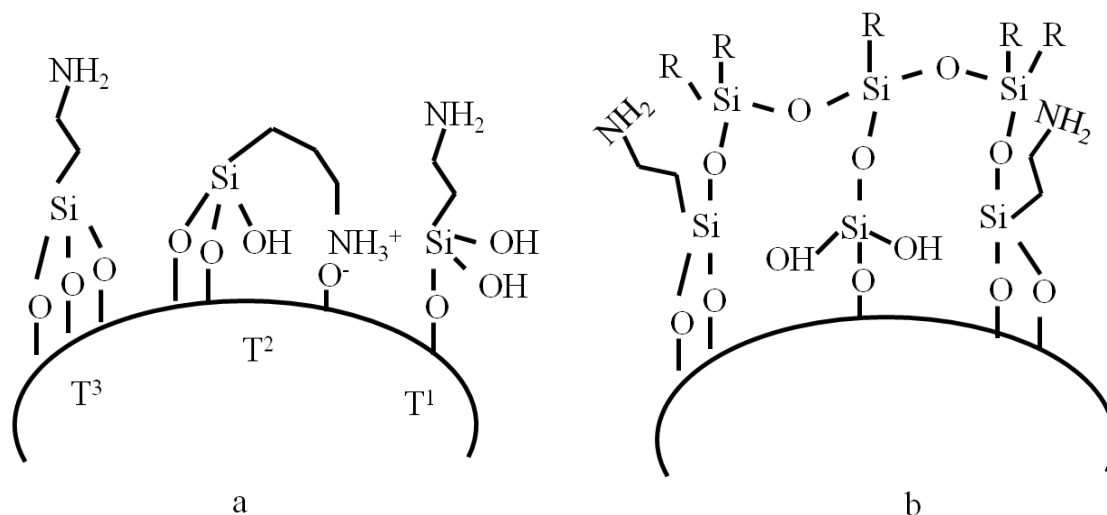
6.2. Surface sites of imogolite-type materials

A schematic representation of imogolite and methyl-imogolite tube composition is given in Scheme 1. As confirmed by MAS NMR reported in Chapter 3, inner silicon atoms are in tetrahedral coordination, while $\text{Al}(\text{OH})\text{Al}$ outer network is constituted by six-coordinated aluminum atoms.



Scheme 1: Representation of imogolite and methyl-imogolite bulky and surface sites.

According to the minimum formula of imogolite, $(\text{OH})_3\text{Al}_2\text{O}_3\text{Si-X}$, where $\text{X}=\text{OH}$ or CH_3 , aluminum atoms are connected to two different hydroxyl groups, bridged and terminal, the former expected to be more acidic. In case of aminated methyl-imogolite, more complex surface sites are present (Scheme 2).



Scheme 2: Representation of aminated methyl-imogolite outer surface, (a) T^x species and (b) aminated groups deriving from the oligomerization of 3-APS.

As already figured out in previous chapters, ²⁷Al MAS-NMR results showed that bulky and surface aluminols in Imo, Me-Imo and Me-Imo-NH₂ samples are only six-coordinated. Nevertheless, it is likely for the surface aluminols to have slightly perturbed Al^{VI} sites, since one coordination involves the Al^{VI}(O)Si^{IV} bond, leading to a distortion of the classical Al^{VI} environment (Scheme 1). Considering instead the internal surface, catalytic activity, if any, should be related only to inner silanols present in Imo and reasonably not to the Si-CH₃ groups of Me-Imo and Me-Imo-NH₂.

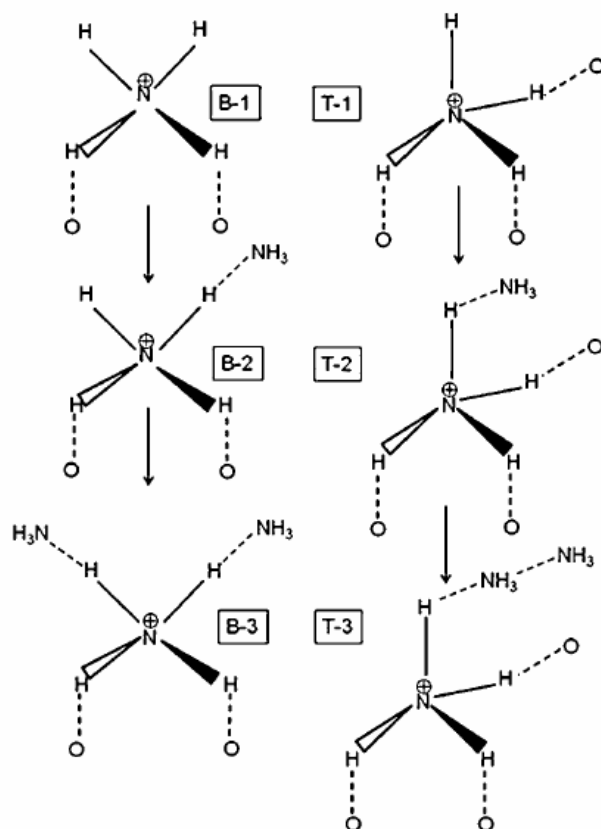
With *ammonia*, in case of imogolite materials an analogue interaction mechanism occurring on zeolitic materials surface is expected. In fact, it is known from the literature that gaseous ammonia can interact with acidic hydroxyl sites (Z), according to the following equilibrium



in which case ammonium cations are formed (Scheme 3) [12,13]. This behavior is also proper of pure alumina samples [16] and free silanols groups interacting with ammonia [12,14]. However, once ammonium species are formed, new NH₃ molecules can interact by H-bond,



showing the formation of a solvated ammonium cation, $N_2H_7^+$ (shorten notation for $NH_4^+ \cdot NH_3$). At this condition, only monosolvated ammonium species are formed. On the contrary, if the equilibrium pressure of ammonia is further increased, di-solvated species generate

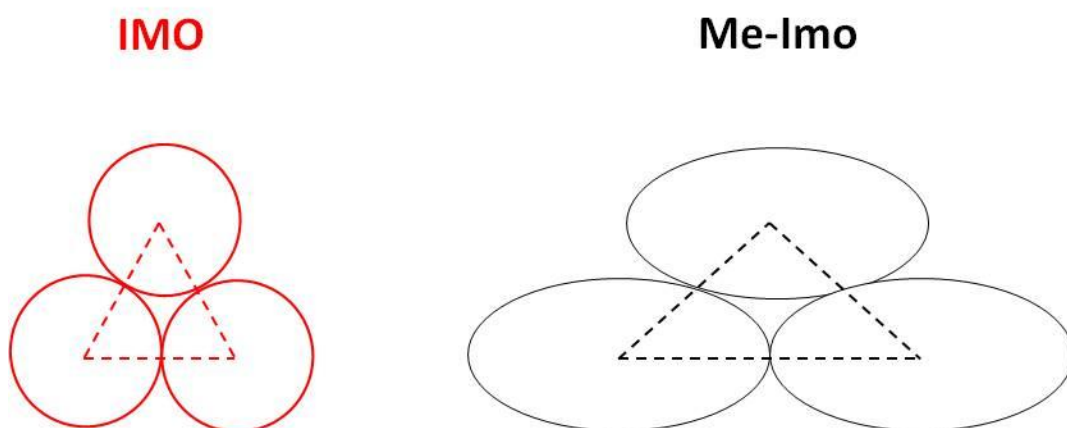


Scheme 3: Surface species that can be formed by the interaction of ammonia with acidic hydroxyl groups of NH_4 -ZSM-5 zeolites. *B-1, B-2 and B-3, represent the bare bidentate ammonium, bidentate ammonium species H-bonded to an NH_3 molecule and ammonia molecules interacting with NH_4^+ species, respectively. T-1, T-2 and T-3 show the bare tridentate NH_4^+ species, tridentate NH_4^+ species H-bonded to one ammonia molecule and NH_3 molecule H-bonded to the NH_4^+ species already solvating the ammonium species [13].*

With *carbon monoxide*, the most important interactions expected are those involving the bridge oxygen framework of $Al^{VI}(O)Si^{IV}$ and hydroxyl framework of $Al(OH)Al$, respectively. For Imo, physically adsorbed gas could be also present at lower wavenumbers with respect of free gas [17].

With 0.376 nm, the kinetic diameter of CO is far smaller than the inner diameter of the nanotubes, allowing its unhindered entrance into the nanotubes and the interaction with silanols at the inner surface. In the presence of free silanols, the characteristic 2156 cm^{-1} band is expected to appear as a consequence of the stretch mode of carbon monoxide interacting with Si-OH groups [18]. Accordingly, Eischens *et al.* [19] published for the first time in 1954 a study describing IR spectra of adsorbed species by the interaction of carbon monoxide on silica-supported metals. Moreover, with metal oxides, Lavalley pointed out that CO [20,21] can react with highly basic sites present on their surface.

As a whole, carbon monoxide interaction at nominal 77 K can be used to characterize both the presence of acidic and basic sites on the surface. As already discussed, imogolite nanotubes are known to form not isolated but in interwoven bundles, in which three main types of porosity can be identified [22]: i) intra-tube pores (about 1 nm wide); ii) inter-tube pores, *i.e.* the spacings between three aligned tubes in a regular packing (0.3–0.4 nm wide); iii) slit mesopores among bundles. On the contrary, Me-Imo tubes resulted to be not exactly spherical but quite ellipsoidal with longer diameters. As diffraction analysis revealed, a larger curvature can be explained by the presence of methyl groups, for either steric or electronic effects [23]. As a consequence, since experimental porosity values showed that type-B pores of Imo are *ca* 3 times smaller with respect to Me-Imo (Scheme 4), they are likely to be too narrow to allow any adsorption phenomenon by probe molecules, such as ammonia and carbon monoxide, as already considered by other authors [22,24].



Scheme 4: Type B pores hindrance of Imo and Me-Imo, as evaluated from porosimetry measurements.

6.3. FT-IR spectra of imogolite-type materials outgassed at high temperatures

Figure 1a, 1b and 1c show fresh Imo, Me-Imo and Me-Imo-NH₃⁺-30 FTIR spectra outgassed at 150 °C, 300 °C and 500 °C, respectively.

Features at 150°C have been already discussed in previous chapters. Nevertheless, it is worth noting that only Imo-150 still presents adsorbed water, as the broad band at *ca* 1640 cm⁻¹ confirms (asterisk). Signals in the C-H stretching region are due to carbon impurities of the sample holder.

Water is completely removed from all adsorbents at 300 °C. Nanotubes integrity is also maintained, despite grafted aminogroups of Me-Imo-NH₃⁺-30 are totally lost, as the absence of NH₂ stretching and bending modes reveals, in agreement with MAS NMR results (Chapter 5). As a whole, Me-Imo and Me-Imo-NH₃⁺-30 show analogue spectral features.

Lamellar imogolite is formed after adsorbents pre-treating at 500 °C. This finding has been confirmed by XRD and MAS NMR results (Chapter 5). FT-IR measurements reported here are also in fair agreement. Particularly, with Imo-500, new peaks are seen at 3742 and 3655 cm⁻¹, assigned to hydrogen bonded of isolated hydroxyl groups. At lower wavenumbers, the band at 1595 cm⁻¹ can be assigned to carbonate-like species at the outer surface, like those formed on aluminum hydroxide [15]. With lamellar Me-Imo and Me-Imo-NH₃⁺-30, new broad bands are also arising in the O-H stretching region, due to isolated hydroxyls groups involved in hydrogen bonding. Interestingly, the C-H stretching and bending modes are still present, confirming the carbo-aluminosilane lamellar fragments formed for both hydrophobic and aminated imogolite-like materials (Chapter 5).

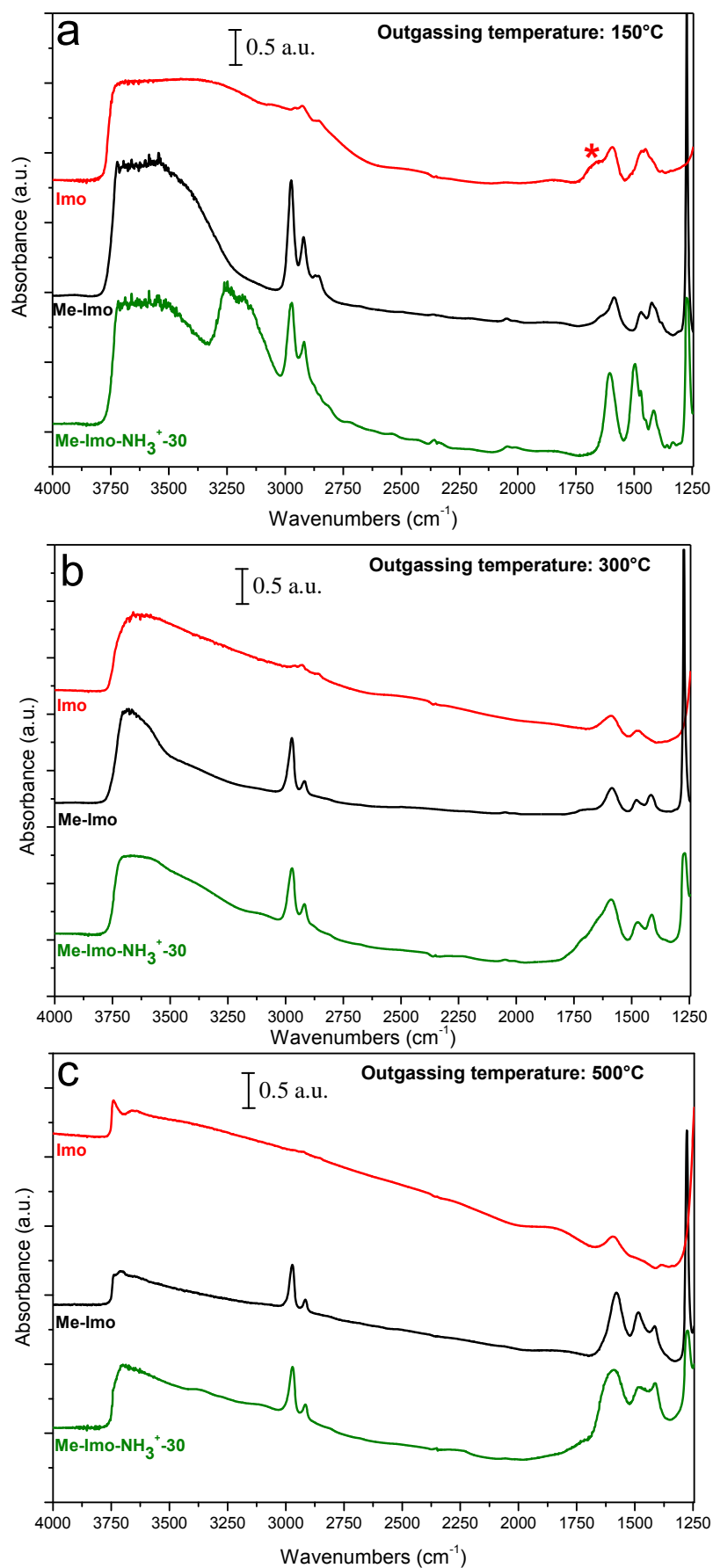


Figure 1: Fresh Imo, Me-Imo and Me-Imo-NH₃⁺·30 FT-IR spectra outgassed at (a) 150 °C, (b) 300 °C and (c) 500 °C, respectively.

6.4. NH₃ adsorption

Figure 2a, 2b and 2c show the FT-IR difference spectra collected following ammonia adsorption in the pressure range 0-20 mbar, for Imo, Me-Imo and Me-Imo-NH₃⁺-30 outgassed at 150 °C, respectively.

The interaction of gaseous ammonia at high equilibrium pressures with Imo-150, evidenced that in the OH stretching region the gas interacts, besides the silanols, also with water molecules. In fact, the decrease of the 3745 cm⁻¹ band of Si-OH hydroxyls groups involved in NH₄⁺ formation, is seen, while a new broad band shifted of *ca* 600 cm⁻¹ (3200 - 3000 cm⁻¹ range) is formed due to H-bonding. Moreover, the second new band centered at 2750 cm⁻¹ can be assigned to the stretching mode of the N-H group of the ammonium species H-bonded to ammonia, *i.e.* the monosolvated species, N₂H₇⁺, which are known to form on protonic zeolites [12,13]. This can be also confirmed by the presence of the 1450 cm⁻¹ band, which shifts to 1460 cm⁻¹ at higher ammonia pressure, generally assigned to the formation of ammonium species formed on Brønsted acidic sites, like those occurring upon ammonia adsorption on Brønsted sites inside zeolites micro cavities [12]. Finally, the bands at 1625 and 1300 cm⁻¹ bands are, respectively, due to the asymmetric and symmetric bending modes of gaseous NH₃ molecules coordinated to outer Al³⁺ Lewis sites [10].

On the contrary, Me-Imo-150, which has no more adsorbed water if pretreated at this temperature [23], showed a different interaction mechanism. In fact, we can assume that in this case gaseous ammonia interacts with external Al(OH)Al bridged groups, as the decrease of the 3732 cm⁻¹ band reveals, since the interaction with inner Si-CH₃ group is less probable. As expected, in the O-H stretching region we do not see the formation of the broad band due to H-bonding, while we can assign the two bands at 3380 and 3280 cm⁻¹, appearing at higher equilibrium pressure of ammonia, as the presence of ammonium species in interaction with external bridged Al(OH)Al groups (asterisks). This interpretation is also confirmed by the ammonium bending mode band present at 1447 cm⁻¹, shifted to 1460 cm⁻¹ at higher coverage, as commonly observed in zeolites materials [12,25]. Moreover, we are also able to distinguish the two contributions of the $\nu(\text{Al-O})$ modes (inset) assigned to the 1203 and 1281 cm⁻¹ negative bands (asterisks), respectively, present between the two isosbestic points at 1229 and 1151 cm⁻¹.

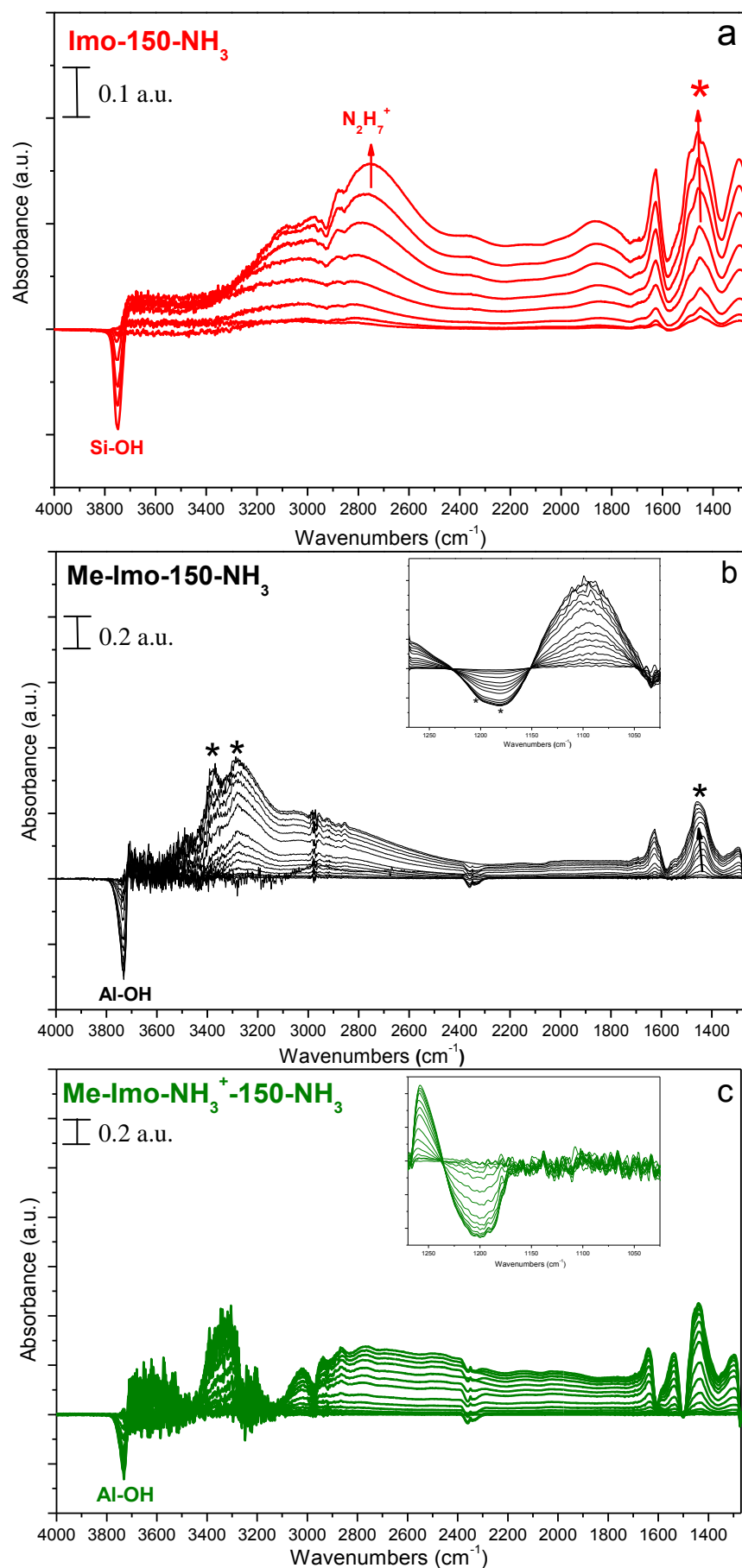


Figure 2: Difference FT-IR spectra obtained after dosing increasing NH₃ pressure (0–20 mbar) on (a) Imo, (b) Me-Imo and (c) Me-Imo-NH₃⁺-30 outgassed at 150 °C.

As a consequence, a new broad band centered at 1100 cm^{-1} is formed. Interestingly, ammonia interaction with the external surface of Imo is not detectable (inset not shown). In fact, starting from the mere geometrical considerations discussed above, it results to be reasonable, probing that B-type pores of Imo are evidently too narrow to be accessible.

Interaction of the gas with the surface of Me-Imo-NH₃⁺-30 is quite complex. In agreement with MAS NMR results, the Al-OH band at 3731 cm^{-1} is slightly less intense as compared to that of Me-Imo-150, probing the functionalization of one third of the surface accessible aluminol group.

Figure 3a, 3b and 3c report the FT-IR difference spectra collected following ammonia adsorption in the pressure range 0-20 mbar, for Imo, Me-Imo and Me-Imo-NH₃⁺-30 outgassed at $300\text{ }^{\circ}\text{C}$, respectively.

With Imo-300, the negative band of silanols interacting with ammonia is broader, probably because after the complete removal of water, all silanols are then accessible to NH₃. Spectral features at lower wavenumbers are comparable to those of Imo-150.

With Me-Imo-300, aluminol groups interacting with ammonia are detected by a sharp band centered at 3718 cm^{-1} . Additionally, the two bands at 3373 and 3264 cm^{-1} are assigned to the stretching modes of molecular ammonia, whose bendings are found at 1625 and 1296 cm^{-1} , respectively. Besides these modes, the formation of ammonium is seen by the band at 1460 cm^{-1} . The amount of ammonia adsorbed by Me-Imo-300 seems slightly higher than that at Me-Imo-150 surface. This could be due to the heating process that induces some mechanical changing in the structure, *e.g.* cleavage of a minor part of the bundles of nanotubes, as shown by Wilson *et al.* [26] for the unmodified imogolite. This breakdown of longer nanotubes could create higher number of the opening sites of nanotubes, hence creating more acidic sites.

According to MAS NMR evidence, integrity of Me-Imo-NH₃⁺-30 nanotubes outgassed at 300°C is maintained, while aminopropyl groups grafted at the outer surface are lost. FT-IR spectra shown in Figure 2c confirmed the presence of aluminol species interacting with ammonia (3729 cm^{-1} band vs. 3718 cm^{-1} for Me-Imo-300). Moreover, the bands likely due to the stretching modes of molecular ammonia are found at 3254 and 3063 cm^{-1} , respectively, and shift to 3018 and 3036 cm^{-1} at high coverage of ammonia. The bending region of NH₃ ($1629/1310\text{ cm}^{-1}$) and NH₄⁺ (1448 cm^{-1}) modes is almost unaltered.

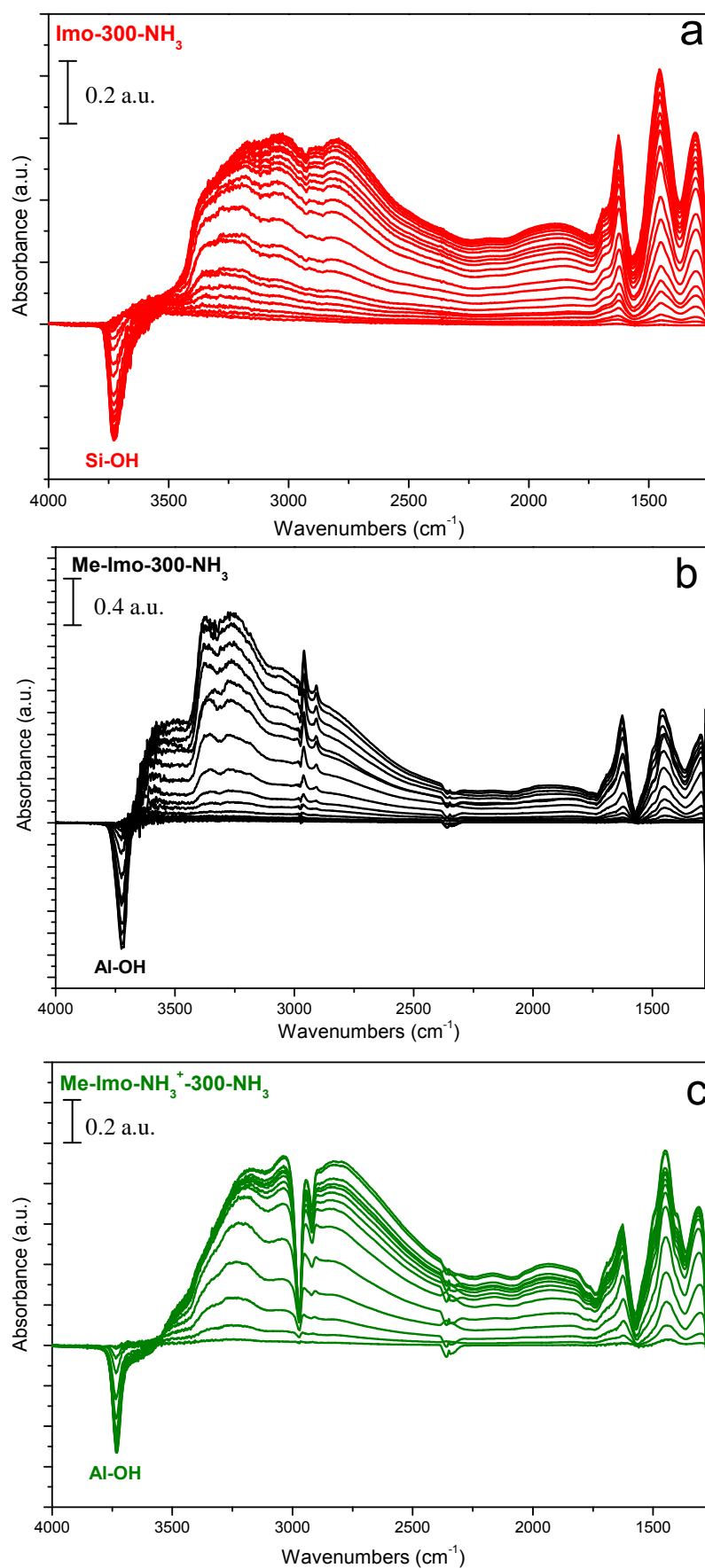


Figure 3: Difference FT-IR spectra obtained after dosing increasing NH₃ pressure (0–20 mbar) on (a) Imo, (b) Me-Imo and (c) Me-Imo-NH₃⁺-30 outgassed at 300 °C.

Figure 4a, 4b and 4c report the FT-IR difference spectra collected following ammonia adsorption in the pressure range 0-20 mbar, for Imo, Me-Imo and Me-Imo-NH₃⁺-30 outgassed at 500 °C, respectively.

With Imo-500, adsorption of NH₃ reveals the presence of both Lewis and Brønsted sites and a component at 3660 cm⁻¹ (inset) due to the presence of more acidic OH species with respect to Me-Imo-500. In fact, Imo shows stronger interaction with NH₃, which leads to the formation of more ammonium species, as detected by the more intense band of the bending and stretching vibrational modes of N-H bonds. This interaction occurs through inner silanols, as seen by the negative band centered at 3740 cm⁻¹.

Accordingly, this frequency is not detected with Me-Imo-500. The negative band assigned to hydroxyl groups, which undergoes interaction with ammonia, reveals the presence of several components formed after the cleavage of the nanotubes: a band at 3660 cm⁻¹, assignable to the Si-CH₂-O-Al fragments of the lamellar phase proposed in Chapter 5, as well as the band at 3739 cm⁻¹, that could be due to terminal isolated silanols. The 3718 cm⁻¹ band is instead assigned to isolated Al-OH groups, analogue to those found on transition Al₂O₃ [15,16].

With Me-Imo-NH₃⁺-30 outgassed at 500 °C a comparable result with Me-Imo-500 is obtained, confirming that the two samples may collapse by the same mechanism and into the same segregated phase. As a whole, only after thermal treatment at 500 °C the interaction results to be reversible, indicating the strong acidic straight of lamellar imogolite-like materials.

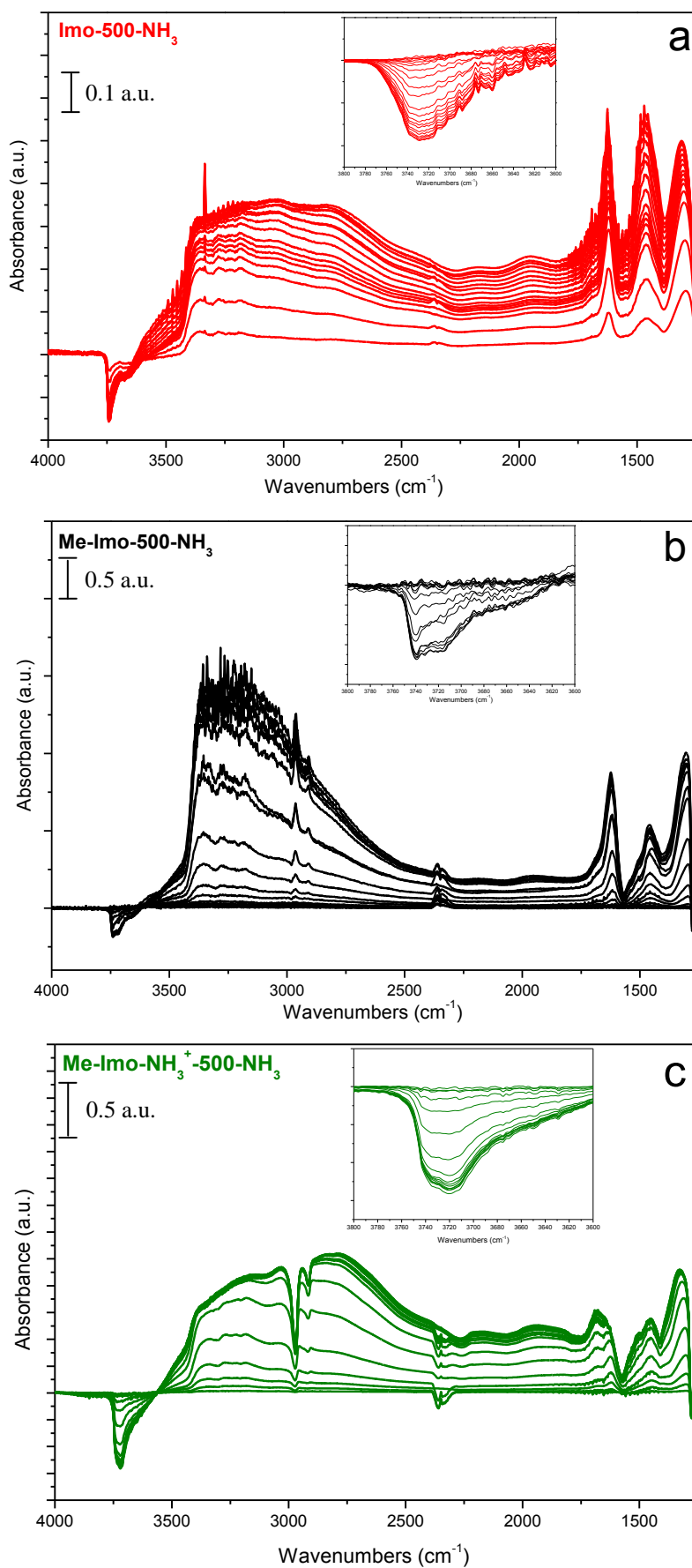


Figure 4: Difference FT-IR spectra obtained after dosing increasing NH₃ pressure (0–20 mbar) on (a) Imo, (b) Me-Imo and (c) Me-Imo-NH₃⁺-30 outgassed at 500 °C.

6.5. CO adsorption

Figure 5a, 5b and 5c show the FT-IR difference spectra collected following ammonia adsorption in the pressure range 0-20 mbar, for Imo, Me-Imo and Me-Imo-NH₃⁺-30 outgassed at 150 °C, respectively.

Imo-150 shows the only band at 2150 cm⁻¹. In the literature, this wavenumber value is commonly assigned to CO/H₂O dimeric complexes formed after CO adsorption on ice, indicating a weak electrostatic interaction of the gas with water molecules, probably at the outer surface [27].

Not only for Imo-150 but also in the case of Me-Imo-150, a single intense band is observed but at lower wavenumbers, 2146 cm⁻¹. This value is less likely due to the CO condensation into the nanotube cavity, since the frequency of the “liquid-like” phase is generally known to be at 2138 cm⁻¹. The slight shift from the vibration of the unperturbed gas phase indicates instead that also in this sample a weak perturbation of electrostatic nature on the 5σ orbital of CO occurs.

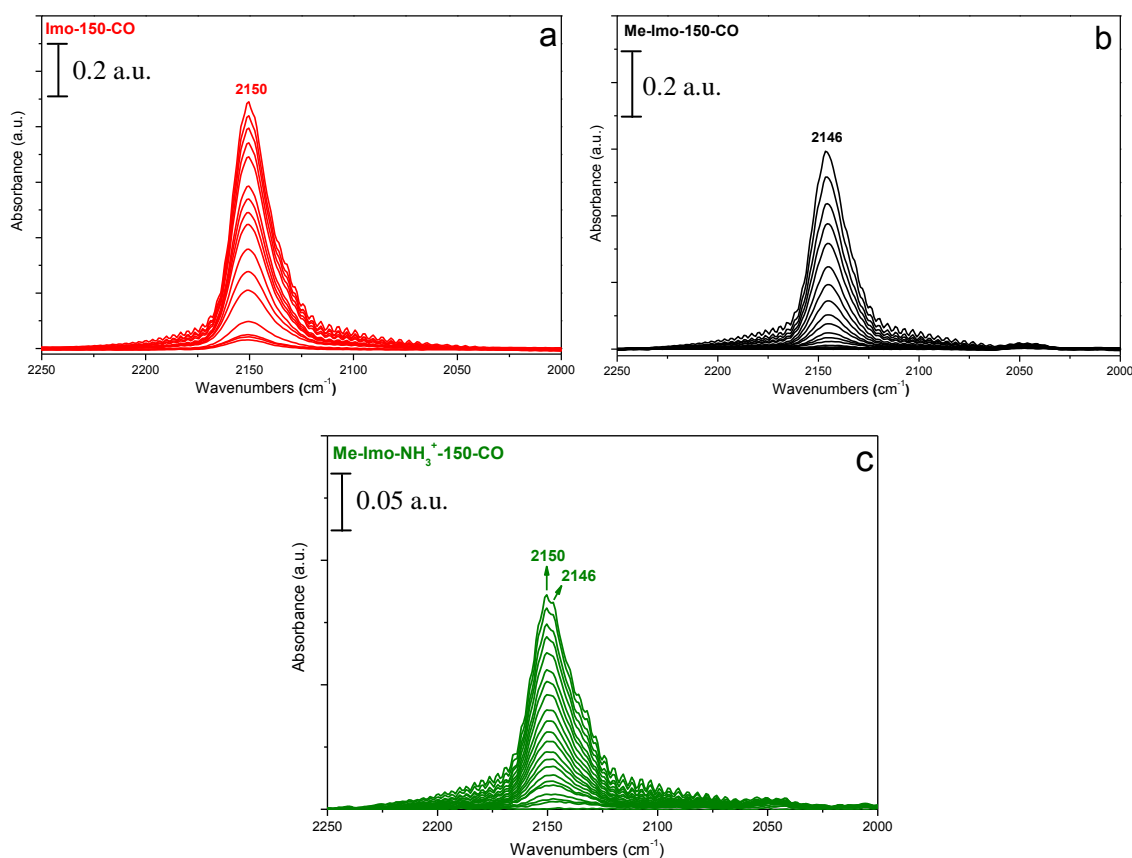


Figure 5: Difference FT-IR spectra in the 2250-2000 cm⁻¹ region obtained after dosing CO in the 0–20 mbar pressure range on (a) Imo, (b) Me-Imo and (c) Me-Imo-NH₃⁺-30 outgassed at 150 °C.

With Me-Imo-NH₃⁺-30 outgassed at 150 °C, the CO band seems to be formed by the two contributions at 2150 and 2146 cm⁻¹, respectively.

Figure 6a, 6b and 6c show the IR difference spectra collected following ammonia adsorption in the pressure range 0-20 mbar, for Imo, Me-Imo and Me-Imo-NH₃⁺-30 outgassed at 300 °C, respectively.

With Imo-300, the expected band centered at 2158 cm⁻¹ due to CO on inner silanols is observed [28], together with a minor band at *ca* 2190 cm⁻¹ (asterisk) probably due to CO adsorbed on weak Al³⁺ Lewis sites at the outer surface [18].

With Me-Imo-300, the frequency of CO vibration at 2154 cm⁻¹, shifting with coverage to 2151 cm⁻¹, indicates a stronger interaction than the one observed for Me-Imo-150, probably with weak Al-OH groups, analogous to those found on transition alumina [15,16]. Unfortunately, the region of O-H stretching is too noisy and do not allow the analysis of involved sites.

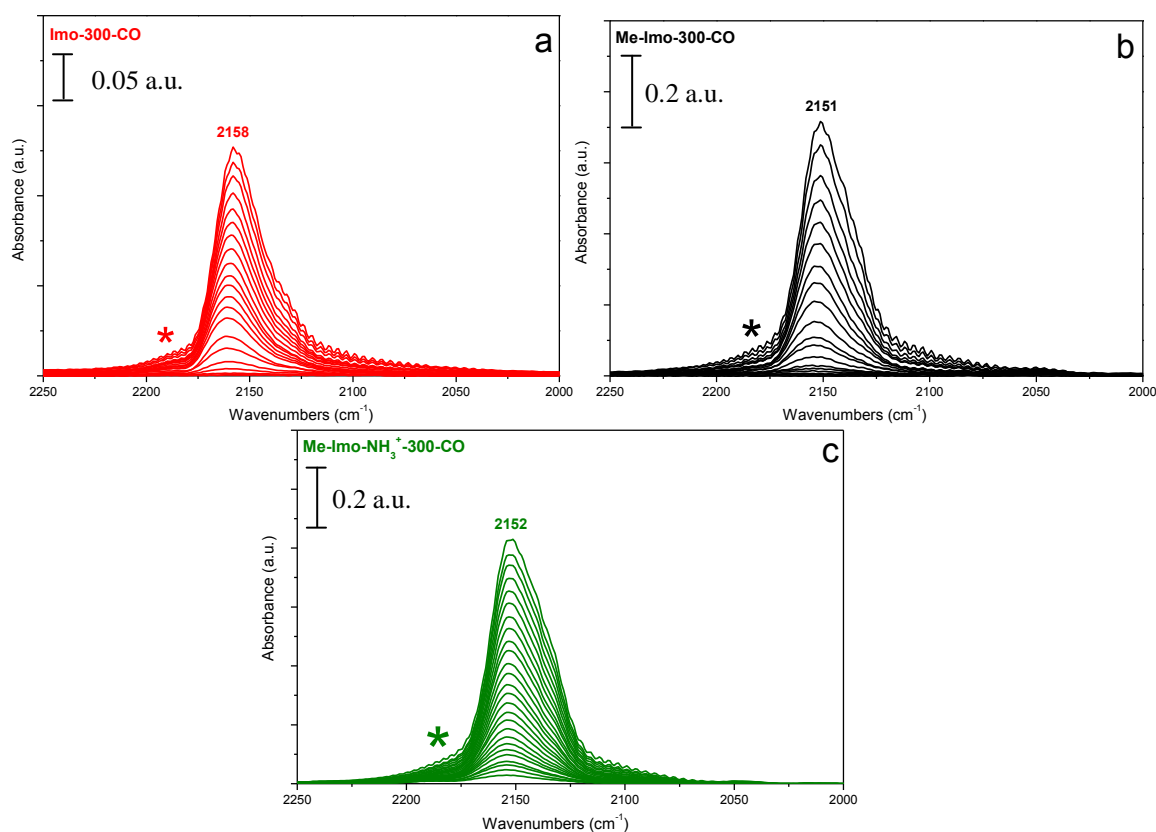


Figure 6: Difference FT-IR spectra in the 2250-2000 cm⁻¹ region obtained after dosing CO in the 0–20 mbar pressure range on (a) Imo, (b) Me-Imo and (c) Me-Imo-NH₃⁺-30 outgassed at 300 °C.

With Me-Imo-NH₃⁺-30 outgassed at 300 °C, the CO band is centered at 2152 cm⁻¹, analogously to Me-Imo-300. Al³⁺ sites are also detected at *ca* 2190 cm⁻¹ (asterisk).

As a whole, carbon monoxide interaction confirmed that aluminum environment has changed due to thermal treatment at 300 °C, as evidenced by ²⁷Al MAS NMR spectra.

Figure 7a, 7b and 7c show the IR difference spectra collected following ammonia adsorption in the pressure range 0-20 mbar, for Imo, Me-Imo and Me-Imo-NH₃⁺-30 outgassed at 500 °C, respectively.

With Imo-500, bands are less intense, indicating that fewer sites are accessible to this probe. In the CO stretching range, a weak band is seen at 2203 cm⁻¹, shifting with coverage to 2188 cm⁻¹, together with a main band at 2170 cm⁻¹, shifting to 2166 cm⁻¹. Both bands are reversible upon evacuation at low temperature: the former is assigned to CO adsorbed onto coordinatively unsaturated Al³⁺, like those at the surface of transition aluminas [15], the latter to CO interacting with hydroxyls more acidic than silanols. Interestingly, no band was observed at 2157 cm⁻¹, corresponding to CO adsorbed on accessible silanols, in fair agreement with the model reported in Scheme 3 of Chapter 5.

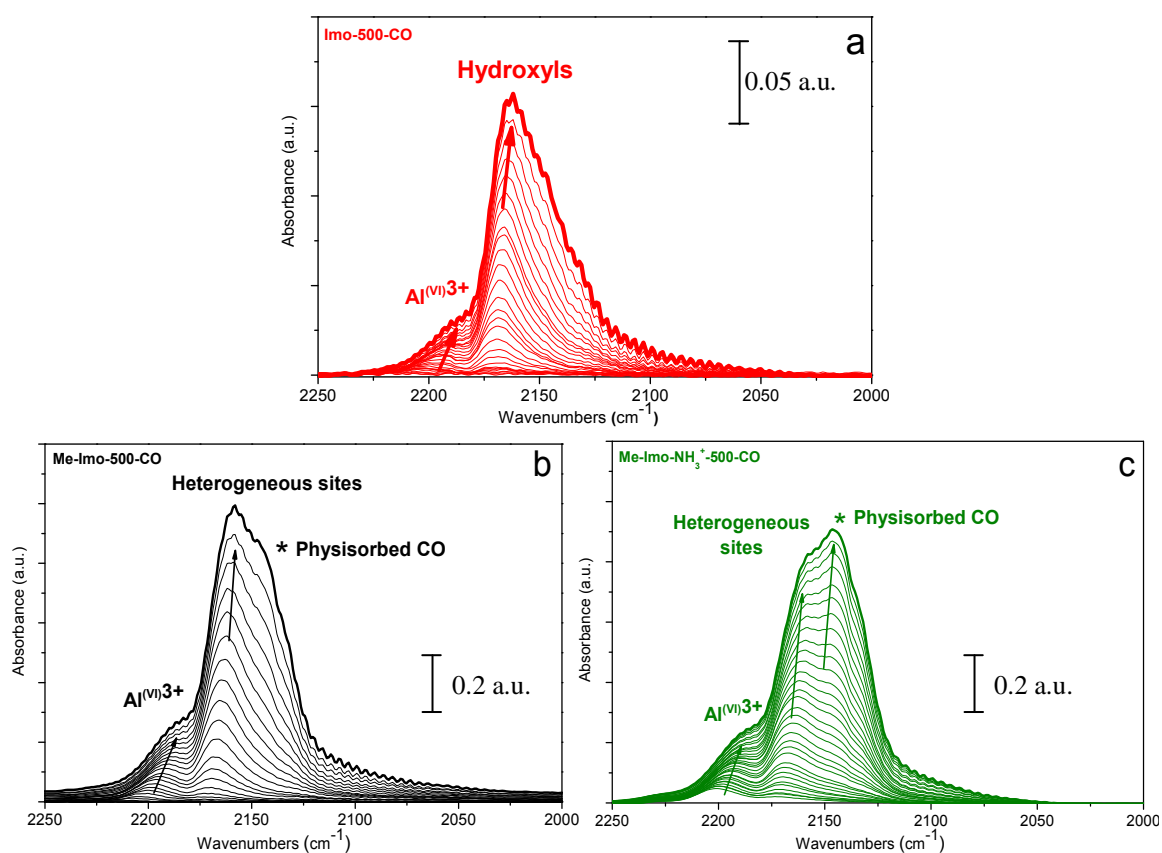


Figure 7: Difference FT-IR spectra in the 2250-2000 cm⁻¹ region obtained after dosing CO in the 0–20 mbar pressure range on (a) Imo, (b) Me-Imo and (c) Me-Imo-NH₃⁺-30 outgassed at 500 °C.

With Me-Imo-500, several new bands can be observed corresponding to Lewis and Brønsted sites formed after thermal treatment. In the CO stretch range, two components are seen: the major band at 2169 cm^{-1} shifts to 2158 cm^{-1} with increasing CO pressure and it is assigned to hydroxyl groups more acidic than silanols; a minor band at 2203 cm^{-1} , shifting to 2188 cm^{-1} , is due to CO adsorbed onto coordinatively unsaturated Al^{3+} sites, as at the surface of transition aluminas [15]. The shoulder at 2140 cm^{-1} is instead assigned to physisorbed CO [18].

With Me-Imo- NH_3^+ -30 outgassed at $500\text{ }^\circ\text{C}$, analogue bands to Me-Imo-500 are found, except that the amount of physisorbed CO (asterisk) is slightly higher. Interestingly, the overall shape of Me-Imo and Me-Imo- NH_3^+ -30 is quite specular.

The OH stretch region ($3800\text{--}3000\text{ cm}^{-1}$) of the difference spectra of the three samples is reported in Figure 8a, 8b and 8c, respectively. In all cases, negative bands correspond to hydroxyls interacting with CO, while the broad positive absorption is instead due to H-bond formation. Moreover, the sharp positive peak at 3750 cm^{-1} is due to changes in the temperature of the sample as a function of the CO pressures, affecting the location of the Si-OH stretching, often observed during experiments at 77 K .

With Imo-500, the negative band of hydroxyls interacting with CO is rather broad, indicating heterogeneity of sites. Particularly, at least three components may be figured out at 3743 , 3725 and 3660 cm^{-1} , shifted downward by 233 , 245 and 210 cm^{-1} , respectively, in agreement with the literature [29] that reports a $\Delta\nu(\text{OH})$ of $200\text{--}240\text{ cm}^{-1}$ for a $\nu(\text{CO})$ of $2166\text{--}2170\text{ cm}^{-1}$. The observed shifts are too large to be due to Si-OH or Al-OH species, since silanols suffer with CO a shift of about 100 cm^{-1} [28], whereas hydroxyls at the surface of transition aluminas evidence a hypsochromic shift by $70\text{--}95\text{ cm}^{-1}$ [15,29], and have to be ascribed to more acidic Brønsted-like sites.

With Me-Imo-500 and Me-Imo- NH_3^+ -30 outgassed at $500\text{ }^\circ\text{C}$, the negative band of H-bonded hydroxyls to CO is rather broad, with three main components at 3740 , 3718 and 3668 cm^{-1} . The band at 3740 cm^{-1} shifts of 95 cm^{-1} with increasing pressure and it is due to isolated silanols, while the 3718 cm^{-1} band shifts of 100 cm^{-1} and can be assigned to Al-OH groups, analogue to those found on transition Al_2O_3 [15]. Finally, the band at 3663 cm^{-1} moves of about 210 cm^{-1} and could be assigned to heterogeneous acidic sites, Si- $\text{CH}_2\text{-O-Al}$, also found in Al-rich microporous silicates [30]. As a whole, these new lamellar materials, *i.e.* Imo-500, Me-Imo-500 and Me-Imo- NH_3^+ -30 outgassed at $500\text{ }^\circ\text{C}$, present coherently similar acidic features.

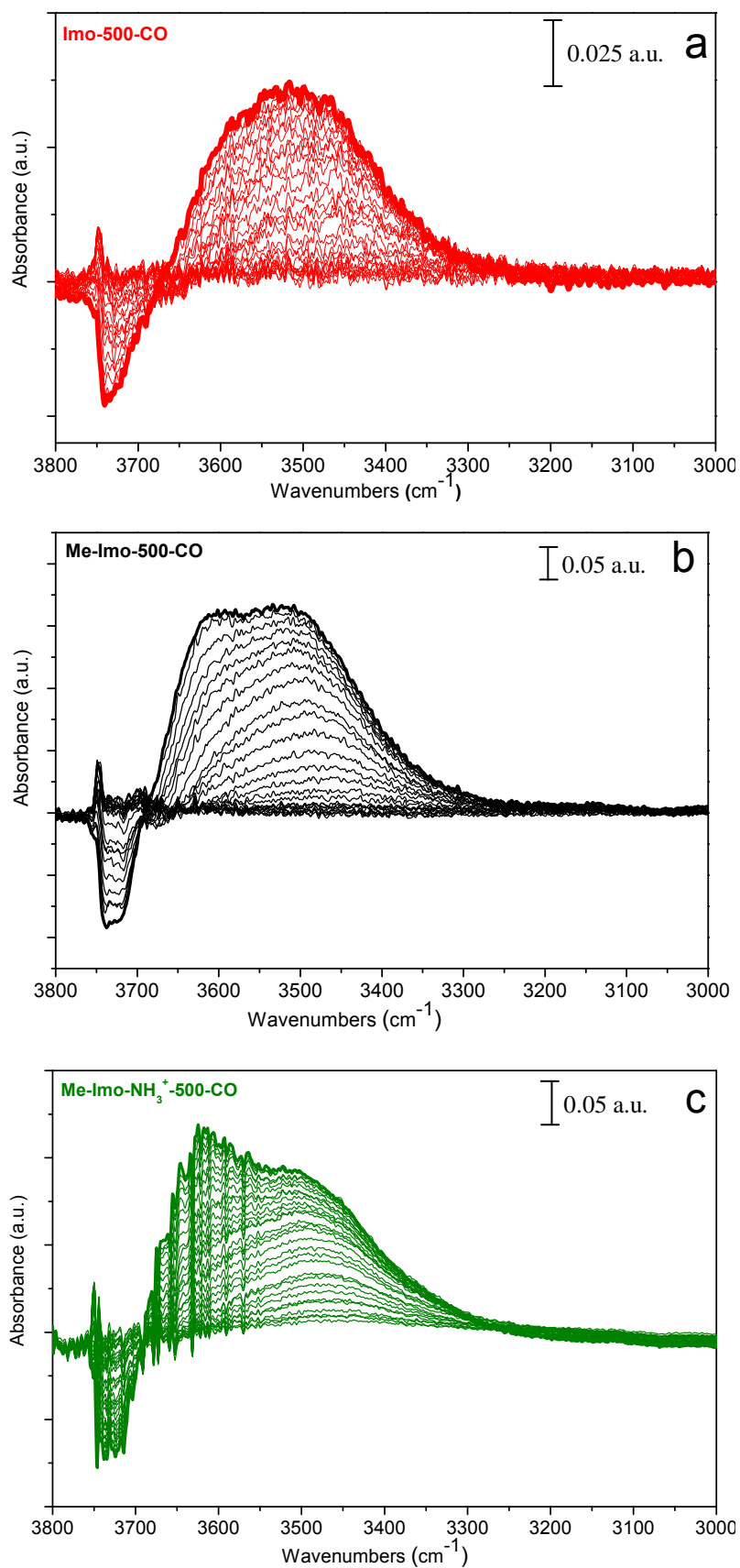


Figure 8: Difference FT-IR spectra in the 3800-3000 cm⁻¹ region obtained after dosing CO in the 0–20 mbar pressure range on (a) Imo, (b) Me-Imo and (c) Me-Imo-NH₃⁺-30 outgassed at 500 °C.

6.6. Conclusions

Interaction of gaseous ammonia and carbon monoxide at high equilibrium pressures on imogolite-like samples pre-treated at different outgassing temperature, confirmed that molecular water is completely removed from Imo and both Me-Imo/Me-Imo-NH₃⁺-30 surfaces, at 300 °C and 150 °C, respectively.

NH₃ adsorption showed, that type-B pores of Imo are too narrow to be accessible by the gas. Thus, external bridged more acidic Al(OH)Al species are detectable only in case of Me-Imo and Me-Imo-NH₃⁺-30. Particularly, the intensity of the decreased band at 3731 cm⁻¹ of aminated methyl-imogolite is *ca* one third of the correspondent Me-Imo signal, probing the successful functionalization. Moreover, CO adsorption on each imogolite-like sample indicated a weak electrostatic interaction. Particularly, with Imo pre-treated at 150 °C, CO interacts with water molecules probably at the outer surface, as the 2150 cm⁻¹ band reveals. With Me-Imo-150, the slightly shifted 2146 cm⁻¹ band indicates instead a weak perturbation of the gas. Me-Imo-NH₃⁺-30 showed both contributions. Nanotubes integrity is maintained up to 300 °C, despite amino functionalities are lost. Moreover, in agreement with MAS NMR results, aluminum environment has changed, as the presence of coordinatively unsaturated Al³⁺ sites reveals, like those of transition aluminas [15,16]

Lamellar imogolite phase is obtained at 500 °C. Both NH₃ and CO interaction confirmed that with Imo, more acidic silanols are formed, coherently with the lamellar structure proposed by MacKenzie [31]. On the contrary, with lamellar Me-Imo and Me-Imo-NH₃⁺-30, physisorbed CO as well as heterogeneous acidic sites are found, analogously to Al-rich microporous silicates [30].

6.7. References

- [1] W. Suétaka, J.T. Yates, "Surface Infrared and Raman Spectroscopy, methods and applications", Kluwer (1995) Dordrecht.
- [2] T.E. Maday, J.T. Yates, "Vibrational spectroscopy of molecules on surfaces" Kluwer (1987) Dordrecht.
- [3] H. Knözinger, S. Huber, *J. Chem. Soc. Faraday Trans.* 94 (1998) 2047.
- [4] R.M.A. Roque-Malherbe, "Adsorption and diffusion in nanoporous materials" Taylor & Francis Group (2008) CRC Press.
- [5] L. Kustov, *Top. Catal.* 4 (1997) 131.
- [6] K.I. Hadjiivanov, G.N. Vayssilov, *Adv. Catal.* 47 (2002) 307.
- [7] G. Busca, *Phys. Chem. Chem. Phys.* 1 (1999) 723.
- [8] A. Zecchina, C. Lamberti, S. Bordiga, *Catal. Today* 41 (1998) 169.
- [9] B. Hunger, H. Miessner, M. Szombathley, E. Geidel, *J. Chem. Soc. Faraday Trans.* 92 (1996) 499.
- [10] J.A. Lercher, C. Gründling, G. Eder-Mirth, *Catal. Today* 27 (1996) 353.
- [11] M. Muscas, V. Solinas, S. Gontier, A. Tuel, A. Auroux, *Stud. Surf. Sci. Catal.* 94 (1995) 101.
- [12] A. Zecchina, L. Marchese, S. Bordiga, C. Pazè, E. Gianotti, *J. Phys. Chem. B* 101 (1997) 10128.
- [13] B. Bonelli, M. Armandi, C.O. Areán, E. Garrone, *Chem. Phys. Chem.* 11 (2010) 3255.
- [14] E. Garrone, P. Ugliengo, *Langmuir* 7 (1991) 1409.
- [15] C. Morterra, G. Magnacca, *Cat. Today* 27 (1996) 497.
- [16] J. Shen, R.D. Cortright, Y. Chen, J.A. Dumesic, *J. Phys. Chem.* 98 (1994) 8067.
- [17] B. Bonelli, I. Bottero, N. Ballarini, S. Passeri, F. Cavani, E. Garrone, *J. Cat.* 264 (2009) 15.
- [18] B. Bonelli, B. Onida, J.D. Chen, A. Galarneau, F. Di Renzo, F. Fajula, E. Garrone, *Micr. Mes. Mater.* 67 (2004) 95.
- [19] R.P. Eischens, W.A. Pliskin, S.A. Francis, *J. Chem. Phys.* 22 (1954) 194.
- [20] J.C. Lavalley, *Trends Phys. Chem.* 2 (1991) 305.
- [21] J.C. Lavalley, *Cat. Today* 27 (1996) 377.
- [22] M.A. Wilson, G.S.H. Lee, R.C. Taylor, *Clays Clay Min.* 50(3) (2002) 348.
- [23] I. Bottero, B. Bonelli, S. Ashbrook, P. Wright, W. Zhou, M. Tagliabue, M. Armandi, E. Garrone, *Phys. Chem. Chem. Phys.* 13 (2011) 744.
- [24] W.C. Ackerman, D.M. Smith, J.C. Huling, Y.W. Kim, J.K. Bailey, C.J. Brinkertps, *Langmuir* 9 (1993) 1051.
- [25] J. Dakta, K. Gorà-Marek, *Cat. Today* 114 (2006) 205.
- [26] M.A. Wilson, K. Wada, S.I. Wada, Y. Kakuto, *Clay Miner.* 23 (1988) 175.
- [27] A. Givan, A. Loewenschuss, C.J. Nielsen, *Vib. Spectrosc.* 12 (1996) 1.
- [28] G. Ghiotti, E. Garrone, C. Morterra, F. Boccuzzi, *J. Phys. Chem.* 83 (1979) 2863.
- [29] O. Cairon, T. Chevreau, J.C. Lavalley, *J. Chem. Soc. Faraday Trans.* 94 (1998) 3039 and references therein.
- [30] W. Daniell, U. Schubert, R. Glöckler, A. Meyer, K. Noweck, H. Knözinger, *Appl. Catal. A* 196 (2000) 247.
- [31] K.J.D. MacKenzie, M.E. Bowden, I.W.M. Brown, R.H. Meinhold, *Clays and Clay Min.* 37(4) (1989) 317.

Appendix I

Characterization techniques

XPS (*X-ray Photoelectron Spectroscopy*) spectra were recorded on an PHI 5000 Versa Probe equipment using a band-pass energy of 187.85 eV, a 45° take off angle and a X-ray spot size diameter of 100.0 μm.

XRD (*X-ray Diffraction*) patterns of powder samples were obtained on a X'Pert Phillips diffractometer using Cu Kα radiation in the 2.5 – 30° 2θ range (step width = 0.02°).

Field Emission Scanning Electron Microscopy (**FE-SEM**) pictures were collected with a high resolution SEM instrument (LEO 1525) equipped with a Gemini field emission column; **HR-TEM**, *High Resolution Transmission Electron Microscopy*, were recorded with a Jeol JEM 2010 electron microscope operating at an accelerating voltage of 200 kV.

BET (*Brunauer-Emmet-Teller*) *Specific Surface Area* (**SSA**) and *Pore Size Distributions* (**PSD**) were measured by means of N₂ adsorption/desorption at 77 K on a Quantacrome Autosorb 1C instrument. The Non-Local-Density Functional Theory (NL-DFT) method was used to evaluate pores size distribution by applying a N₂-silica kernel.

Thermal stability of the samples was studied by *Thermogravimetric Analysis* (**TGA**) and *Mass Spectrometry* (**MS**) in flowing Ar using a SDT 2960 DTA/TGA-MS machine.

FTIR, *Fourier Transform Infrared*, spectra were collected on a Bruker Equinox 55 spectrophotometer equipped with MCT cryodetector: self-supporting wafers were studied under a residual pressure < 10⁻³ mbar.

All solid-state **MAS NMR** (*Magic Angle Spinning Nuclear Magnetic Resonance*) spectra were recorded on a Bruker Avance-400 (9.4T) spectrometer using 4 mm-OD zirconia rotors and a spinning frequency of 12 kHz. $\{^1\text{H}\}$ - ^{13}C cross-polarization (CP) MAS experiments were performed using a contact time of 2 ms and a recycle time of 1 s. Single pulse excitation (30° flip angle) and 30 s recycling delay was used for ^{29}Si MAS NMR experiments. A two-pulse echo sequence with 1 s recycling delay was used for ^1H MAS NMR measurements. The delay between the two pulses was set in order to suppress the broad signal due to water or strongly dipolar coupled hydroxyls. Tetramethylsilane (TMS) was used as chemical shift reference for ^1H , ^{13}C and ^{29}Si nuclei. ^{27}Al MAS NMR measurements were performed using a selective pulse ($\pi/12$ flip angle) and 1 s recycling delay. A 0.1 M $\text{Al}(\text{NO}_3)_3$ solution was used as chemical shift reference for the ^{27}Al . 2D Heteronuclear Correlation spectra (HETCOR) between protons and carbons was recorded using the cross-polarization condition above mentioned. As the experiment was rotor synchronized, the spectra window in the proton dimension is exactly equal to the spinning frequency (12 kHz).

Particularly, the basics of MAS NMR theory along with the description of the sequences that have been run will be briefly discussed in Appendix II.

Appendix II

MAS NMR sequences

A.II.1. Introduction

NMR (Nuclear Magnetic Resonance) is a useful technique for identifying and analyzing the structure of liquid molecules and solid powders. Particularly, I had the opportunity to test imogolite samples with a solid-state NMR instrument. Details of the applied sequences will be described further on in this appendix.

NMR technique is based on the interaction between nuclei of non-zero spin quantum number placed in a magnetic field, B_0 . Each nucleus is characterized by the spin angular momentum, P , which is discrete and can assume the following values

$$P = \sqrt{I(I + 1)} \cdot \hbar \quad (\text{Eq. 1})$$

where I is the nucleus spin and \hbar is correlated to the Planck's constant, h ($\hbar = h/2\pi$). Spin angular momentum is directly related to the magnetic moment of the nucleus, μ , according to Eq. 2,

$$\mu = \gamma \cdot P = \gamma \cdot \sqrt{I(I + 1)} \cdot \hbar \quad (\text{Eq. 2})$$

where γ is the gyromagnetic ratio, proper of each nucleus. As the case of spin angular momentum, the magnetic moment cannot assume any values but it is quantized. Particularly, in classical mechanics the quantization of μ is represented by the Larmor precession around the axis, ω_0 , to which the magnetic field is oriented (z-axis, Figure 1). Moreover, the frequency of the precession depends on the intensity of the magnetic field and on the intrinsic properties of nuclei, which are summed in the gyromagnetic parameter,

$$\omega_0 = \left| \frac{\gamma}{2\pi} \right| B_0 \quad (\text{Eq. 3})$$

Magnetic momentum quantization concerns only the z-component (parallel to the direction of B_0), while the orientations along the x-axis and y-axis are random, due to the Larmor precession. The vectorial sum of μ_z defines the macroscopic magnetization, M_0 .

$$\sum_i^N \mu_z = M_0 \quad (\text{Eq. 4a})$$

$$\sum_i^N \mu_x = \sum_i^N \mu_y = 0 \quad (\text{Eq. 4b})$$

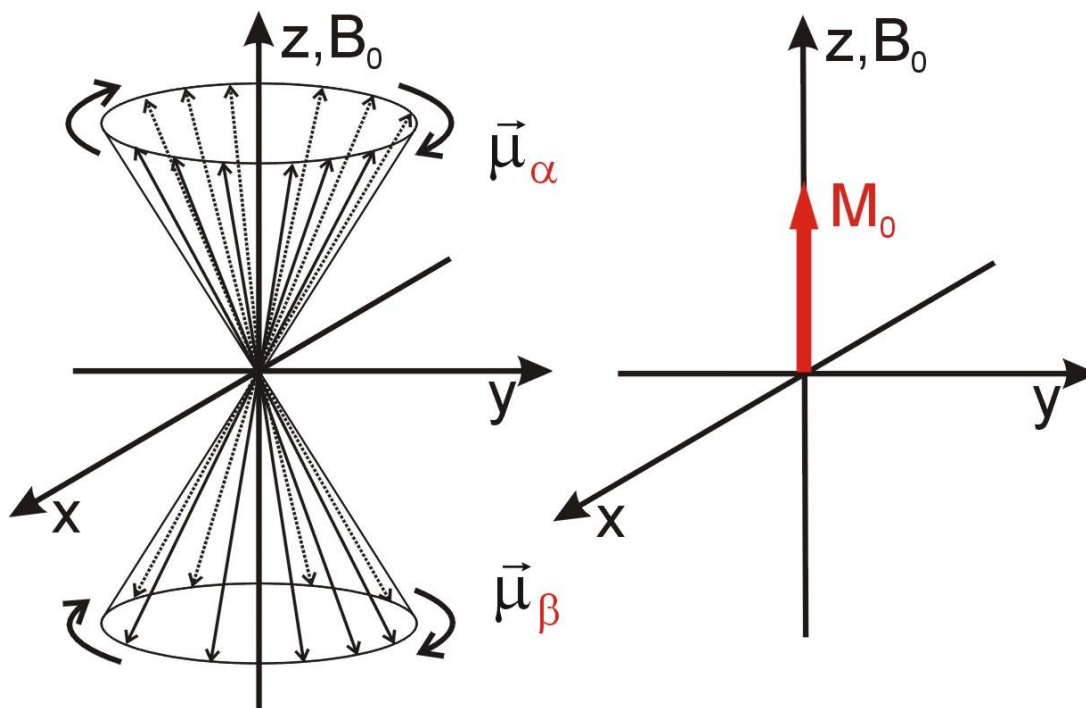


Figure 1: Schematic representation of the net macroscopic magnetization, M_0 [1].

As for other kinds of spectroscopy, in NMR it is necessary to perturb the equilibrium states of the energy levels so recording the response, which is called Free Induction Decay (FID), by detecting the time evolution of the magnetization in the XY-plane. In pulsed NMR, a Radio Frequency (RF) field is applied for a very short time.

In contrast with solution NMR technique, the nuclear spin interactions (chemical shielding, dipole-dipole coupling and quadrupole coupling) are all dependent on the crystallite orientation and affect solid-state spectra, which are also said to be *anisotropic*. As a consequence, they show broad lines, or *powder patterns*, as all the different molecular orientations present in the sample give rise to different spectral frequencies. Additionally, dipolar coupling of abundant nuclei, e.g. ^1H , leads to considerable lines broadening and poor resolution. Hence, in solid state NMR is mandatory to apply techniques to achieve high resolution spectra.

Among these, MAS, Magic Angle Spinning and Cross-Polarization (CP) techniques, are the ones that are routinely used, as in case of my experiments. NMR properties of the nuclei present in imogolite samples are reported in Table 1.

Table 1: NMR properties of imogolite nuclei.

Nucleus	Spin ^a	Natural Abundance (%)	Gyromagnetic ratio ^b ($\gamma/10^6$ rad/sT)	Quadrupole moment ($10^{28}Q$)/m ²	Frequency at 9.4T ($\omega_0/2\pi$)/MHz
¹ H	1/2	99.99	267.522		400.000
¹³ C	1/2	1.1	67.283		100.58
¹⁷ O	5/2	0.04	-36.281	$-2.6 \cdot 10^{-2}$	54.244
²⁷ Al	5/2	100	69.763	0.15	104.308
²⁹ Si	1/2	4.7	-53.190		79.468
¹⁴ N	1	99.6	19.338	$1 \cdot 10^{-2}$	28.912
¹⁵ N	1/2	0.37	-27.126		40.544

^a Ground state spin.

^b The gyromagnetic ratio, γ , is a constant characteristic of each nucleus. It is defined as the ratio of the magnetic moment, μ , to the spin angular momentum, P .

A.II.2. Magic Angle Spinning (MAS)

MAS technique is of paramount importance to remove the effects of chemical shift anisotropy and to assist the removal of heteronuclear dipolar coupling effects. It is also useful to narrow lines from quadrupolar nuclei (*e.g.* ²⁷Al and ²⁹Si). In solution NMR spectra, effects so far described are rarely observed. In fact, the rapid isotropic tumbling of molecules in solution averages the molecular orientation dependence of the transition frequencies. Magic-angle spinning achieves the same result for solids.

Figure 2 shows the MAS experiment. Molecular orientation dependence of the nuclear spin interaction is defined by the following value, $\alpha = 3\cos^2\theta - 1$, where θ is the angle that describes the orientation of the shielding tensor, i.e. the spin interaction tensor. If the sample is spin about an axis inclined at the *magic angle*, 54.74°, i.e. the angular value able to null α ($\cos^2\theta = 1/3$), it is possible to remove the effects of chemical shielding anisotropy and heteronuclear dipolar coupling.

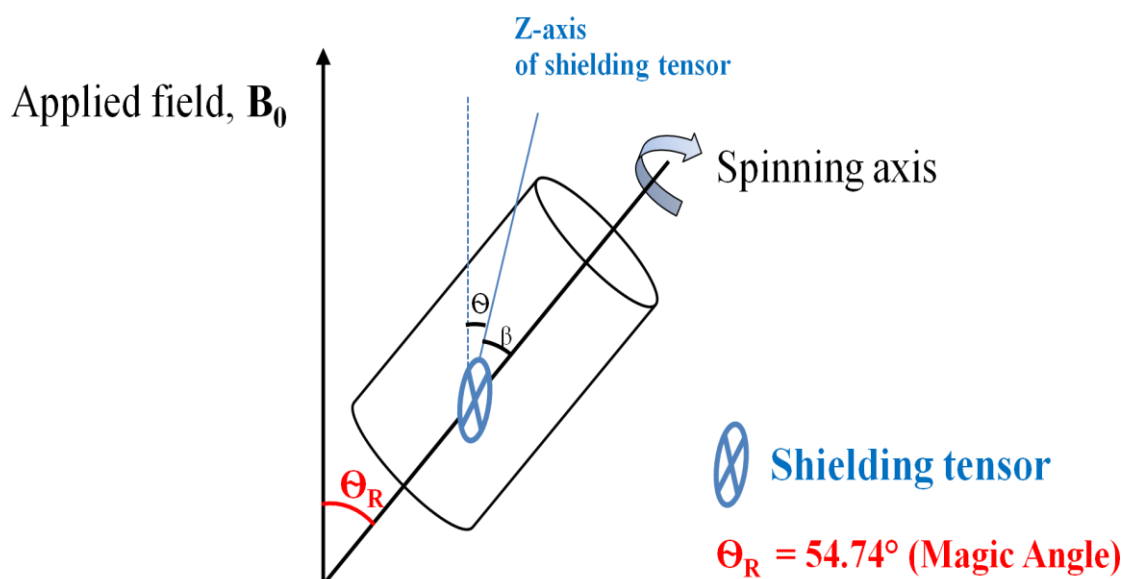


Figure 2: Magic Angle Spinning experiment.

The sample is spun rapidly in a 7 mm rotor about a spinning axis oriented at the magic angle, $\Theta_R = 54.74^\circ$, with respect to the applied magnetic field, B_0 . Magic angle value is calculated by nulling the molecular orientation dependence of the nuclear spin interaction, α , equal to $3\cos^2\theta - 1$. This rotation removes the effects of chemical shielding anisotropy and heteronuclear dipolar coupling. The chemical shielding tensor is fixed in the molecule to which it applies and so rotates with the sample. Θ is the angle between the applied field and the principal z-axis of the shielding tensor, while β is the angle between the z-axis of the shielding tensor and the spinning axis. The latter angle is fixed for a given nucleus.

The average of α , under certain circumstances, can be shown to be dependent on the overall orientations as follows,

$$\alpha = 3\cos^2\theta - 1 = \frac{1}{2}(3\cos^2\theta_R - 1)(3\cos^2\beta - 1) \quad (\text{Eq. 5})$$

Electrons that surround a nucleus are not impassive in the magnetic field used in the NMR experiment, but react to produce a secondary field. This secondary field contributes to the total field felt by the nucleus, and therefore it has the power to change the resonance frequency of the nucleus. This interaction of the secondary field produced by the electrons with the nucleus is called the *shielding interaction*.

The total spectral frequency, ω , in absolute units is the sum of the Larmor frequency, ω_0 , and the chemical shift contribution, ω_{cs} ,

$$\omega = \omega_0 + \omega_{cs} \quad (\text{Eq. 6})$$

Actually, when performing NMR experiments, absolute frequencies are not measured, while a reference substance is used and relative *chemical shifts* with respect to that substance (or offset frequencies) are measured. The chemical shift, δ , is defined as follows

$$\delta = \frac{\nu - \nu_{Ref}}{\nu_{Ref}} \quad (\text{Eq. 7})$$

It can be expressed in Hz or in ppm (part-per-million). TMS (tetramethylsilane) was used as reference for ^1H , ^{29}Si and ^{13}C nuclei; aluminum nitrate for ^{27}Al .

In order for the magic angle spinning to reduce powder pattern broadening, the rate of the sample spinning must be fast at least three or four times greater than the anisotropy of the interaction being spun out. Slow spinning produces a set of *spinning sidebands*, whose intensity may be enhanced in solid-state spectra of hydrated powders. This type of signal can be very useful to determine details of the anisotropy and asymmetries of nuclear spin interactions being averaged by the magic angle spinning.

Therefore, it is clearly evident the importance to set the magic angle accurately before running any experiment, since it is known that a mis-setting can lead to a noticeable line broadening and poor resolution [2].

A.II.3. Cross Polarization (CP) technique

Cross Polarization (CP) sequence was first reported by Pines *et al.* in 1973 [3]. It is usually used to assist in observing dilute spins, *e.g.* ^{13}C . Drawbacks of observing dilute spins include

1. Poor signal-to-noise ratio due to the low abundance of these nuclei.
2. The relaxation times of low abundance nuclei tend to be very long because the strong homonuclear dipolar interactions, which can stimulate relaxations, are almost absent.

Both problems can be overcome with the CP sequence (Figure 3): the dilute nucleus X derives its magnetization from a nearby network of abundant spins, *e.g.* ^1H (Figure 3). Particularly, in my CP-MAS NMR experiments, X nuclei considered were ^{13}C and quadrupolar ^{29}Si .

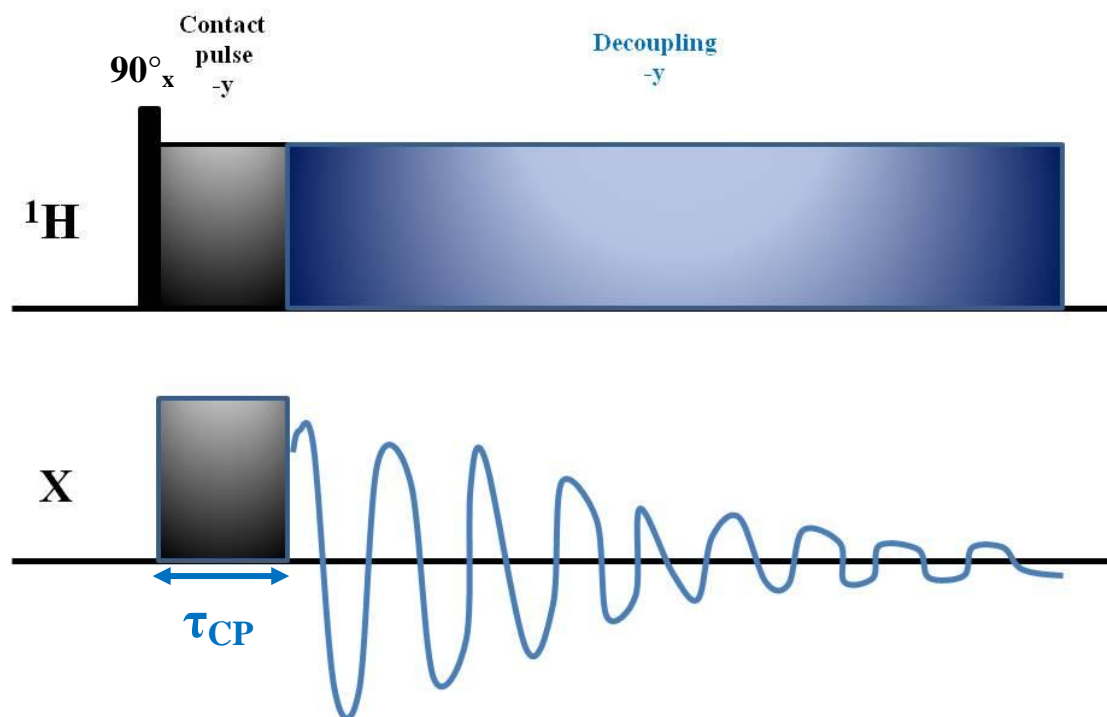


Figure 3: The CP (Cross Polarization) pulse sequence. The effect of the sequence is to transfer magnetization from the abundant ^1H spins to the X spin via the agency of the dipolar coupling between ^1H and X spins.

An initial ^1H 90°_x pulse creates the ^1H magnetization along $-y$ in the ^1H rotating frame. An on-resonance $-y$ ^1H contact pulse is then applied (Figure 4). The field due to this pulse is known as the *spin-lock field*, $B_1(^1\text{H})$. X spins are now considered during the simultaneous X contact pulse (with concomitant spin-lock field $B_1(X)$) rotating at the X radiofrequency pulse. Amplitudes of the two contact pulses in the cross-polarization experiment have to be carefully set so as to achieve the **Hartmann-Hahn (HH) matching condition**

$$\gamma_H B_1(^1\text{H}) = \gamma_X B_1(X) \quad (\text{Eq. 8})$$

$$\omega_{1,H} = \gamma_H B_1(^1\text{H}) \quad (\text{Eq. 8a})$$

$$\omega_{1,X} = \gamma_X B_1(X) \quad (\text{Eq. 8b})$$

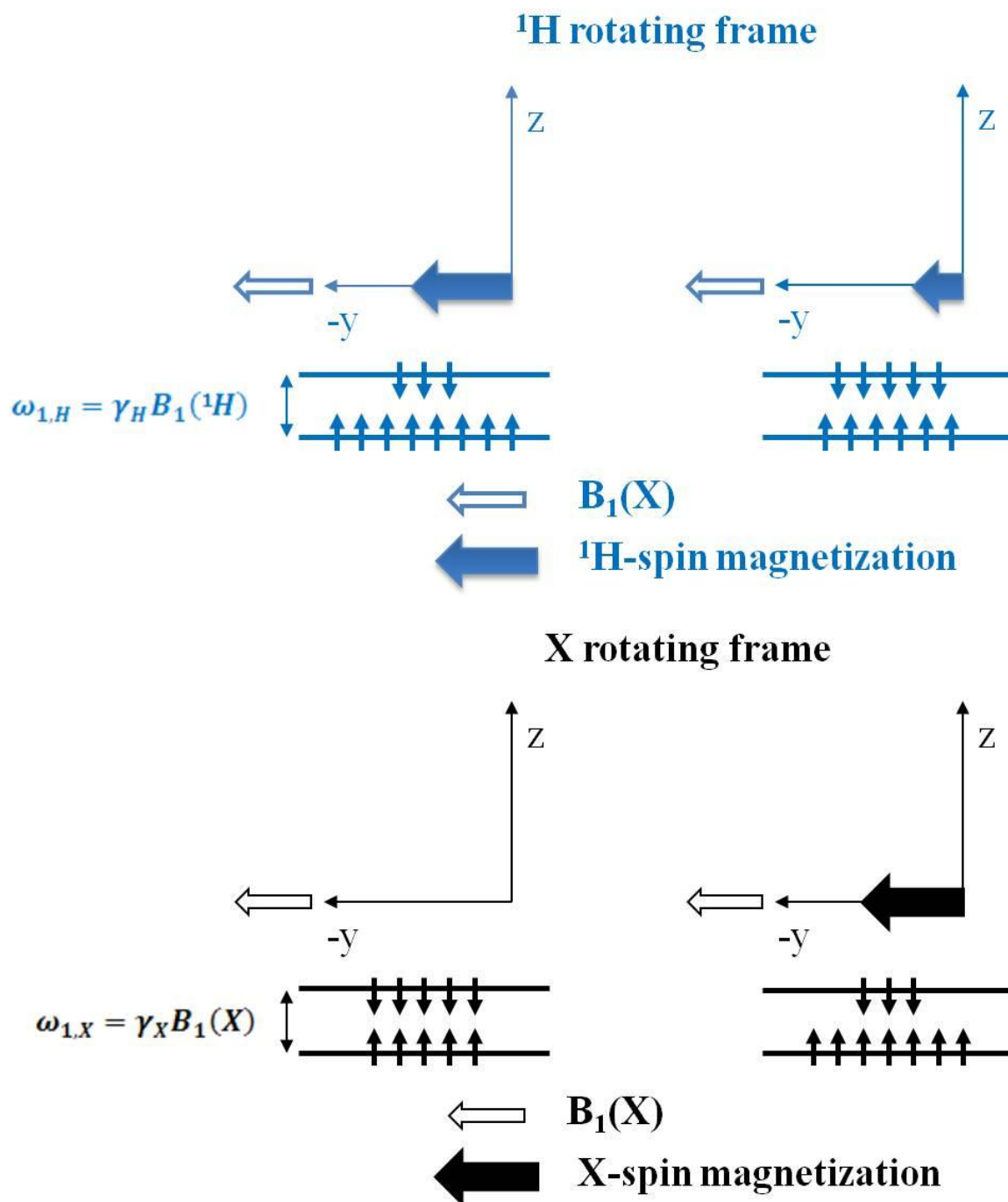


Figure 4: Schematization of the cross-polarization experiment.

^1H magnetization is transferred to the X spins via the dipolar coupling between ^1H and X during a contact pulse applied simultaneously to both spin types after an initial 90° pulse to the abundant ^1H spins. A doubly rotating frame of reference is considered such that the pulses applied to both spins appear stationary along $-y$. The α^* and β^* states are the spin states in their respective rotating frames in the absence of any other interactions. When the Hartmann–Hahn condition is met, the energy gaps between the rotating frames ^1H and X spin states are the same.

according to which the energy gaps between the respective rotating frame spin states of ^1H and X have to be equal. This is true for spin-1/2 nuclei.

In case of quadrupolar nuclei S , the HH condition is replaced by the more general condition that $\omega_{1,\text{H}}$ should be equal to ω_{nut} , the nutation frequency of the quadrupolar nucleus transition that is being polarized. The nutation behavior of a quadrupolar spin depends on the relative magnitudes of the quadrupolar splitting, ω_Q , and $\omega_{1,\text{S}}$. There are two limiting cases

1. $\omega_Q \ll \omega_{1,\text{S}}$, the nutation frequency is not affected by the quadrupolar coupling, so that ω_{nut} is equal to $\omega_{1,\text{S}}$, as for any uncoupled spin system.
2. $\omega_Q \gg \omega_{1,\text{S}}$, only the transition on resonance is irradiated.

A.II.4. Multiple-Quantum MAS (MQMAS) technique

The bidimensional MQMAS was first proposed in the literature in 1995 [4] with the aim of achieving high resolved spectra for half-integer quadrupolar nuclei. The pulse sequence that explains the basics of two-dimensional (or in general multidimensional) NMR experiments is shown in Figure 5.

An initial sequence of rf pulses creates a non-equilibrium spin state. In the following period t_1 , the desired *coherence* of order n , selected by *phase cycling*, is allowed to evolve. In quantum mechanics it is said that there is “*a coherence between two basic functions ϕ_i and ϕ_j in the superposition state, Ψ , which describes the spin system, if the off-diagonal elements of the density matrix representing the sample are not null*”.

The *density matrix* or *density operator* is useful to describe a general spin system, whose state cannot be known. The probability p_ψ of it being in a particular state, ψ , is the only information that can be achieved. This is why each spin system is defined by a superposition state ψ ,

$$\Psi = \sum_{\psi} \sqrt{p_{\psi}} \psi = \sum_{\psi} \sqrt{p_{\psi}} \sum_i c_{\psi i} \phi_i \quad (\text{Eq. 9})$$

depending on p_{ψ} and the product $c_{\psi i} \phi_i$, which represents the linear combination of the basic set of the spin system.

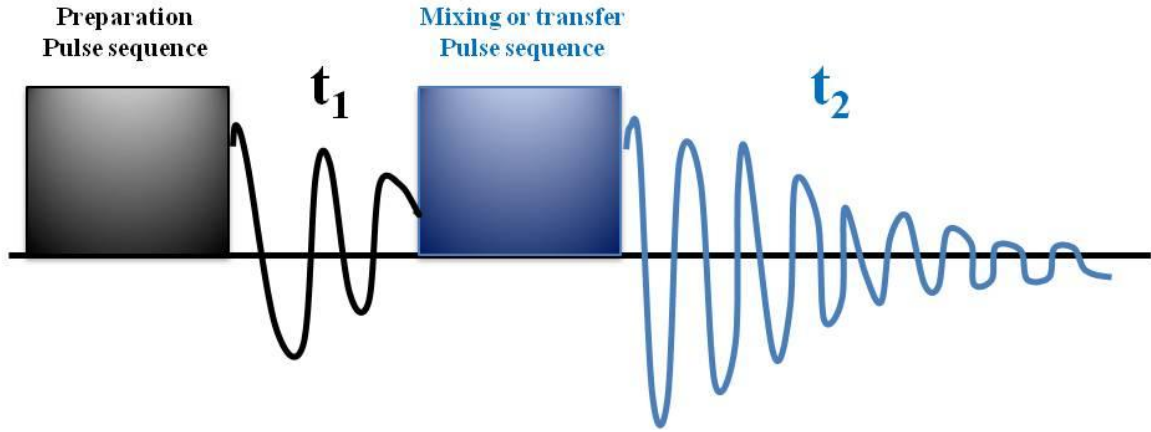


Figure 5: The general form of a two-dimensional NMR pulse sequence.

Finally, the density operator, $\hat{\rho}$ (Eq.10), as well as its diagonal (Eq. 10a) and off-diagonal elements (Eq. 10b), respectively, are the following

$$\hat{\rho} = \langle \Psi | \hat{\rho} | \Psi \rangle = \sum_{\psi} p_{\psi} |\psi\rangle \langle \psi| \quad (\text{Eq. 10})$$

$$\rho_{ii} = \sum_{\psi} p_{\psi} c_{\psi i}^* c_{\psi i} = \overline{c_{\psi i}^* c_{\psi i}} \quad (\text{Eq. 10a})$$

$$\rho_{ij} = \sum_{\psi} p_{\psi} c_{\psi i}^* c_{\psi j} = \overline{c_{\psi i}^* c_{\psi j}} \quad (\text{Eq. 10b})$$

The main rule that needs to be followed in phase cycling is the following: “If the phase of a pulse is changed by ϕ , a coherence undergoing a change in coherence level of Δp acquires a phase shift of $-\Delta p \cdot \phi$ ” [2].

Once the phase cycling is completed, the transfer (or mixing) pulse sequence at the end of t_1 transforms the selected n-order coherence into observable -1 coherence to be observed during t_2 . The signal in t_2 has either its amplitude or phase (or both) modulated, according to the evolution in t_1 . As a consequence, by repeating the experiment for several and successive values of t_1 , a two-dimensional time-domain dataset is obtained. It contains information on the evolution of the -1-order coherence in the t_2 dimension and information on the evolution of the n-order coherence in the t_1 dimension, respectively. Moreover, it can be transformed to the frequency domain by Fourier transformation to produce a 2D frequency spectrum, in which the F1 dimension contains the characteristic evolution frequencies of the n-order coherences in t_1 , while the F2 dimension contains those of the -1-order coherences, present in t_2 .

A.II.5. Simulated ^1H and ^{13}C NMR spectra of 3-APS

Simulated (ACD software, [5]) ^1H and ^{13}C NMR spectra of 3-APS with terminal amino group unprotonated and protonated, are reported in Figures 6a, 6b, 7a and 7b, respectively.

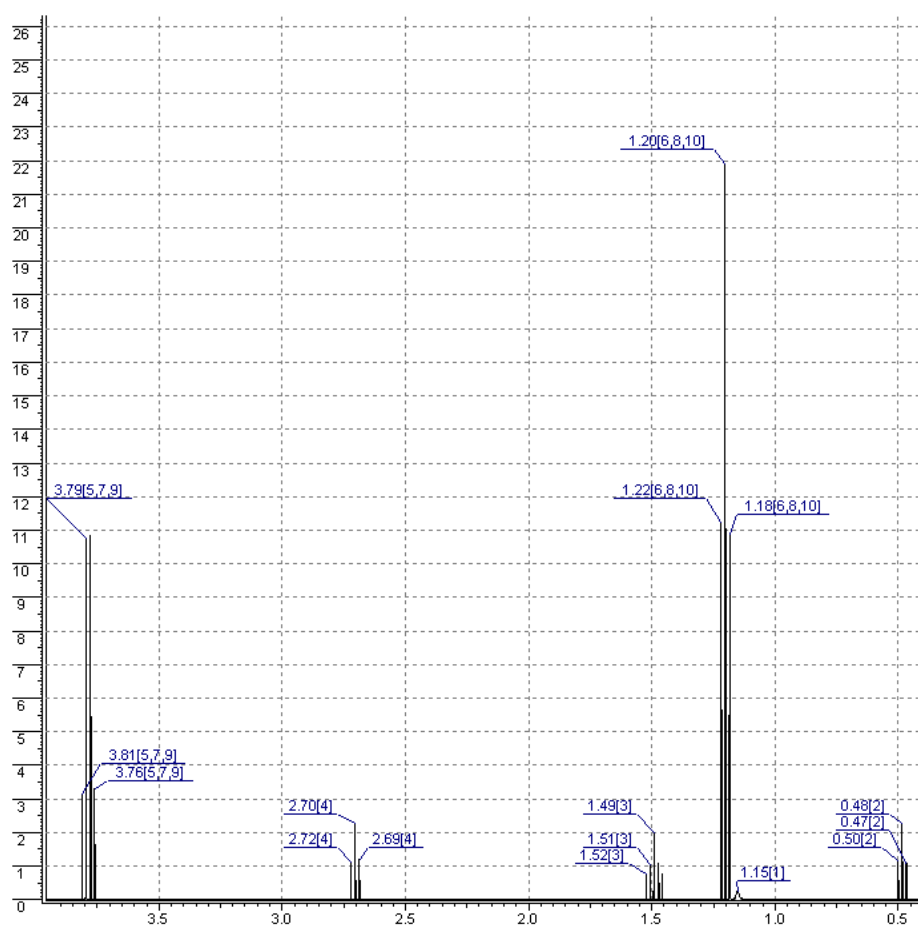
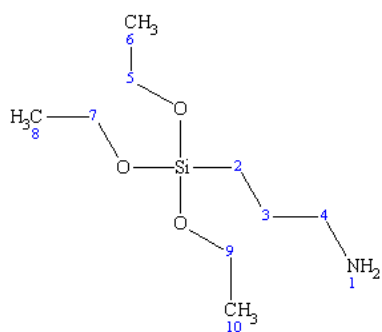


Figure 6a: ^1H NMR spectra of 3-APS with terminal amino group unprotonated.

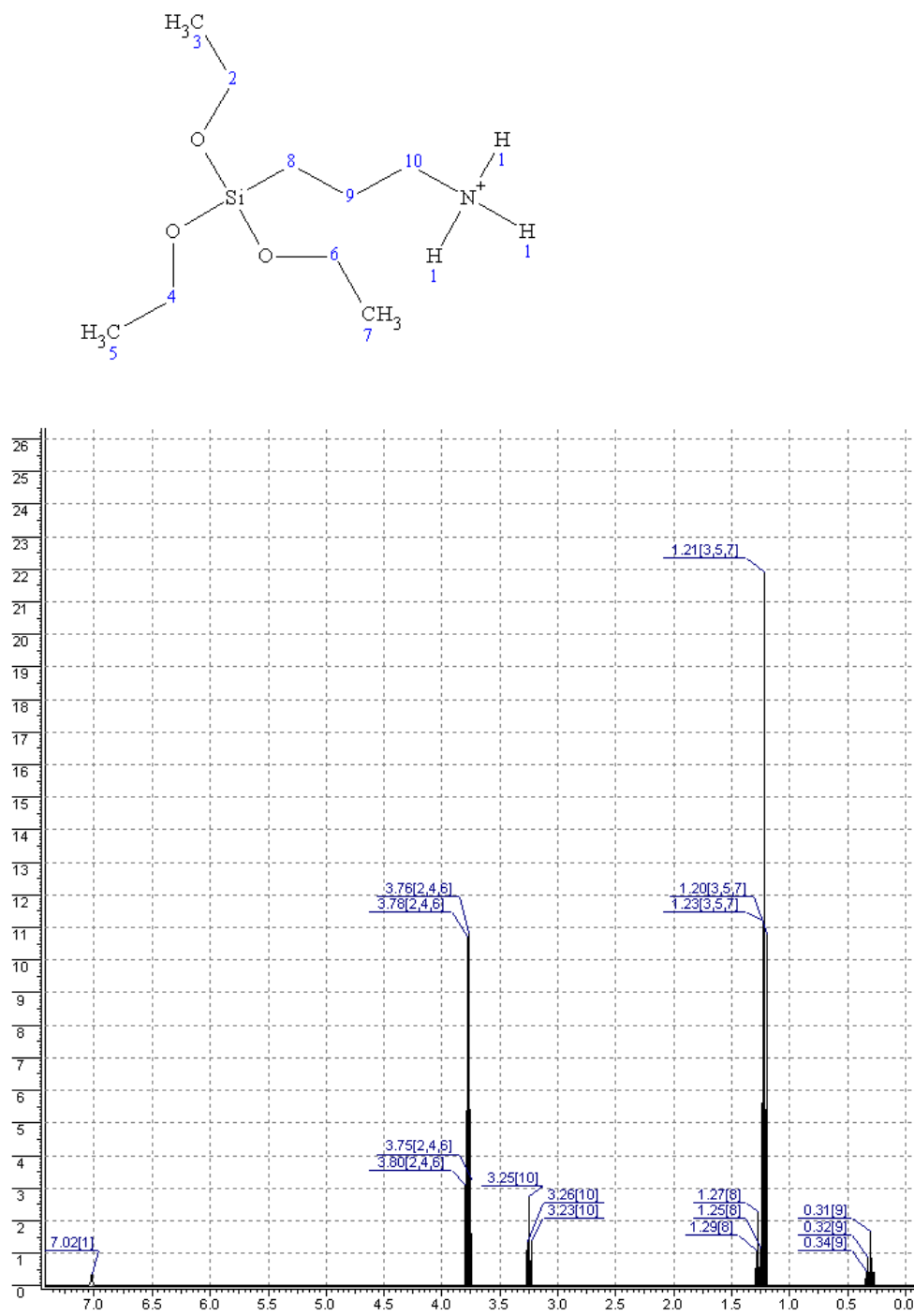


Figure 6b: ¹H NMR spectra of 3-APS with terminal amino group protonated.

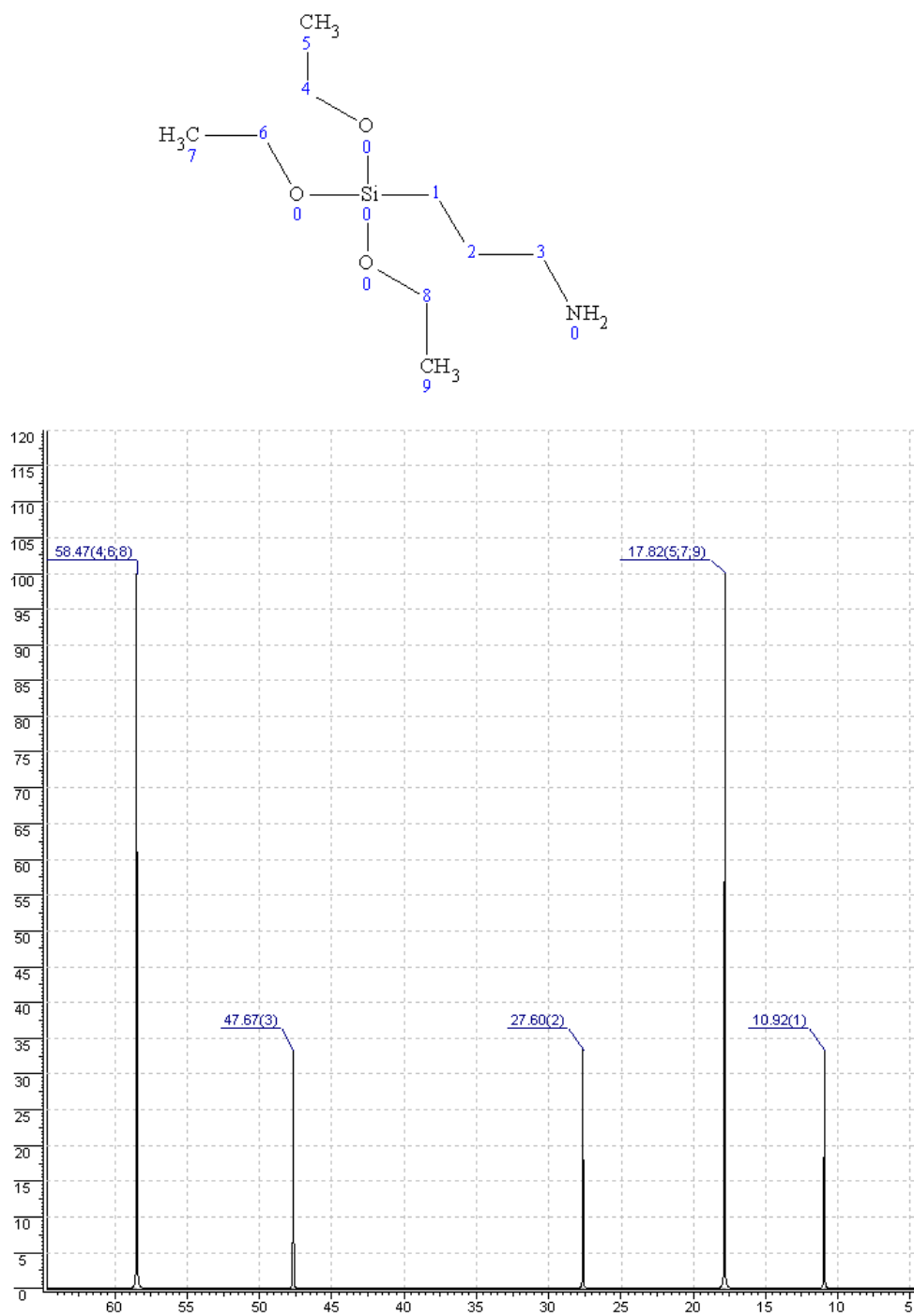


Figure 7a: ^{13}C NMR spectra of 3-APS with terminal amino group unprotonated.

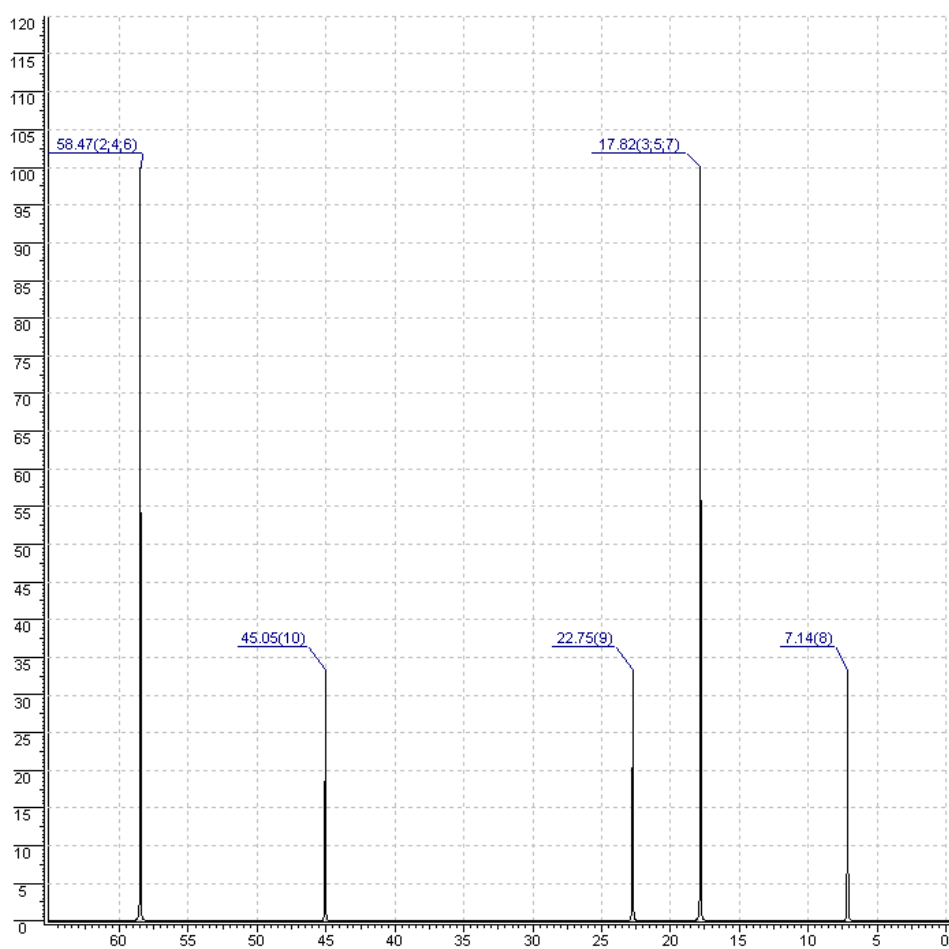
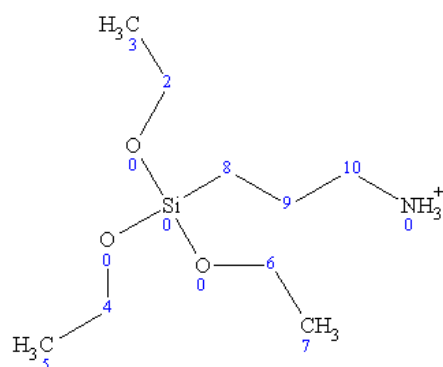


Figure 7b: ^{13}C NMR spectra of 3-APS with terminal amino group protonated.

A.II.6. References

- [1] *Notes on NMR spectroscopy*, edited by Prof. Roberto Gobetto, University of Turin (Italy).
- [2] *Introduction to solid-state NMR spectroscopy*, M.J. Duer, Blackwell Publishing L.t.d., 2004.
- [3] A. Pines, M.G. Gibby, J.S. Waugh, *J. Chem. Phys.* 59 (1973) 569.
- [4] L. Frydman, J.S. Harwood, *J. Am. Chem. Soc.* 117 (1995) 5367.
- [5] <http://www.acdlabs.com/products/adh/nmr/>

Appendix III

*Imogolite as a possible negative
control for HARNs,
High-Aspect Ratio Nanomaterials*

A.III.1. Introduction

The evaluation of inorganic carriers, scaffolds and excipients toxicology for biomedicine applications are of paramount importance. So far, clay materials which are actually used in pharmaceutical formulations, due to their a high specific area, sorptive capacity, rheological properties, chemical inertness and most of all low or null toxicity for the patient are smectites, palygorskite, kaolinite and talc [1].

The main route of exposure of High Aspect Ratio tubular Nanoparticles (HARNs), like asbestos, carbon nanotubes, is through inhalation and, to a lesser extent, ingestion. Imogolite, as well as halloysite, is also a HARN-type material. Therefore, in view of a correct conduction of toxicological studies on their pathogenicity, there is an urgent need to identify appropriate reference materials acting as positive and negative controls made up by particles of similar size and shape.

This is the reason why in collaboration with Prof. Bice Fubini (Interdepartmental Centre “G. Scansetti” and Dept. of Chemistry, University of Torino, Italy) and prof. Ovidio Bussolati (Dept. Cl. Med. Nephrology and Health Sciences & Dept. Exp. Medicine, University of Parma, Italy) a study was undertaken to assess the biological responses in vitro to imogolite in view of its use as negative control for possible applications in the biomedical field. Macrophages and airway epithelial cells were chosen as main components of the lung-blood barrier, given that inhalation is the most likely exposure route under occupational or environmental scenarios.

Usually, macrophages represent the first cell type of natural immunity encountered by foreign materials. They may react to nanomaterials eliciting several distinct activation pathways that determine the outcome of the exposure, in terms of tolerance or ability to cause either inflammatory or fibrotic alterations [2-6].

Airway epithelial cells are the first barrier that nanomaterials have to cross to reach the lung interstitial tissues and to be transported thereafter to other districts of the organism. Interestingly, both fibrous silicates [7-9] and carbon nanotubes, either single-walled (SW) or multi-walled (MW) carbon nanotubes (CNTs) [10,11], have been reported to alter the barrier properties of airway epithelial cells in vitro.

A.III.1.1. Materials and methods

The following materials were tested

1. *Imogolite nanotubes (INTs)*, which were obtained according to the method described in Chapter 1.
2. *Commercial multi walled carbon nanotubes, MWCNTs*, provided by Sigma–Aldrich (Aldrich 659258), Milan, Italy. As declared by the manufacturer, their length is 110-170 nm x 5-9 μm , the BET SSA is *ca* $22.6 \pm 0.38 \text{ m}^2/\text{g}$ and are largely made of multi-walled nanotubes (at least 90%), with residual amorphous carbon (iron < 0.1%).
3. *Commercial single walled carbon nanotubes, SWCNTs* (Aldrich 636797, 1.1 nm x 0.5–100 μm , BET 400 m^2/g). They consist of SWCNT (> 50%) and of other nanotubes (40%) with 3% amorphous carbon and traces of metals.

FE-SEM pictures are reported in Figure 1. The murine macrophage lines *RAW264.7*, provided by Istituto Zooprofilattico Sperimentale della Lombardia (Brescia, Italy), and *MH-S* [12], by prof. Dario Ghigo, Department of Biochemistry, University of Turin, were cultured in RPMI media supplemented with 10% Fetal Bovine Serum (*FBS*). Both culture media and FBS were purchased from EuroClone SpA, Pero, Milan, Italy. These two macrophage lines, derived, respectively, from peritoneal and alveolar macrophages, have been extensively used in toxicological studies [2, 13-16].

Additionally, *Calu-3 cells*, derived from a human lung adenocarcinoma [17], were also purchased from Istituto Zooprofilattico Sperimentale della Lombardia (Brescia, Italy) and then cultured in Eagle's Minimum Essential Medium (EMEM) supplemented with 1mM sodium pyruvate and 10% FBS. Calu-3 cells have been extensively used in recent studies to investigate airway epithelium permeability [18-24]. All cells were routinely cultured in 10-cm diameter dishes maintained in a humidified atmosphere of 5% CO_2 in air in the presence of streptomycin (100 $\mu\text{g}/\text{ml}$) and penicillin (100 U/ml).

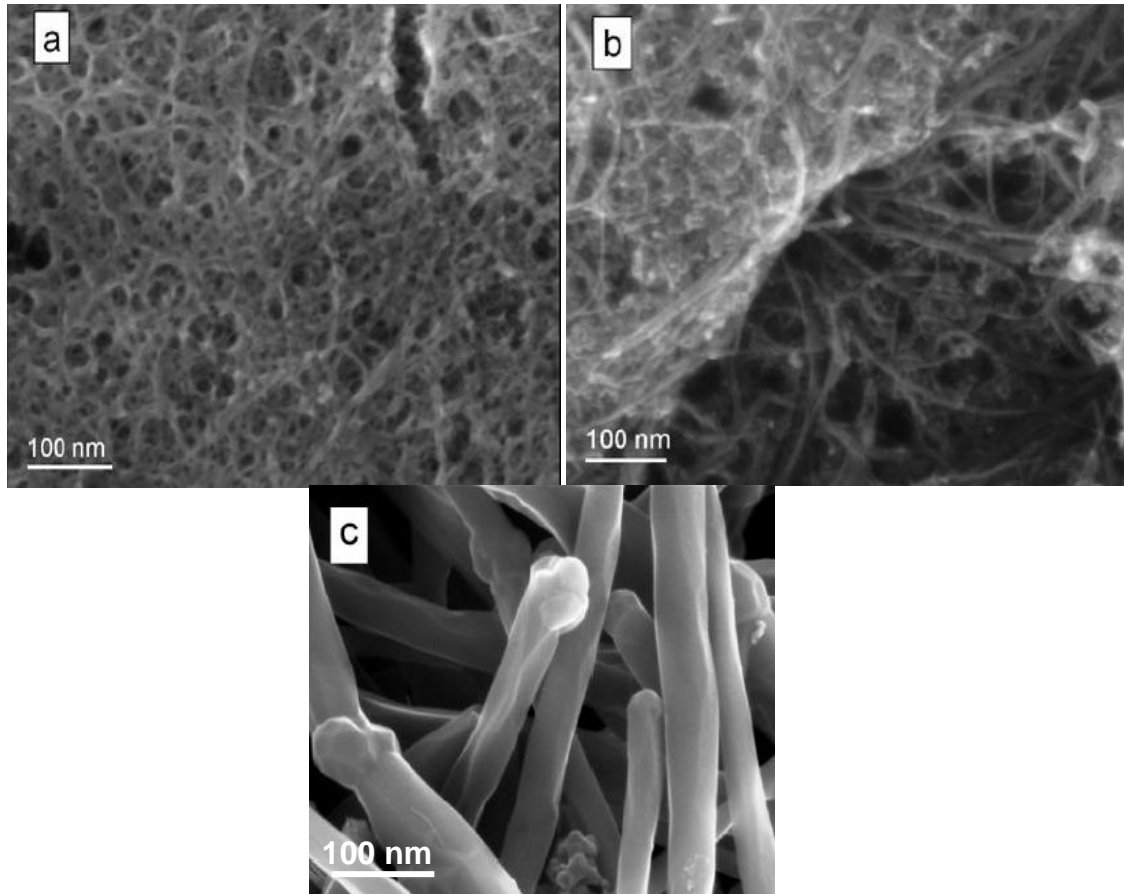


Figure 1: FE-SEM picture of (a) INT, (b) SWNTs and (c) MWNTs. Particularly, MW tubes show the presence of large, 100–200-nm and wide tubes, with respect to SWNTs.

Before the experiments, INTs, SWCNTs and MWCNTs were heated at 220 °C for 3h to eliminate possible contamination from lipopolysaccharide. After cooling at room temperature, nanomaterials were dispersed at a concentration of 1mg/ml in sterile phosphate-buffered saline (PBS) to obtain stock suspensions for a series of experiments. Immediately before each experiment, they were extensively vortexed, sonicated three times for 15 min in a Bransonic Ultrasonic ultrasound bath, and then added to normal growth medium to reach the desired concentration. No detergent was used to improve their solubility in aqueous solutions. Subsequently, we noticed that MWCNTs and INTs tend to precipitate and form more or less expanded agglomerates that come into contact with the cell monolayer. Taking into account the volume/surface ratio of the various culture systems adopted, we have expressed the nominal doses as μg of materials per cm^2 of monolayer.

Cell viability was tested with the resazurin method [25]. According to this method, viable cells reduce the non-fluorescent compound resazurin into the fluorescent

resorufin that accumulates into the medium. Cells were incubated for 1 h with fresh, serum-free medium supplemented with 44 μ M resazurin; fluorescence was then measured at 572 nm with a fluorimeter (Wallac 1420 Victor2 Multilabel Counter, Perkin Elmer). For Calu-3 monolayers grown in a double chamber culture system, resazurin was added at both sides of the monolayer and fluorescence was measured in the apical compartment [11]. Since SWCNTs produce a significant dose-dependent quenching of resorufin fluorescence (see Figure 1), data obtained in the presence of these nanomaterials were adequately corrected.

Total RNA, extracted from cultures grown in 6-well dishes with RNeasy Mini Kit® (Qiagen S.p.a. Milano, Italy), was reverse transcribed and 40 ng of cDNA amplified as described previously and then treated with the same method [26]. The forward and reverse primers (5 pmol each) used are gathered in Table 1. Quantitative PCR was performed in a 36 well Rotor Gene™ 3000, version 5.0.60 (Corbett Research, Rotor-Gene™ 3000, version 5.0.60, Mortlake, Australia). Fluorescence was monitored at the end of each extension step. A no-template, noreverse transcriptase control was included in each experiment. At the end of the amplification cycles a melting curve analysis was added. RT-PCR data are expressed as the ratio between the mRNA of interest and Gapdh mRNA.

For *TransEpithelial Electrical Resistance (TEER) measurements*, Calu-3 cells were seeded into cell culture inserts with membrane filters (pore size of 0.4 μ m) for Falcon 24-well-multitrays (Cat. N° 3095, Becton, Dickinson & Company, Franklin Lakes, NJ, USA), at a density of 75×10^3 cells/300 μ l. Measurements of TEER were made on monolayers grown for 10–14 d, using an epithelial voltohmmeter (EVOM, World Precision Instruments Inc., Sarasota, FL, USA). Materials were added in the apical chamber from a 1 mg/ml stock solution without changing the medium. TEER changes were expressed as the percentage of the initial value adjusted for control cell layers according to the following equation (Eq.1) [27].

$$\Delta_{TEER}(\%) = \frac{Final\ TEER_{treated}}{Final\ TEER_{control}} \cdot \frac{Initial\ TEER_{control}}{Initial\ TEER_{treated}} \cdot 100 \quad (Eq. 1)$$

Values of viability, TEER, and nitrite production were analyzed with ANOVA using post hoc Bonferroni test and expression data were evaluated with a t-test for unpaired data. Finally, recombinant human interleukin-4, *rIL-4*, was obtained from RELIA Thech

GmbH, Wolfenbuttel, Germany. Sigma–Aldrich (Milan, Italy) was the source of all other chemicals.

Table 1: Primers used for RT-PCR studies

Gene	Forward	Reverse
Arg1	5' CAG AAG AAT GGA AGA GTC AG 3'	5' GGA GTG TTG ATG TCA GTG TG 3'
Nos2	5' GTT CTC AGC CCA ACA ATA CAA GA 3'	5' GTG GAC GGG TCG ATG TCA C 3'
Il6	5' TAG TCC TTC CTA CCC CAA TTT CC 3'	5' TTG GTC CTT AGC CAC TCC TTC 3'
Gapdh	5' TGT TCC TAC CCC CAA TGT GT 3'	5' GGT CCT CAG TGT AGC CCA AG 3'

A.III.1.2. Results and discussion

The experiments performed led to following three main evidence,

1. Imogolite nanotubes are less toxic than carbon nanotubes on macrophages

In a preliminary experiment, the materials to be tested have been evaluated for possible interferences with the resazurin method (Figure 2). The results indicate that INTs neither exhibit autofluorescence nor quenched resorufin fluorescence. Also MWCNTs did not exhibit any interference with the method, while SWCNTs caused a significant quench of fluorescence both in the presence and in the absence of cells.

The effects of INTs and both carbon nanotubes on the viability of the murine macrophage lines RAW264.7 and MH-S are shown in Figure 3. A clear cut dose-dependent toxicity was already evident for both SWCNTs and MWCNTs after 24h of incubation, with a significant decrease in viability detected in either cell line with the minimal nominal dose used ($10 \mu\text{g}/\text{cm}^2$) and a viability loss $\geq 80\%$, detected at the maximal dose of $120 \mu\text{g}/\text{cm}^2$. On the contrary, at the same experimental time, INTs were completely ineffective up to $120 \mu\text{g}/\text{cm}^2$ on MH-S cells while a modest 15% viability decrease was detected at 80 and $120 \mu\text{g}/\text{cm}^2$ with RAW264.7 cells.

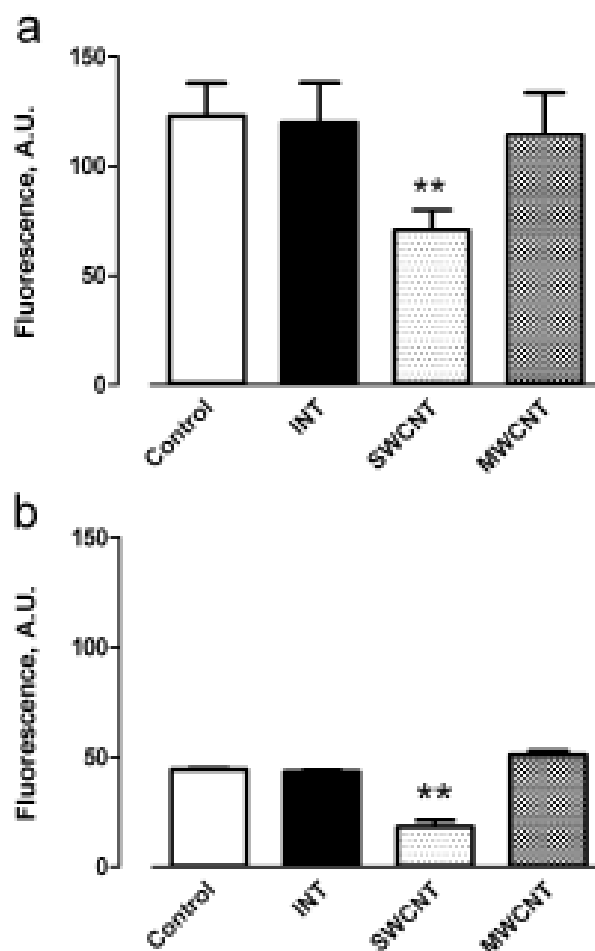


Figure 2: Validation of resazurin viability test in the presence of INTs and CNTs.
(a) RAW264.7 cells were incubated for 1 h with resazurin. Immediately before fluorescence reading, the indicated nanomaterials were added to the incubation medium; (b) Resazurin was added to 24-well dishes in the absence of cells and the incubation prolonged for 1 h at 37 °C under the conditions detailed. For both panels, the nanotubes were added at a nominal dose of 80 $\mu\text{g}/\text{cm}^2$ and five wells were used for each condition. Data are means \pm S.D. ** $p < 0.01$ vs. control (absence of nanomaterials).

At later times of treatment, INTs had more marked effects on cell viability, with a maximal decrease of 35% obtained at the maximal INT nominal dose of 120 $\mu\text{g}/\text{cm}^2$ after 72 h of treatment. Under the same conditions, the viability of the two macrophage lines was completely suppressed by either SWCNTs or MWCNTs.

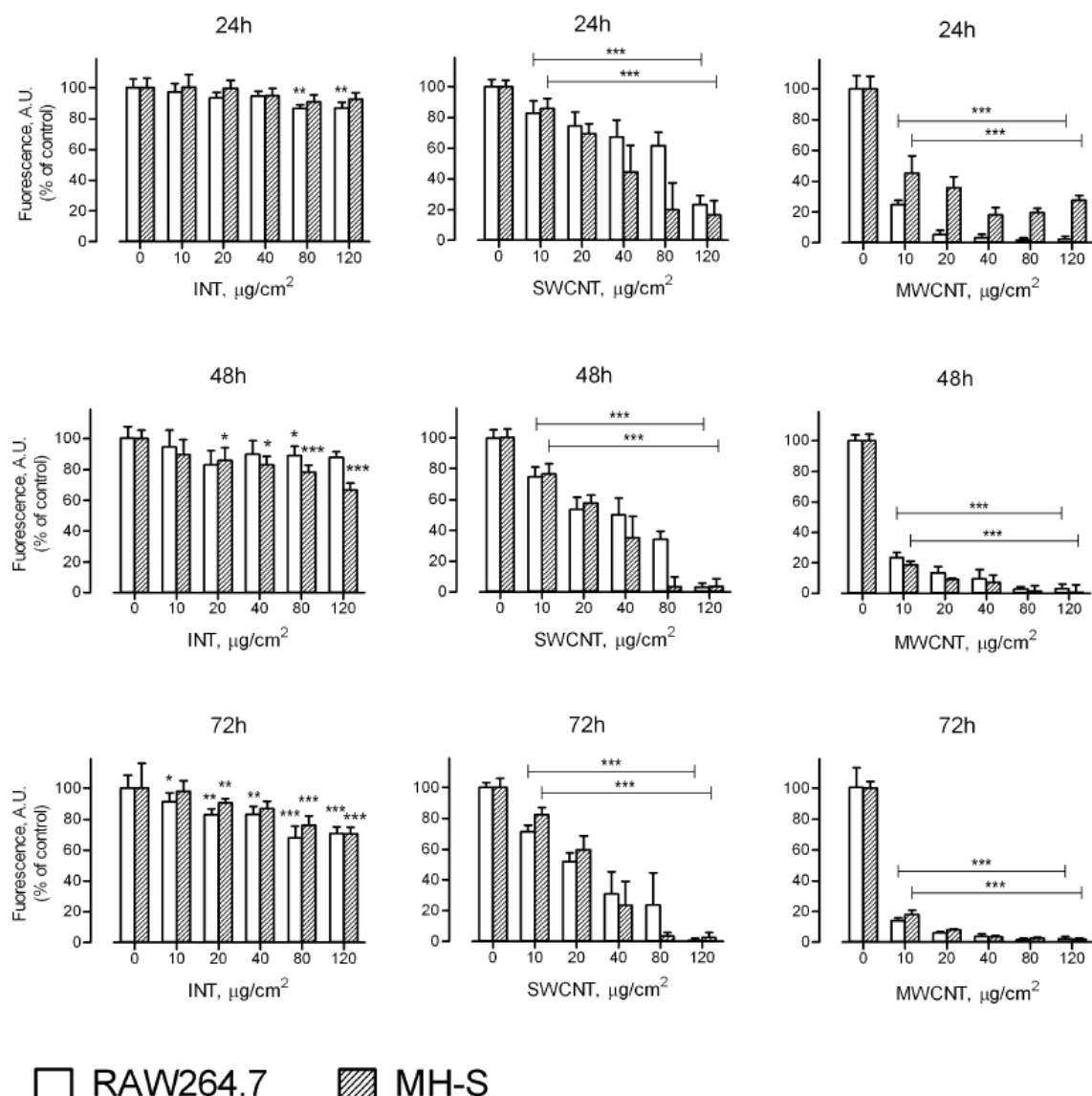


Figure 3: INT and SWCNT effects on macrophage viability. Subconfluent cultures of RAW264.7 and MH-S murine macrophages, grown on 96-well dishes, were exposed for the indicated times to nominal doses of INT, SWCNT and MWCNT ranging from 0 to 120 $\mu\text{g}/\text{cm}^2$. At the selected times, viability was assessed with the resazurin method. Data are means of 5 independent determinations with SD * $p < 0.05$, ** $p < 0.01$, *** $p < 0.001$ vs. control, untreated cultures.

2. Imogolite nanotubes do not induce markers of classical or alternative macrophage activation

In the experiments shown in Figure 4, the effects of INTs on the expression of activation markers of macrophages are reported.

In both RAW264.7 and MH-S macrophages, the gene for Arginase 1 (*Arg1*), a typical marker of alternate macrophage activation [28-31], was not induced by INTs, but readily responsive to the incubation with IL-4, used as a positive control (Figure 5a and 5d).

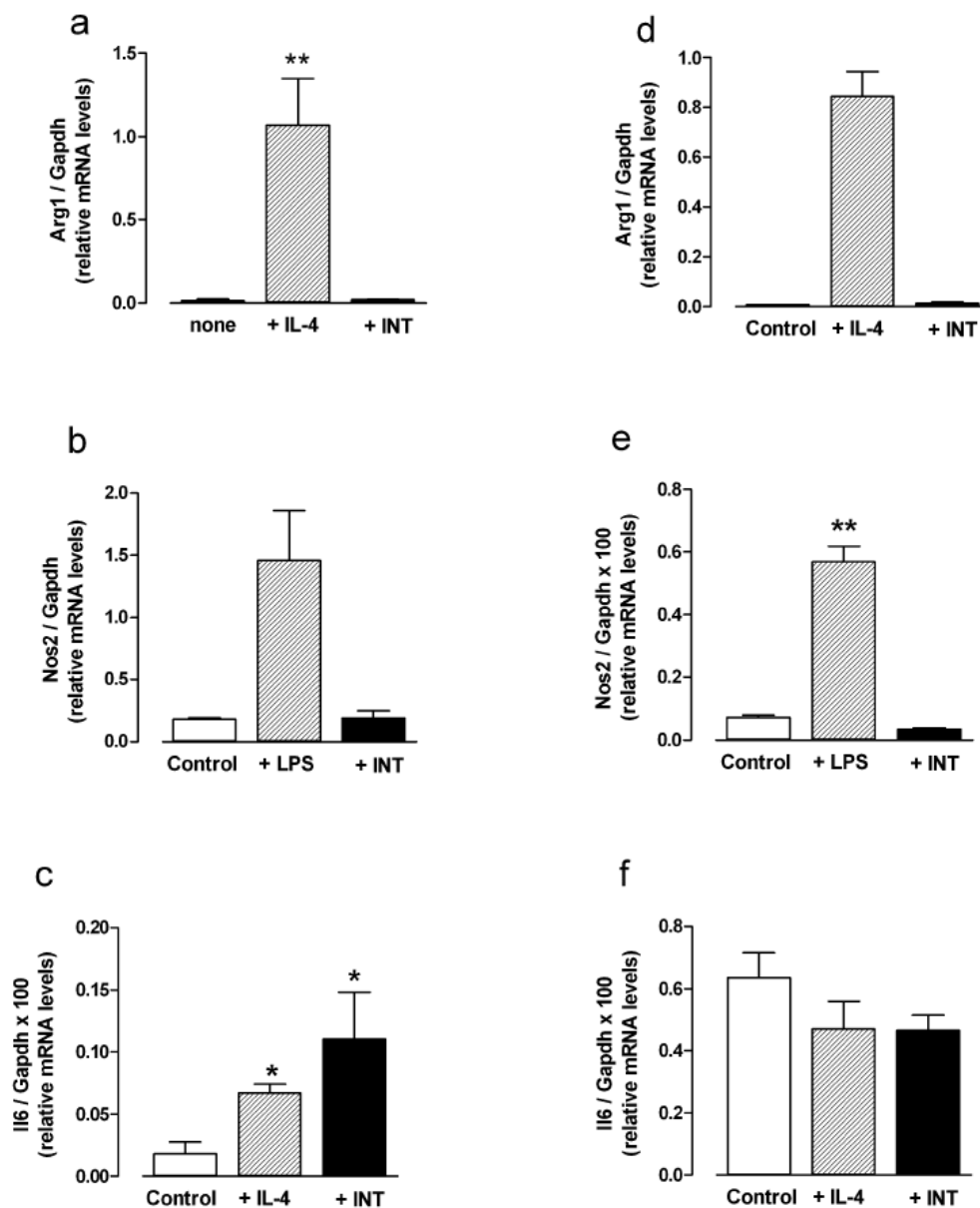


Figure 4: INTs effects on gene expression in murine macrophages. RAW264.7 (a, b, c) or MH-S cells (d, e, f) were incubated for 72 h in the presence of INTs (120 $\mu\text{g}/\text{cm}^2$, 72h), IL-4 (10 ng/ml, 24h), or LPS (0.1 $\mu\text{g}/\text{ml}$, 18h), as indicated. At the end of the treatment, mRNA was extracted and the abundance of the mRNAs of *Arg1* (a, d), *Nos2* (b, e), and *Il-6* (c, f) was determined and expressed vs. the abundance of *Gapdh* mRNA. Data represent means of three independent determinations, each performed in replicate, with SD shown * $p < 0.05$, ** $p < 0.01$ vs. control.

Also the expression of *Nos2* for the inducible isoform of nitric-oxide synthase, a marker of classical macrophage activation [32-34], was not stimulated by INTs although readily several-fold increased by LPS (b and e). Interestingly, the expression level of this marker was very different for the macrophage populations, as a likely result of the different tissue origin and differentiated phenotype demonstrated. The absence of *Nos2* induction was consistent with the lack of accumulation of nitrites in the culture medium of RAW264.7 cells (Figure 5). However, the gene for Interleukin 6 (*Il6*), a pro-inflammatory cytokine not specifically associated either to classical or alternative macrophage activation was modestly induced by INTs in RAW264.7 cells (c) but not in MH-S macrophages (f).

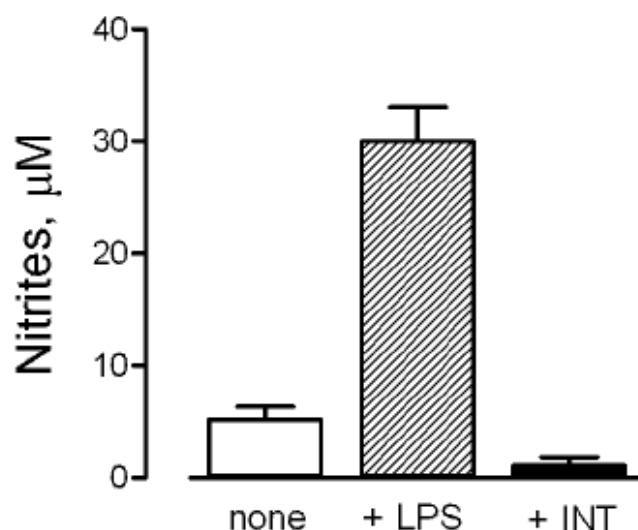


Figure 5: INT effects on nitrite production in murine macrophages. RAW264.7 cells were incubated for 72 h in the presence of INT ($120 \mu\text{g}/\text{cm}^2$, 72 h) or LPS ($0.1 \mu\text{g}/\text{ml}$, 18 h), as indicated. At the end of the treatment, the concentration of nitrites in the extracellular medium was determined. Data represent means of five independent determinations with SD obtained in a representative experiment, repeated twice with comparable results ** $p < 0.01$ vs. control

3. Imogolite nanotubes do not markedly alter the permeability of airway epithelial cell monolayers

A prolonged incubation with SWCNTs or MWCNTs progressively impairs the barrier properties of airway epithelial cells in a dose-dependent way [10,11].

To compare the effects of these nanotubes and INTs on the airway epithelial barrier, we incubated confluent monolayers of Calu-3 cells with either nanomaterials (at a nominal dose of $80 \mu\text{g}/\text{cm}^2$ of monolayer) and measured the trans-epithelial electrical resistance (TEER) up to seven days of treatment (Figure 6a). As expected, MWCNTs and SWCNTs caused a significant increase in the monolayer permeability.

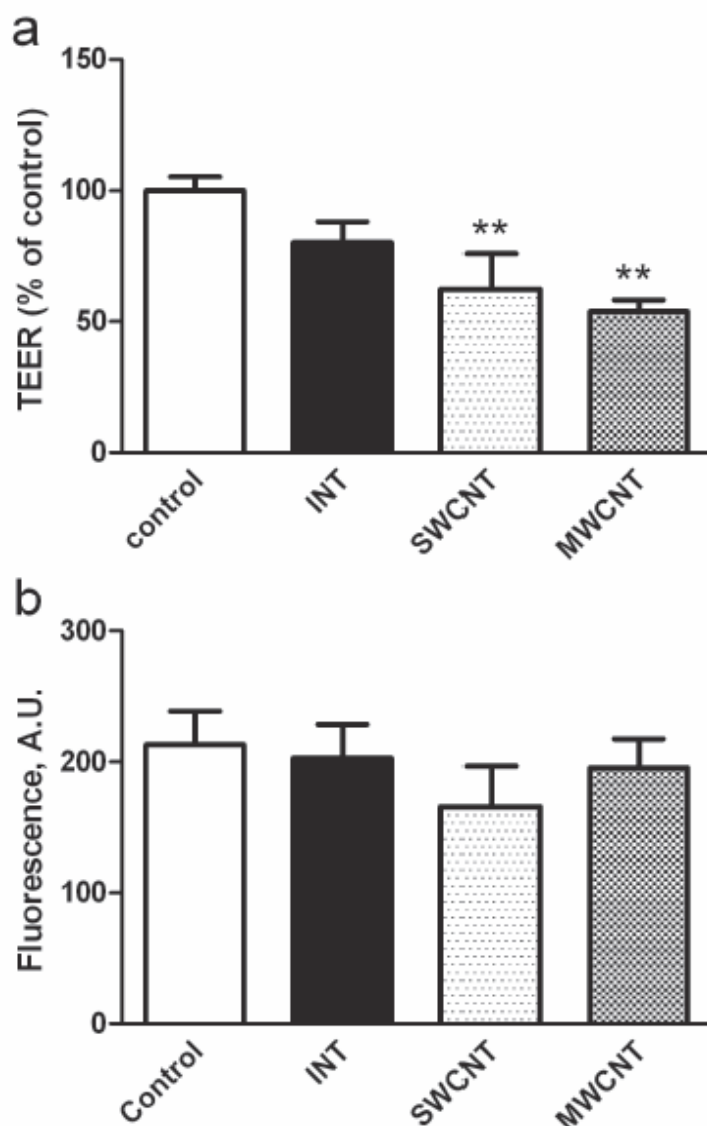


Figure 6: Differential effects of INTs, MWCNTs and SWCNTs on the trans-epithelial electrical resistance (TEER) and viability of Calu-3 monolayers. Calu-3 cells were cultured for 10 days on $0.4 \mu\text{m}$ membrane filters. At the end of this period, INT, MWCNT, or SWCNT, all at $80 \mu\text{g}/\text{cm}^2$, were added to the apical chamber of the culture system. TEER (A) and viability (B) were determined after 7 days. Empty bar, control monolayers maintained in the absence of nanomaterials. The figure shows a representative experiment repeated twice with comparable results. Data are means \pm S.D ($n = 4$). ** $p < 0.01$ vs. control, untreated cultures.

Indeed, TEER was 50 % lower than control for MWCNTs and 40 % lower for SWCNTs. On the contrary, INTs did not alter TEER significantly. Cell viability, evaluated with resazurin method (Figure 6b) in the same monolayers, was not significantly affected by any nanotubes. We can conclude that imogolite nanotubes behave as a very low-toxicity material, which modestly affect macrophage viability. Indeed, INTs do not induce macrophage activation and do not significantly alter the barrier properties of airway epithelial monolayers. Bridged Al(OH)Al groups exposed at the outer surface may play a role in the observed low toxicity. Additionally, it is known since the beginning of the last century that aluminum ions are able to reduce the toxicity of crystalline silica [35]. The impregnation of quartz powders with an aluminum salt inhibits most adverse reactions to silica *in vivo* and decrease the generation of ROS and DNA damage caused by silica [36,37] by selectively blunting surface active sites. The findings reported in the present study are relevant under two distinct points of view.

First, a low cytotoxicity and the lack of activating effects on macrophage cultures suggest that INTs may provide highly bio-compatible scaffolds for cell growth *in vitro* and *in vivo*. Indeed, the macrophage reaction to bio-materials constitutes a fundamental step in the definition of the biological outcomes of the exposure to foreign materials [38-40]. Both classical and alternative activation modalities are important in this context, since classical activation may justify acute inflammatory reactions, while alternative activation would favor fibrosis and neoangiogenesis. Thus the absence of induction of activation markers upon treatment with INTs represents a good indicator of inertness *in vivo*. Moreover, lack of proactivation effects of INTs has been documented in two distinct macrophage lines (RAW264.7 and MH-S cells) of different tissue origin (peritoneal vs. alveolar) and with distinct polarization towards activation pathways, as indicated by the much higher basal expression of the classical marker *Nos2* detected in RAW264.7 cells.

Second, the availability of reference materials is badly needed in the relatively novel nanotoxicological field. MWCNTs are known to exert significant toxicity in a variety of biological models and, in particular, in macrophages and airway epithelial cells [10,41-43]. On the other hand, SWCNTs are characterized by a low acute toxicity towards macrophages and airway epithelial cells. The exposure to SWCNT, however, is associated *in vivo* to accelerated fibrosis and enhanced formation of granuloma [44,45], a fact consistent with their capability to trigger strong macrophage activation [46].

Iron contamination was proposed as one of the causes of SWCNTs toxicity. Interestingly nanosized fibers of synthetic chrysotile were inert but became toxic upon iron doping [47]. Physico-chemical characteristics of nanomaterials are important determinants of the interaction with biological systems and should be carefully considered when planning in vitro and in vivo studies aimed at assessing adverse effects [48-50].

In the case of INTs, the abundance of OH groups renders the structure very hydrophilic, in particular at the inner surface [51]. The presence of relatively strongly adsorbed water, however, hinders molecular diffusion inside the narrow micropores [52]. Thus, the high hydrophilicity of INT and the exposure of Al may prevent free radical release thus explaining low cytotoxicity towards macrophages. Moreover, silanols, which have been identified as the surface functionalities responsible for silica related cell membrane damage [53], are all exposed in the inside of the imogolite nanotube and, hence, not available to cells.

A.III.1.3. Conclusions

In spite of their shared fibrous nature and comparable dimensions INTs and SWCNTs appear to induce very different responses in macrophages and airway epithelial cells. These differences are likely related to the different chemical nature of the materials. Therefore, we propose that, at least for the effects studied here, INTs are good candidates as a low-toxicity reference material for in vitro toxicological studies on HARNs. Moreover, the substantial inertness of macrophages towards INTs may ensure high biocompatibility as a scaffold for cell growth in different medical settings.

A.III.2. Toxicology of synthetic halloysite

Vergaro *et al.* in 2010 [54] performed a biocompatibility study by MTT method for halloysite nanotubes (HNTs) against MCF-7 (breast cancer) and HeLa (cervical cancer) cells. The MTT assay allows measuring the activity of living cells via mitochondrial dehydrogenase activity. Results are shown in Figure 7. The halloysite suspensions at different concentration (from 1 $\mu\text{g/mL}$ to 1 mg/mL) were diluted with complete culture medium.

The MTT HeLa and MCF-7 cells (105 cells/mL) were added to six-well culture plates at 2 mL/well and incubated with the nanotubes at 37 °C in 5 % CO₂, 95 % relative humidity for 24 to 48 to 72 h. After an appropriate incubation period, cultures were removed from the incubator, and resulting MTT formazane crystals were dissolved with acidified isopropanol solution at equal volume with culture.

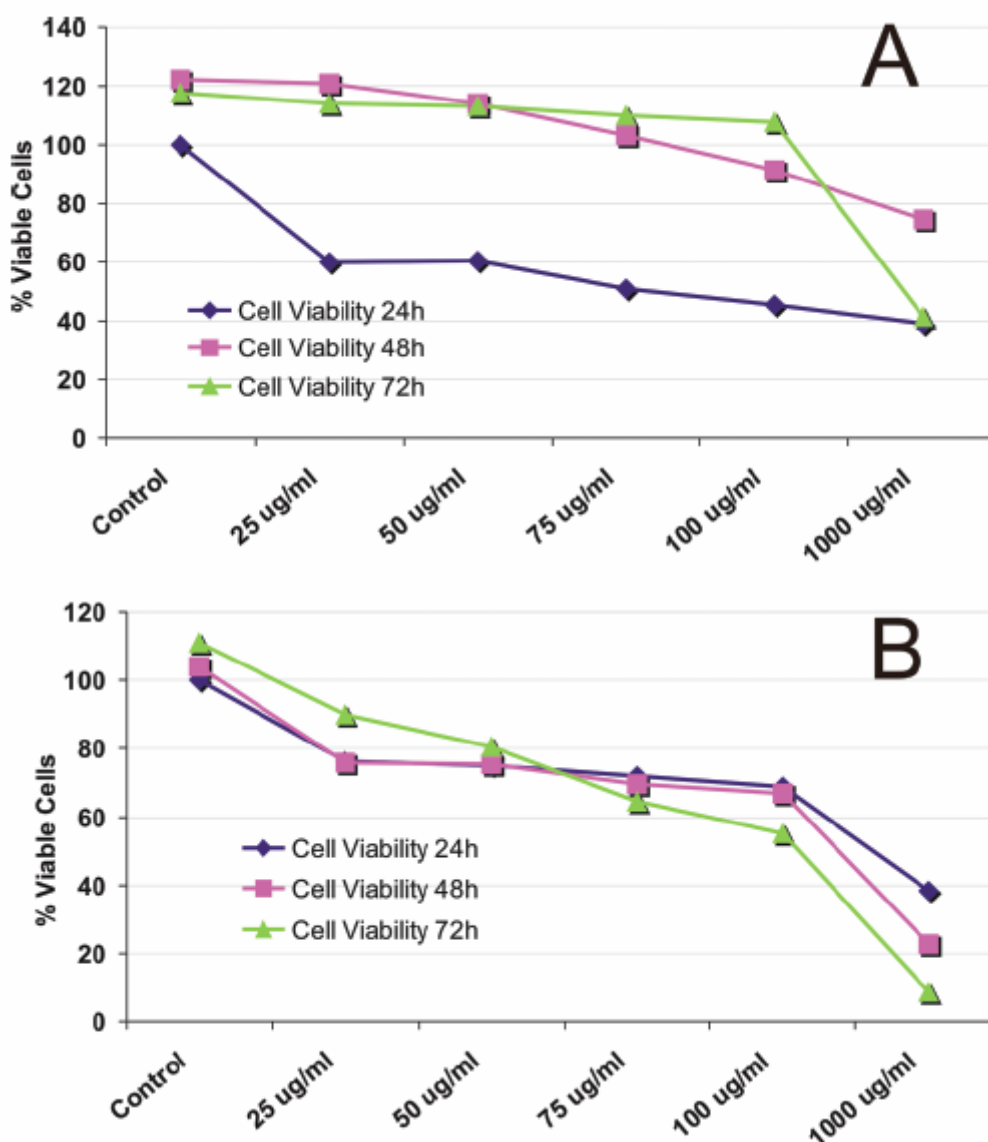


Figure 7: MTT assay of halloysite taken up by (A) HeLa and (B) MCF-7 cell % viability vs. halloysite concentration for 24, 48 and 72 h [54].

Results demonstrated that HNTs are not toxic for cells, i.e. they did not kill the cells, up to concentrations of 75 $\mu\text{g/mL}$, which corresponds to *ca* 10^{11} particles per gram of cells (for comparison, the addition of only 50 $\mu\text{g/mL}$ of usual NaCl killed all the cells).

Being fibrous materials, the comparison of halloysite as well as imogolite, with asbestos is also important. Particularly, as compared to halloysite, asbestos disease is caused by a much smaller number of asbestos fibers per gram of lung, with a concentration of ca. 10^8 particles per gram, 1000 lower than the limit estimated for halloysite.

Additionally, halloysite tubes length is of *ca* 1 μm , thus it is much shorter and thinner than asbestos fibers allowing, analogously to imogolite, their easier removal by macrophages. Toxicity of halloysite may be compared also with that of silica nanoparticles because its external surface exposed to intracellular media is silica. In fact, it is known that many diseases, such as fibrosing collagenous pneumoconiosis and silicosis, are related to prolonged lung exposure to fine inorganic nanoparticles, like crystalline silica. Silica particles in the 0.5-1.5 μm range are generally considered not toxic [82], while if they are larger than 5 μm were found to be more fibrogenic [55-57].

A.III.3. Toxicology of asbestos

Generally speaking, cytotoxicity of asbestos fibers is much higher as compared with that of other minerals [57]. Following inhalation, asbestos are deposited on the epithelial surface of the respiratory tract. The fate of these types of fibers depends on their morphology, on the site of deposition and the aerodynamic characteristics [58,59]. Imogolite and halloysite are hopefully chemically different from asbestos, which are magnesium silicates (chrysolite), or less common Na and Fe, Mg silicates (amphiboles). Additionally, asbestos are constituted by very long fiber structure (5-20 μm length). In a recent review on mechanisms of asbestos pathogenesis [57], it is indicated that asbestos fibers shorter than 5 μm are safer, i.e. are short enough to be removed through phagocytosis by macrophages [60], while long thin fibers are more potent inducers of cell injury and inflammation and can be carried deeper into the distal airways and alveolar regions [58,59].

A.III.4. Toxicology of carbon nanotubes

As already discussed previously, a superficial resemblance between carbon nanotubes (CNTs) and asbestos fibers has motivated several groups in recent years to study the potential health and also environmental risk (ecotoxicity) of CNTs exposure.

The results obtained were not encouraging and has been raising considerable public concern [61], since *in vivo* measurements revealed that they are able to kill cells [62,63]. Evidence exists that a fraction of CNTs can reach the pleura, which represents the site of retention of long fibers and undergoes inflammation, fibrosis and several pathologies including mesothelioma [61].

However, as already discussed and proved in the previous paragraphs, a distinction must be made between single walled nanotubes (SWNTs), consisting of a single layer of graphene sheet rolled into a cylindrical tube and multi walled tubes (MWNTs), comprising two or more layers of concentric cylinders with a separation of about of 0.34 nm between the adjacent layers. In fact, extensive *in vitro* and *in vivo* toxicological assessments of as-grown SWNTs for various exposure pathways, pointed out that single walled tubes have low toxicities. They showed to be nonirritant and a nondermal sensitizer by skin sensitization and conjunctival irritation tests, respectively. The negative mutagenic and dastogenic potentials suggest that they are not carcinogenic. However, Poland *et al.* [61] suggest the need for further studies and great caution be exercised before introducing products containing CNTs into the market, if longterm harm is to be avoided.

A.III.5. References

- [1] L.B. Williams, D.W. Metge, D.D. Eberl, R.W. Harvey, A.G. Turner, P. Prapaipong, A.T. Poret-Peterson *Env. Sci. Technol.* 45 (2011) 3768.
- [2] B. Li, S. Yu, J.Y. Hwang, S. Shi, *J. Miner. Mater. Charact. Eng.* 1 (2002) 61.
- [3] J. Sawai, T. Yoshikawa, *J. App. Microb.* 96 (2004) 803.
- [4] F.G. Ferris, W.S. Fyfe, T. J. Beveridge, *Chem. Geol.* 63 (1987) 225.
- [5] R.M. Torres Sánchez, *Coll. Surf. A* 127 (1997) 135.
- [6] L.M. Liz-Marzan, A.P. Philipse, *J. Phys. Chem.* 99 (1995) 15120.
- [7] S.M. Magaña, P. Quintana, D.H. Aguilar, J.A. Toledo, C. Ángeles-Chávez, M.A. Cortés, L. León, Y. Freile-Pelegrín, T. López, R.M. Torres Sánchez, *J. Mol. Cat. A: Chemical* 281 (2008) 192.
- [8] C.J. Clark, M.B. McBride, *Clays and Clay Min.* 32 (1984) 291.
- [9] B.A. Goodman, H.L. Green, D.B. McPhail, *Geochim. Cosmochim.* 48 (1984) 2143.
- [10] S. Imamura, T. Kokubu, T. Yamashita, Y. Okamoto, K. Kajiwara, H. Kanai, *J. Cat.* 160 (1996) 137.
- [11] Y. Onodera, T. Iwasaki, A. Chatterjee, T. Ebina, T. Satoh, T. Suzuki, H. Mimura, *App. Clay Sc.* 18 (2001) 123.
- [12] Y. Onodera, S. Sunayama, A. Chatterjee, T. Iwasaki, T. Satoh, T. Suzuki, H. Mimura, *App. Clay Sc.* 18 (2001) 135.
- [13] D.M. Moore, R.C. Reynolds, *X-ray Diffraction and the Identification and Analysis of Clay Minerals*, second ed., Oxford University Press, New York, 1997.
- [14] C. Viseras, C. Aguzzi, P. Cerezo, A. Lopez-Galindo, *Appl. Clay Sci.* 36 (2007) 37.
- [15] E. Bojemueller, A. Nennemann, G. Lagaly, *Appl. Clay Sci.* 18 (2001) 277.
- [16] C.H. Hu, M.S. Xia, *Appl. Clay Sci.* 31 (2006) 180.
- [17] B. Lombardi, M. Baschini, R.M. Torres Sánchez, *Appl. Clay Sci.* 24 (2003) 43.
- [18] M. Damonte, R.M. Torres Sánchez, M. dos Santos Afonso, *Appl. Clay Sci.* 36 (2007) 86.
- [19] J.W. Jaynes, R. Zartman, W. Hudnall, *Appl. Clay Sci.* 36 (2007) 197.
- [20] F. Bonina, M. Giannossi, L. Medici, C. Puglia, V. Summa, F. Tateo, *Appl. Clay Sci.* 36 (2007) 77.
- [21] S. Wada, K. Wada, *Clay Min.* 12 (1977) 289.
- [22] K. Wada, *Adsorption phenomena of soils*. Nippon Dojohiryogakukai. Hakuyusha, Tokyo, (1981) 43.
- [23] R.A. Dahlgren, F.C. Ugolini, *Geochim. Cosmochim. Acta.* 53 (1989) 1897.
- [24] T. Takahashi, T. Fukuoka, R.A. Dahlgren, *Soil Sci. Plant Nutr.* 41 (1995) 119.
- [25] Y. Yagasaki, J. Mulder, M. Okazaki, *Geoderma* 137 (2006) 40.
- [26] R.A. Dahlgren, M. Saigusa, F.C. Ugolini, *Adv. Agron.* 82 (2004) 113.
- [27] M. Nanzyo, R.A. Dahlgren, S. Shoji, *Chemical characteristics of volcanic ash soils*. In *Volcanic Ash Soils – Genesis, Properties and Utilization*; Editors: S. Shoji, M. Nanzyo, R.A. Dahlgren, Elsevier, Amsterdam. (1993) 145.
- [28] M. Isabel Carretero, *App. Clay Sc.* 21 (2002) 155.
- [29] T. Xia, M. Kovochich, J. Brant, M. Hotze, J. Sempf, T. Oberley, C. Sioutas, J.I. Yeh, M.R. Wiesner, *Nano Lett.* 6 (2006) 1794.
- [30] E. Bergamaschi, O. Bussolati, A. Magrini, M. Bottini, L. Migliore, S. Bellucci, I. Iavicoli, A. Bergamaschi, *Int. J. Immunopathol. Pharmacol.* 19 (2006) 3.
- [31] V.C. Sanchez, J.R. Pietruska, N.R. Miselis, R.H. Hurt, A.B. Kane, *Wiley Interdiscip. Rev. Nanomed. Nanobiotechnol.* 1 (2009) 511.
- [32] A.A. Shvedova, V.E. Kagan, *J. Intern. Med.* 267 (2010) 106.
- [33] H. Nagai, S. Toyokuni, *Arch. Biochem. Biophys.* 502 (2010) 1.
- [34] M.W. Peterson, M.E. Walter, T.J. Gross, *Am. J. Physiol.* 265 (1993) 308.
- [35] S.Y. Gardner, A.R. Brody, J.B. Mangum, J.I. Everitt, *Exp. Lung. Res.* 23 (1997) 1.
- [36] M.W. Peterson, J. Kirschbaum, *Am. J. Physiol.* 275 (1998) 262.
- [37] B.M. Rotoli, O. Bussolati, M.G. Bianchi, A. Barilli, C. Balasubramanian, S. Bellucci, E. Bergamaschi, *Toxicol. Lett.* 178 (2008) 95.
- [38] B.M. Rotoli, O. Bussolati, A. Barilli, P.P. Zanello, M.G. Bianchi, A. Magrini, A. Pietroiusti, A. Bergamaschi, E. Bergamaschi, *Hum. Exp. Toxicol.* 28 (2009) 361.
- [39] I.N. Mbawuike, H.B. Herscowitz, *J. Leukoc. Biol.* 46 (1989) 119.
- [40] M. Thibodeau, C. Giardina, A.K. Hubbard, *Toxicol. Sci.* 76 (2003) 91.
- [41] K. Soto, K.M. Garza, L.E. Murr, *Acta Biomater.* 3 (2007) 351.
- [42] J. Scheel, S. Weimans, A. Thiemann, E. Heisler, M. Hermann, *Toxicol. In Vitro* 23 (2009) 531.
- [43] M. Ghiazza, M. Polimeni, I. Fenoglio, E. Gazzano, D. Ghigo, B. Fubini, *Chem. Res. Toxicol.* 23 (2010) 620.

- [44] W.E. Finkbeiner, S.D. Carrier, C.E. Teresi, *Am. J. Respir. Cell. Mol. Biol.* 9 (1993) 547.
- [45] C.I. Grainger, L.L. Greenwell, G.P. Martin, B. Forbes, *Eur. J. Pharm. Biopharm.* 71 (2009) 318.
- [46] K. Togami, S. Chono, T. Seki, K. Morimoto, *Drug Metab. Pharmacokinet.* 24 (2009) 411.
- [47] B. Slutter, S.M. Bal, I. Que, E. Kaijzel, C. Lowik, J. Bouwstra, W. Jiskoot, *Mol. Pharm.* 7 (2010) 2207.
- [48] J. Brillault, W.V. De Castro, W. Couet, *Antimicrob. Agents Chemother.* 54 (2010) 543.
- [49] B. Bharatwaj, L. Wu, J.A. Whittum-Hudson, S.R. da Rocha, *Biomaterials* 31 (2010) 7376.
- [50] M. Bur, H. Huwer, L. Muys, C.M. Lehr, *J. Aerosol Med. Pulm. Drug Deliv.* 23 (2010) 119.
- [51] B.L. Burgess, G. Cavigliolo, M.V. Fannucchi, B. Illek, T.M. Forte, M.N. Oda, *Int. J. Pharm.* 399 (2010) 148.
- [52] J. O'Brien, I. Wilson, T. Orton, F. Pognan, *Eur. J. Biochem.* 267 (2000) 5421.
- [53] M.G. Bianchi, G.C. Gazzola, L. Tognazzi, O. Bussolati, *Neuroscience* 151 (2008) 1042.
- [54] L.B. Salem, C. Bosquillon, L.A. Dailey, L. Delattre, G.P. Martin, B. Evrard, B. Forbes, *J. Control Release*, 136 (2009) 110
- [55] C.A. Louis, V. Mody, W.L. Jr. Henry, J.S. Reichner, J.E. Albina, *Am. J. Physiol.* 276 (1999) 237.
- [56] S.M. Morris, D. Kepka-Lenhart, L.C. Chen, *Am. J. Physiol.* 275 (1998) 740.
- [57] C. Stempin, L. Giordanengo, S. Gea, F. Cerban, *J. Leukoc. Biol.* 27 (2002) 727.
- [58] G. Raes, R. Van den Bergh, P. De Baetselier, G.H. Ghassabeh, C. Scotton, M. Locati, A. Mantovani, S. Sozzani, *J. Immunol.* 174 (2005) 6561.
- [59] M. Yamashita, H. Niki, M. Yamada, S. Mue, K. Ohuchi, *Eur. J. Pharmacol.* 338 (1997) 151.
- [60] M. Munder, K. Eichmann, J.M. Moran, F. Centeno, G. Soler, M. Modolell, *J. Immunol.* 163 (1999) 3771.
- [61] D. Chakravorty, Y. Kato, T. Sugiyama, N. Koide, M.M. Mu, T. Yoshida, T. Yokochi, *J. Immunol.* 166 (2001) 2011.
- [62] B. Fubini, Health effects of silica. In: *The surface properties of silicas*, 5 Edited by L.J.P. Chichester, J. Wiley and Sons (1998) 415.
- [63] R. Duffin, P.S. Gilmour, R.P. Schins, A. Clouter, K. Guy, D.M. Brown, W. MacNee, P.J. Borm, K. Donaldson, V. Stone, *Toxicol. Appl. Pharmacol.* 176 (2001) 10
- [64] A.M. Knaapen, C. Albrecht, A. Becker, D. Hohl, A. Winzer, G.R. Haenen, P.J. Borm, R.P. Schins, *Carcinogenesis* 23 (2002) 1111.
- [65] Z. Xia, J.T. Triffitt, *Biomed. Mater.* 1 (2006) 1.
- [66] K.S. Jones, *Semin. Immunol.* 20 (2008) 130.
- [67] J.M. Anderson, A. Rodriguez, D.T. Chang, *Semin. Immunol.* 20 (2008) 86.
- [68] S. Hirano, S. Kanno, A. Furuyama, *Toxicol. Appl. Pharmacol.* 232 (2008) 244.
- [69] H.L. Karlsson, P. Cronholm, J. Gustafsson, L. Moller, *Chem. Res. Toxicol.* 21 (2008) 1726.
- [70] L. Tabet, C. Bussy, N. Amara, A. Setyan, A. Grodet, M.J. Rossi, J.C. Pairon, J. Boczkowski, S. Lanone, *J. Toxicol. Environ. Health A*, 27 (2009) 60.
- [71] A.A. Shvedova, E.R. Kisin, R. Mercer, A.R. Murray, V.J. Johnson, A.I. Potapovich, Y.Y. Tyurina, O. Gorelik, S. Arepalli, D. Schwegler-Berry, *Am. J. Physiol. Lung Cell Mol. Physiol.* 289 (2005) 698.
- [72] J.B. Mangum, E.A. Turpin, A. Antao-Menezes, M.F. Cesta, E. Bermudez, J.C. Bonner, *Part. Fibre Toxicol.* 3 (2006) 15.
- [73] C.C. Chou, H.Y. Hsiao, Q.S. Hong, C.H. Chen, Y.W. Peng, H.W. Chen, P.C. Yang, *Nano Lett.* 8 (2008) 437.
- [74] E. Gazzano, F. Turci, E. Foresti, M.G. Putzu, E. Aldieri, F. Silvagno, I.G. Lesci, M. Tomatis, C. Riganti, C. Romano, *Chem. Res. Toxicol.* 20 (2007) 380.
- [75] A.E. Nel, L. Madler, D. Velegol, T. Xia, E.M. Hoek, P. Somasundaran, F. Klaessig, V. Castranova, M. Thompson, *Nat. Mater.* 8 (2009) 543.
- [76] V. Stone, H. Johnston, R.P. Schins, *Crit. Rev. Toxicol.* 39 (2009) 613.
- [77] B. Fubini, M. Ghiazza, I. Fenoglio, *Nanotoxicology* 4 (2010) 347.
- [78] B. Creton, D. Bougeard, K.S. Smirnov, J. Guilment, O. Poncelet, *Phys. Chem. Chem. Phys.* 10 (2008) 4879.
- [79] B. Bonelli, I. Bottero, N. Ballarini, S. Passeri, F. Cavani, E. Garrone, *J. Cat.* 264 (2009) 15.
- [80] I.I. Slowing, C.W. Wu, J.L. Vivero-Escoto, V.S. Lin, *Small* 5 (2009) 57.
- [81] V. Vergaro, E. Abdullayev, Y.M. Lvov, A. Zeitoun, R. Cingolani, R. Rinaldi, S. Leporatti, *Biomacromolecules* 11 (2010) 820.
- [82] J. Wiessner, N. Mandel, P. Sohnle, G. Mandel, *Exp. Lung. Res.* 15 (1989) 801.
- [83] B. Mossman, A. Churg, *Am. J. Respir. Crit. Care Med.* 157 (1998) 1666.
- [84] G. Hart, T. Hesterberg, *J. Occup. Environ. Med.* 40 (1998) 29.
- [85] Agency for Toxic Substances and Disease Registry (ATSDR) (2001). *Toxicological profile for asbestos*. US department of Health and Human Services. Atlanta, US.

PhD Thesis: Hybrid organic/inorganic nanotubes of imogolite type

- [86] Risk Assessment Information System (RAIS, 1995), Toxicity summary for asbestos, Chemical Hazard Evaluation and Communication Group, Biomedical and Environmental Information Analysis Section Health and Safety Research Division.
- [87] International Programme on Chemical Safety (IPCS) (1986). Asbestos and other natural mineral fibres. Environmental Health Criteria 53. WHO. Geneva.
- [88] C.A. Poland, R. Duffin, I. Kinloch, A. Maynard, W.A.H. Wallace, A. Seaton, V. Stone, S. Brown, W. MacNee, K. Donaldson, Nature Nanotechnol. 3 (2008) 423.
- [89] A. Porter, M. Gass, K. Muller, J. Skepper, P. Midgley, M. Welland, Nat. Mater. 2 (2007) 713.
- [90] A. Nel, T. Xia, L. Madler, N. Li, Science 311 (2006) 622.

Conclusions

The work described in the present PhD work is focused on the synthesis and characterization of two new modified imogolite nanotubes, obtained either by direct or post-synthesis reactions. Unmodified synthetic imogolite, labeled as Imo, was also synthesized and considered as reference material.

Following the guidelines proposed by Farmer and co-workers [1], **Imo** nanotubes were obtained via sol-gel synthesis in acid environment and mild conditions using a silicon precursor, TEOS (tetraethoxysilane), letting react with an aluminum precursor, *i.e.* aluminum sec-Butoxide (ASB) [2], in a 75 mM aqueous solution of HClO₄, according to the following molar ratios, Si:Al:HClO₄ = 1,x:2:1. A slight excess of TEOS was used in order to prevent the preferential formation of gibbsite (aluminum hydroxide) during hydrolysis. A polymerization step follows, before collecting nanotubes powder. Systematic studies were run in order to optimize the synthesis conditions. It resulted that the polymerization step at 100 °C is critical for the synthesis success. Moreover, filtration can efficiently substitute the dialysis step before final drying, as FT-IR spectra confirmed. Finally, if dried powder is washed against deionized water for a night, crystallinity of the sample is enhanced, as XRD patterns revealed. In contrast to natural imogolite [3], the outer diameter of synthetic Imo is larger, *ca* 2.4 nm (vs. 2 nm), as XRD patterns confirmed. Moreover, N₂ adsorption/desorption isotherms of Imo at nominal 77 K resulted to be of Type I, typical of microporous materials [4]. For the first time, an imogolite sample with total surface of 1378 m²/g was obtained, due to particularly likely controlled operative conditions, confirming how the reproducibility of this synthesis is hard to achieve. On the contrary, statistically imogolite samples with surface area of *ca* 300 m²/g were collected.

The first new hybrid material of imogolite type was synthesized by a direct method replacing TEOS with a new silicon precursor, *i.e.* TEMS, triethoxymethylsilane. The complete hydrophobization of the internal surface was achieved, as FTIR and MAS NMR measurements confirmed, and methyl-imogolite, labeled as **Me-Imo**, with stoichiometric formula, (OH)₃Al₂O₃SiCH₃, was collected [5,6]. Electron microscopy images showed a material composed of interwoven bundles of nanotubes, similar to those of Imo. However, Me-Imo fibers have larger diameter (*ca* 15-20 nm) and longer length (*ca* 200 nm) as compared to Imo nanotubes. As can be seen from XRD patterns of Me-Imo tubes collected after several batch syntheses, if the polymerization step is run at too high temperature (T ≥ 105°C), impurities can be formed.

Particularly, according to literature, this can be disclosed by the presence of an aluminum oxide polymorph, called nordstrandite [7,8]. Type I adsorption/desorption isotherms of N₂ at nominal 77 K of Me-Imo were also obtained, as in case of Imo. It resulted that the average specific surface area of Me-Imo is roughly more than twice as that of imogolite. Inner diameter length, corresponding to the relative Pore Size Distributions (PSDs) calculated applying the Non Local-Density Functional Theory (NL-DFT) method, is increased from 0.95 nm (Imo) to 1.63 nm, thus confirming the increased SSA value. In fact, larger pores may form as cavities in the fibrous network of heterogeneous imogolite bundles. Finally, volumetric CH₄ adsorption was measured. It turned out that both Imo and Me-Imo can reversibly adsorb methane in the explored pressure range, 5-35 bar. Furthermore, second adsorption run values are not affected by the additional outgassing treatment, pointing out the thermal stability of the adsorbent. Curve-fits obtained by assuming a Langmuir model of adsorption, are in fair agreement with experimental points: both the maximum adsorbed volumes (76.81 and 29.65 cm³/g for Me-Imo and Imo, respectively) and equilibrium constants (0.03 and 0.06 bar⁻¹ for Me-Imo and Imo, respectively), were calculated.

The second new material of imogolite-type was obtained by the subsequent post-synthesis silylation reaction of Me-Imo with 3-aminopropyltriethoxysilane (3-APS) in anhydrous conditions. Morphology of *Me-Imo-NH₂* is unaltered after the grafting procedure, while it is noteworthy that all diffraction patterns showed basically the same reflections, although at different intensities, so ruling out the possibility that functionalization only introduced some disordering in the nanotube array. Porosimetry measurements evidenced a small decreasing in specific surface area, probably due to the blockage of pores mouth by grafted 3-APS. MAS NMR technique was a crucial tool to demonstrate the successful synthesis: ²⁹Si, ¹³C and 2D-HETCOR ¹H-¹³C MAS NMR experiments were useful to distinguish the presence of two sources of silicon and carbon, inner Si-CH₃ and outer Si-CH₂CH₂CH₂NH₃⁺ groups, respectively. Moreover, it was possible to identify the structure of the grafted species at the outer surface, by considering the resulting different silicon environments: T^x species and silicon atoms involved in the expected oligomerization of 3-APS are present, respectively. These evidence explain the protonation of terminal amino group, which was also confirmed by ¹H-Echo MAS NMR and FT-IR spectra of the as-synthesized sample. Moreover, a mild treatment with a 0.001 M NaOH solution, was able to convert ammonium ions into substituted amine species.

In fact, carbamic species were seen in collected FT-IR spectra after dosing of CO₂ on unprotonated Me-Imo-NH₂, thus further confirming the successful functionalization. Finally, comparable volumetric adsorption measurements of CO₂ were found, according to the following sequence, Me-Imo > Me-Imo-NH₂-30 > Imo. This result is reasonable, since not all the outer surface of Me-Imo has been functionalized.

Study of imogolite-like nanotubes stability revealed that structure integrity of Imo, Me-Imo and Me-Imo-NH₃⁺-30 is maintained within 300 °C. Particularly, the leaching of grafted amino groups from Me-Imo-NH₃⁺-30 occurs above 150 °C. As nanotubes are organized in a network of interwoven bundles, three kinds of pores can be distinguished [9-10]: i) intra-tube pores (the voids of constituent nanotubes, about 1 nm wide); ii) inter-tube pores, i.e. spacings between three aligned tubes in a regular packing (0.3–0.4 nm wide); iii) slit mesopores among bundles. NH₃ adsorption showed, as also expected by porosimetry results, that type-B pores of Imo are too narrow to be accessible by the gas. Thus, external bridged more acidic Al(OH)Al species are detectable only in case of Me-Imo and Me-Imo-NH₃⁺-30.

Collapsing of nanotubes structure is evidenced by the formation of a lamellar phase at 500 °C. The mechanism proposed wants the cleavage of nanotubes to happen across their diameter, causing the formation of the following repeating sequence, Al-O-Si-O-Si-O-Al, for Imo, and Si-CH₂-O-Al, in case of Me-Imo and Me-Imo-NH₃⁺-30. Both NH₃ and CO interaction confirmed that with Imo, more acidic silanols are formed, coherently with the lamellar structure proposed by MacKenzie [11]. On the contrary, with lamellar Me-Imo and Me-Imo-NH₃⁺-30, physisorbed CO along with heterogeneous acidic sites are found, analogously to Al-rich microporous silicates [12].

In spite of their shared fibrous nature, according to the preliminary study performed, imogolite nanotubes can be proposed as good candidates as a low-toxicity reference material for in vitro toxicological studies on HARNs, High Aspect Ratio Nanomaterials. Moreover, the substantial inertness of macrophages towards the tubes, may ensure high bio-compatibility as a scaffold for cell growth in different medical settings.

As a general conclusion, it is worth noting that, in contrast with the more famous carbon nanotubes, Imo-derived nanotubes may be functionalized under mild conditions by means of direct or post-synthesis procedure.

In particular, properties of both the inner and the outer surface may be properly changed, and the hydrophilicity of the material may be modulated as well as porosity and thermal stability. This may open the way to new and promising applications.

References

- [1] V.C. Farmer, A.R. Fraser in M .M. Mortland and V.C. Farmer (Eds.), Proc. Int. Clay Conf., Oxford, (1978), Elsevier, Amsterdam, 547.
- [2] B. Bonelli, I. Bottero, N. Ballarini, S. Passeri, F. Cavani, E. Garrone, *J. Cat.* 264 (2009) 15.
- [3] N. Yoshinaga, A. Aomine, *Soil Sci. Plant Nutr.* 8(3) (1962) 22.
- [4] S.J. Gregg K.S.W. Sing, *Adsorption, Surface Area and Porosity*, 2nd ed; Academic Press: (1982) London
- [5] I. Bottero, B. Bonelli, S. Ashbrook, P. Wright, W. Zhou, M. Tagliabue, M. Armandi, E. Garrone, *Phys. Chem. Chem. Phys.*, 13 (2011) 744 -750.
- [6] B. Bonelli, I. Bottero and E. Garrone, Italian patent 0001380065.
- [7] A. Violante, P.M. Huang, *Clays and clay Min.* 41(5) (1993) 590.
- [8] P. Violante, A. Violante, J.M. Tait, *Clays and Clay Min.* 30(6) (1982) 431.
- [9] W.C.Ackerman, D.M.Smith, J.C.Huling, Y. Kim, J.K.Bailey, C.J. Brinker, *Langmuir* 9 (1993) 1051.
- [10] M.A.Wilson, G.S.H.Lee, R.C.Taylor, *Clays Clay Miner.* 50(3) (2002) 348.
- [11] K.J. MacKenzie, M.E. Bowden, J.W.M. Brown, R.H. Meinhold, *Clays and Clay Min.* 37(4) (1989) 317.
- [12] W. Daniell, U. Schubert, R. Glöckler, A. Meyer, K. Noweck, H. Knözinger, *Appl. Catal. A* 196 (2000) 247.

Acknowledgments

I wish to express my sincerest gratitude to **Prof. Barbara Bonelli** and **Prof. Edoardo Garrone**, whose scientific supervision and guidance have been fundamental during these three years. Additionally, I wish to thank my French supervisors, **Prof. Christian Fernandez** and **Dr. Aurélie Vicente**, for their professionalism and precious help concerning MAS NMR characterizations. The foreign period spent in Caen, represented for me an excellent chance to learn new skills, so improving my professional background.

My PhD period would not have been so pleasant if true friends had not been present, always encouraging me: **Svetla, Roberto, Massimo, Davide, Clara, Monica, Claudio** and **Ratna**, are the dearest of mine. Thank you all for your friendship.

Finally, I want to thank my **big family** for all their love and support never missed every day.

*Publications, congress and school
participations
2009-2011*

Publications

P. Antoniotti, L. Operti, R. Rabezzana, F. Turco, C. Zanzottera, M. Giordani, F. Grandinetti, “*Gas-phase reactions of XH_3^+ ($X = C, Si, Ge$) with NF_3 : a comparative investigation on the detailed mechanistic aspects*”, Journal of Mass Spectrometry, 44 (2009) 1348.

D. Barbera, F. Cavani, T. D'Alessandro, G. Fornasari, S. Guidetti, A. Aloise, G. Giordano, M. Piumetti, B. Bonelli, C. Zanzottera, “*The control of selectivity in benzene hydroxylation catalyzed by TS-1: The solvent effect and the role of crystallite size*”, Journal of Catalysis, 275 (2010) 158.

C. Zanzottera, A. Vicente, E. Celasco, C. Fernandez, E. Garrone, B. Bonelli, “*Synthesis and characterization of imogolite nanotubes functionalized on both external and internal surfaces*” submitted to Journal of Physical Chemistry C

O. Bussolati, B.M. Rotoli, P.P. Zanello, B. Bonelli, C. Zanzottera, E. Garrone, I. Fenoglio, B. Fubini, M. Ghiazza, E. Bergamaschi, “*Nanotubes of the Aluminosilicate Imogolite exhibit Mild Toxicity for Macrophages and Airway Epithelial Cells*” (editing).

Congress participations

Oral presentation

B. Bonelli, C. Zanzottera, I. Bottero, E. Garrone, M. Tagliabue, S.E. Ashbrook, P.A. Wright, “*Hybrid organic/inorganic nanotubes of imogolite type*” 22nd NAM Conference, Detroit (USA), **5-10th June 2011**.

Poster

I. Bottero, C. Zanzottera, M. Armandi, E. Garrone, B. Bonelli, “*Capture and release of CO₂ by imogolite-like nanotubes*”, IZC - IMMS 2010 Conference, Sorrento (Italy), **4-9th July 2010**.

C. Zanzottera, B. Bonelli, A. Vicente, C. Fernandez, E. Garrone, “*Hybrid organic/inorganic nanotubes of imogolite type*”, 5th International FEZA Conference, Valencia (Spain), **3-7th July 2011**.

C. Zanzottera, B. Bonelli, A. Vicente, C. Fernandez, E. Garrone, “*Hybrid organic/inorganic nanotubes of imogolite type*”, 4th International Symposium on Advanced micro- and mesoporous materials, Riviera Resort – Varna (Bulgaria), **6-9th September 2011**.

B. Bonelli, C. Zanzottera, A. Vicente, C. Fernandez, E. Garrone, “*Hybrid organic/inorganic nanotubes of the imogolite type*”, 5th IDECAT/ERIC-JCAT Conference on Catalysis, Bertinoro (Italy), **22-25th September 2011**.

School participations

AIC International School, “*Scattering techniques, from microscopic to atomic structures*”, **30th August - 4th September 2009**, Camerino (Italy).

Summer School of Calorimetry “*Calorimetry and thermal methods in catalysis*”, **21-25th June 2010**, Lyon (F).

